Appendix 3.6.2

THERMAL EVALUATION OF THE ES-3100 SHIPPING CONTAINER FOR NCT AND HAC (FINAL DESIGN WITH CATALOG 277-4 NEUTRON ABSORBER)

THIS PAGE INTENTIONALLY LEFT BLANK.

Appendix 3.6.2

THERMAL EVALUATION OF THE ES-3100 SHIPPING CONTAINER FOR NCT AND HAC (FINAL DESIGN WITH CATALOG 277-4 NEUTRON ABSORBER)

INTRODUCTION

Thermal analyses of the ES-3100 shipping container are performed to determine the temperature distribution within the packaging during Normal Conditions of Transport (NCT) as specified in 10 CFR 71.71(c)(1).[1] Transient thermal analyses are performed by treating the problem as a cyclic transient with the incident heat flux due to solar radiation applied and not applied in alternating 12-hour periods.

Additionally, thermal analyses of the ES-3100 shipping container are performed to determine the thermal response of the packaging to Hypothetical Accident Conditions (HAC) as specified in 10 CFR 71.73(c)(4).[1] Since physical testing of the ES-3100 shipping container was conducted with no internal heat source or insolation during cool-down,[2] temperature increases due to internal heat loads of 0.4, 20, and 30 W as well as temperature increases due to the application of insolation during cool-down following the HAC fire are calculated. Although earlier revisions of 10 CFR 71 specifically state that insolation does not need to be evaluated before, during, or after HAC, the current version of 10 CFR 71 and associated guidance are unclear regarding the need for consideration following HAC testing. Since the Nuclear Regulatory Commission (NRC) has taken the position that insolation must be considered and evaluated following fire testing, analyses are conducted to determine the effect of insolation following the HAC fire on the ES-3100 shipping container. The predicted temperature increases may be used to adjust physical test data for those loads not included in the physical tests.

FINITE ELEMENT MODEL DESCRIPTION

A two-dimensional axisymmetric finite element model of the ES-3100 shipping container is constructed using MSC.Patran[3] and imported as an orphaned mesh into ABAQUS/CAE[4] for application of boundary conditions, interactions, and loads. The model is constructed of DCAX4 (four-node linear axisymmetric heat transfer quadrilateral) and DCAX3 (3-node linear axisymmetric heat transfer triangular) elements for evaluation for NCT and HAC. The actual contents of the ES-3100 shipping container are not specifically modeled—instead, the content source heat load (if desired) is modeled by applying a uniform heat flux to the inner surfaces of the containment vessel. This is a conservative approach in that package temperatures will not be reduced in a transient analysis by the heat capacity of the contents. A schematic of the finite element model is presented in Figure 1 with details of the upper and lower portions of the model shown in Figure 2 and Figure 3, respectively. The model consists of five materials: stainless steel (drum, liners, and containment vessel), Kaolite, neutron absorber, silicone rubber, and air in the gaps between the drum liner and containment vessel and between the drum liner and top plug. Degree-of-freedom "ties" are made at the interfaces of the different material regions in order to allow the heat to flow through the model. Thermal properties of the materials used in the analysis are presented in Table 1.

Heat is transferred to the model from the contents (i.e., decay heat of the contents) via heat flux boundary conditions applied to the inner surface of the elements representing the containment vessel. Additionally, solar heat fluxes are applied to the model during NCT and HAC post-fire cool-down via heat flux boundary conditions. The heat applied to the model via the boundary conditions is transferred through the model via conduction and thermal radiation. Heat is rejected from the external surfaces of the model via natural convection and thermal radiation boundary conditions.

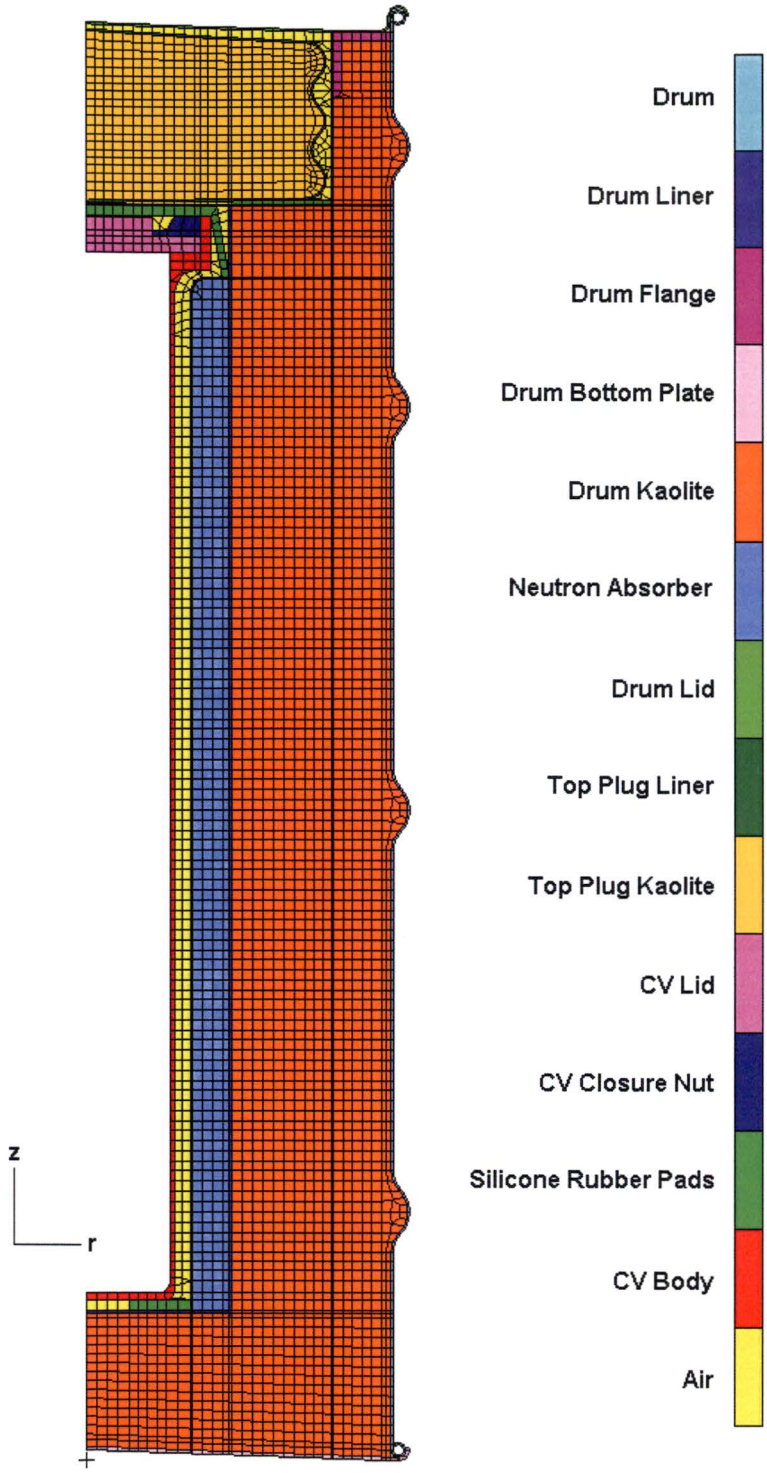

Figure 1. MSC.Patran axisymmetric finite element model of the ES-3100 shipping container.

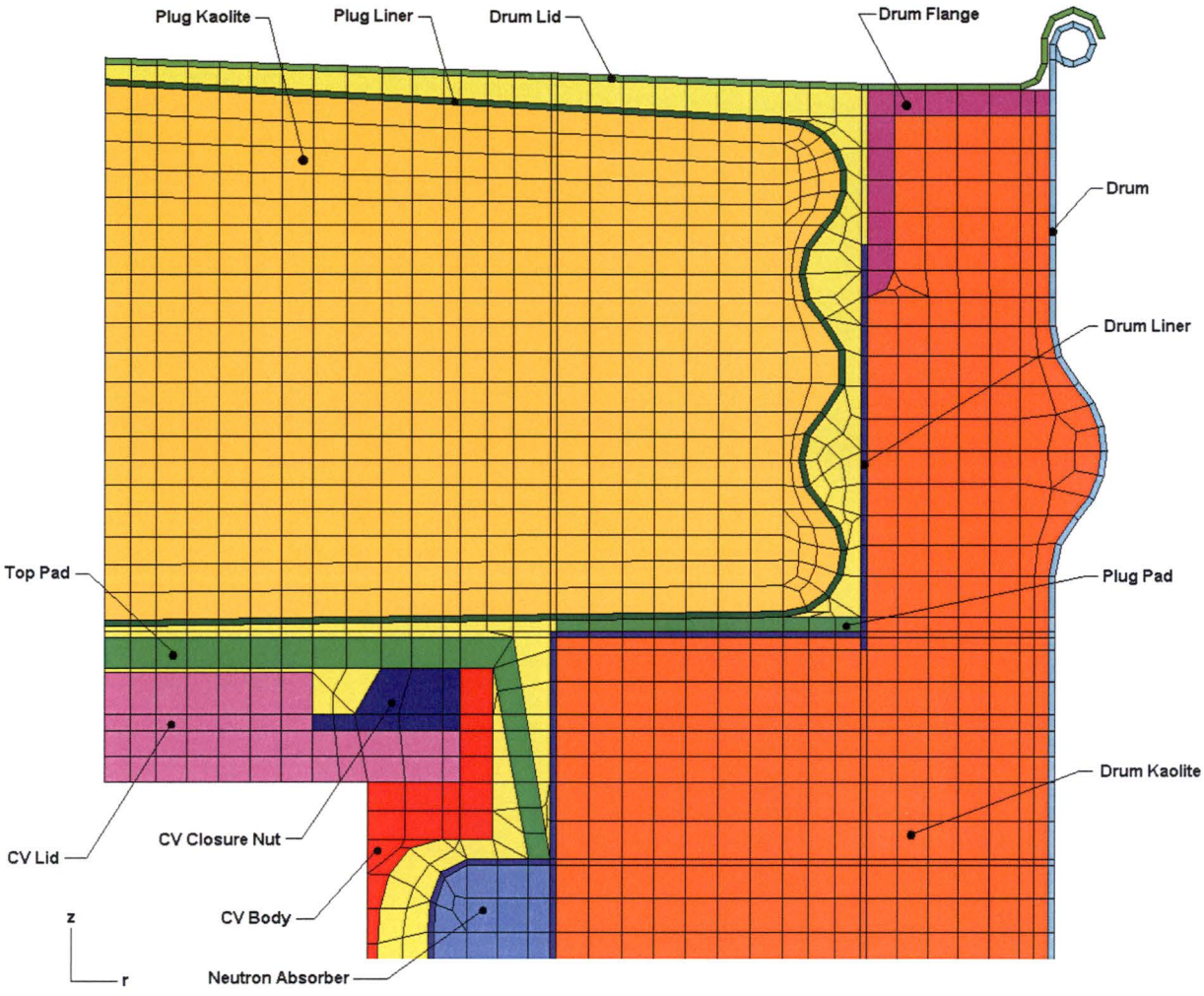

Figure 2. MSC.Patran axisymmetric finite element model of the ES-3100 shipping container (upper portion detail).

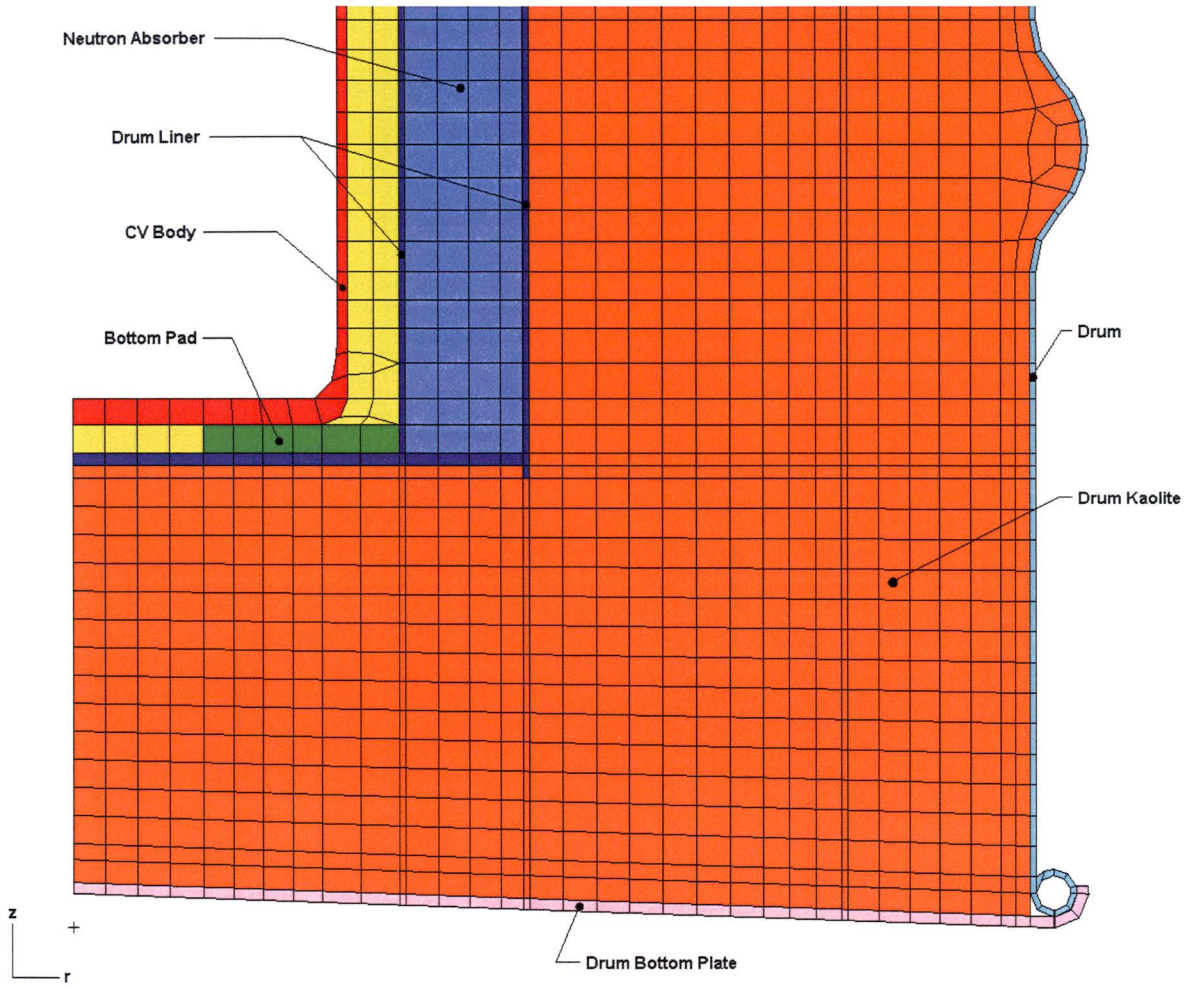

Figure 3. MSC.Patran axisymmetric finite element model of the ES-3100 shipping container (lower portion detail).

Table 1. Thermal properties of the materials used in the thermal analyses.

Material	Temperature (°F)	Thermal Conductivity (Btu/h-in.-°F)	Density (lbm/in.^{3})	Specific heat (Btu/lbm-°F)	Emissivity
Stainless steel	-279.67	0.443[(a)]	0.285[(a)]	0.065[(a)]	0.22[(a)]
	-99.67	0.607	–	0.096	–
	260.33	0.799	–	0.123	–
	620.33	0.953	–	0.133	–
	980.33	1.088	–	0.139	–
	1340.33	1.223	–	0.146	–
	1700.33	1.348	–	0.153	–
	2240.33	1.526	–	0.163	–
Kaolite 1600	68	0.0093[(b)]	0.011[(c)]	0.2[(d)]	–
	212	0.0091	–	–	–
	392	0.0081	–	–	–
	572	0.0072	–	–	–
	1112	0.0082	–	–	–
Neutron absorber (Catalog No. 277-4)	-31	0.0457[(e)]	0.0579[(f)]	0.125[(e)]	–
	73.4	0.0485	–	0.186	–
	140	0.0400	–	0.239	–
	212	0.0295	–	0.242	–
	302	0.0305	–	0.291	–
Silicone rubber	–	0.0161[(g)]	0.047[(g)]	0.300[(g)]	1.0[(h)]
Air	-9.67	1.074×10^{-3}[(a)]	4.064×10^{-5}[(a),(i)]	0.240[(a)]	–
	80.33	1.266×10^{-3}	–	0.241	–
	170.33	1.445×10^{-3}	–	0.241	–
	260.33	1.628×10^{-3}	–	0.242	–
	350.33	1.796×10^{-3}	–	0.244	–
	440.33	1.960×10^{-3}	–	0.246	–
	530.33	2.114×10^{-3}	–	0.248	–
	620.33	2.258×10^{-3}	–	0.251	–
	710.33	2.393×10^{-3}	–	0.254	–
	800.33	2.523×10^{-3}	–	0.257	–
	890.33	2.644×10^{-3}	–	0.260	–
	980.33	2.759×10^{-3}	–	0.263	–
	1070.33	2.870×10^{-3}	–	0.265	–
	1160.33	2.985×10^{-3}	–	0.268	–
	1250.33	3.096×10^{-3}	–	0.270	–
	1340.33	3.212×10^{-3}	–	0.273	–
	1520.33	3.443×10^{-3}	–	0.277	–

Notes:
(a) F. P. Incropera and D. P. DeWitt, *Fundamentals of Heat and Mass Transfer*, 2nd edition, John Wiley & Sons, New York, 1985.
(b) Hsin Wang, *Thermal Conductivity Measurements of Kaolite*, ORNL/TM-2003/49.
(c) Based on a baked density of 19.4 lbm/ft^3 (0.011 lbm/in^3). Specification JS-YMN3-801580-A003 requires a baked density of 22.4 ± 3 lbm/ft^3. Using a lower value for the Kaolite density results in higher temperatures on the containment vessel because the heat capacity of the Kaolite is minimized—allowing more heat to flow to the containment vessel; therefore, the thermal analyses are performed using a low-end density of 19.4 lbm/ft^3. The HAC analyses also consider a high-end density of 30 lbm/ft^3.
(d) FAX communication from J. W. Breuer of Thermal Ceramics, Engineering Department, August 11, 1995.
(e) W. D. Porter and H. Wang, *Thermophyical Properties of Heat Resistant Shielding Material*, ORNL/TM-2004/290, ORNL, Dec. 2004. Specific heat values are presented in MJ/m^3-K in ORNL/TM-2004/290—converted to mass-based units using a density of 105 lbm/ft^3.
(f) Based on a cured density of density of 100 lbm/ft^3 (0.0579 lbm/in^3). B. F. Smith and G. A. Byington, *Mechanical Properties of 277-4*, Y/DW-1987, January 19, 2005presents a range of measured densities between approximately 100 and 110 lbm/ft^3 for Catalog No. 277-4. Therefore, in order to minimize the heat capacity of the material and allow more heat to be transferred to the containment vessel, the lower-bound value is used. The HAC analyses also consider a high-end density of 110 lbm/ft^3.
(g) THERM 1.2, thermal properties database by R. A. Bailey.
(h) Conservatively modeled as 1.0.
(i) Constant density value evaluated at 100°F.

MODELED HEAT TRANSFER MECHANISMS

The heat transfer mechanisms included in the thermal model such, as thermal radiation, natural convection, and insolation (solar heat flux) are described in detail in the following sections.

Heat Transfer Between Package Exterior and Ambient

The heat transfer between the exterior of the package and the ambient (or fire) is modeled as a combination of radiant heat transfer and natural convection. The heat transfer due to radiant exchange with the environment is calculated as:[5]

$$q''_{rad} = \sigma F_e \left(T_s^4 - T_a^4 \right), \tag{1}$$

where σ = Stefan-Boltzmann constant,
F_e = overall exchange factor,
T_s = container outer surface temperature (absolute), and
T_a = ambient or fire temperature (absolute).

The overall interchange factor is calculated as:[5]

$$F_e = \left[\frac{1}{\frac{1}{\varepsilon_p} + \frac{A_p}{A_s}\left(\frac{1}{\varepsilon_s} - 1 \right)} \right], \tag{2}$$

where ε_p = emissivity of package surface,
A_p = surface area of the package,
A_s = surface area of the surroundings, and
ε_s = emissivity of surroundings.

For NCT and the cool-down period following the HAC fire, the area of the surroundings is assumed to be much larger than the surface area of the package; therefore, Eq. 2 reduces to:

$$F_e \approx \varepsilon_p . \tag{3}$$

An emissivity value of 0.22,[6] which is typical of clean stainless steel, is assumed for the outer surfaces of the drum during NCT and during the cool-down period following the HAC fire. In reality, the outer surfaces of the drum will have a much higher emissivity following the HAC fire; therefore, this assumption is conservative.

During the HAC fire, the area of the surroundings is assumed to be approximately equal to the surface area of the drum; therefore, Eq. 2 reduces to:

$$F_e = \left[\frac{1}{\frac{1}{\varepsilon_p} + \frac{1}{\varepsilon_s} - 1} \right]. \tag{4}$$

During the HAC 30-minute fire, an emissivity of 0.8 is assumed for the drum, and an emissivity of 0.9 is assumed for the fire per the guidance of 10 CFR 71.74(c)(4).[1] This results in an overall exchange factor of 0.7347 during the HAC fire using Eq. 4.

The natural convection heat transfer from the package surface to the ambient air is calculated as:

$$q''_{convection} = h\left(T_s - T_a\right). \tag{5}$$

where h = natural convection heat transfer coefficient,
T_s = container outer surface temperature, and
T_a = ambient or fire temperature.

During the NCT transient thermal analyses and the steady-state thermal analyses (used to obtain the starting temperature distribution in the package for NCT and HAC when a content heat load is present), the shipping container is assumed to be in an upright (vertical) orientation. The top of the drum is modeled as a heated horizontal flat plate facing up using the following correlation:[6]

$$h = \left(\frac{k}{L}\right) C_1 \, Ra^{C_2}, \tag{6}$$

where k = thermal conductivity of air,
L = characteristic length (= D/4 per Ref. 6),
D = diameter of the package,
Ra = Rayleigh number,
C_1 = constant (see Table 2), and
C_2 = constant (see Table 2).

The Rayleigh number in Eq. 6 is defined as:

$$Ra = \frac{g \beta \Delta T L^3}{\nu \alpha}, \tag{7}$$

where g = acceleration of gravity,
β = coefficient of thermal expansion,
ΔT = temperature difference,
ν = kinematic viscosity [μ/ρ],
μ = absolute viscosity,
α = thermal diffusivity [$k/(\rho C_p)$],
ρ = density of air, and
C_p = specific heat of air.

The properties of air used in the natural convection calculations are presented in Table 3.

Table 2. Coefficients for natural convection correlations.

Coefficient	Rayleigh Number Range	Value
C_1	$10^4 < Ra < 10^7$ $10^7 < Ra < 10^{11}$	0.54 0.15
C_2	$10^4 < Ra < 10^7$ $10^7 < Ra < 10^{11}$	0.25 1/3
C_3	$Ra < 10^9$ $Ra > 10^9$	0.680 0.825
C_4	$Ra < 10^9$ $Ra > 10^9$	0.670 0.387
C_5	$Ra < 10^9$ $Ra > 10^9$	0.25 1/6
C_6	$Ra < 10^9$ $Ra > 10^9$	4/9 8/27
C_7	$Ra < 10^9$ $Ra > 10^9$	1 2

Source: F. P. Incropera and D. P. DeWitt, *Fundamentals of Heat and Mass Transfer*, 2nd ed., John Wiley & Sons, New York, 1985.

Table 3. Properties of air used in natural convection calculations.

Temperature (°F)	Thermal Conductivity (Btu/h-in.-°F)	Density (lbm/in.^{3})	Specific Heat (Btu/lbm-°F)	Kinematic Viscosity (in.^{2}/h)	Thermal Diffusivity (in.^{2}/h)	Prandtl Number
-9.67	1.074×10^{-3}	5.039×10^{-5}	0.240	6.384×10^{1}	8.872×10^{1}	0.720
80.33	1.266×10^{-3}	4.196×10^{-5}	0.241	8.867×10^{1}	1.255×10^{2}	0.707
170.33	1.445×10^{-3}	3.595×10^{-5}	0.241	1.167×10^{2}	1.668×10^{2}	0.700
260.33	1.628×10^{-3}	3.147×10^{-5}	0.242	1.474×10^{2}	2.137×10^{2}	0.690
350.33	1.796×10^{-3}	2.796×10^{-5}	0.244	1.807×10^{2}	2.634×10^{2}	0.686
440.33	1.960×10^{-3}	2.516×10^{-5}	0.246	2.164×10^{2}	3.164×10^{2}	0.684
530.33	2.114×10^{-3}	2.286×10^{-5}	0.248	2.543×10^{2}	3.722×10^{2}	0.683
620.33	2.258×10^{-3}	2.097×10^{-5}	0.251	2.940×10^{2}	4.291×10^{2}	0.685
710.33	2.393×10^{-3}	1.935×10^{-5}	0.254	3.360×10^{2}	4.871×10^{2}	0.690
800.33	2.523×10^{-3}	1.797×10^{-5}	0.257	3.800×10^{2}	5.468×10^{2}	0.695
890.33	2.644×10^{-3}	1.677×10^{-5}	0.260	4.261×10^{2}	6.082×10^{2}	0.702
980.33	2.759×10^{-3}	1.573×10^{-5}	0.263	4.739×10^{2}	6.696×10^{2}	0.709
1070.33	2.870×10^{-3}	1.480×10^{-5}	0.265	5.234×10^{2}	7.310×10^{2}	0.716
1160.33	2.985×10^{-3}	1.397×10^{-5}	0.268	5.742×10^{2}	7.979×10^{2}	0.720
1250.33	3.096×10^{-3}	1.324×10^{-5}	0.270	6.261×10^{2}	8.649×10^{2}	0.723
1340.33	3.212×10^{-3}	1.258×10^{-5}	0.273	6.802×10^{2}	9.374×10^{2}	0.726
1520.33	3.443×10^{-3}	1.144×10^{-5}	0.277	7.912×10^{2}	1.088×10^{3}	0.728

Source: F. P. Incropera and D. P. DeWitt, *Fundamentals of Heat and Mass Transfer*, 2nd ed., John Wiley & Sons, New York, 1985.

During the NCT transient thermal analyses and the steady-state thermal analyses, the sides of the drum are modeled as a vertical flat plate using the following correlation:[6]

$$h = \left(\frac{k}{L}\right)\left[C_3 + \frac{C_4\,Ra^{C_5}}{\left(1+\left[\frac{0.492}{Pr}\right]^{9/16}\right)^{C_6}}\right]^{C_7}, \qquad (8)$$

where L = characteristic length = the drum height,
C_3 = constant (see Table 2),
C_4 = constant (see Table 2),
C_5 = constant (see Table 2),
C_6 = constant (see Table 2),
C_7 = constant (see Table 2), and
Pr = Prandtl number.

The bottom of the drum is conservatively modeled as adiabatic during the NCT transient analyses and the steady-state analyses.

During the HAC 30-minute fire and the post-fire cool-down, the shipping container is assumed to be in a horizontal orientation (as it is during furnace testing). As such, the top and bottom of the drum are modeled as vertical flat plates using Eq. 8 having a characteristic length, L, equivalent to the drum diameter, and the sides of the drum are modeled as a horizontal cylinder using the following correlation ($10^{-5} < Ra < 10^{12}$):[6]

$$h = \left(\frac{k}{D}\right)\left[0.60 + \frac{0.387\,Ra^{1/6}}{\left(1+\left[\frac{0.559}{Pr}\right]^{9/16}\right)^{8/27}}\right]^2, \qquad (9)$$

where D = diameter of the package,

The calculated natural convection film coefficients used in the thermal analyses of the ES-3100 are presented graphically in Figure 4 and Figure 5 for NCT and HAC, respectively.

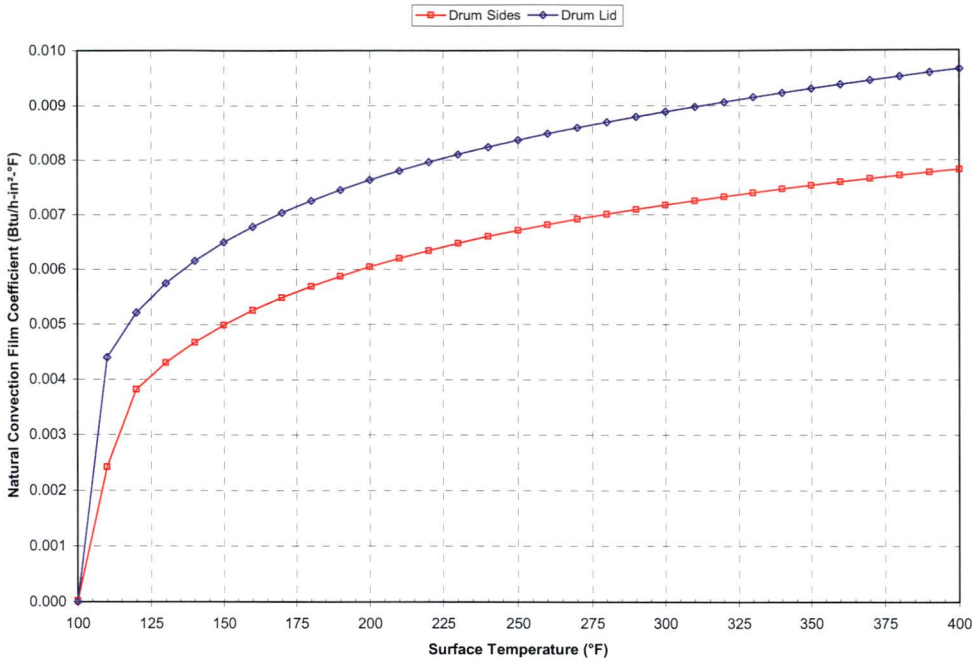

Figure 4. Natural convection film coefficients applied to the drum surfaces during NCT and steady-state conditions.

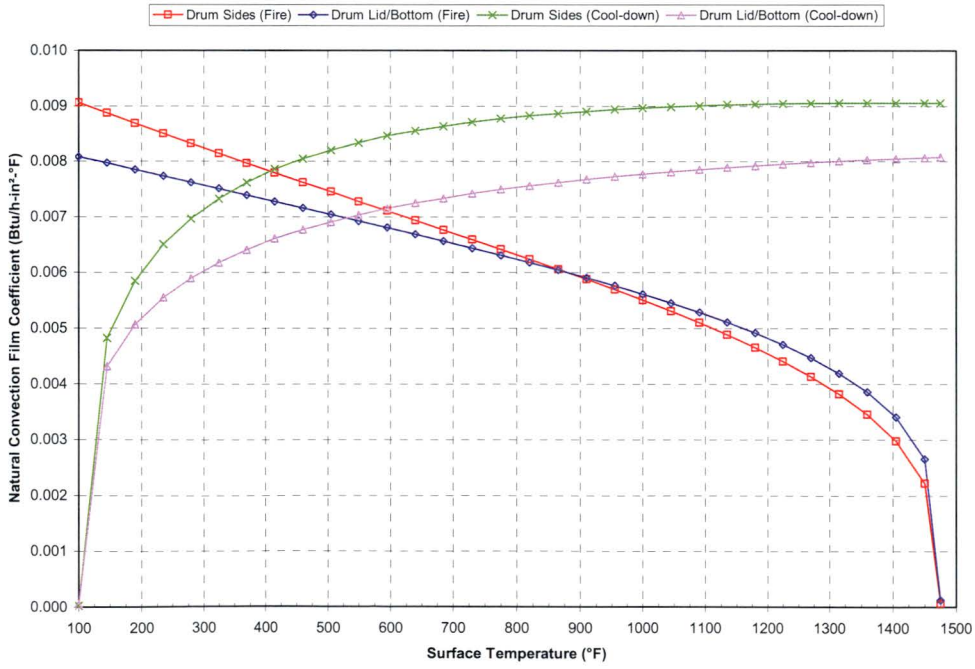

Figure 5. Natural convection film coefficients applied to the drum surfaces during HAC.

Insolation

The following insolation (incident solar radiation) data is required for NCT per 10 CFR 71.71(c)(1):[1]

Form and location of surface	Total insolation for a 12-hour period (cal/cm²)
Flat surfaces transported horizontally	
Base	None
Other surfaces	800
Flat surfaces not transported horizontally	200
Curved surfaces	400

The total insolation values specified in the previous table are for a 12-hour period. For analytical purposes, these values are "time-averaged" over the entire 12-hour period (i.e., divided by 12). Therefore, the incident solar heat fluxes ($q''_{solar,i}$) used in the analyses for NCT and cool-down following the HAC fire are as follows:

During NCT, the drum is in an upright (vertical) orientation; therefore, the following heat fluxes are applied to the external surfaces of the drum to represent insolation:

Top $$q''_{solar,i} = 1.7074\ \text{Btu/h} - \text{in.}^2, \quad (10)$$

Sides $$q''_{solar,i} = 0.8537\ \text{Btu/h} - \text{in.}^2, \quad (11)$$

Bottom $$q''_{solar,i} = 0. \quad (12)$$

During the cool-down period following the HAC 30-minute fire, the drum is assumed to be in a horizontal orientation; therefore, the following heat fluxes are applied to the external surfaces of the drum to represent insolation:

Top $$q''_{solar,i} = 0.4269\ \text{Btu/h} - \text{in.}^2, \quad (13)$$

Sides $$q''_{solar,i} = 0.8537\ \text{Btu/h} - \text{in.}^2, \quad (14)$$

Bottom $$q''_{solar,i} = 0.4269\ \text{Btu/h} - \text{in.}^2. \quad (15)$$

The insolation is applied as a square-wave function (i.e., alternating on and off in 12-hour periods) in the thermal analysis. The heat flux values presented in Eqs. 10–15 represent the insolation absorbed by the package surface since a drum absorptivity of 1.0 was conservatively assumed. An analytical study has been performed on a similar shipping package that investigated three methods of applying the insolation.[7] The three methods consisted of 1) performing a steady-state analysis assuming the insolation is applied continuously by distributing the heat flux evenly throughout a 24-hour period, 2) performing a transient analysis assuming the insolation is represented by a step function (i.e., applied and then not applied in 12-hour cycles, and 3) performing a transient analysis where the incident insolation is represented by a sinusoidal function that varies throughout the day. The results of the study indicate that the method used in applying the insolation has a significant effect on the temperatures of the outermost portions of the package. However, since the total insolation over any 24-hour period is the same for all cases, internal package temperatures are relatively unaffected by the way in which the insolation is applied. Since the containment vessel O-ring temperatures are of primary concern in this evaluation, the step function method for applying the insolation is suitable.

Heat Transfer Across Gaps in the Package

Heat transfer across all gaps in the package is modeled by a combination of radiant exchange and conduction. Natural convection heat transfer is not included across the gaps in the model. Scoping studies performed for a similar shipping package indicate that the heat transfer due to natural convection in relatively small gaps is approximately a factor of 6 times less than the heat transfer due to radiant exchange.[7] These calculations assumed a temperature difference of 9°F across the gap. Based on these previous calculations, the effect of neglecting the natural convection in the gap regions is minimal. The emissivity values used in the analysis for all internal radiating surfaces in the model are presented in Table 1.

Radiant exchange across gaps is modeled using the cavity radiation feature of ABAQUS/Standard.[8] For each cavity (or enclosure), radiation surfaces are defined as shown in Figure 6 and Figure 7.

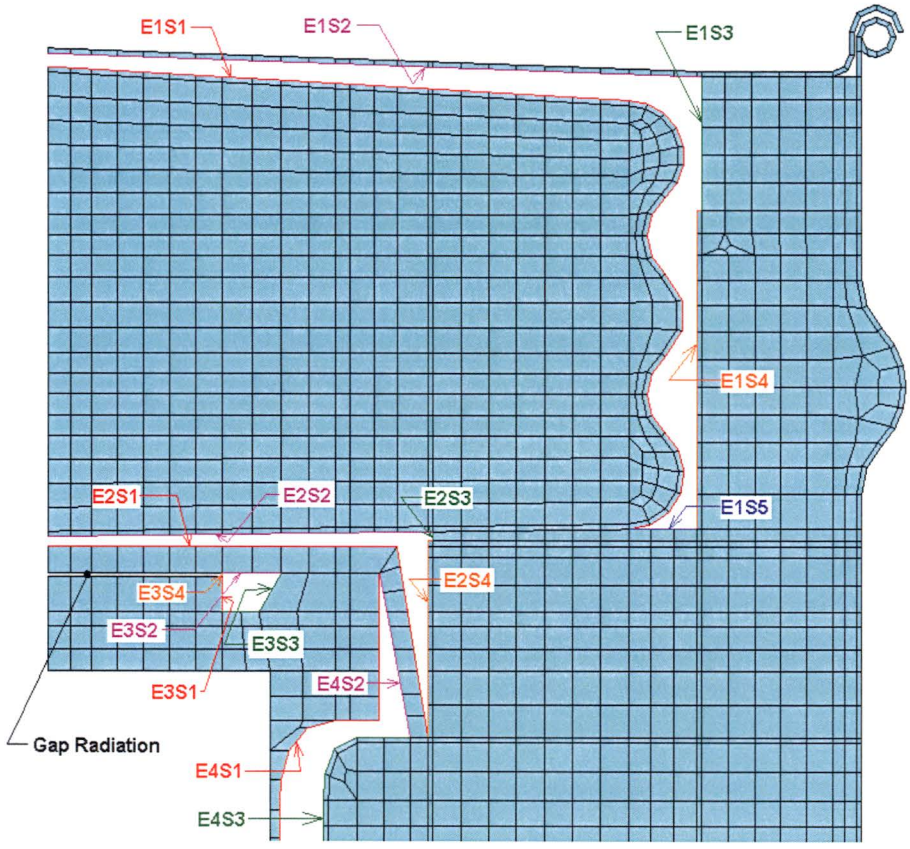

Figure 6. Radiation cavity surface definitions (top portion of the model).

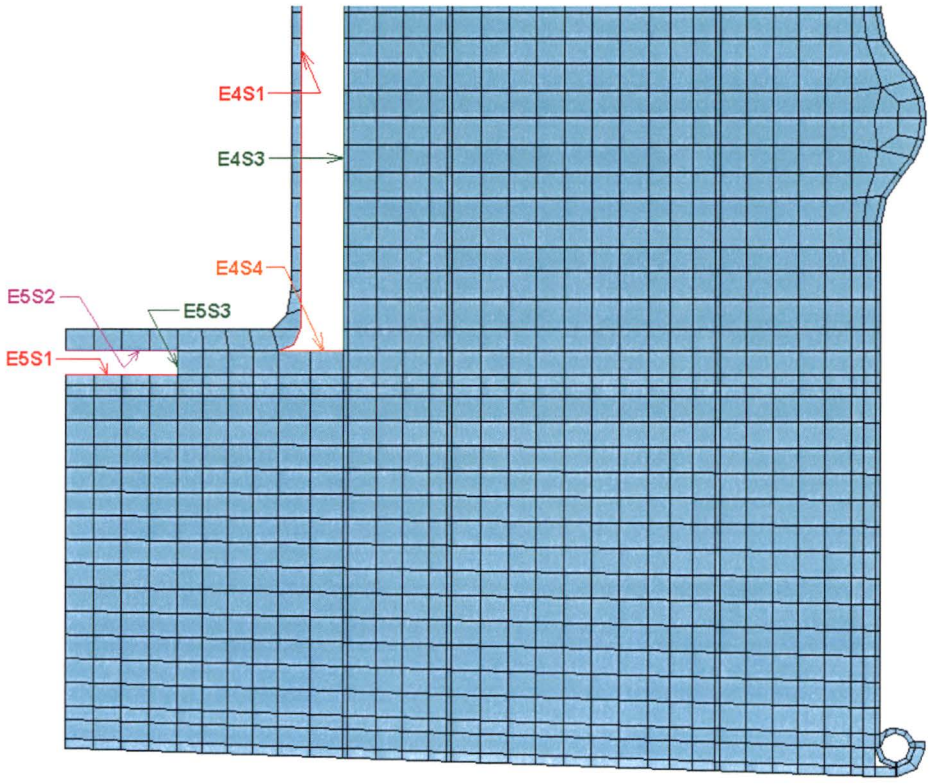

Figure 7. Radiation cavity surface definitions (bottom portion of the model).

As shown in Figure 6 and Figure 7, the various gaps in the model are divided into five separate cavities (designated 'E1' through 'E5' in the figures) with between three and five surfaces (designated 'S1' through 'S5' in the figures) in each cavity for radiation calculations. Because the gap between the CV lid and top pad is small in relation to its characteristic length, radiation exchange is modeled using the gap radiation feature in ABAQUS/Standard with a view factor of 1.0 assigned. As a result, a shell element (type DSAX1) is defined in the model with the radiation surface E3S4 (see Figure 6) superimposed to close off cavity 3. The DSAX1 element is assigned the properties of air, and surface E3S4 is assigned a small emissivity value of 0.01 since it is an imaginary surface used to close the cavity.

Content Heat Load

In order to simulate the decay heat generated by the ES-3100 shipping container contents, a uniform heat flux is applied to the element edges representing the inner surface of the containment vessel in the model. Content heat loads of 0, 0.4, 20, and 30 W are investigated in this report. The uniform heat flux (q''_{source}) for a given content heat load is calculated using the following equation:

$$q''_{source} = \frac{Q \times 3.4123}{2\left(\frac{\pi D_i^{\,2}}{4}\right) + \pi(D_i)(H)}, \qquad (16)$$

where, Q = content heat load (W),
D_i = inside diameter of the containment vessel (5.06 in.),
H = height of the containment vessel cavity (31.00 in.).

Using Eq. 16, a content heat load of 0.4 W results in a uniform heat flux of 2.5608×10^{-3} Btu/h-in.^{2}, a content heat load of 20 W results in a uniform heat flux of 0.12804 Btu/h-in.^{2}, and a content heat load of 30 W results in a uniform heat flux of 0.19206 Btu/h-in.^{2}.

DISCUSSION OF ANALYTICAL RESULTS

All thermal analyses discussed in this report were performed using ABAQUS/Standard[8] on an Intel Pentium 4–based Microsoft Windows 2000 computer. Temperatures are monitored at selected locations in the model as shown in Figure 8 through Figure 11.

Steady-state Conditions Analyses Results

Steady-state thermal analyses are performed on the finite element model of the ES-3100 shipping container for three cases having content heat loads of 0.4, 20, and 30 W. The temperature distribution results from these analyses are used as the starting temperature distributions within the model when performing the transient thermal analyses for NCT and the HAC 30-minute fire. The boundary conditions for these steady-state analyses include a combination of thermal radiation exchange and natural convection applied to the top and sides of the drum using an ambient temperature of 100°F. The bottom of the drum is modeled as an adiabatic surface (i.e., no heat transfer). Additionally, the content heat load is simulated by applying a uniform heat flux to the surfaces of the elements representing the inner surface of the containment vessel. The calculated steady-state temperature distribution within the model of the ES-3100 shipping container for content heat loads of 0.4, 20, and 30 W is presented in Table 4.

As presented in Table 4, the maximum accessible surface temperature of the package when exposed to an ambient temperature of 100°F in the shade is 100.43°F (38.02°C), 114.39°F (45.77°C), and 120.08°F (48.93°C) for content heat loads of 0.4, 20, and 30 W, respectively.

Normal Conditions of Transport Analyses Results

Transient thermal analyses are performed on the finite element model of the ES-3100 shipping container to simulate NCT with content heat loads of 0, 0.4, 20, and 30 W. The insolation required for NCT per 10 CFR 71.71(c)(1)[1] is applied to the top and sides of the drum in alternating 12-hour periods (i.e., 12 hours on and 12 hours off) with the drum bottom remaining adiabatic during the transient thermal analysis. An ambient temperature of 100°F as stipulated in 10 CFR 71 is used in the NCT analysis. The initial temperature distribution within the package for the NCT transients was determined from steady-state analyses (with radiation and natural convection boundary conditions applied to the top and sides of the drum) for each internal heat load. For the case with no internal heat source (0 W), the initial temperature distribution within the package was assumed to be at a uniform 100°F. As with the steady-state analyses discussed previously, applying a uniform heat flux to the internal surfaces of the elements representing the containment vessel simulates the content heat load.

The transient thermal analyses simulate a five-day period of cyclic solar loading with 12 hours of insolation being applied at the beginning of each day (i.e., sunrise) followed by 12 hours in which there is no insolation to end the day (i.e., sunset). This five-day period allows for "quasi steady-state" conditions

to be reached. While the temperature of a particular node within the model changes with respect to time in the transient analyses, the maximum temperature that node reaches from day-to-day does not change once a "quasi steady-state" condition is reached. In particular, the maximum temperature of the key location on the containment vessel (i.e., at the O-ring) on day 5 is within 0.004°F of the maximum temperature of the same location on day 4.

The maximum temperatures of several locations within the model are summarized in Table 5 for content heat loads of 0, 0.4, 20, and 30 W. The maximum temperatures reported in Table 5 represent "quasi steady-state" conditions. Temperature-history plots of several locations within the model are also depicted graphically in Figure 12 through Figure 15 for various content heat loads. Additionally, temperature contours of the model at sunrise (0 hours), sunset (12 hours), and 68 to 70 minutes after sunset for a typical day (after the package temperatures reach "quasi steady-state") of the transient are presented in Figure 16 through Figure 19 for various content heat loads. The temperature contours at 68 to 70 minutes after sunset are presented because the temperature of the CV flange (i.e., O-ring location) peaks at this time. The elements representing the air between the drum liner and containment vessel and between the drum liner and top plug liner are not shown in the temperature contours presented in these figures so that the containment vessel temperature contours can be more easily viewed.

The maximum temperature in the model occurs at the top center of the drum lid in most instances. The drum lid maximum temperature is 243.86°F (117.70°C), 243.89°F (117.72°C), 245.32°F (118.51°C), and 246.03°F (118.91°C) for content heat loads of 0, 0.4, 20, and 30 W, respectively, and occurs at sunset in each case (see Table 5). For the case with a content heat load of 30 W, the maximum temperature in the model occurs in the sidewall of the CV approximately 80 minutes after sunset and is 252.87°F (122.71°C). The maximum temperature at the containment vessel O-ring is 189.28°F (87.38°C), 189.90°F (87.72°C), 217.07°F (102.82°C), and 230.51°F (110.28°C) for content heat loads of 0, 0.4, 20, and 30 W, respectively, and occurs at approximately 68 to 70 minutes after sunset in each case (see Table 5).

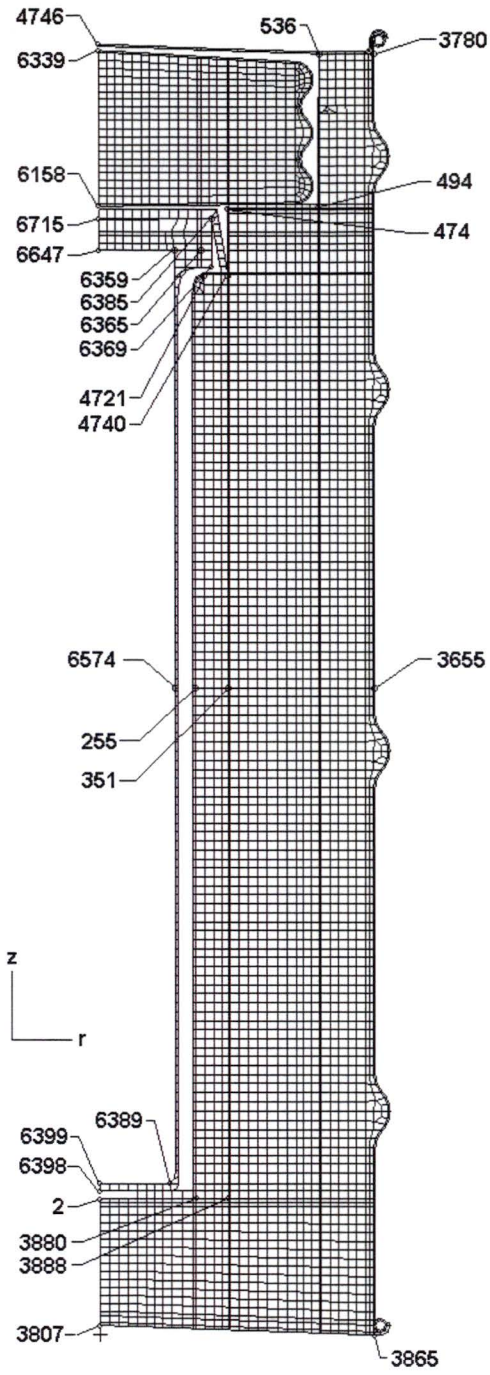

Node	r (in.)	z (in.)
2	0.000	4.505
255	3.180	21.528
351	4.300	21.528
474	4.300	37.535
494	7.325	37.535
536	7.385	42.755
3655	9.185	21.528
3780	9.185	42.755
3807	0.000	0.320
3865	9.185	0.008
3880	3.178	4.505
3888	4.300	4.505
4721	3.500	35.275
4740	4.300	35.275
4746	0.000	43.065
6158	0.000	37.579
6339	0.000	42.859
6359	2.530	36.075
6365	3.425	36.075
6369	3.750	35.525
6385	3.750	37.175
6389	2.310	5.025
6398	0.000	4.775
6399	0.000	5.025
6574	2.530	21.528
6647	0.000	36.075
6715	0.000	37.135

Figure 8. ABAQUS axisymmetric finite element model of the ES-3100 shipping container—nodal locations of interest defined in Table 3.4a (elements representing air not shown for clarity).

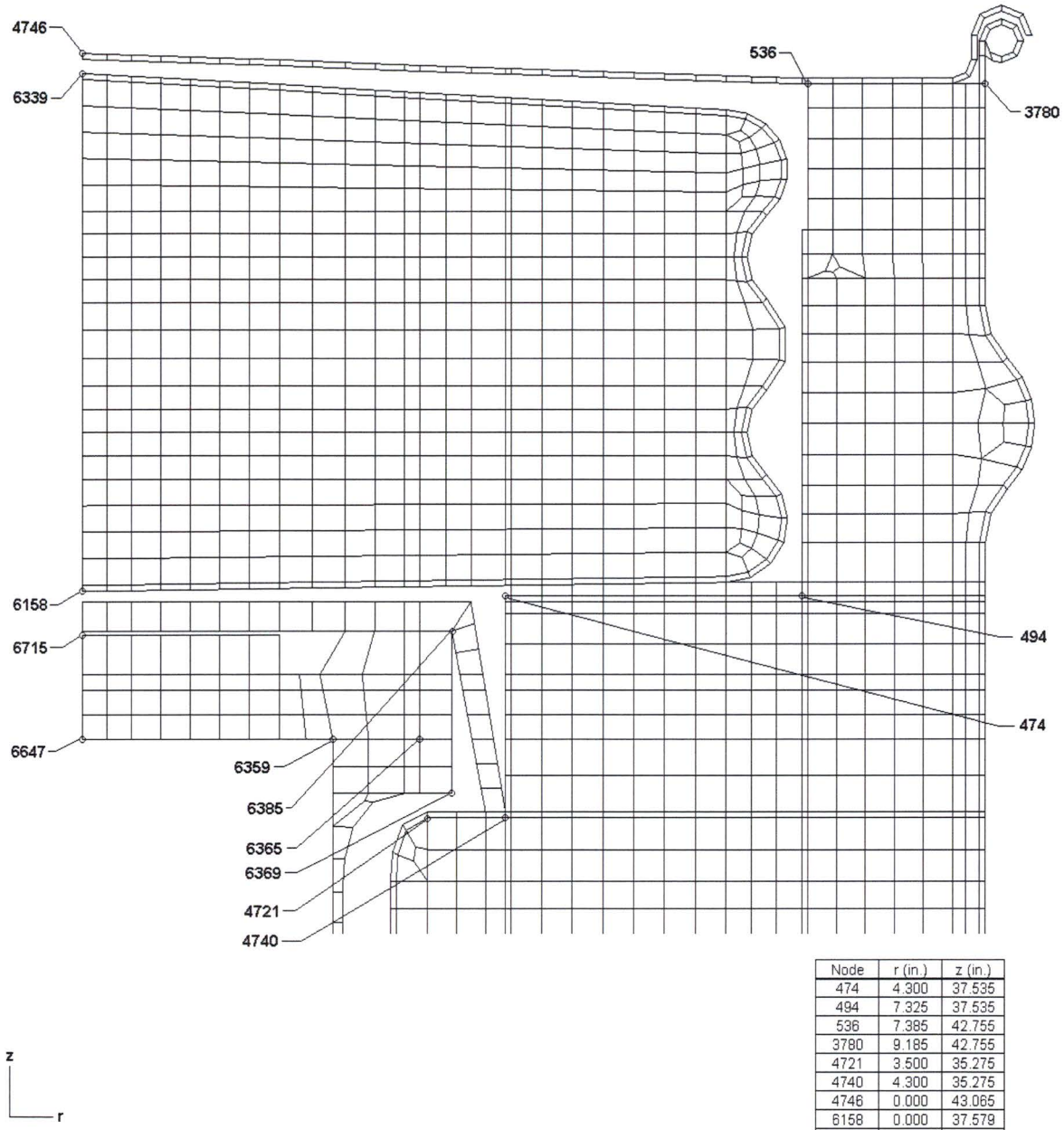

Node	r (in.)	z (in.)
474	4.300	37.535
494	7.325	37.535
536	7.385	42.755
3780	9.185	42.755
4721	3.500	35.275
4740	4.300	35.275
4746	0.000	43.065
6158	0.000	37.579
6339	0.000	42.859
6359	2.530	36.075
6365	3.425	36.075
6369	3.750	35.525
6385	3.750	37.175
6647	0.000	36.075
6715	0.000	37.135

Figure 9. ABAQUS axisymmetric finite element model of the ES-3100 shipping container—nodal locations of interest (elements representing air not shown for clarity), upper portion detail.

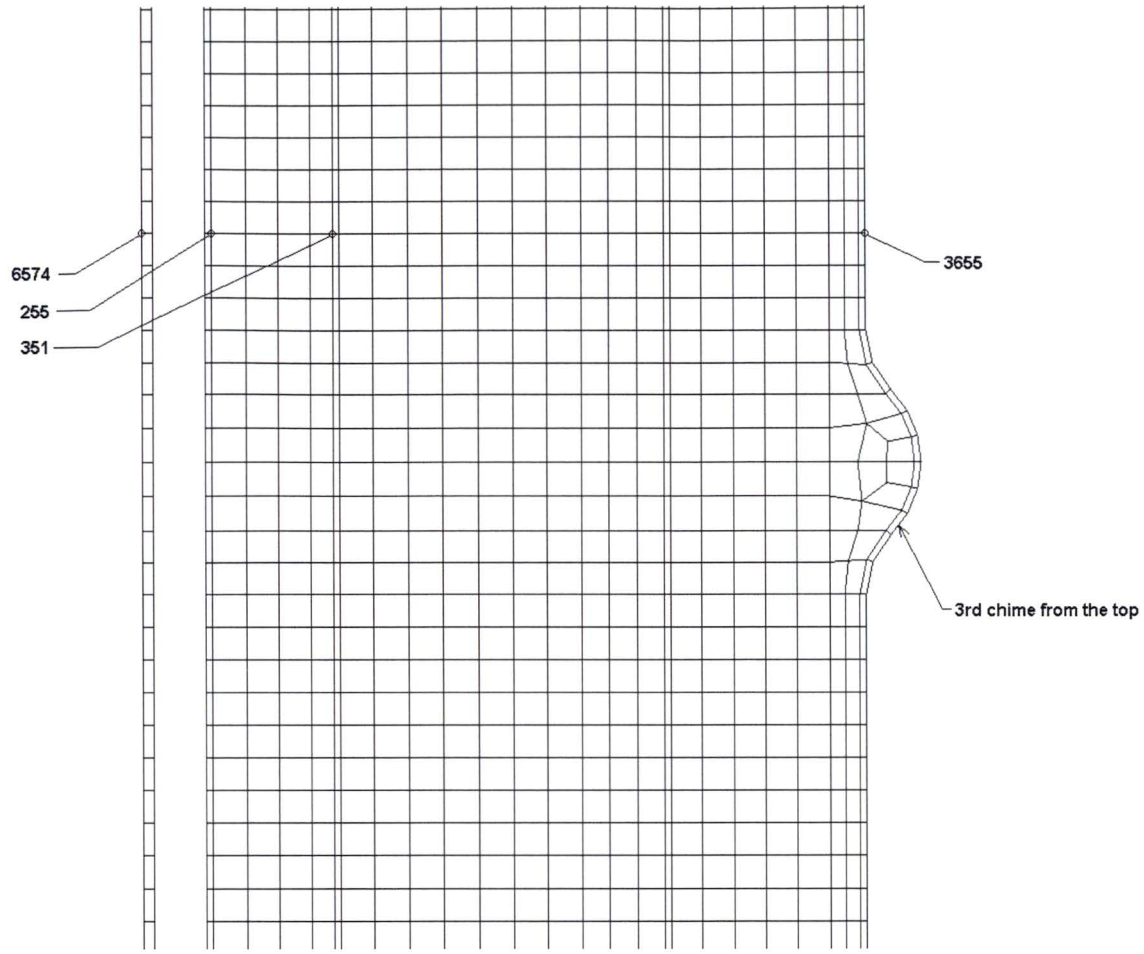

Node	r (in.)	z (in.)
255	3.180	21.528
351	4.300	21.528
3655	9.185	21.528
6574	2.530	21.528

Figure 10. ABAQUS axisymmetric finite element model of the ES-3100 shipping container—nodal locations of interest (elements representing air not shown for clarity), middle portion detail.

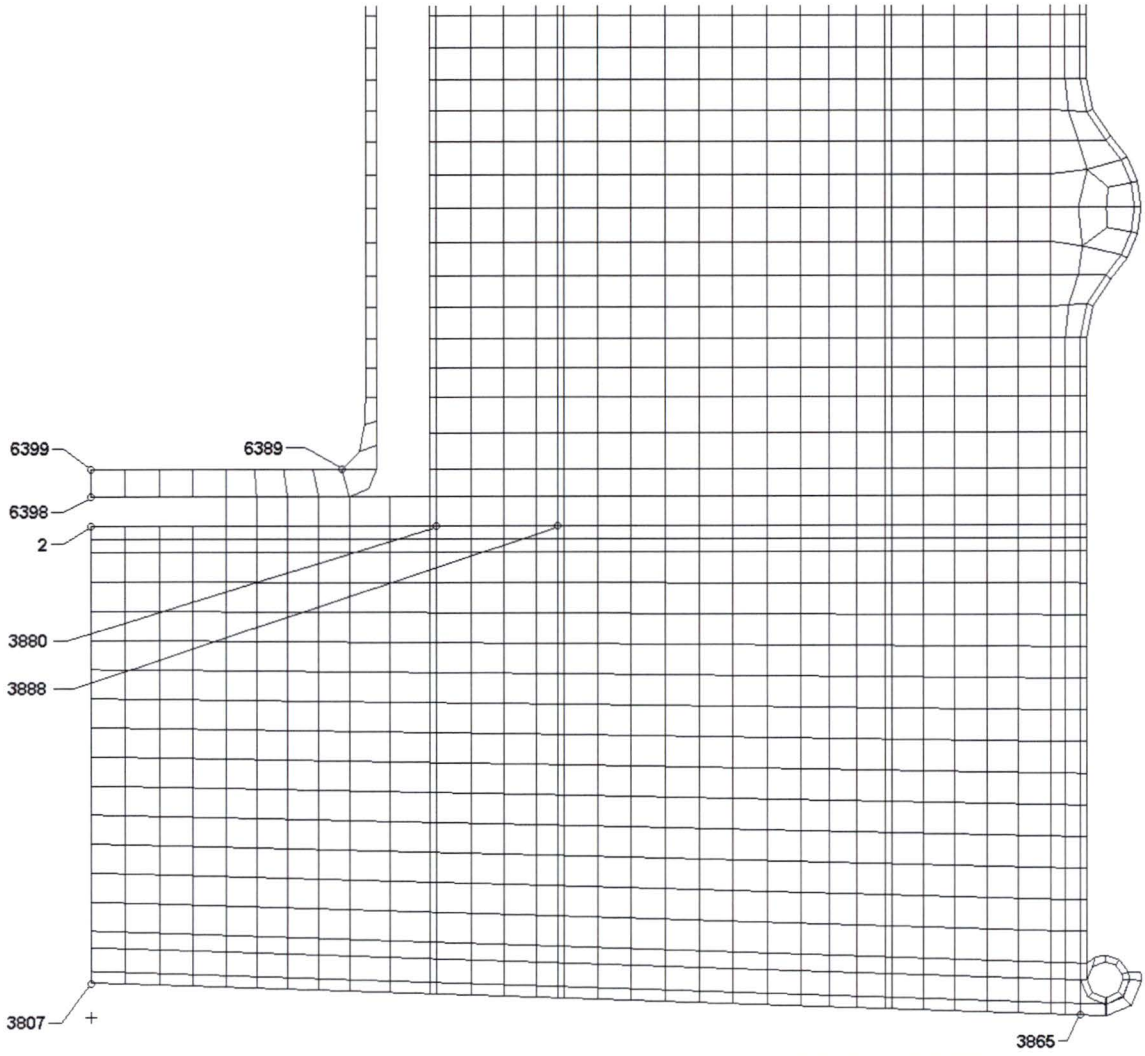

Node	r (in.)	z (in.)
2	0.000	4.505
3807	0.000	0.320
3865	9.185	0.008
3880	3.178	4.505
3888	4.300	4.505
6389	2.310	5.025
6398	0.000	4.775
6399	0.000	5.025

Figure 11. ABAQUS axisymmetric finite element model of the ES-3100 shipping container—nodal locations of interest (elements representing air not shown for clarity), lower portion detail.

Table 4. ES-3100 shipping container steady-state temperatures (100°F ambient temperature, no insolation).

Node map [a]	Node coordinates (in.)			Maximum steady-state temperature (°F)		
	No.	r	z	0.4 W	20 W	30 W
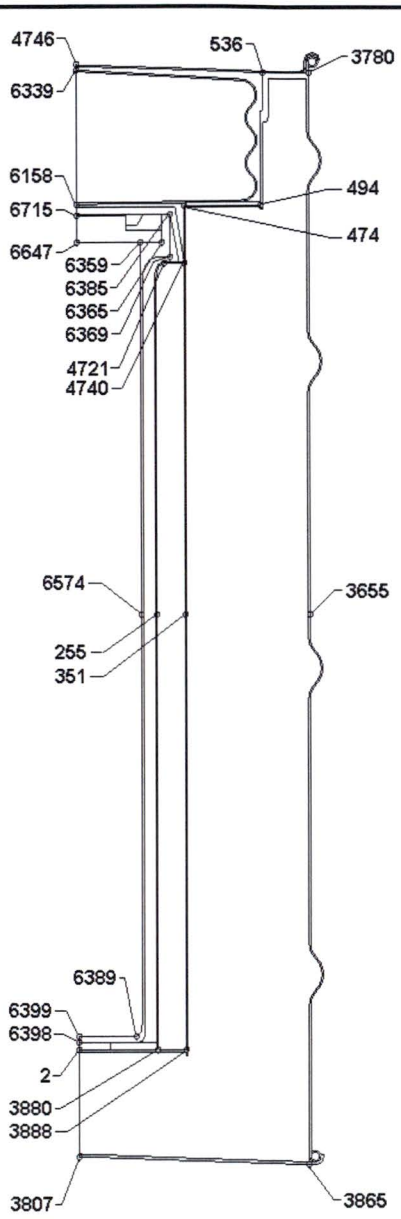	2	0.000	4.505	100.83	134.54	150.15
	255	3.180	21.528	100.75	131.57	146.21
	351	4.300	21.528	100.71	129.45	142.87
	474	4.300	37.535	100.46	117.90	125.67
	494	7.325	37.535	100.32	110.87	115.19
	536	7.385	42.755	100.21	105.50	107.19
	3655 [b]	9.185	21.528	100.28	107.58	109.92
	3780 [b]	9.185	42.755	100.21	105.29	106.89
	3807 [b]	0.000	0.320	100.43	114.39	120.08
	3865 [b]	9.185	0.008	100.32	108.97	111.97
	3880	3.178	4.505	100.74	130.48	144.23
	3888	4.300	4.505	100.71	128.60	141.42
	4721	3.500	35.275	100.59	124.08	134.90
	4740	4.300	35.275	100.57	122.92	133.15
	4746 [b]	0.000	43.065	100.20	104.99	106.43
	6158	0.000	37.579	100.57	123.14	133.42
	6339	0.000	42.859	100.25	107.42	110.04
	6359 [c]	2.530	36.075	100.80	133.51	148.56
	6365 [c]	3.425	36.075	100.79	133.33	148.28
	6369	3.750	35.525	100.79	133.27	148.20
	6385	3.750	37.175	100.78	132.85	147.58
	6389	2.310	5.025	100.97	141.27	160.06
	6398	0.000	4.775	100.96	140.91	159.55
	6399	0.000	5.025	100.96	140.94	159.60
	6574	2.530	21.528	101.33	157.70	183.56
	6647	0.000	36.075	100.80	133.56	148.63
	6715	0.000	37.135	100.79	133.40	148.40

Notes: (a) See Table 3.4a and Figs. 8–11 for details of node locations.
(b) These are nodes at the accessible surfaces of the package (i.e., the drum, drum lid, and drum bottom plate).
(c) Approximate location of the CV O-ring.

Table 5. ES-3100 shipping container maximum "quasi steady-state" temperatures during NCT with various content heat loads.

Node map [a]	Node coordinates (in.)			Maximum "quasi steady-state" temperature (°F)			
	No.	r	z	0 W	0.4 W	20 W	30 W
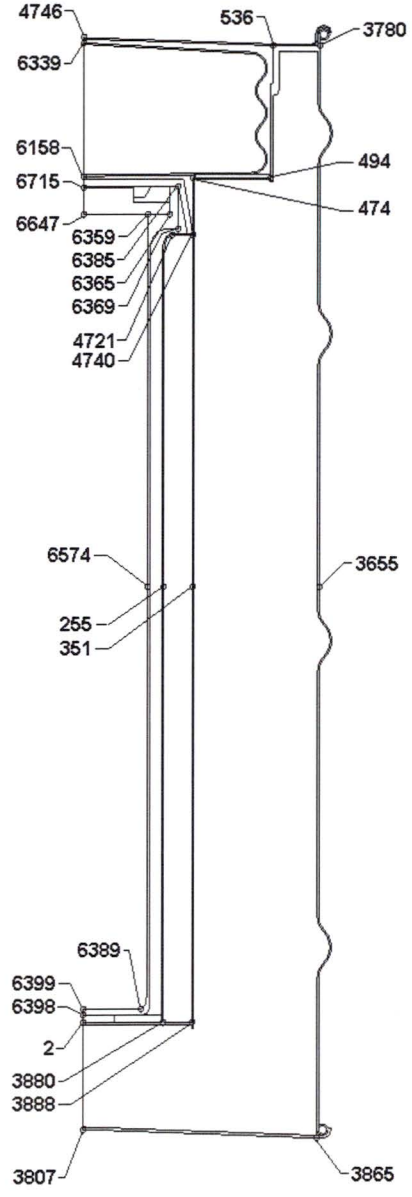	2	0.000	4.505	180.59	181.23	210.15	224.69
	255	3.180	21.528	179.33	179.93	207.32	221.43
	351	4.300	21.528	179.59	180.14	204.73	217.27
	474	4.300	37.535	198.88	199.20	212.72	219.58
	494	7.325	37.535	207.40	207.56	214.40	217.87
	536	7.385	42.755	226.44	226.49	228.31	229.24
	3655	9.185	21.528	198.09	198.15	200.81	202.16
	3780	9.185	42.755	223.47	223.51	225.13	225.95
	3807	0.000	0.320	190.48	190.70	199.84	204.43
	3865	9.185	0.008	195.87	195.97	199.91	201.90
	3880	3.178	4.505	180.72	181.28	206.65	219.52
	3888	4.300	4.505	181.03	181.55	205.08	217.01
	4721	3.500	35.275	189.45	189.90	209.53	219.47
	4740	4.300	35.275	190.56	190.98	209.37	218.68
	4746	0.000	43.065	243.86	243.89	245.32	246.03
	6158	0.000	37.579	198.42	198.84	217.12	226.32
	6339	0.000	42.859	233.98	234.06	237.32	238.95
	6359 [b]	2.530	36.075	189.28	189.90	217.07	230.51
	6365 [b]	3.425	36.075	189.27	189.88	216.88	230.23
	6369	3.750	35.525	189.23	189.85	216.79	230.12
	6385	3.750	37.175	189.39	190.00	216.57	229.72
	6389	2.310	5.025	179.94	180.70	215.75	233.27
	6398	0.000	4.775	179.99	180.76	215.52	232.92
	6399	0.000	5.025	179.99	180.76	215.55	232.96
	6574	2.530	21.528	179.27	180.35	229.19	252.87
	6647	0.000	36.075	189.40	190.02	217.24	230.72
	6715	0.000	37.135	189.44	190.06	217.14	230.54

Notes: (a) See Table 3.4a and Figs. 8–11 for details of node locations.
(b) Approximate location of the CV O-ring.

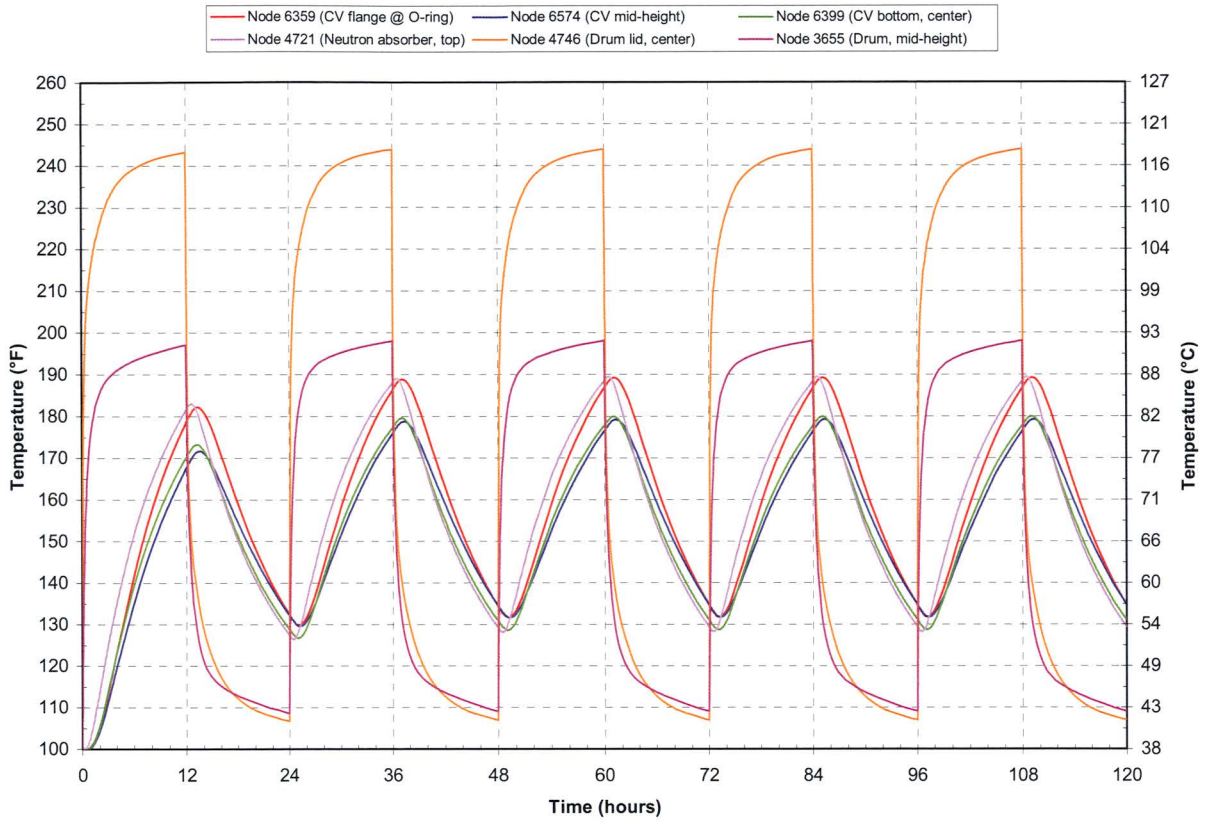

Figure 12. Transient temperatures of the ES-3100 shipping container for NCT (no content heat load) see Figure 8 through Figure 11 for node locations.

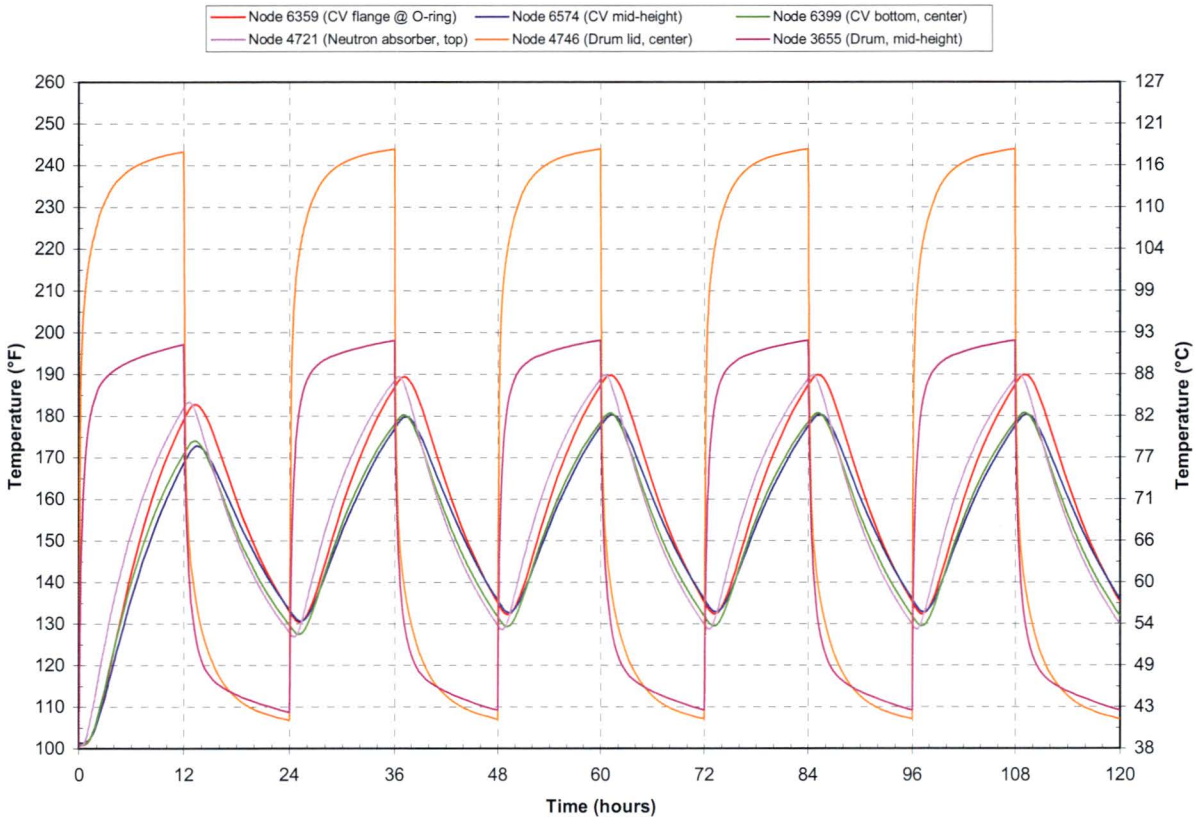

Figure 13. Transient temperatures of the ES-3100 shipping container for NCT (0.4 W content heat load) see Figure 8 through Figure 11 for node locations.

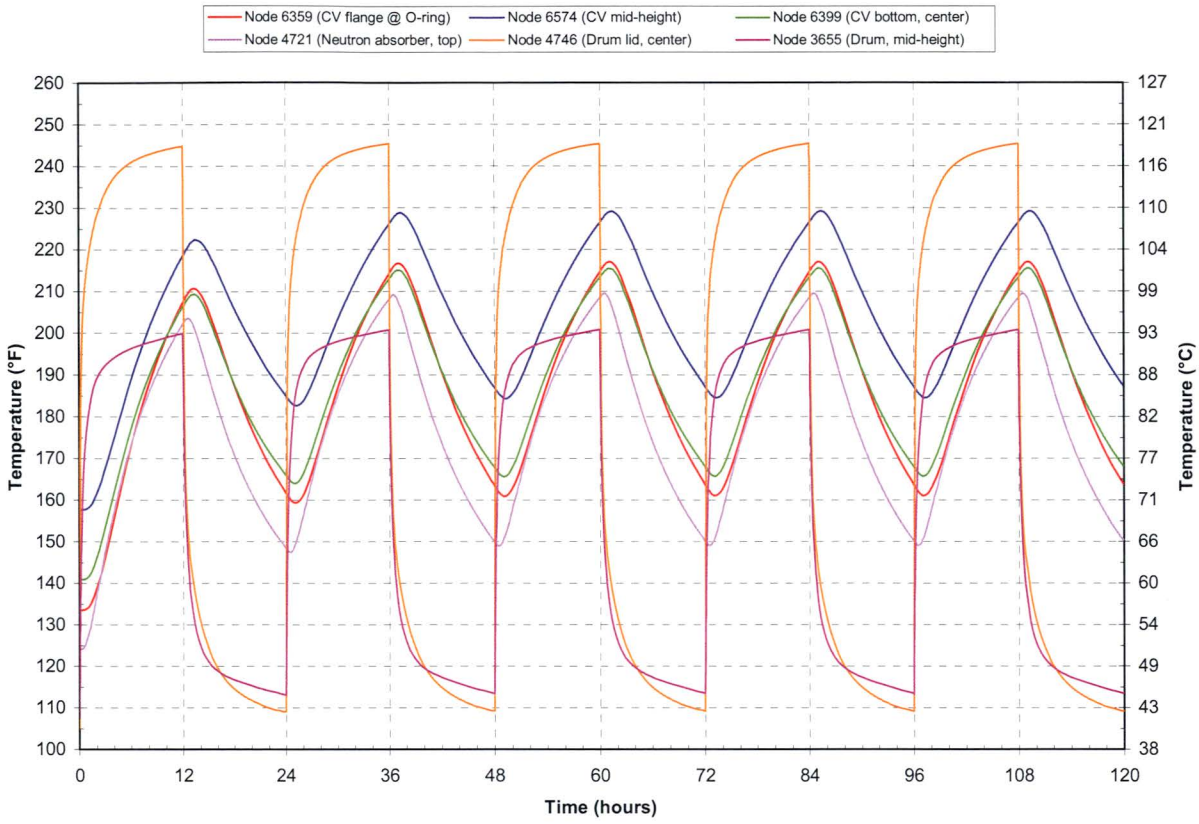

Figure 14. Transient temperatures of the ES-3100 shipping container for NCT (20 W content heat load) see Figure 8 through Figure 11 for node locations.

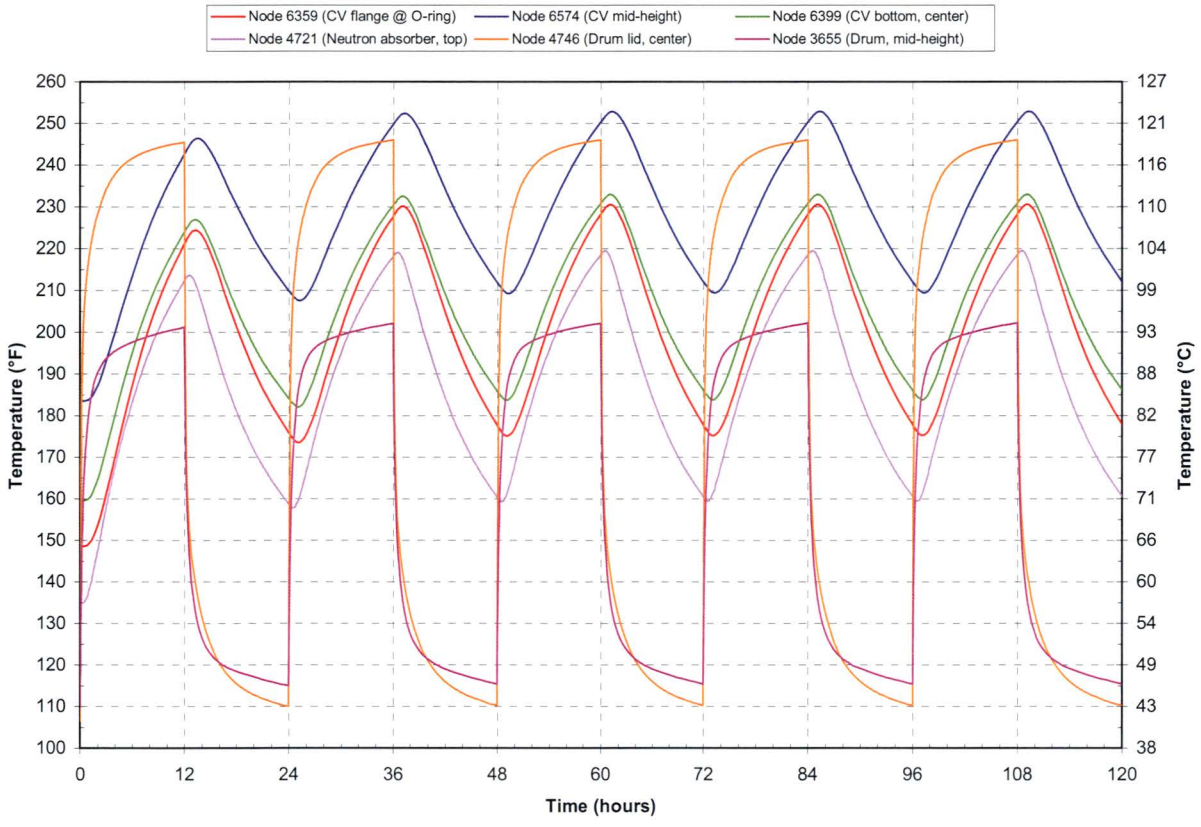

Figure 15. Transient temperatures of the ES-3100 shipping container for NCT (30 W content heat load) see Figure 8 through Figure 11 for node locations.

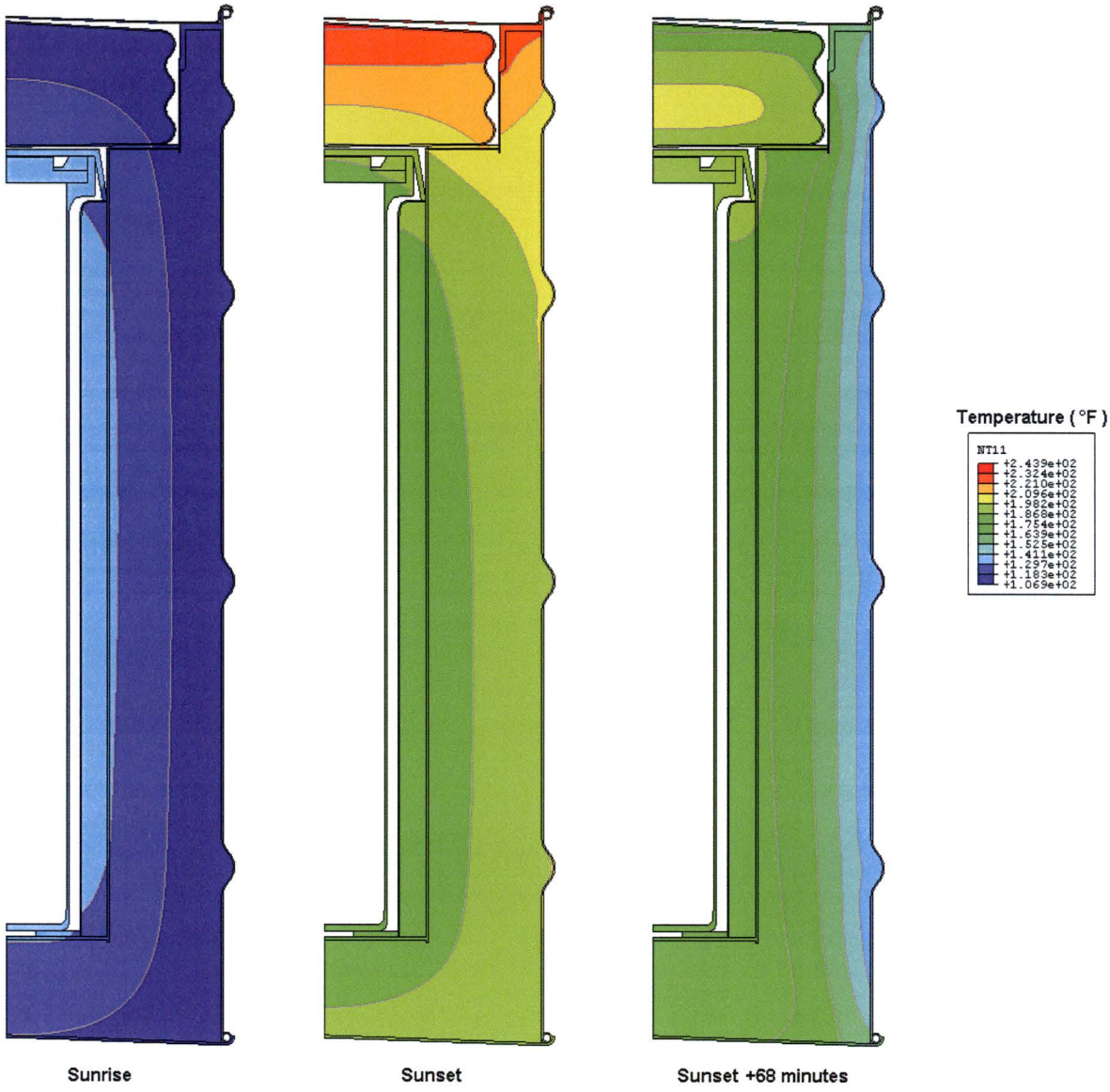

Figure 16. Temperature distribution in the ES-3100 shipping container for NCT (no content heat load) typical day of transient analysis (elements representing air not shown for clarity).

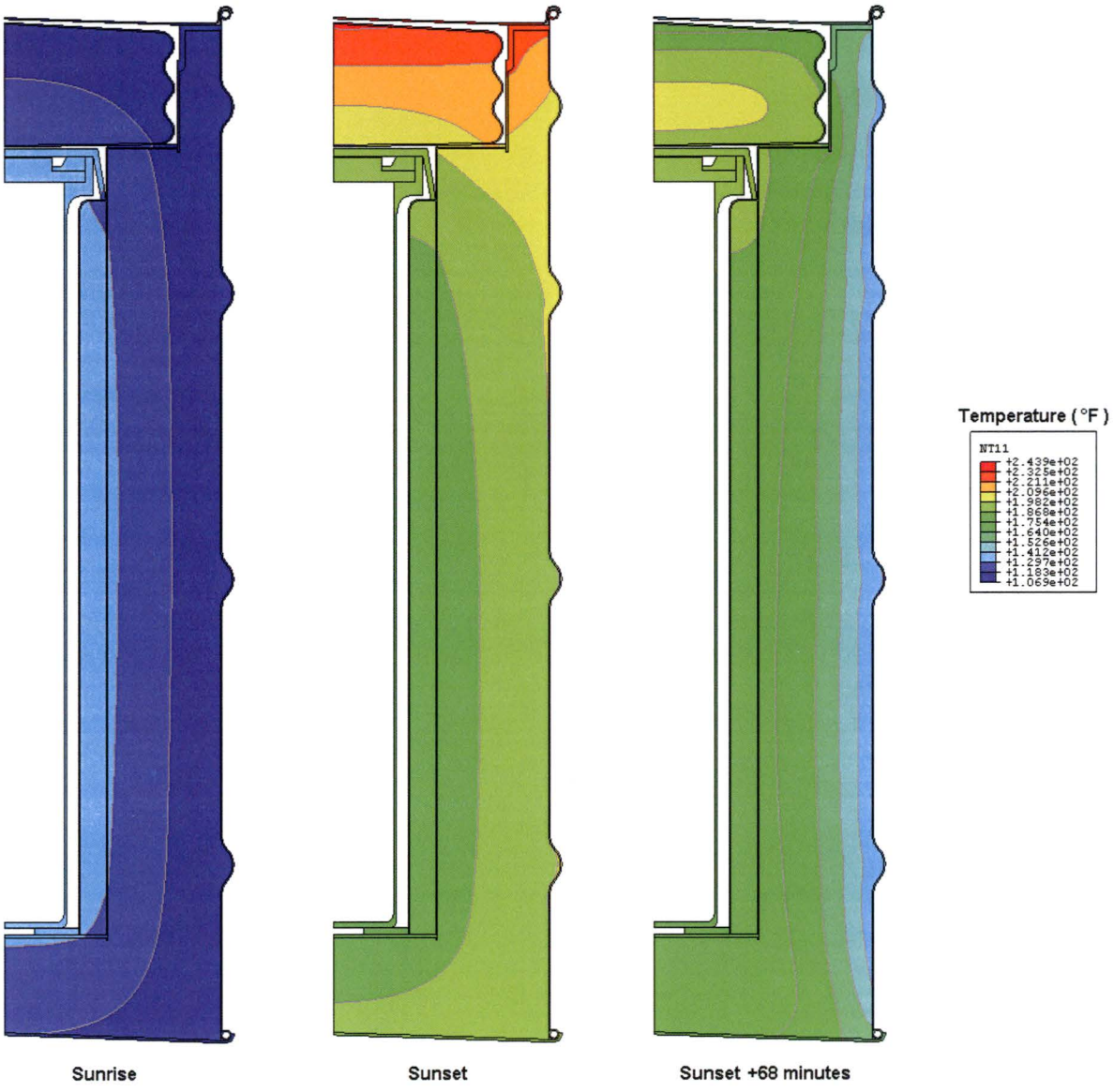

Figure 17. Temperature distribution in the ES-3100 shipping container for NCT (0.4 W content heat load) typical day of transient analysis (elements representing air not shown for clarity).

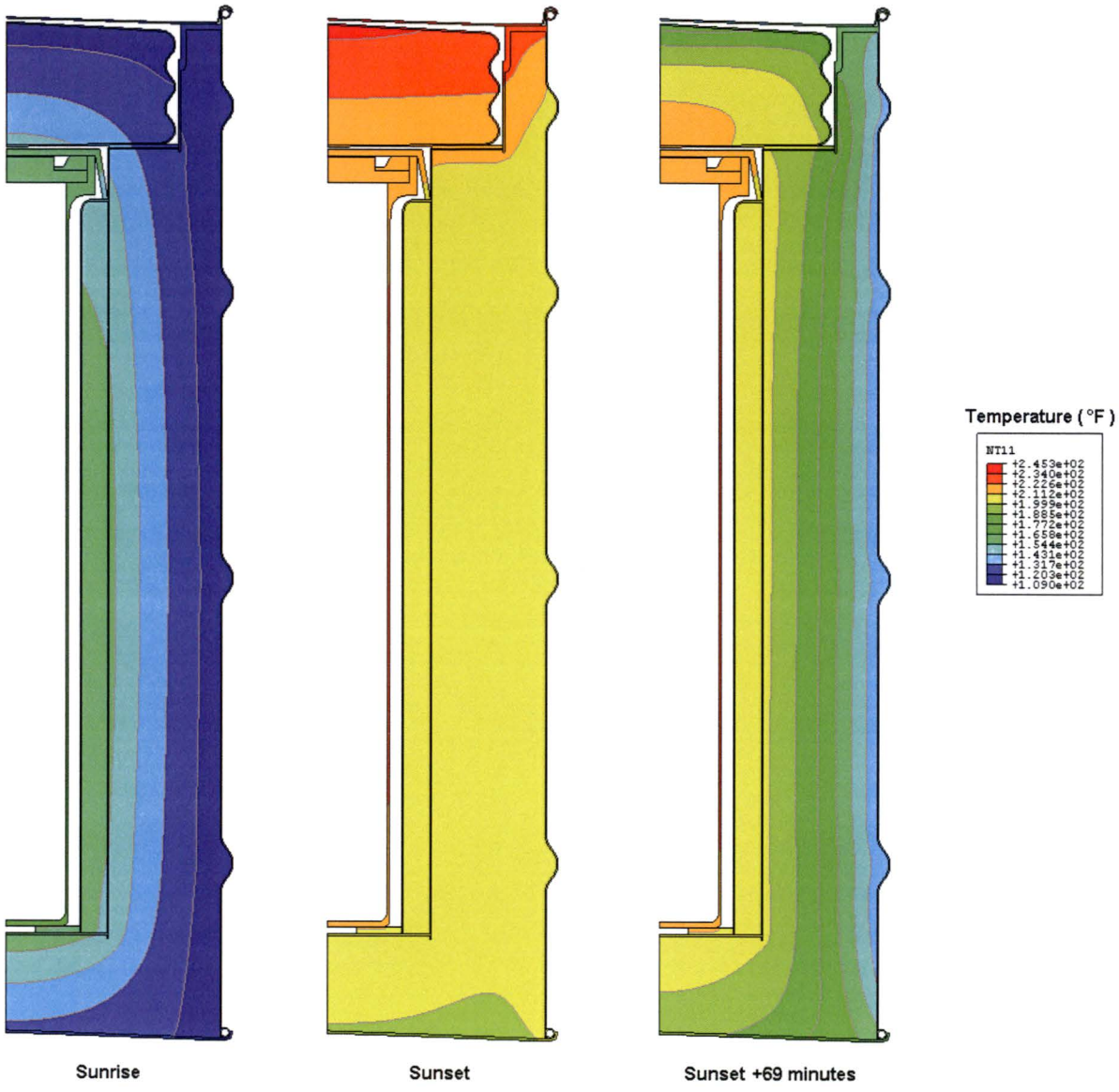

Figure 18. Temperature distribution in the ES-3100 shipping container for NCT (20 W content heat load) typical day of transient analysis (elements representing air not shown for clarity).

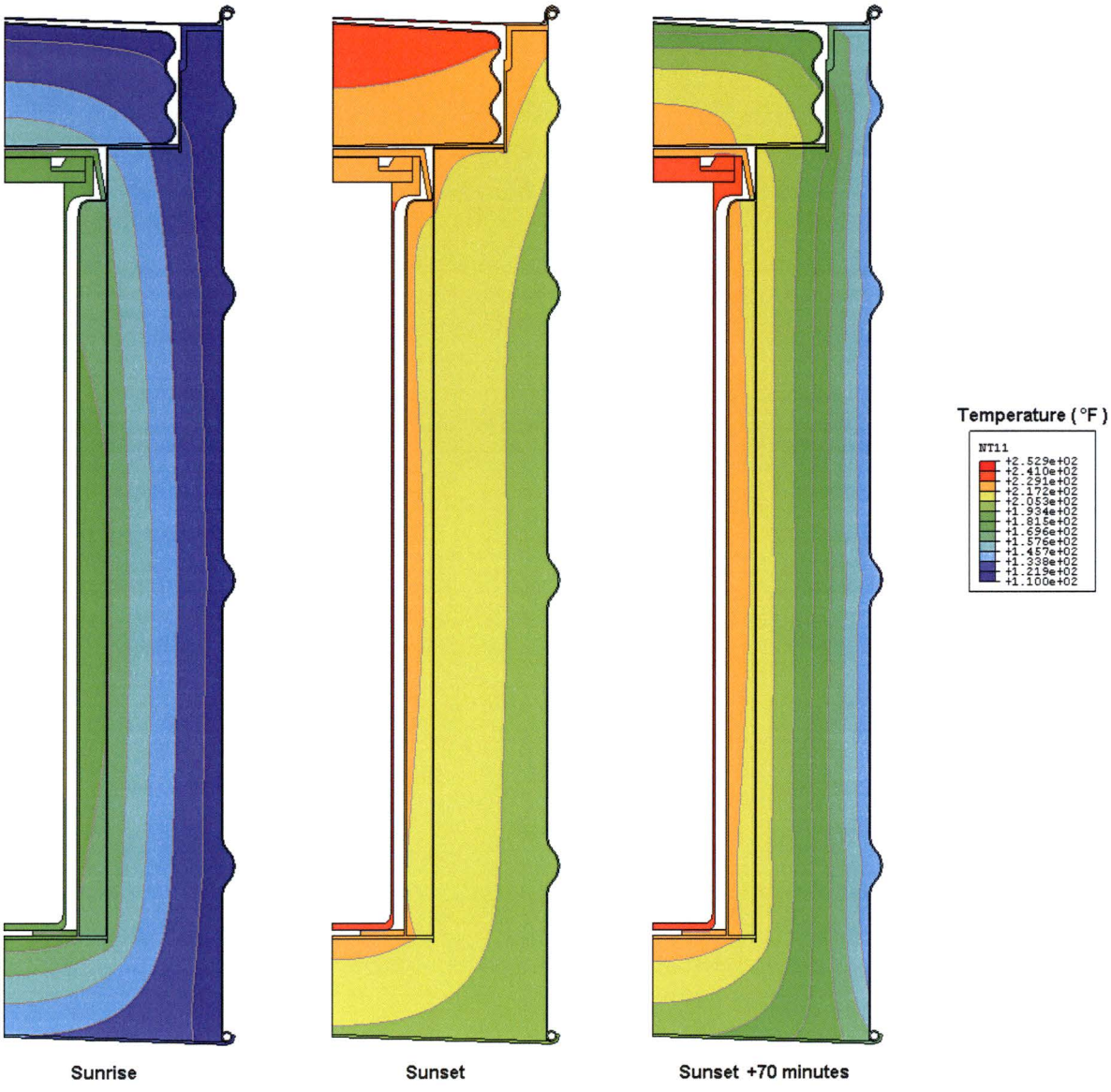

Figure 19. Temperature distribution in the ES-3100 shipping container for NCT (30 W content heat load) typical day of transient analysis (elements representing air not shown for clarity).

Hypothetical Accident Conditions Analyses Results

Transient thermal analyses are performed on the finite element model of the ES-3100 shipping container (undamaged configuration) to simulate HAC as prescribed by 10 CFR 71.73(c)(4).[1] A 30-minute fire of 1475°F (800°C) is simulated by applying natural convection and radiant exchange boundary conditions to all external surfaces of the drum (assuming the drum is in a horizontal orientation) with content heat loads of 0, 0.4, 20, and 30 W. There are no heat flux boundary conditions simulating insolation applied to the model before and during the 30-minute fire. The initial temperature distribution within the package having content heat loads of 0.4, 20, and 30 W is obtained from their respective steady-state analyses. The initial temperature distribution within the package having no content heat load (0 W) is assumed to be at a uniform temperature equal to the ambient temperature of 100°F (37.8°C). As with the steady-state analyses discussed previously, applying a uniform heat flux to the internal surfaces of the elements representing the containment vessel simulates the content heat load.

Following the 30-minute fire transient analyses, 48-hour cool-down transient thermal analyses are performed using the temperature distribution at the end of the fire as the initial temperature distribution. During post-fire cool-down, natural convection and radiant exchange boundary conditions are applied to all external surfaces of the drum (assuming the drum is in a horizontal orientation). Additionally, cases are analyzed in which insolation is included during the post-fire cool-down. For the cases in which insolation is applied to the model during cool-down, insolation is applied during the first 12-hour period following the 30-minute fire, then alternated (off, then on) as was done for NCT.

Based on previous analyses of a similar package[9] (see Appendix 3.6.1), it was noted that using the low-end density of Kaolite results in higher containment vessel temperatures than using the high-end density of Kaolite. For this reason, the NCT and HAC thermal analyses were run using a density of 19.4 lbm/ft^3 (see Table 1). Similarly, the low-end density of the neutron absorber (100 lbm/ft^3) was also used in these analyses. However, while using these low-end densities will result in higher temperatures to the containment vessel, using the high-end densities for these two materials will result in higher temperature differences from the baseline HAC case. Thus, runs are also made for heat loads of 0, 0.4, 20, and 30 W using a Kaolite density of 30 lbm/ft^3 and a neutron absorber density of 110 lbm/ft^3.

The maximum temperatures calculated for the ES-3100 shipping container for HAC are summarized in Table 6 for the analyses using a Kaolite density of 19.4 lbm/ft^3 and a neutron absorber density of 100 lbm/ft^3. The maximum temperatures calculated for the ES-3100 shipping container for HAC are summarized in Table 7 for the analyses using a Kaolite density of 30 lbm/ft^3 and a neutron absorber density of 110 lbm/ft^3. The thermal analyses that use the low-end density values for Kaolite and the neutron absorber achieve the higher package temperatures (see Table 6). Temperature-history plots of several locations within the model are also depicted graphically in Figure 20 through Figure 23 for content heat loads of 0, 0.4, 20, and 30 W for the analyses using a Kaolite density of 19.4 lbm/ft^3 and a neutron absorber density of 100 lbm/ft^3.

The HAC thermal analyses presented in this report are performed using a finite element model that represents an undamaged ES-3100 shipping container. While the cumulative damage from NCT and HAC drop tests, crush tests, and puncture tests, must be considered when evaluating the performance of the package to HAC, the temperature differences (i.e., adjustments) calculated from the data presented in Table 6 and Table 7 are of value when combined with the physical test data when making this assessment.

Table 6. ES-3100 shipping container HAC maximum temperatures (Kaolite density of 19.4 lbm/ft^3 and neutron absorber density of 100 lbm/ft^3).

Node map [a]	Node coordinates (in.)			HAC maximum temperature (°F)							
				0 W		0.4 W		20 W		30 W	
	No.	r	z	Insolation during cool-down?		Insolation during cool-down?		Insolation during cool-down?		Insolation during cool-down?	
				No [b]	Yes	No	Yes	No	Yes	No	Yes
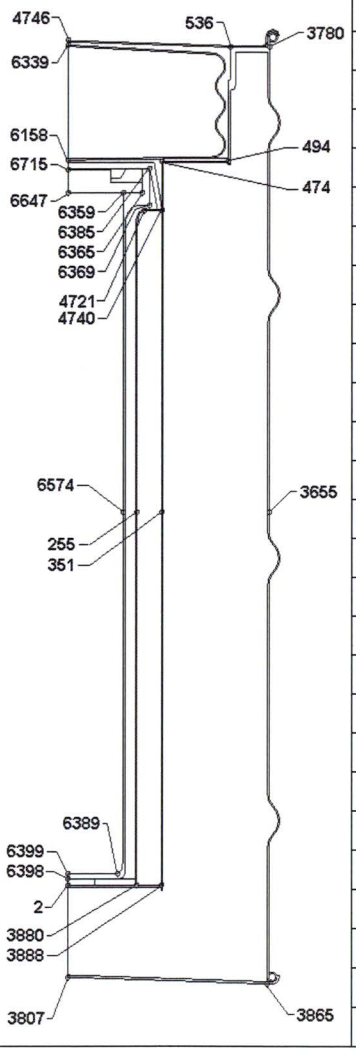	2	0.000	4.505	225.5	232.1	226.2	232.8	255.5	261.7	269.5	275.7
	255	3.180	21.528	194.5	212.5	195.2	213.2	223.8	241.3	237.8	255.3
	351	4.300	21.528	195.8	211.9	196.4	212.5	222.3	237.8	234.8	250.3
	474	4.300	37.535	392.9	395.0	393.2	395.4	407.6	409.7	414.2	416.3
	494	7.325	37.535	671.2	672.0	671.4	672.3	679.1	680.0	682.5	683.3
	536	7.385	42.755	1380.4	1380.4	1380.4	1380.4	1380.9	1380.9	1381.1	1381.1
	3655	9.185	21.528	1457.8	1457.8	1457.8	1457.8	1458.0	1458.0	1458.1	1458.1
	3780	9.185	42.755	1427.8	1427.8	1427.9	1427.9	1428.1	1428.1	1428.2	1428.2
	3807	0.000	0.320	1454.5	1454.5	1454.5	1454.5	1454.9	1454.9	1455.0	1455.0
	3865	9.185	0.008	1470.1	1470.1	1470.1	1470.1	1470.1	1470.1	1470.2	1470.2
	3880	3.178	4.505	230.6	236.4	231.2	237.0	257.1	262.5	269.4	274.8
	3888	4.300	4.505	236.9	241.7	237.5	242.3	261.5	266.1	272.9	277.5
	4721	3.500	35.275	245.7	252.8	246.2	253.3	266.8	273.8	276.6	283.6
	4740	4.300	35.275	258.4	263.5	258.8	264.0	278.1	283.1	287.1	292.1
	4746	0.000	43.065	1448.0	1448.0	1448.0	1448.0	1448.2	1448.2	1448.3	1448.3
	6158	0.000	37.579	308.7	311.6	309.1	312.0	328.3	331.2	337.3	340.2
	6339	0.000	42.859	1335.1	1335.1	1335.2	1335.2	1336.4	1336.4	1336.9	1336.9
	6359 [c]	2.530	36.075	236.7	247.6	237.3	248.3	266.2	276.6	279.8	289.9
	6365 [c]	3.425	36.075	236.6	247.6	237.3	248.3	266.0	276.4	279.5	289.7
	6369	3.750	35.525	236.5	247.6	237.2	248.2	265.8	276.2	279.3	289.5
	6385	3.750	37.175	237.3	248.2	237.9	248.8	266.1	276.4	279.4	289.5
	6389	2.310	5.025	219.0	227.4	219.9	228.2	255.3	263.1	272.2	279.9
	6398	0.000	4.775	219.7	227.9	220.5	228.7	255.6	263.3	272.5	280.0
	6399	0.000	5.025	219.7	227.9	220.5	228.7	255.6	263.3	272.5	280.0
	6574	2.530	21.528	196.1	214.9	197.3	216.0	246.7	263.8	269.9	286.5
	6647	0.000	36.075	237.2	248.0	237.9	248.6	266.8	277.0	280.4	290.4
	6715	0.000	37.135	237.4	248.1	238.0	248.8	266.8	277.0	280.4	290.4

Notes: (a) See Table 3.4a and Figs. 8–11 for details of node locations.
(b) Baseline case for ΔT comparisons.
(c) Approximate location of the CV O-ring.

Table 7. ES-3100 shipping container HAC maximum temperatures (Kaolite density of 30 lbm/ft^3 and neutron absorber density of 110 lbm/ft^3).

Node map [a]	Node coordinates (in.)			HAC maximum temperature (°F)							
				0 W		0.4 W		20 W		30 W	
	No.	r	z	Insolation during cool-down?		Insolation during cool-down?		Insolation during cool-down?		Insolation during cool-down?	
				No [b]	Yes	No	Yes	No	Yes	No	Yes
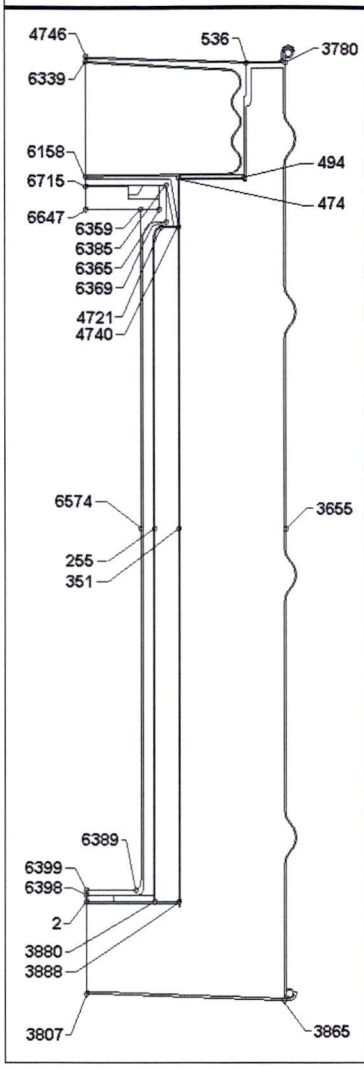	2	0.000	4.505	209.9	218.9	210.6	219.6	240.4	248.8	254.6	262.8
	255	3.180	21.528	185.5	207.7	186.1	208.4	215.1	236.6	229.3	250.6
	351	4.300	21.528	185.6	207.4	186.2	208.0	212.3	233.3	225.0	245.9
	474	4.300	37.535	342.9	345.5	343.3	345.9	358.1	360.7	365.0	367.5
	494	7.325	37.535	596.3	597.4	596.5	597.6	604.7	605.8	608.3	609.4
	536	7.385	42.755	1366.8	1366.8	1366.8	1366.8	1367.4	1367.4	1367.6	1367.6
	3655	9.185	21.528	1452.8	1452.8	1452.8	1452.8	1453.0	1453.0	1453.1	1453.1
	3780	9.185	42.755	1420.8	1420.8	1420.8	1420.8	1421.0	1421.0	1421.2	1421.2
	3807	0.000	0.320	1449.4	1449.4	1449.4	1449.4	1449.8	1449.8	1449.9	1449.9
	3865	9.185	0.008	1467.3	1467.3	1467.3	1467.3	1467.4	1467.4	1467.4	1467.4
	3880	3.178	4.505	213.1	221.4	213.7	222.0	240.0	247.9	252.5	260.3
	3888	4.300	4.505	217.0	224.4	217.6	225.0	242.1	249.1	253.8	260.7
	4721	3.500	35.275	228.0	237.5	228.5	238.0	249.7	259.0	259.7	269.0
	4740	4.300	35.275	236.5	243.8	236.9	244.3	256.7	263.9	266.0	273.2
	4746	0.000	43.065	1441.8	1441.8	1441.8	1441.8	1442.0	1442.0	1442.1	1442.
	6158	0.000	37.579	277.3	281.8	277.8	282.3	297.5	302.0	306.7	311.2
	6339	0.000	42.859	1299.5	1299.5	1299.6	1299.6	1301.1	1301.1	1301.7	1301.7
	6359 [c]	2.530	36.075	225.1	237.3	225.8	237.9	254.7	266.1	268.3	279.6
	6365 [c]	3.425	36.075	225.0	237.3	225.7	237.9	254.5	266.0	268.1	279.3
	6369	3.750	35.525	224.9	237.2	225.6	237.8	254.3	265.8	267.9	279.2
	6385	3.750	37.175	225.5	237.6	226.2	238.3	254.6	266.1	268.0	279.2
	6389	2.310	5.025	205.3	215.9	206.2	216.8	242.0	251.9	259.2	268.9
	6398	0.000	4.775	205.8	216.3	206.7	217.1	242.2	252.0	259.2	268.8
	6399	0.000	5.025	205.8	216.3	206.7	217.1	242.2	252.0	259.3	268.8
	6574	2.530	21.528	187.8	209.1	189.0	210.2	238.9	258.4	262.4	281.3
	6647	0.000	36.075	225.6	237.7	226.3	238.3	255.2	266.5	268.9	280.0
	6715	0.000	37.135	225.8	237.8	226.4	238.4	255.2	266.5	268.9	280.0

Notes: (a) See Table 3.4a and Figs. 8–11 for details of node locations.
(b) Baseline case for ΔT comparisons.
(c) Approximate location of the CV O-ring.

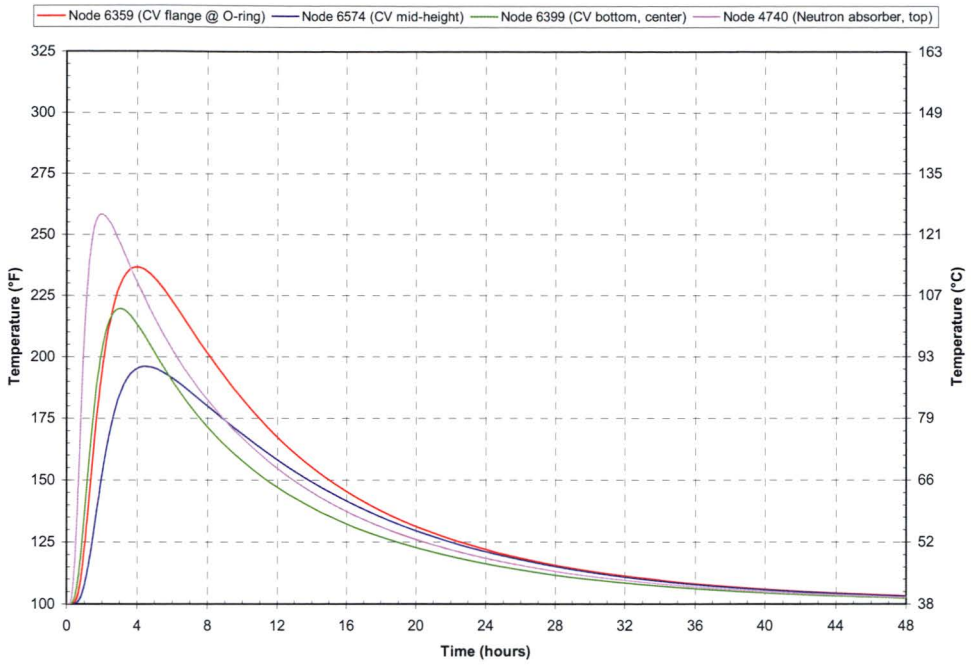

(a) No insolation during post-fire cool-down.

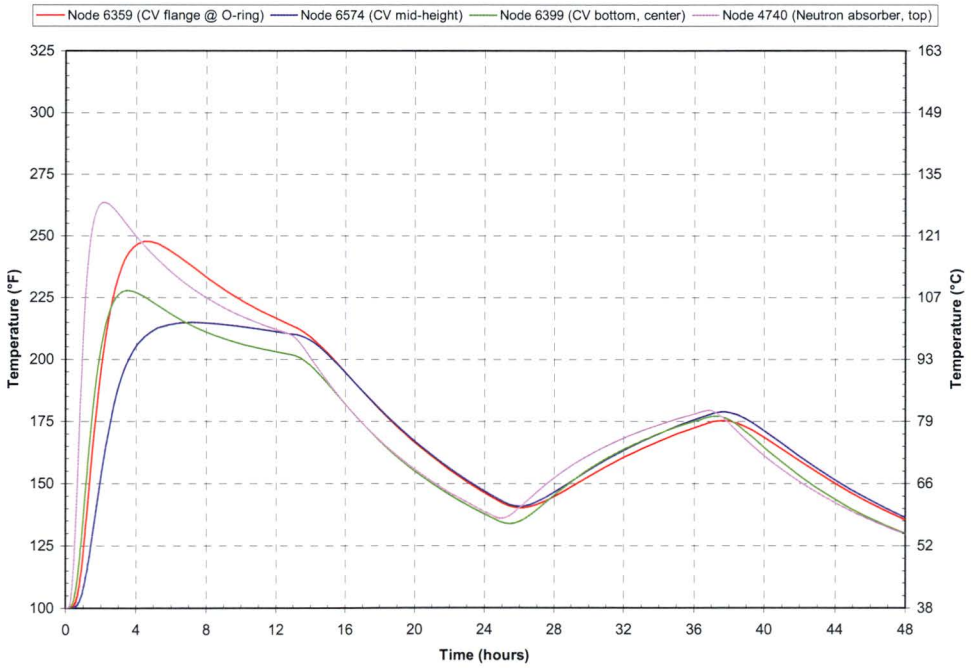

(b) Insolation during post-fire cool-down.

Figure 20. ES-3100 shipping container transient temperatures for HAC—no content heat load and lower bound Kaolite and neutron absorber densities (see Figure 8 through Figure 11 for node locations).

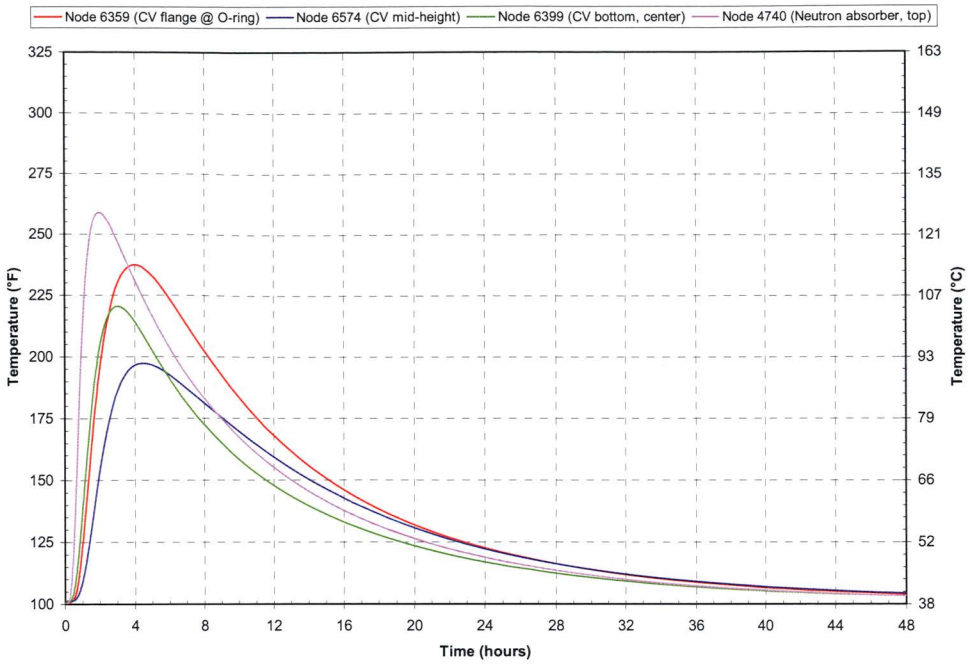

(a) No insolation during post-fire cool-down.

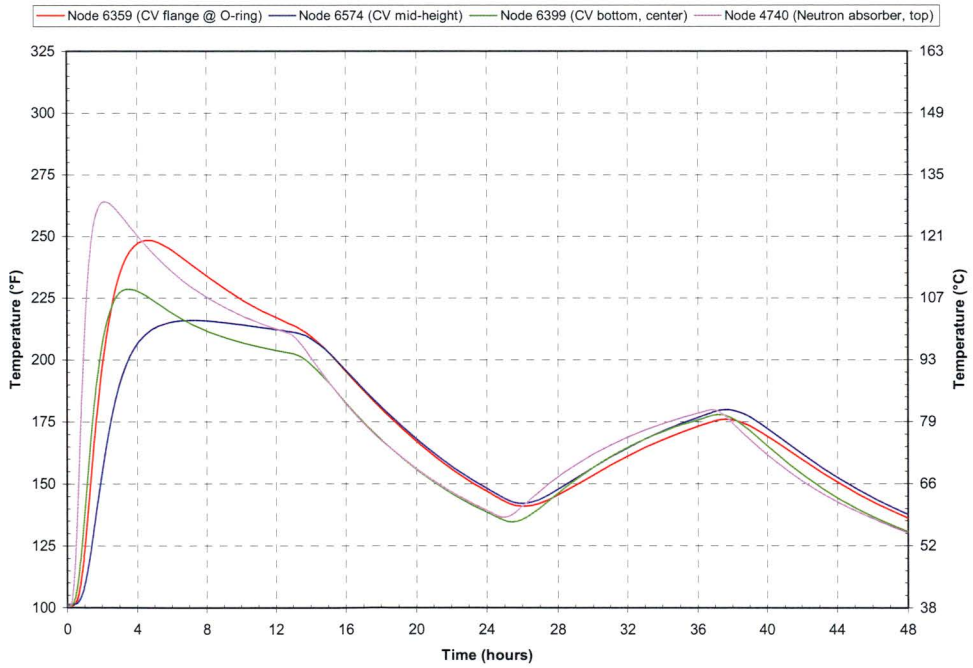

(b) Insolation during post-fire cool-down.

Figure 21. ES-3100 shipping container transient temperatures for HAC, 0.4 W content heat load and lower bound Kaolite and neutron absorber densities (see Figure 8 for through Figure 11 for node locations).

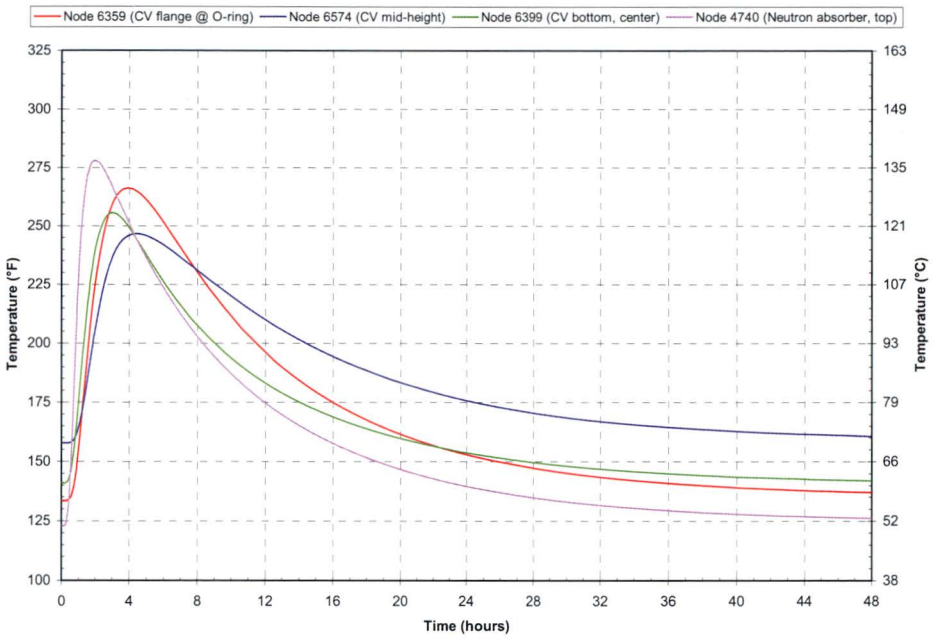

(a) No insolation during post-fire cool-down.

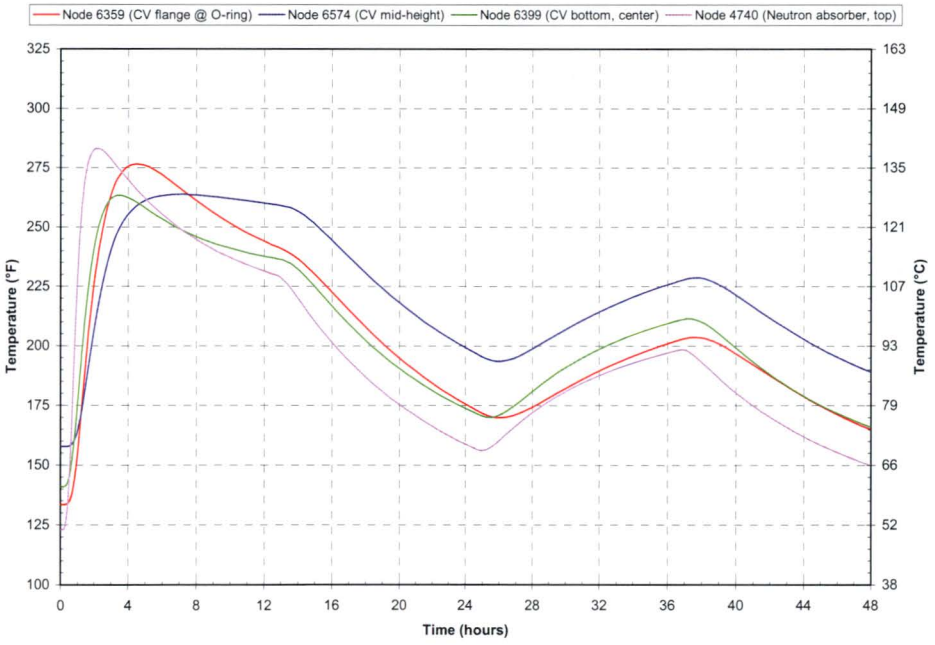

(b) Insolation during post-fire cool-down.

Figure 22. ES-3100 shipping container transient temperatures for HAC, 20 W content heat load and lower bound Kaolite and neutron absorber densities (see Figure 8 through Figure 11 for node locations).

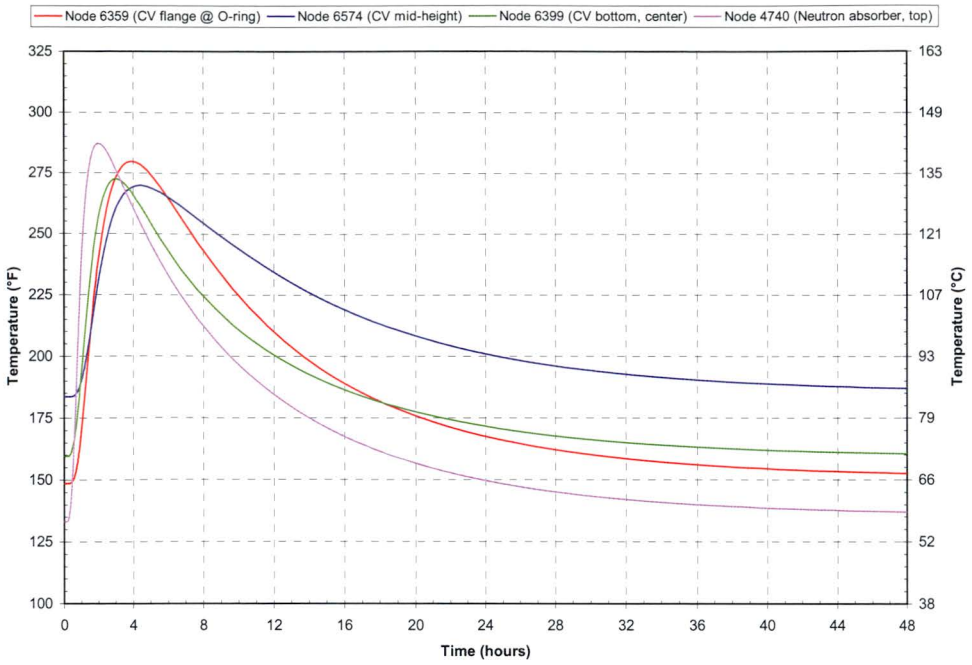

(a) No insolation during post-fire cool-down.

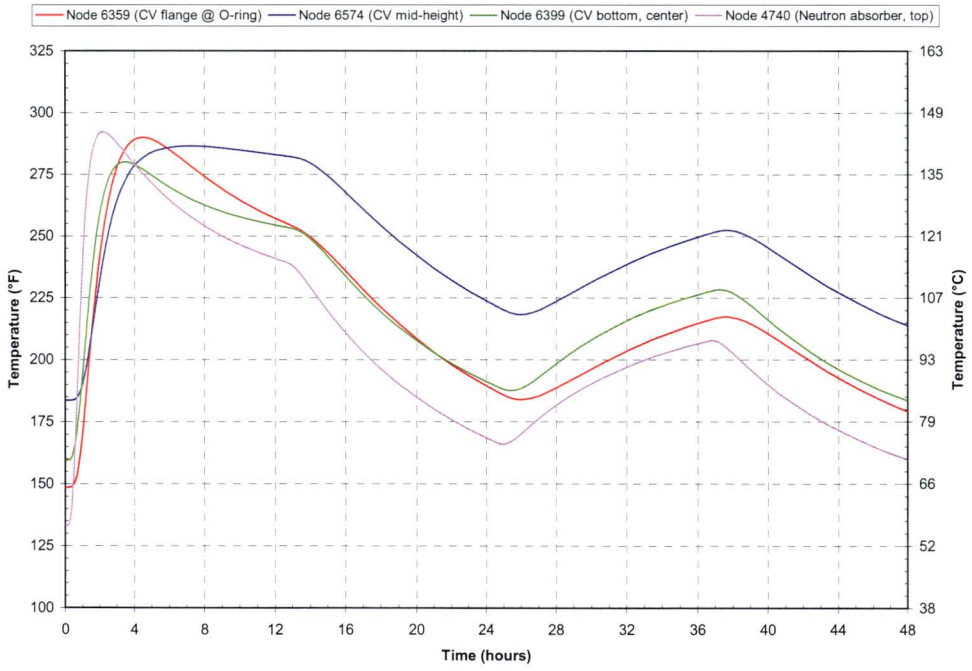

(b) Insolation during post-fire cool-down.

Figure 23. ES-3100 shipping container transient temperatures for HAC, 30 W content heat load and lower bound Kaolite and neutron absorber densities (see Figure 8 through Figure 11 for node locations)

APPENDIX 3.6.2 REFERENCES

1. *Packaging and Transportation of Radioactive Materials*, U.S. Nuclear Regulatory Commission, Code of Federal Regulations, Title 10 – Energy, Part 71, January 1, 2004.

2. L. S. Dickerson, M. R. Feldman, and R. D. Michaelhaugh, *Test Report of the ES-3100 Package*, Volumes 1–3, ORNL/NTRC-013, Rev. 0, Nuclear Science and Technology Division, Oak Ridge National Laboratory, Oak Ridge, Tennessee, September 10, 2004.

3. MSC. Patran 2004, Version 12.0.044, MacNeal Schwendler Corporation, 2004.

4. ABAQUS/CAE, Version 6.4-1, Build ID: 2003_09_29-11.18.28 46457, Abaqus, Inc., 2003.

5. R. Siegel and J. R. Howell, *Thermal Radiation Heat Transfer*, Second Edition, Hemisphere Publishing Corporation, 1981.

6. F. P. Incropera and D. P. DeWitt, *Fundamentals of Heat and Mass Transfer*, Second Edition, John Wiley & Sons, New York, 1985.

7. J. C. Anderson and M. R. Feldman, *Thermal Modeling of Packages for Normal Conditions of Transport with Insolation*, Proceedings of the ASME Heat Transfer Division, HTD-Vol. 317-2, 1995, International Mechanical Engineering Congress and Exposition, November 1995.

8. ABAQUS/Standard, Version 6.4-1, 2003_09_29-11.18.28 46457, Abaqus, Inc. , 2003.

9. P. A. Bales, *Thermal Analyses of the ES-3100 Shipping Container for NCT and HAC*, DAC-PKG-801699-A001, Rev. 1, BWXT Y-12, December 30, 2004.

THIS PAGE INTENTIONALLY LEFT BLANK.

Appendix 3.6.3

THERMAL STRESS EVALUATION OF THE ES-3100 SHIPPING CONTAINER DRUM BODY ASSEMBLY FOR NCT (FINAL DESIGN WITH CATALOG 277-4 NEUTRON ABSORBER)

THIS PAGE INTENTIONALLY LEFT BLANK.

Appendix 3.6.3

THERMAL STRESS EVALUATION OF THE ES-3100 SHIPPING CONTAINER DRUM BODY ASSEMBLY FOR NCT (FINAL DESIGN WITH CATALOG 277-4 NEUTRON ABSORBER)

INTRODUCTION

Static stress analyses of the ES-3100 shipping container are performed to determine the maximum thermal stresses within the packaging when exposed to Normal Conditions of Transport (NCT) as specified in 10 CFR 71.71(c)(1).[1] Transient thermal analyses were previously performed[2] (see Appendix 3.6.2) on the ES-3100 shipping container to determine its response to NCT. The thermal analyses treat the problem as a cyclic transient with the incident heat flux due to solar radiation applied and not applied in alternating 12-hour periods. The calculated temperature distributions within the drum body assembly for NCT at various times are then mapped onto the structural model, and static analyses are performed for each time step in the thermal analyses.

FINITE ELEMENT MODEL DESCRIPTION

A two-dimensional axisymmetric finite element model of the ES-3100 shipping container is constructed using MSC.Patran[3] and imported as an orphaned mesh into ABAQUS/CAE[4] for application of boundary conditions, interactions, and loads. The model is constructed of CAX4I (four-node bilinear axisymmetric quadrilateral, incompatible mode) elements for stress evaluation. These elements are chosen because they can accurately capture bending stresses with only one element through the thickness of a structure. A schematic of the finite element model is presented in Figure 1 with details of the upper and lower portions of the model shown in Figure 2 and Figure 3, respectively. The model consists of three materials: stainless steel (drum, drum bottom plate, and drum liner weldment), Kaolite, and neutron absorber. Details of the model are discussed in the following sections.

Surface-to-surface contact interactions are modeled between contacting surfaces in the static stress model. These interactions are shown graphically in Figure 2 and Figure 3. For all interactions, the tangential behavior is modeled as "frictionless" while the normal behavior is modeled as "hard contact." For the interactions modeled between the bottom of the neutron absorber and the drum liner and between the drum Kaolite bottom and the drum bottom plate, the contacting surfaces are not allowed to separate after contact is made.

The radial degree-of-freedom (U_r) of each node along the centerline of the model is fixed to simulate symmetry. Additionally, the axial degree-of-freedom (U_z) of one node on the drum bottom plate is fixed.

The temperatures calculated for NCT in Appendix 3.6.2 are stored in the 'NCT.fil' file for each of the content head loads analyzed. The temperature distribution for each time of interest is mapped onto the static stress model using the '`*Temperature`' keyword. The specific times of interest from the transient thermal analyses are at each increment in the final day/night cycle (after "quasi steady-state" is reached).

The mechanical properties of the materials used in the static stress analyses are presented in Table 1. The modulus of elasticity of Kaolite presented in Table 1 is calculated from the first two points of the compressive stress-strain assuming a Poisson's ratio of 0.01.[5]

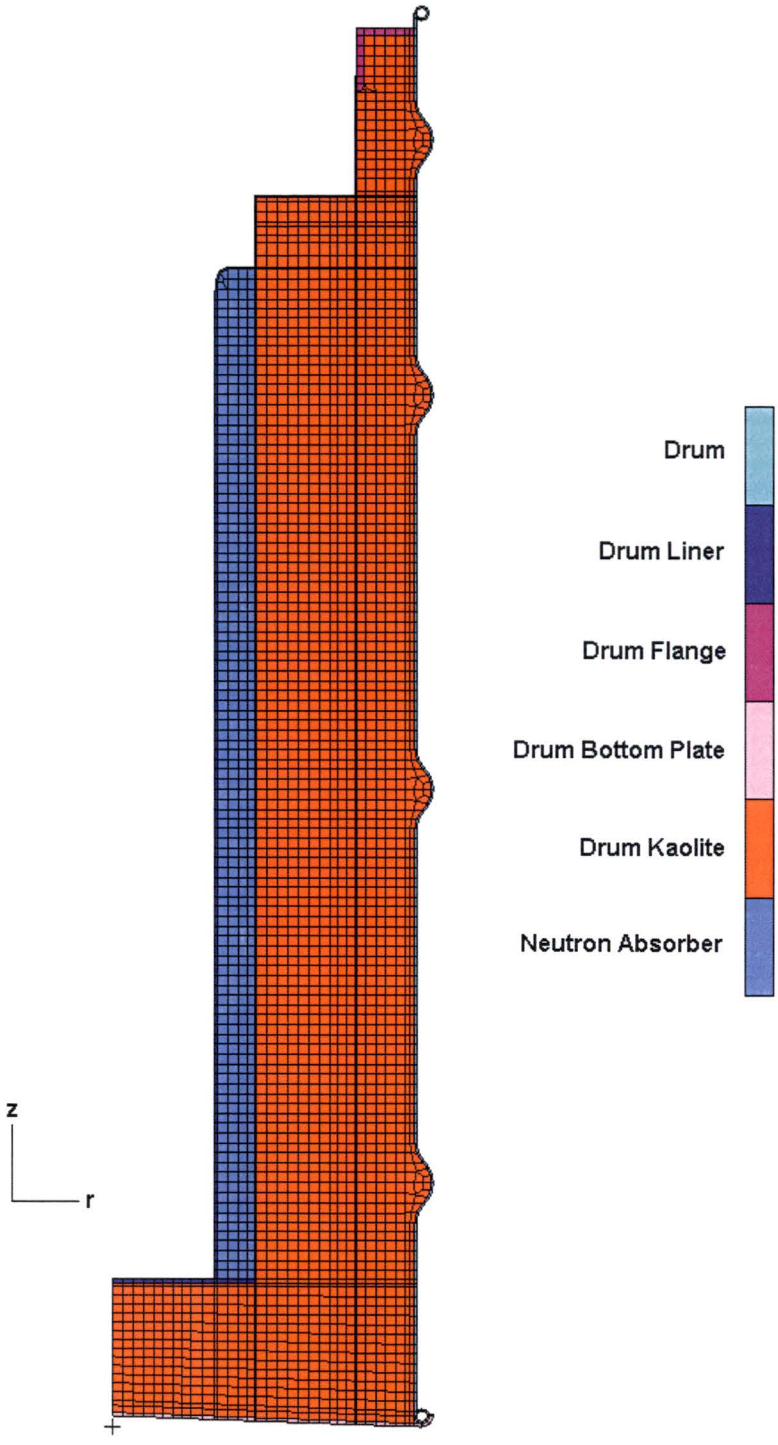

Figure 1. MSC.Patran axisymmetric finite element model of the ES-3100 shipping container drum body assembly.

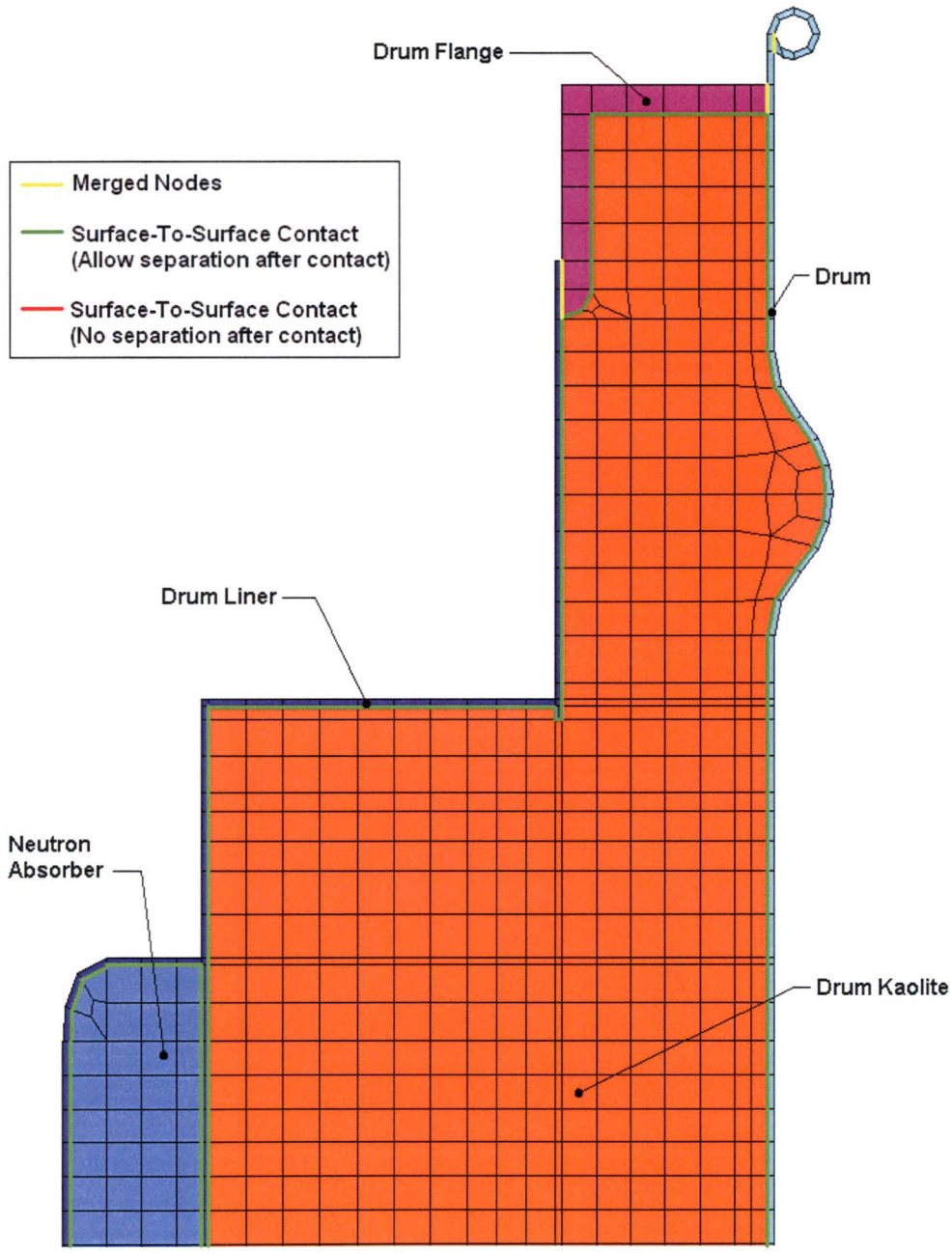

Figure 2. MSC.Patran axisymmetric finite element model of the ES-3100 shipping container drum body assembly (upper portion detail).

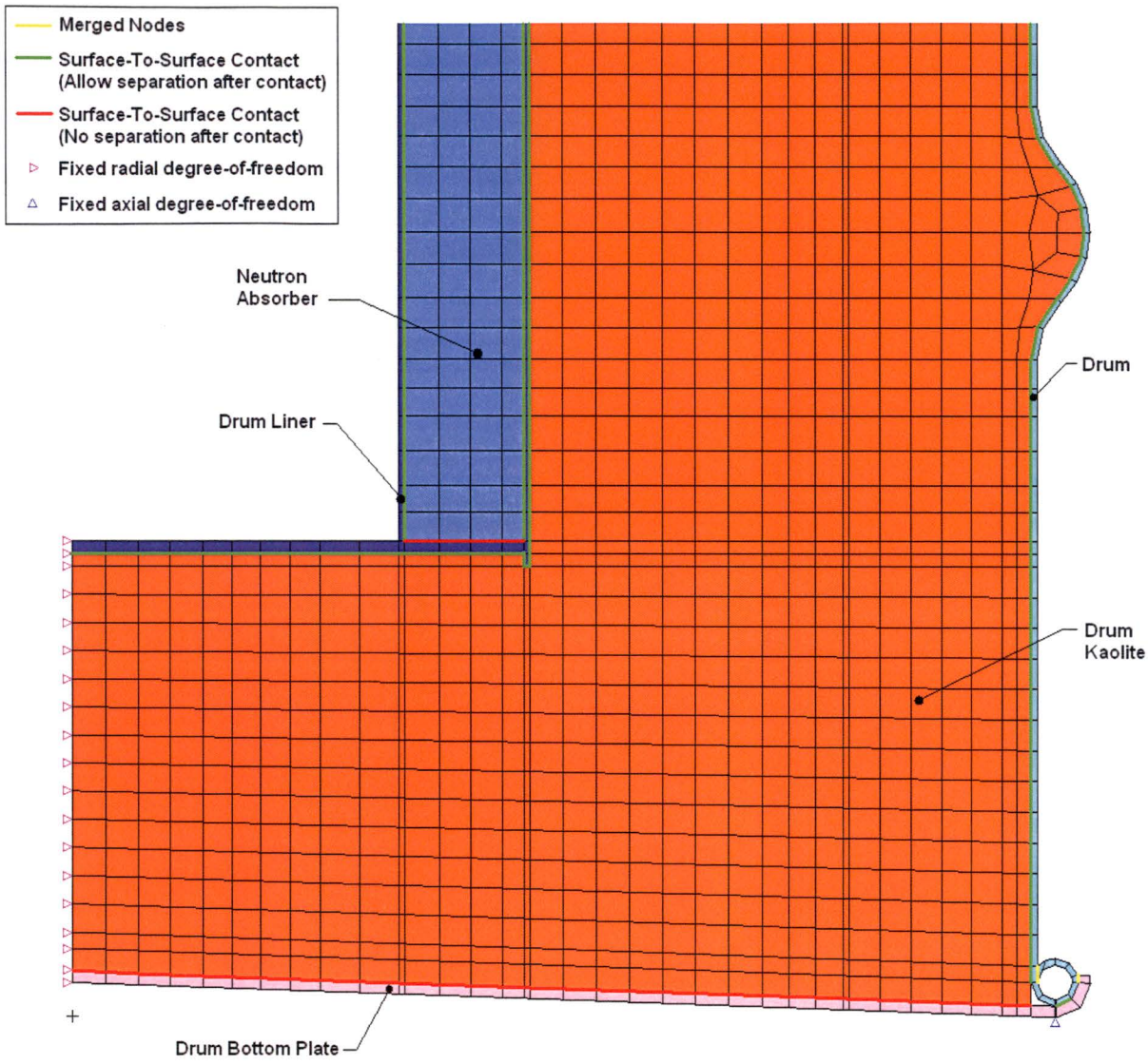

Figure 3. MSC.Patran axisymmetric finite element model of the ES-3100 shipping container drum body assembly (lower portion detail).

Table 1. Mechanical properties of the materials used in the static stress analyses.

Material	Temperature (°F)	Modulus of elasticity (psi)	Poisson's ratio	Density (lbm/in^3)	Coefficient of thermal expansion (in./in./°F)
Stainless Steel	-40	28.6×10^6 [(a)]	0.29 [(b)]	0.285 [(c)]	8.2×10^{-6} [(e)]
	100	28.14×10^6	–	–	8.6×10^{-6}
	200	27.6×10^6	–	–	8.9×10^{-6}
	300	27.0×10^6	–	–	9.2×10^{-6}
Kaolite	–	29,210 [(d)]	0.01 [(d)]	0.013 [(f)]	5.04×10^{-6} [(g)]
Neutron Absorber	-40	1.991×10^6 [(h)]	0.33 [(h)]	0.0608 [(h)]	7.056×10^{-6} [(i)]
	-4	–	–	–	7.222×10^{-6}
	32	–	–	–	7.222×10^{-6}
	70	0.984×10^6	0.28	–	–
	100	0.403×10^6	0.25	–	–
	104	–	–	–	7.000×10^{-6}
	140	–	–	–	6.444×10^{-6}
	176	–	–	–	5.778×10^{-6}
	212	–	–	–	5.389×10^{-6}
	248	–	–	–	5.056×10^{-6}
	284	–	–	–	4.889×10^{-6}
	302	–	–	–	4.833×10^{-6}

Notes:
(a) ASME Boiler and Pressure Vessel Code, Sect. II, Part D, Subpart 2, Tables TE-1, B column, and TM-1.
(b) R. A. Bailey, *Strain – A Material Database*, Lawrence Livermore National Laboratory, 1989.
(c) F. P. Incropera and D. P. DeWitt, *Fundamentals of Heat and Mass Transfer*, 2nd edition, John Wiley & Sons, New York, 1985.
(d) K. D. Handy, *Impact Analysis of ES3100 Design Concepts Using Borobond*, DAC-EA-801699-A001, BWXT Y-12, Oct. 2004. The Poisson's ratio of Kaolite is assumed to be a small value of 0.1.
(e) *Metallic Materials and Elements for Aerospace Vehicle Structures*, MIL-HDBK-5E, May 1986.
(f) Specification JS-YMN3-801580-A003 requires a baked density of 22.4 ± 3 lbm/ft^3.
(g) E-mail communication, Ken Moody (Thermal Ceramics, Inc.) to Paul Bales (BWXT Y-12), 12/9/04.
(h) B. F. Smith and G. A. Byington, Mechanical Properties of 277-4, Y/DW-1987, January 19, 2005.
(i) W. D. Porter and H. Wang, *Thermophysical Properties of Heat Resistant Shielding Material*, ORNL/TM-2004/290, ORNL, Dec. 2004. Coefficient of thermal expansion at each temperature taken as the maximum of values for Runs #2, #3, and #5.

DISCUSSION OF ANALYTICAL RESULTS

All static stress analyses discussed in this report were performed using ABAQUS/Standard[6] on an Intel Pentium 4–based Microsoft Windows 2000 computer. These analyses are sequential-coupled thermal/structural analyses.

As previously stated, the nodal temperature results for the final day/night cycle of the transient thermal analyses of the ES-3100 shipping container were stored in results files (NCT.fil) for each content heat load analyzed. Because automatic time-stepping was used in the transient thermal analyses, the number of increments stored in each 'NCT.fil' file differs for each content heat load analyzed. The static stress analyses of the ES-3100 are performed for each time increment analyzed in the thermal analyses for the final day/night cycle during NCT by copying the 'NCT.fil' and 'NCT.prt' files from the thermal analysis of interest to the directory where the stress analysis is being performed and entering the '`*Temperature`' keyword with the proper syntax for the time of interest. For example, for a content heat load of 0.4 W, the thermal stresses for time = 14.127 hours after sunrise (2.127 hours after sunset) on the final day/night

cycle (i.e., step = 11, increment = 29) are analyzed by entering the following keyword syntax via the keyword editor in ABAQUS/CAE:

```
*Temperature, file=NCT, bstep=11, binc=29, estep=11, einc=29
```

A separate static analysis is performed for each time step in the final day/night cycle of each thermal analysis for each content heat load.

The results of the static stress analyses for content heat loads of 0.4, 20, and 30 W are presented in Figure 4 through Figure 6. The stresses presented in these figures are the maximum nodal Mises stresses of each component at each point in time—as such, they don't necessarily occur at the same node location during the duration of the time period analyzed. The x-axes (i.e., time) are scaled in these figures such that the onset of sunrise on the final day/night cycle from the thermal analyses begins at time = 0 hours. Additionally, the stress (Mises) contours of the components of the finite element model are shown at various times in Figure 7 through Figure 11 for the case with a content heat load of 0.4 W. The time chosen for each stress contour plot coincides with the time that particular component reaches its maximum stress during the day/night cycle. The stress contours for the other heat loads investigated are similar to the 0.4 W case.

In addition to the static stress analyses performed for NCT, a static stress analysis is performed for exposure of the package to a -40°F ambient temperature (i.e., cold condition). A transient thermal analysis (24 hours in duration) is performed on the ES-3100 thermal model described in Appendix 3.6.2 to obtain the temperature distribution within the drum body assembly for exposure to cold conditions (see Appendix C for details). The package is assumed to be at an initial uniform temperature of 77°F, and no content heat load is applied. The natural convection coefficients (applied to the top and sides of the drum) are calculated for a -40°F ambient as described in Appendix 3.6.2 and are shown in Figure 12. A schematic of the thermal model showing several node locations for which the temperatures are tracked is presented in Figure 13. The transient temperatures calculated for cold conditions are presented in Figure 14 for several node locations. The maximum thermal stresses are presented in Figure 15 for this cold condition. Additionally, stress contours of the drum liner weldment, drum, and drum bottom plate are presented in Figure 16 through Figure 18 for the cold conditions at various times.

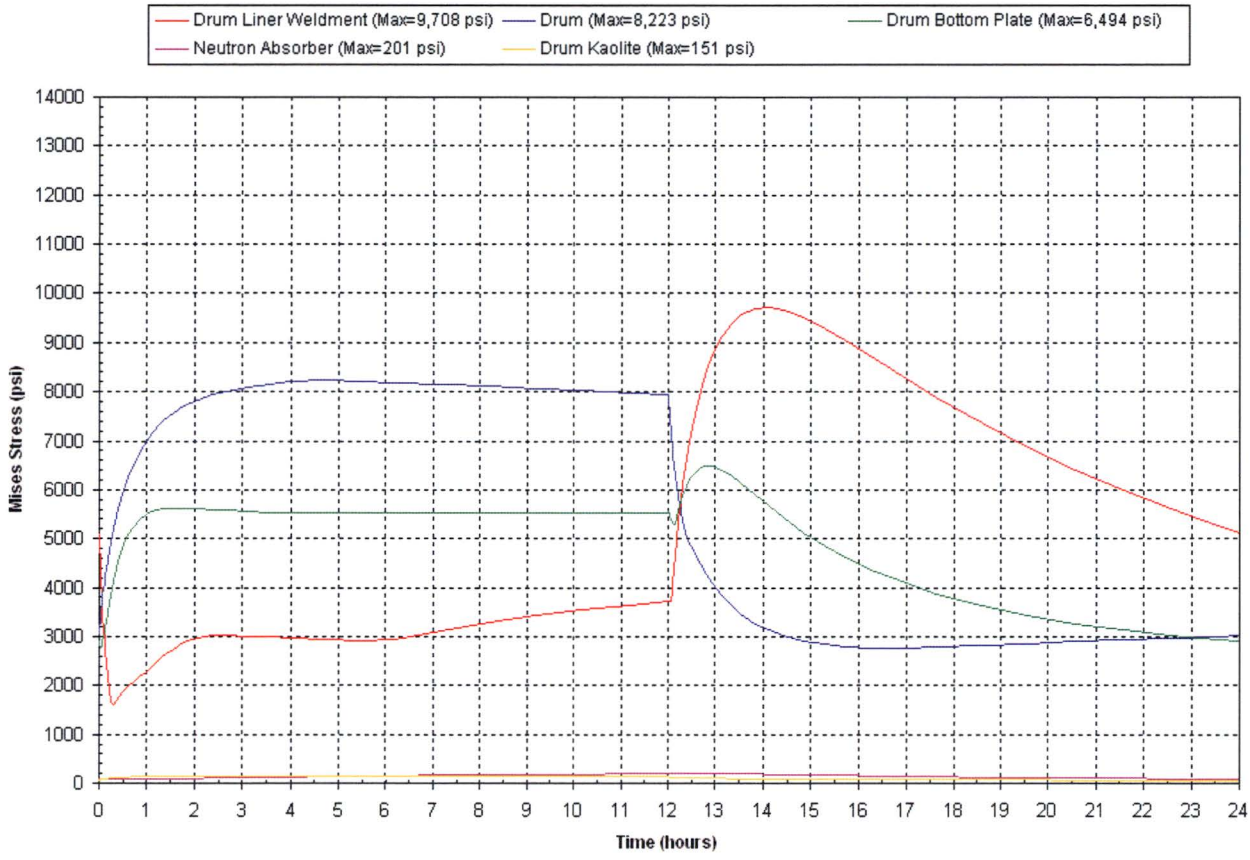

Figure 4. Thermal stresses (Mises) in the ES-3100 shipping container drum body assembly during a typical NCT day/night cycle—0.4 W content heat load.

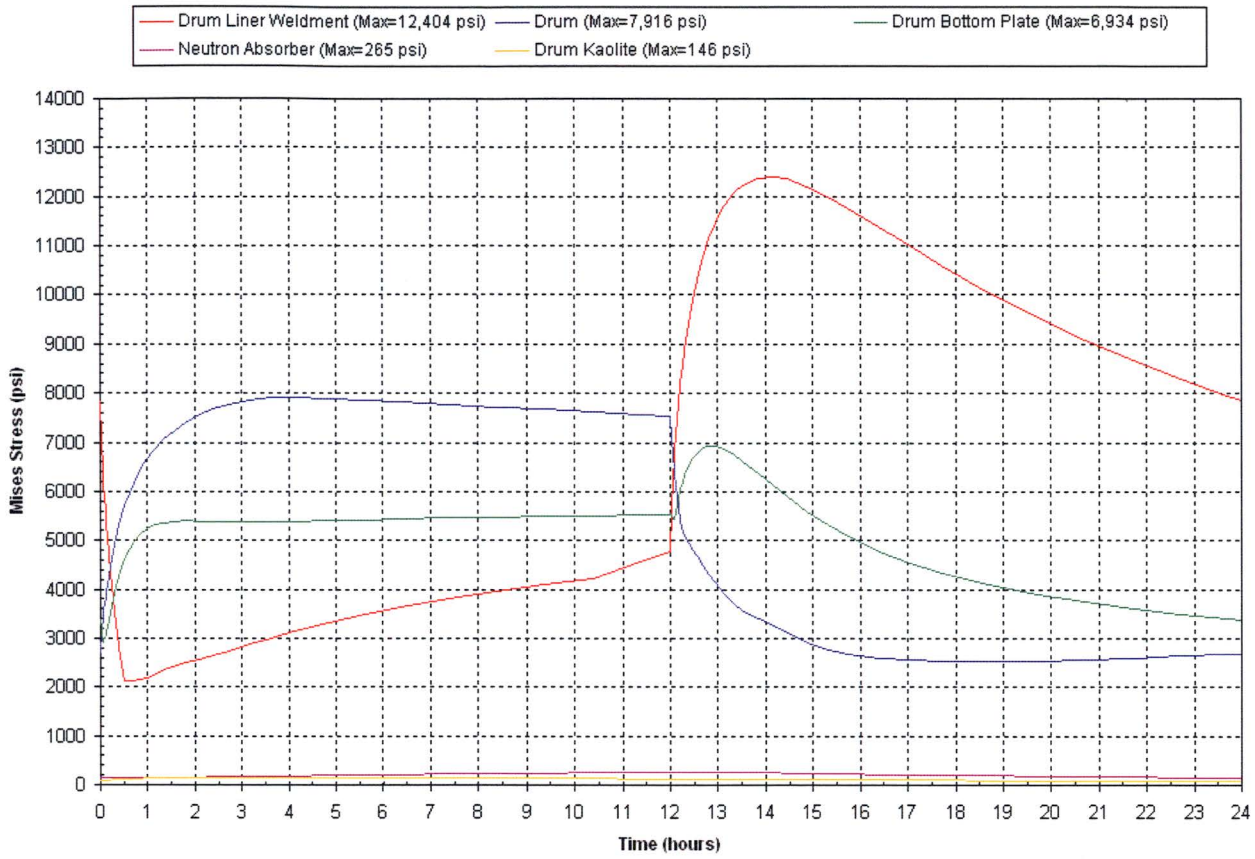

Figure 5. Thermal stresses (Mises) in the ES-3100 shipping container drum body assembly during a typical NCT day/night cycle—20 W content heat load.

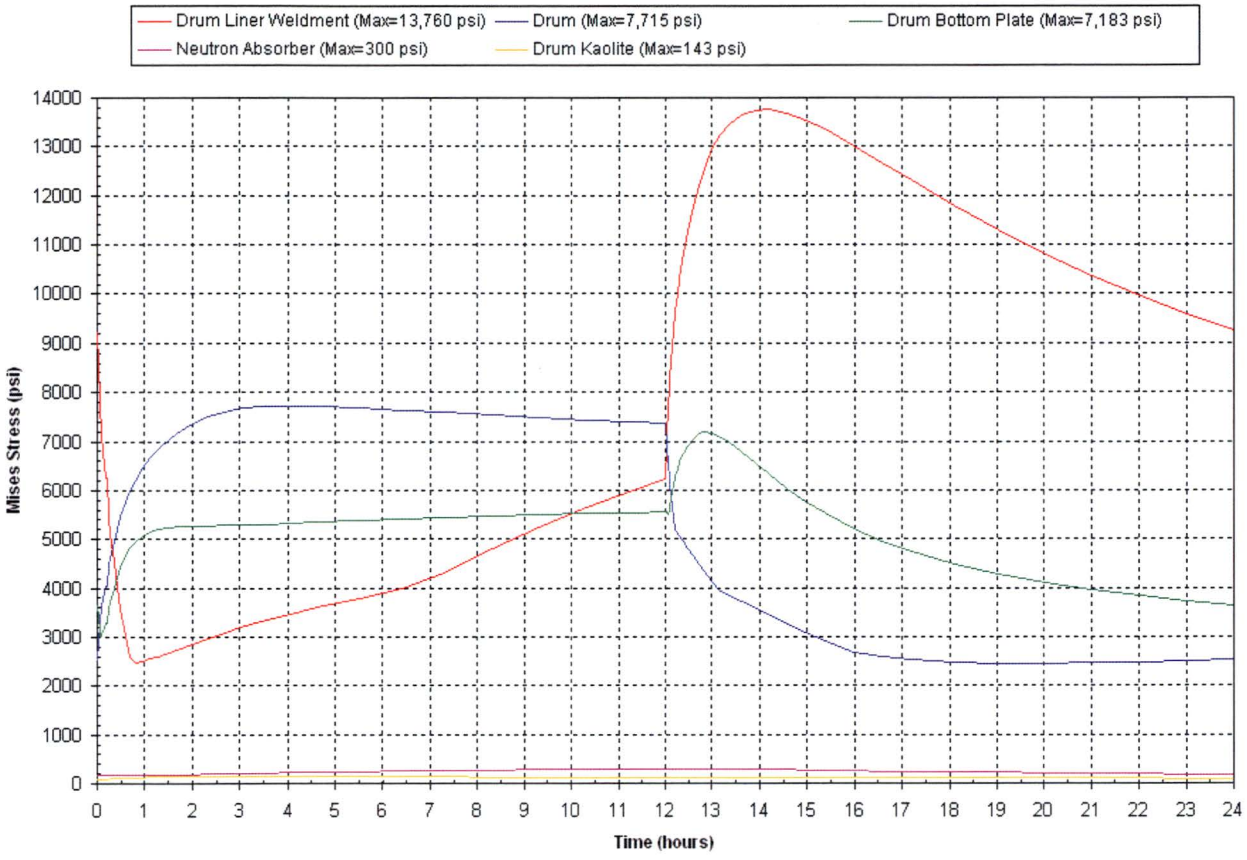

Figure 6. Thermal stresses (Mises) in the ES-3100 shipping container drum body assembly during a typical NCT day/night cycle—30 W content heat load.

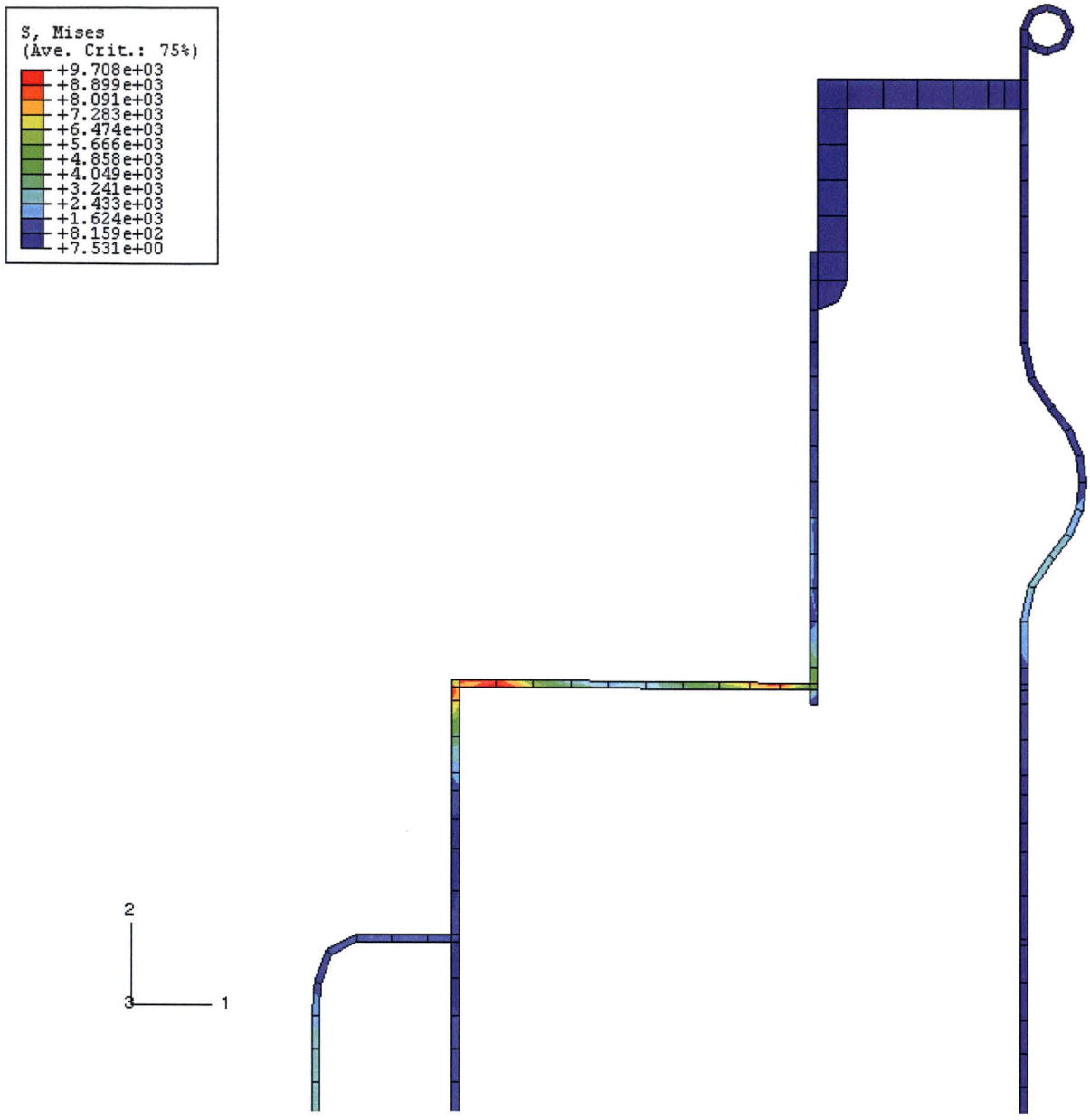

Figure 7. Drum/drum liner weldment Mises stresses (psi) during NCT at t = 14.127 hours (+2.127 hours after sunset)—0.4 W content heat load.

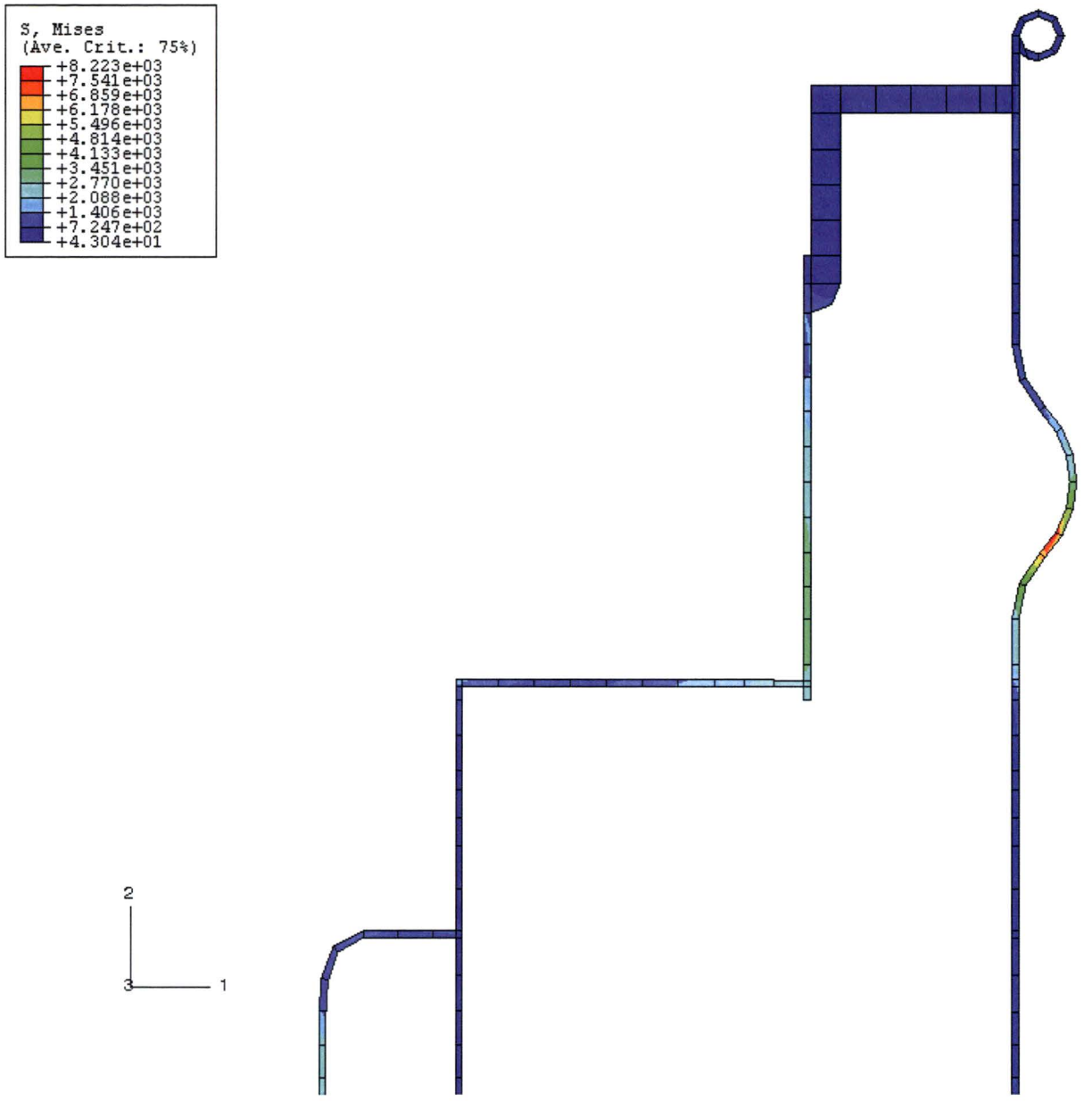

Figure 8. Drum/drum liner weldment Mises stresses (psi) during NCT at t = 4.724 hours (+4.724 hours after sunrise)—0.4 W content heat load.

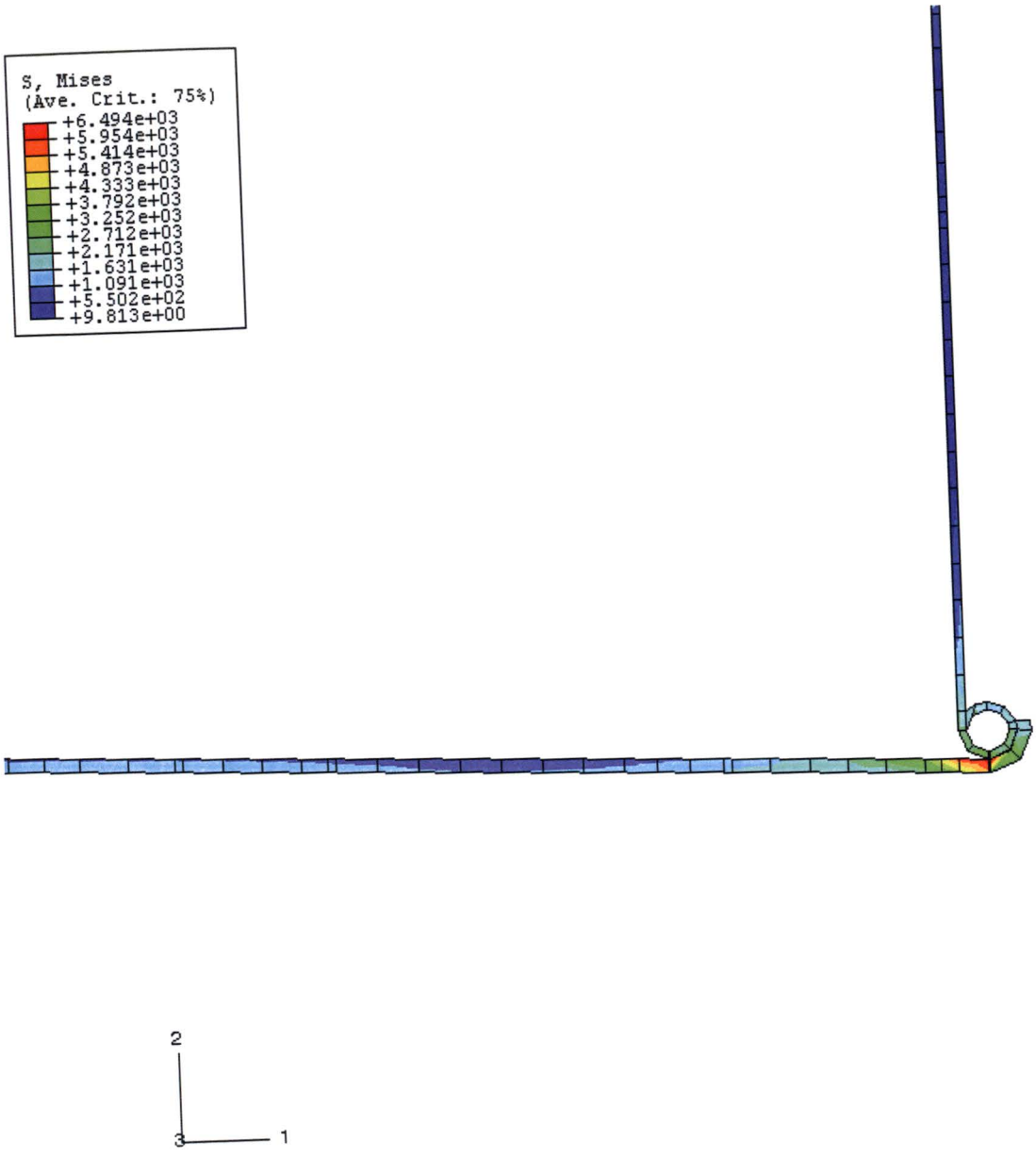

Figure 9. Drum/drum bottom plate Mises stresses (psi) during NCT at t = 12.814 hours (+0.814 hours after sunset)—0.4 W content heat load.

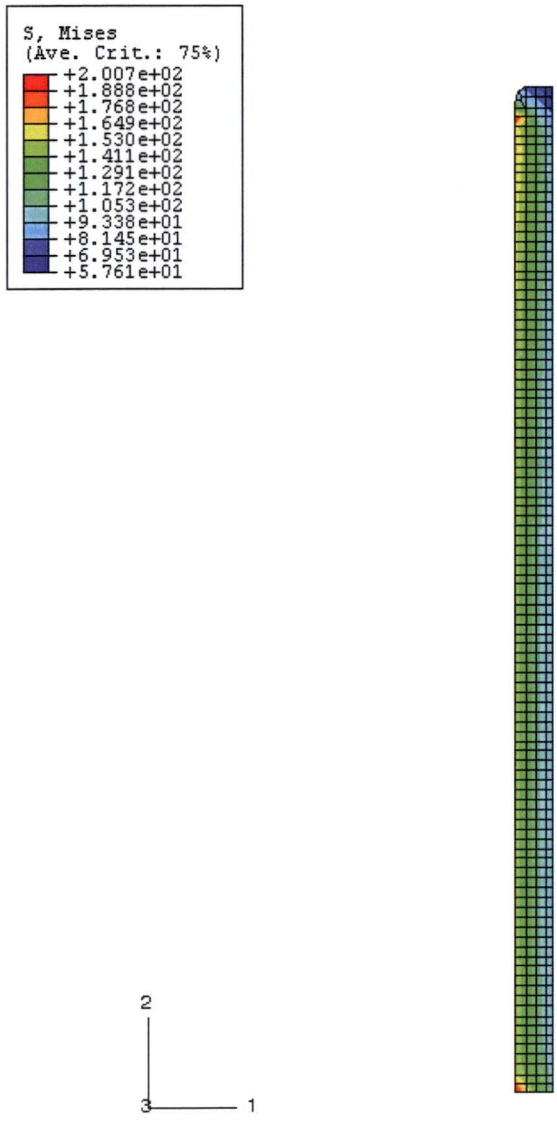

Figure 10. Neutron absorber Mises stresses (psi) during NCT at t = 12.867 hours (+0.867 hours after sunset)—0.4 W content heat load.

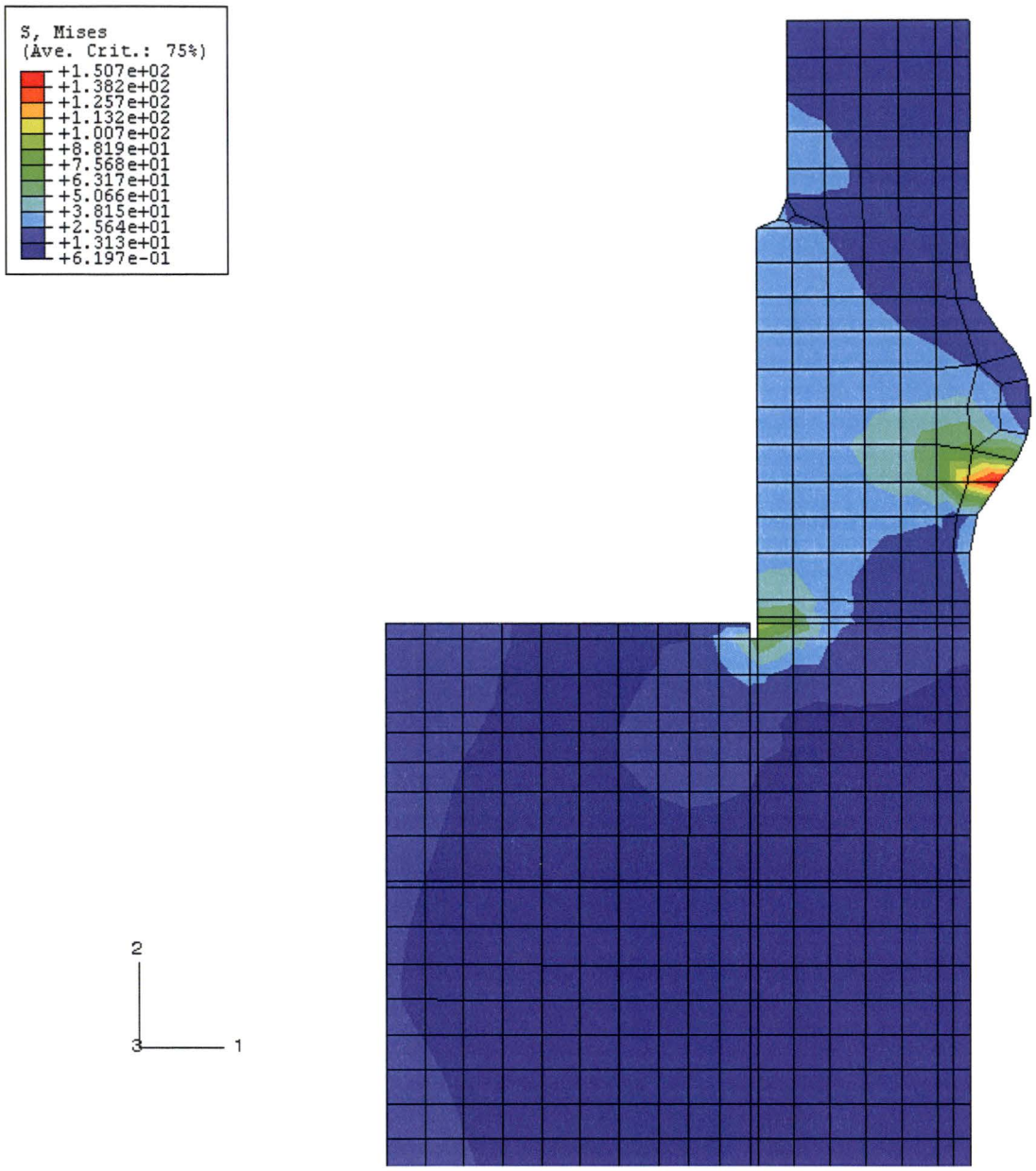

Figure 11. Drum Kaolite Mises stresses (psi) during NCT at t = 3.992 hours (+3.992 hours after sunrise)—0.4 W content heat load.

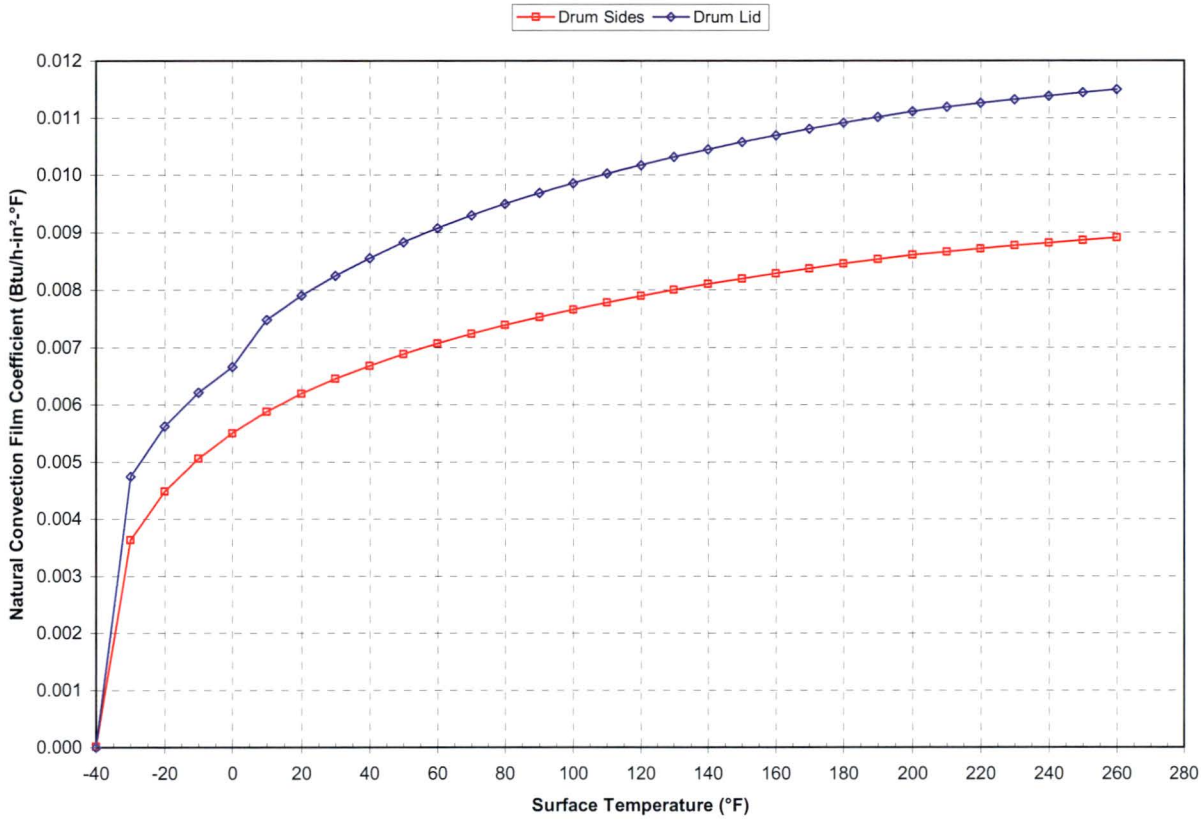

Figure 12. Natural convection film coefficients applied to the drum surfaces during cold conditions.

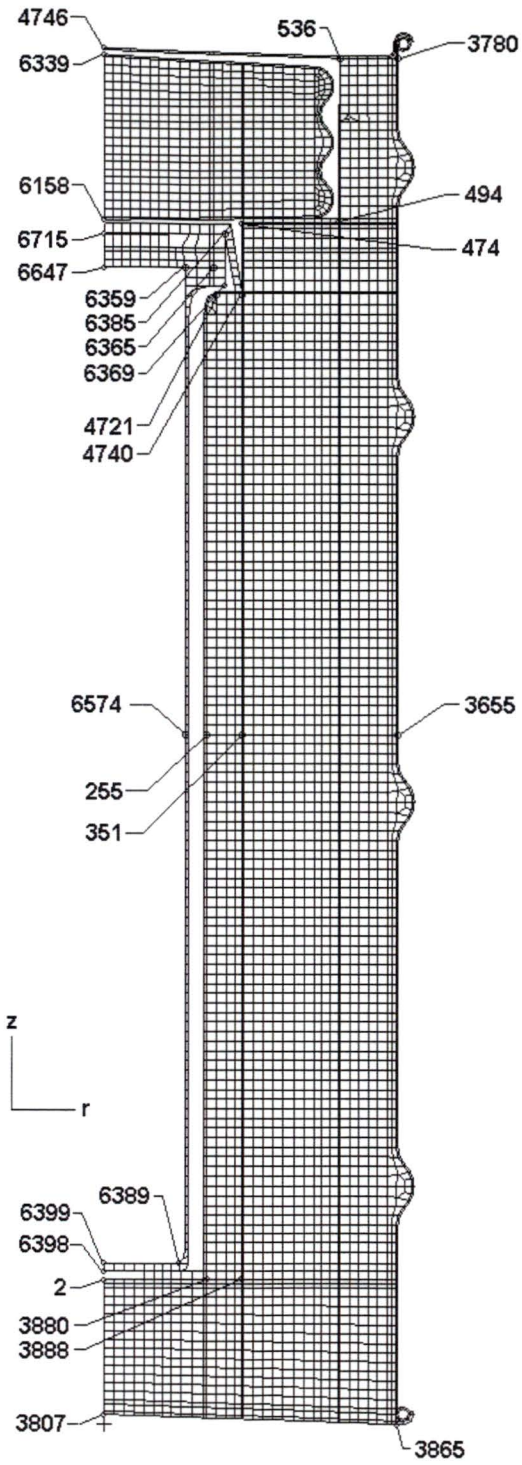

Node	r (in.)	z (in.)
2	0.000	4.505
255	3.180	21.528
351	4.300	21.528
474	4.300	37.535
494	7.325	37.535
536	7.385	42.755
3655	9.185	21.528
3780	9.185	42.755
3807	0.000	0.320
3865	9.185	0.008
3880	3.178	4.505
3888	4.300	4.505
4721	3.500	35.275
4740	4.300	35.275
4746	0.000	43.065
6158	0.000	37.579
6339	0.000	42.859
6359	2.530	36.075
6365	3.425	36.075
6369	3.750	35.525
6385	3.750	37.175
6389	2.310	5.025
6398	0.000	4.775
6399	0.000	5.025
6574	2.530	21.528
6647	0.000	36.075
6715	0.000	37.135

Figure 13. ABAQUS axisymmetric finite element thermal model of the ES-3100 shipping container—nodal locations of interest defined in Table 3.4a (elements representing air not shown for clarity).

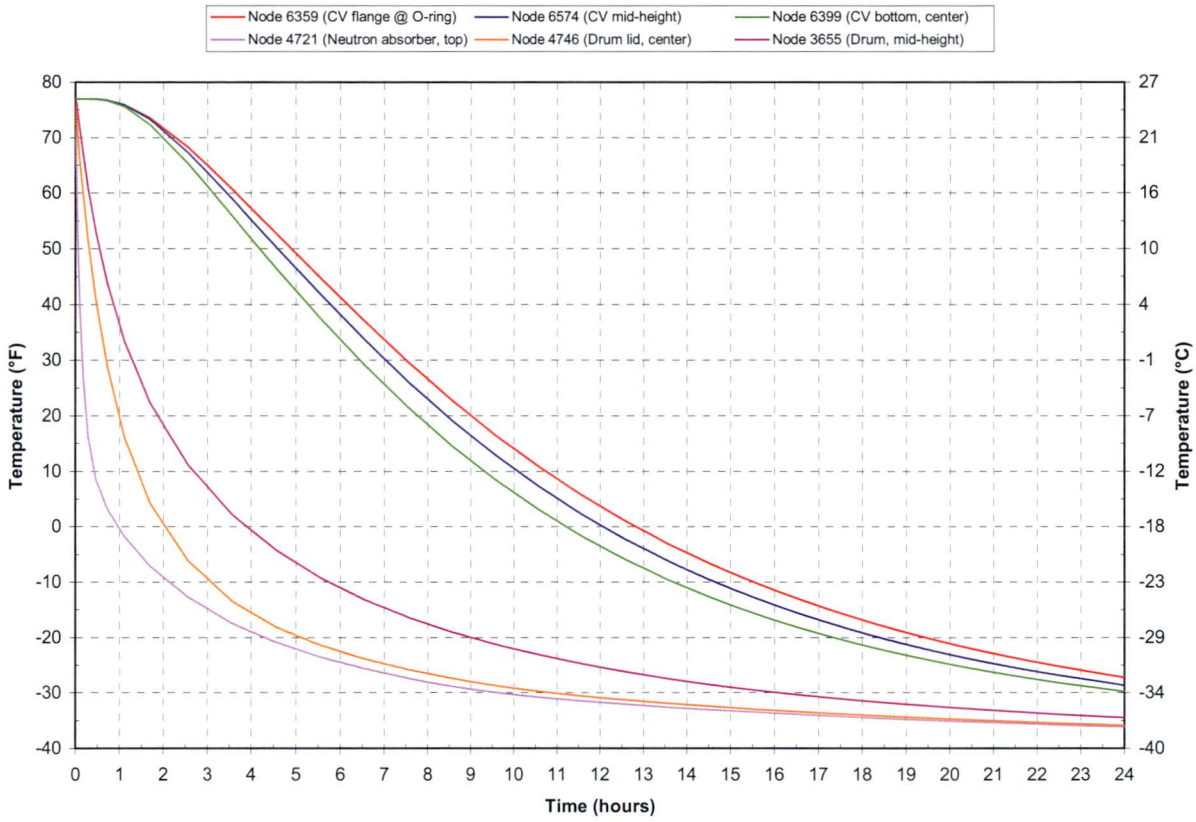

Figure 14. Transient temperatures of the ES-3100 shipping container for cold conditions (no content heat load) see Figure 13 for node locations.

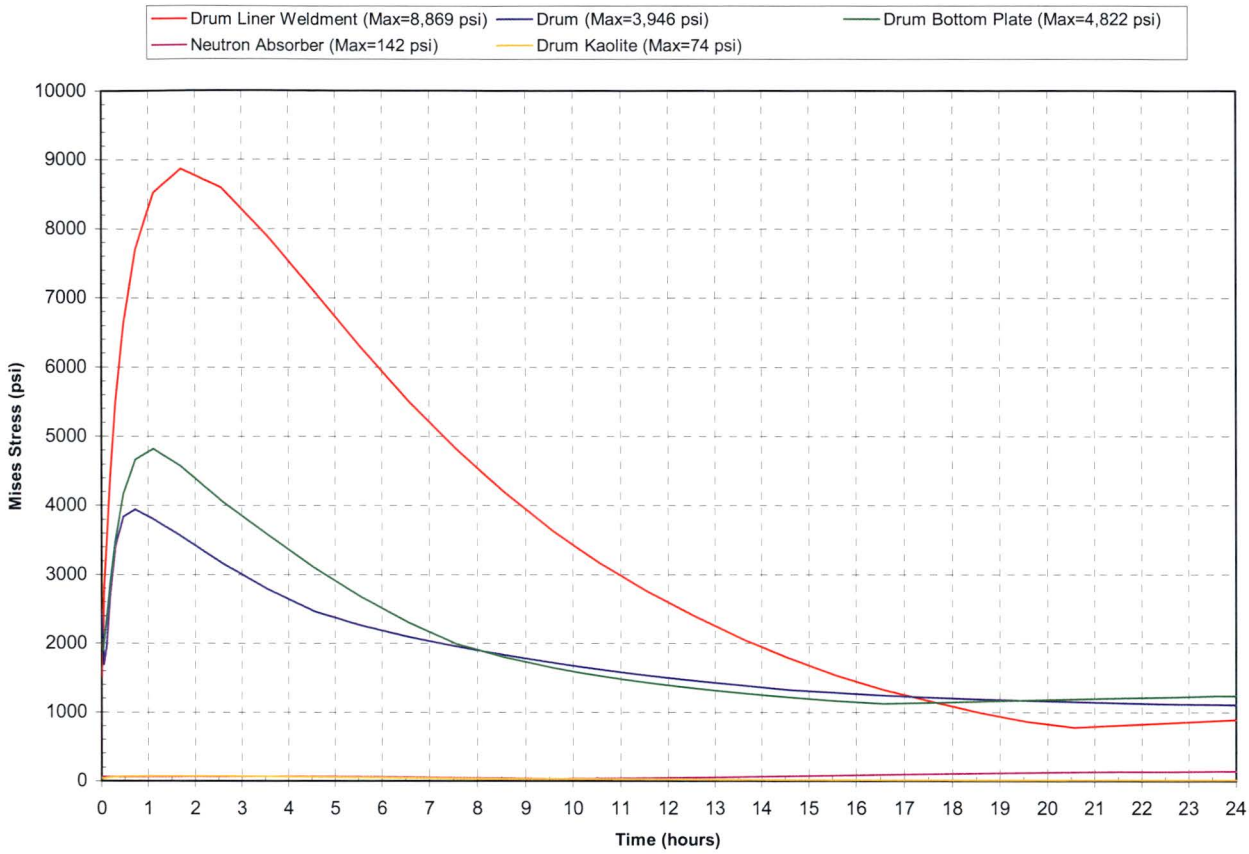

Figure 15. Thermal stresses (Mises) in the ES-3100 shipping container drum body assembly during cold conditions (-40°F ambient temperature)—no content heat load.

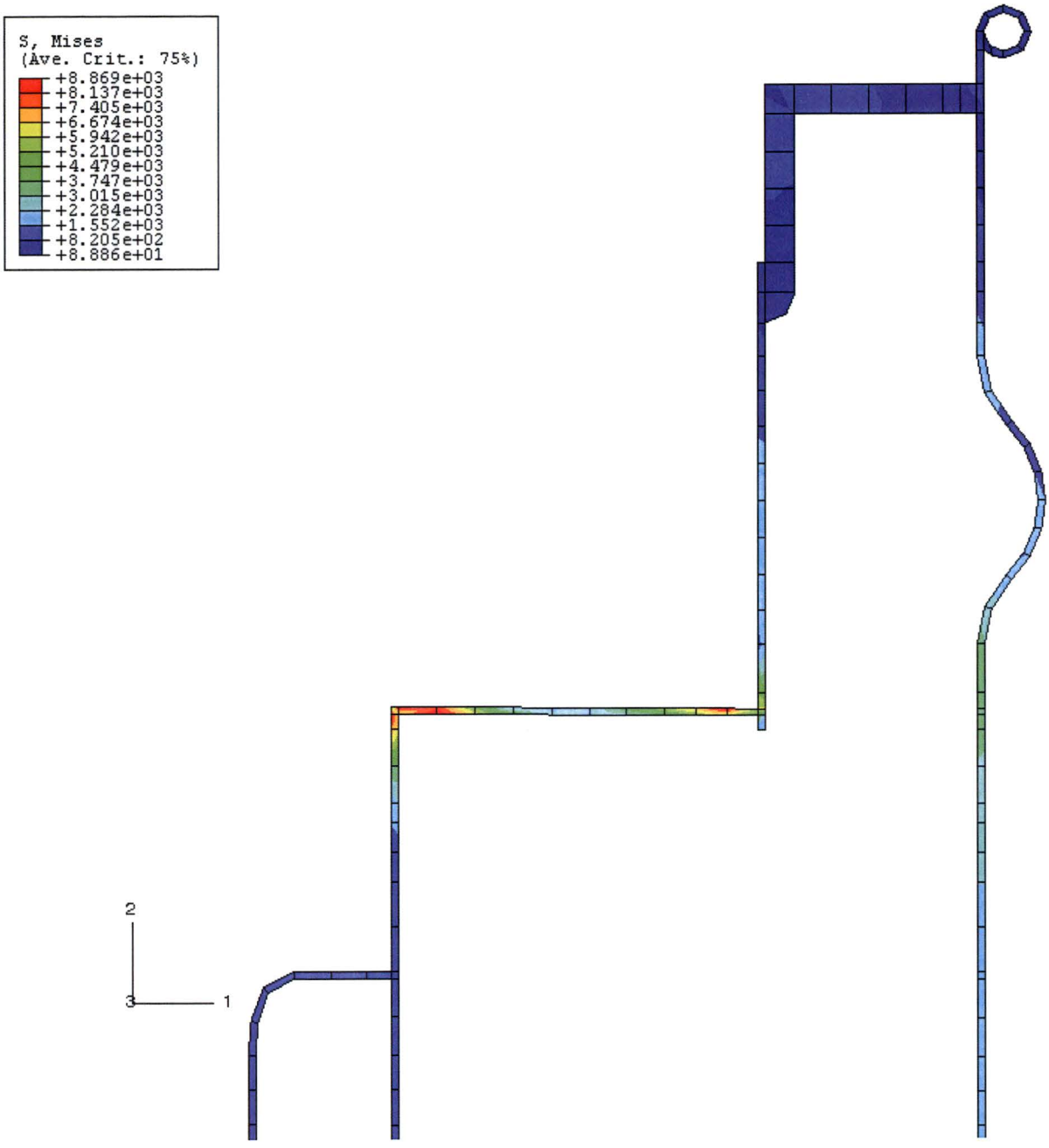

Figure 16. Drum/drum liner weldment Mises stresses (psi) during cold conditions at t = 1.698 hours—no content heat load.

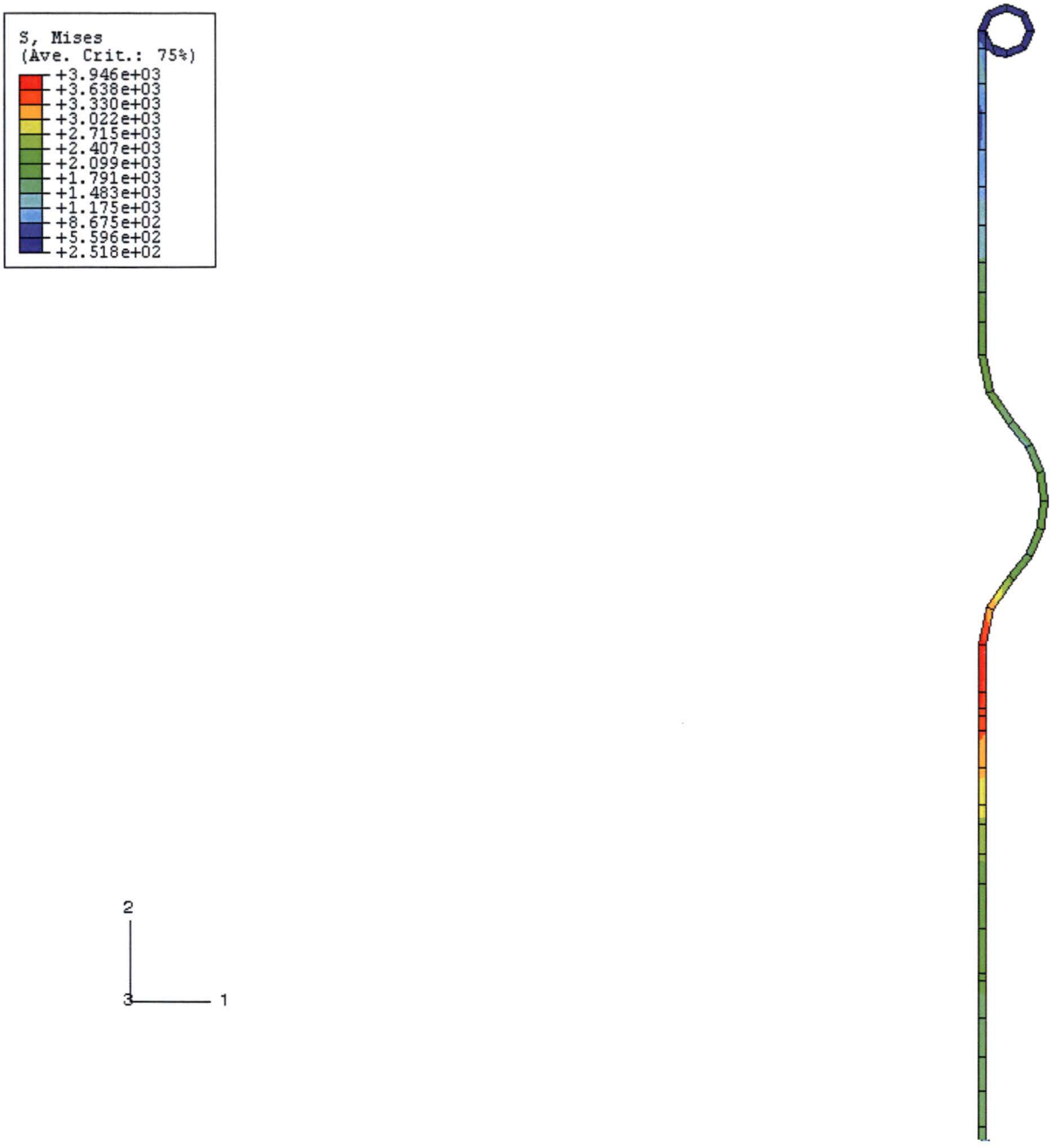

Figure 17. Drum Mises stresses (psi) during cold conditions at t = 0.726 hours — no content heat load.

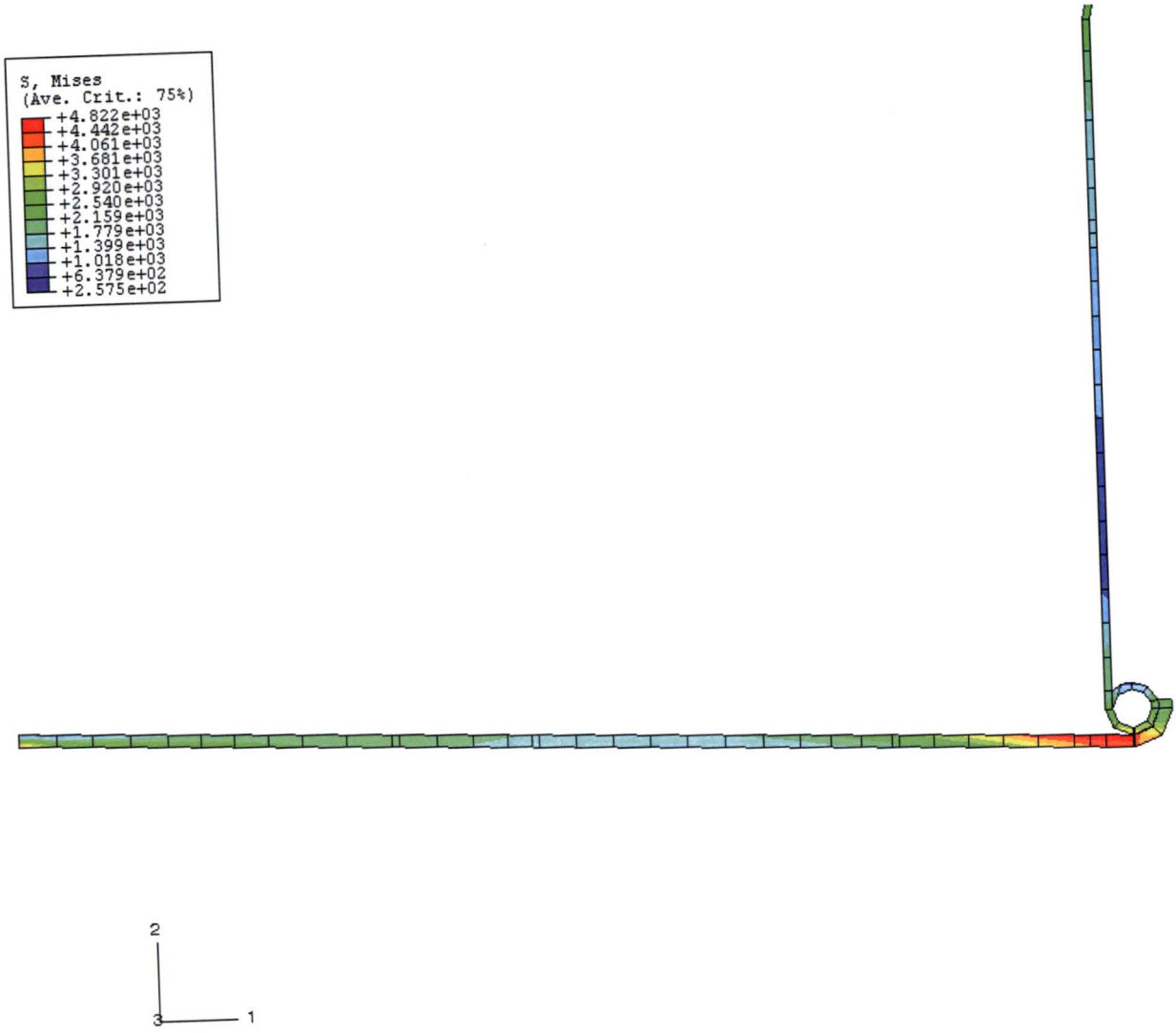

Figure 18. Drum bottom plate Mises stresses (psi) during cold conditions at t = 1.115 hours—no content heat load.

APPENDIX 3.6.3 REFERENCES

1. *Packaging and Transportation of Radioactive Materials*, U.S. Nuclear Regulatory Commission, Code of Federal Regulations, Title 10 – Energy, Part 71, January 1, 2004.

2. P. A. Bales, *Thermal Analyses of the ES-3100 Shipping Container for NCT and HAC (Final Design with 277-4 Neutron Absorber)*, DAC-PKG-801699-A002, Rev. 0, BWXT Y-12, January 31, 2005.

3. MSC. Patran 2004, Version 12.0.044, MacNeal Schwendler Corporation, 2004.

4. ABAQUS/CAE, Version 6.4-1, Build ID: 2003_09_29-11.18.28 46457, Abaqus, Inc., 2003.

5. K. D. Handy, *Impact Analysis of ES3100 Design Concepts Using Borobond*, DAC-EA-801699-A001, BWXT Y-12, Oct. 2004.

6. ABAQUS/Standard, Version 6.4-1, 2003_09-11.18.28 46457, Abaqus, Inc.

Appendix 3.6.4

CONTAINMENT VESSEL PRESSURE DUE TO NORMAL CONDITIONS OF TRANSPORT FOR THE PROPOSED CONTENTS

Prepared by: M. L. Goins
B&W Y-12
December 2007

Reviewed by: Paul Bales
B&W Y-12
January 2008

Revised by: Mark Stansberry
B&W Y-12
February 2009

Reviewed by: Drew Winder
B&W Y-12
February 2009

Revised by: Monty Goins
B&W Y-12
November 2010

Reviewed by: Drew Winder
B&W Y-12
December 2010

Revised by: M. L. Goins
Navarro Research and Engineering
January 2016

Reviewed by: D. A. Wilson
Navarro Research and Engineering
March 2016

THIS PAGE INTENTIONALLY LEFT BLANK.

Appendix 3.6.4

CONTAINMENT VESSEL PRESSURE DUE TO NORMAL CONDITIONS OF TRANSPORT FOR THE PROPOSED CONTENTS

The following calculations determine the pressure of the containment vessel when subjected to the tests and conditions of Normal Condition of Transport per 10 CFR 71.71 for the most restrictive convenience can arrangements shipped in the ES-3100. The following packaging arrangements are evaluated for shipment:

1. one shipment will contain six cans with external dimensions of 4.25-in. diameter by 4.875-in. high;

2. one shipment will contain five cans with external dimensions of 4.25-in. diameter by 4.875-in. high and three can spacers, top can will be empty;

3. one shipment will contain three cans with external dimension of 4.25-in. diameter by 8.75-in. high and two can spacers;

4. one shipment will contain three cans with external dimension of 4.25-in. diameter by 10-in. high; and

5. one shipment will contain six cans with external dimension of 3.00-in. diameter by 4.75-in. high;

6. one shipment will contain three polyethylene bottles with external dimensions of 4.94-in. diameter by 8.7-in. high; and

7. one shipment will contain three Teflon FEP bottles (~400 g Teflon each) with external dimensions of 4.69-in. diameter by 9.4-in. high, limited to 1600 g of offgassing material.

To determine this pressure, the following assumptions have been made:

1. The HEU contents are loaded into convenience cans which are placed inside the ES-3100 containment vessel at standard temperature (T_{amb}) and pressure (P_t) [25°C (77°F) and 101.35 kPa (14.7 psia)] with air at a maximum relative humidity of 100%.

2. The convenience cans are assumed to not be sealed.

3. Except for CVA 7, polyethylene bagging of contents and/or convenience cans is limited to 500 g per containment vessel shipping arrangement.

4. If metal convenience cans are used, the total amount of polyethylene bagging and lifting slings is limited to 500 g per containment vessel shipping arrangement.

5. The mass of offgassing material (polyethylene bagging or bottles, Teflon bottles, silicone pads, lifting slings) is assumed to be 1600 g for the offgassing evaluation of CVA 7. Teflon bottles (~400 g Teflon each) contribute ~1200 g total, therefore the other offgassing material is limited to 400 g.

The offgassing material limits identified in assumptions 4 and 5 have been established based on the needs of shippers. All configurations, except CVA 7, are limited to 500 g of polyethylene in the form of bags, slings, and/or bottles. The upper limit of 1600 g of offgassing material is a combination of three Teflon bottles (400 g Teflon per bottle) and a 400-g allowance for the other offgassing material. These offgassing material limits have been used in calculations pertaining to containment vessel pressure, radioactive material leakage criteria, and criticality control. Therefore, portions of the safety basis for this shipping package have been based on these material limits.

Applying Dalton's law concerning a mixture of gases, the properties of each component are considered as though each component exists separately at the volume and temperature of the mixture. Therefore, the molar quantities of each constituent inside the containment vessel (i.e., dry air, water vapor, polyethylene bagging, and silicone rubber) must be calculated individually.

To calculate these molar properties, the void volume of the containment vessel must be determined. The volume inside an empty ES-3100 containment vessel was determined from Algor finite element software to be 637.18 $in.^3$ (10,441.51 cm^3).

I. Molar quantity determination for dry air and water vapor

According to *Fundamentals of Classical Thermodynamics*,

> "Relative humidity (Φ) is defined as the ratio of the mole fraction in the mixture to the mole fraction of vapor in a saturated mixture at the same temperature and total pressure."

Since the vapor is considered an ideal gas, the definition reduces to the ratio of the partial pressure of the vapor (P_v) as it exists in the mixture to the saturation pressure of the vapor (P_g) at the same temperature.

Therefore,

$$\Phi = P_v / P_g .$$

From the above equation and interpolating the values given in Table A.1.1 of *Fundamentals of Classical Thermodynamics*, the partial pressure of the water vapor at saturation is:

$$P_v = 1.0\ (0.464)\ \text{psia},$$
$$P_v = 0.464\ \text{psia}.$$

The partial pressure of the dry air (P_a) in the volume:

$$P_a = P_t - P_v$$
$$= 14.7 - 0.464$$
$$= 14.236\ \text{psia}.$$

From the ideal gas law, the number of water vapor moles and dry air moles in the void volume (V_V) for each containment vessel arrangement (CVA) is calculated as follows:

$$n_v = \frac{P_v \cdot V_v}{R_u \cdot T_{amb} \cdot 12}, \quad n_a = \frac{P_a \cdot V_v}{R_u \cdot T_{amb} \cdot 12}$$

To determine the number of moles, the void volume of the air mixture must be determined. The void volume (V_V) in the containment vessel for each CVA is calculated as follows:

$$V_V = V_{ECV} - V_{SP} - V_{PB} - V_{SCC} - V_{CS} - V_{CH},$$

where

V_{ECV} = volume inside an empty containment vessel,
V_{SP} = silicone pad volume,
V_{PB} = polyethylene bagging or lifting sling volume,
V_{SCC} = structural volume of the convenience cans or bottles,
V_{CS} = external volume of the can spacers,
V_{CH} = external volume of the convenience can handles.

A summary for each CVA is shown in Table 1.

The bounding case based on the volumes listed in Table 1 is CVA 2 at 526.21 in.^{3}. To determine the minimum volume for this configuration, the mass limit of 15.13 kg of oxides is used in conjunction with the lowest density oxide of 7.3 kg/L (UO_3). The resulting volume is 15.13 kg / 7.3 kg/L × 1 ft^3 / 28.32 L × 1728 in.^{3} / ft^3 = 126.464 in.^{3}. Therefore, the bounding volume for CVA 2 is 526.21 in.^{3} - 126.464 in.^{3} = 399.746 in.^{3}.

Only CVA 7 can accommodate the uranyl nitrate crystals held in the Teflon bottles. CVA 7 is limited to 9.12 kg of the uranyl nitrate hexahydrate crystals and 11.9 kg of uranyl nitrate trihydrate crystals (see Appendix 3.6.7). For the bounding pressure calculation, the smallest resulting free volume in CVA 7 is then 578.90 - 11.9 kg / 2.81 kg/L × 1 ft^3 / 28.32 L × 1728 in.^{3} / ft^3 = 578.90 in.^{3} - 258.4 in.^{3} = 320.50 in.^{3}.

Using the above molar equations and bounding volumes, the number of moles for water vapor and dry air in the vessel for CVAs 2 and 7 are summarized in Table 2.

Table 1. Containment vessel void volume for each CVA

CVA		V_{ECV} ($in.^3$)	V_{SP} [a] ($in.^3$)	V_{PB} ($in.^3$)	V_{SCC} ($in.^3$)	V_{CS} ($in.^3$)	V_{CH} ($in.^3$)	V_V ($in.^3$)
1	Six 4.875-in.-high cans Seven silicone pads Six can handles	637.18	9.35	30.51	7.84	0.00	1.02	588.46
2	Five 4.875-high cans Nine silicone pads Three Cat 277-4 spacers Eight can handles	637.18	12.03	30.51	6.47	60.60	1.36	526.21
3	Three 8.75-in.- high cans Two Cat 277-4 spacers Six silicone pads Five can handles	637.18	8.02	30.51	5.14	40.40	0.85	552.26
4	Three 10-in.-high cans Four silicone pads Three can handles	637.18	5.35	30.51	5.56	0.00	0.51	595.26
5	Six 4.75 in.-high nickel cans	637.18	0.00	30.51	12.64	0.00	1.02	593.01
6	Three 4.94 in. OD polyethylene bottles	637.18	0.00	9.46	21.05	0.00	0.00	606.67
7	Three 4.69 in. OD Teflon FEP bottles	637.18	0.00	24.41	33.88	0.00	0.00	578.90

[a] This assumes that the internal convenience cans, polyethylene or Teflon FEP bottles, and Cat 277-4 spacer cans are not sealed.

Table 2. Water vapor and dry air molar summary for each CVA

CVA	P_a (psia)	P_v (psia)	V_V ($in.^3$)	R_u (ft-lb/lb-mole·R)	T_{amb} (R)	n_v (lb-mole)	n_a (lb-mole)
2	14.236	0.464	399.75	1545.32	537	1.8626E-05	5.7148E-04
7	14.236	0.464	320.50	1545.32	537	1.4934E-05	4.5819E-04

II. Molar quantity determination due to offgassing for each containment vessel arrangement

The maximum temperature calculated for the containment vessel is 87.81°C (190.06°F). This temperature is assumed to be constant throughout the containment vessel and contents. Therefore, the polyethylene bags, polyethylene bottles, Teflon FEP bottles, and silicone rubber can pads are assumed to be at this temperature.

Using the above calculated results and the specific gas generation of polyethylene bags and silicone rubber pad measurements at temperatures up to 170°C (338°F) conducted by the Y-12 Development Division, the amount of gas (V_{bo} and V_{po}) generated due to offgassing of the polyethylene bags and bottles, and silicone rubber can pads at any temperature is estimated by first determining the offgassing volume per unit mass at temperature and multiplying that by the total mass of the bags and can supports inside the containment vessel. Based on testing at a temperature of 93.33°C (200°F), no recordable offgassing occurred in the polyethylene bags and bottles, or silicone rubber pad material

as documented in Y/DZ-2585, Rev. 2 (Appendix 2.10.4). The value for Teflon FEP material offgassing volume per unit mass (V_{tf}) was obtained from Fig. 10 in Appendix 2.10.9. A value of ~0.12 to 0.13 cm^3/g@STP was recorded over a temperature range of 200 to 400°F. This value was conservatively doubled to 0.25 cm^3/g@STP. These values are used to determine the offgassing volumes as shown below:

V_{po} = $W_p \times 0.0 / 16.387$ ($in.^3$) (offgassing volume of silicone rubber pads)

V_{bo} = $W_b \times 0.0 / 16.387$ ($in.^3$) (offgassing volume of polyethylene bags and bottles or lifting sling)

V_{tf} = $W_{tf} \times 0.25 / 16.387$ ($in.^3$) (offgassing volume of Teflon bottles)

From the ideal gas law, the number of gas moles in the volume at standard temperature and pressure is as follows:

$$n_{io} = \frac{P_v \cdot V_i}{R_u \cdot T_{amb} \cdot 12}$$

A summary of the results obtained using the above equations for the bounding containment vessel arrangement is presented in Tables 3, 4, and 5.

Table 3. Molar quantity of gas generated due to the silicone rubber pad offgassing

CVA	W_p (g)	V_{po} ($in.^3$)	P_V (psia)	R_u (ft-lb/lb-mole·R)	T_{amb} (R)	n_{po} (lb-mole)
2	240.09	0.00	14.7	1545.32	537	0.0000E+00
7	0.00	0.00	14.7	1545.32	537	0.0000E+00

Table 4. Molar quantity of gas generated due to the polyethylene bag, sling and bottle offgassing

CVA	W_b (g)	V_{bo} ($in.^3$)	P_V (psia)	R_u (ft-lb/lb-mole·R)	T_{amb} (R)	n_{bo} (lb-mole)
2	500.00	0.00	14.7	1545.32	537	0.0000E+00
7	400.00	0.00	14.7	1545.32	537	0.0000E+00

Table 5. Molar quantity of gas generated due to the Teflon bottle offgassing

CVA	W_{tf} (g)	V_{tf} ($in.^3$)	P_V (psia)	R_u (ft-lb/lb-mole·R)	T_{amb} (R)	n_{tf} (lb-mole)
7	1200.00	18.31	14.7	1545.32	537	2.7025E-05

III. Gas generation due to radiolysis of water

Buildup of hydrogen gas (H_2) and oxygen gas (O_2) in the ES-3100 containment vessel due to radiolysis is incorporated into the pressure calculation by assuming that 5 mol % of the free volume is H_2. Since each mole of H_2 generated is accompanied by 0.5 mole of O_2, the concentration of H_2 will reach 5 mol % when volume of H_2 is 0.05405 times the initial void volume (see Sect. 3.6.7.8 of Appendix 3.6.7). Therefore, the volume of H_2 and O_2 in the void volume (V_v) is determined by the following expressions:

$$V_h = 0.05405 \times V_v \quad \text{and} \quad V_o = 0.5 \times V_h .$$

Using the ideal gas law, the number of gas moles of H_2 and O_2 in the volume at standard temperature and pressure is:

$$n_{r\text{-}H2} = \frac{P_v \cdot V_h}{R_u \cdot T_{amb} \cdot 12} \qquad n_{r\text{-}O2} = \frac{P_v \cdot V_o}{R_u \cdot T_{amb} \cdot 12}$$

where

$n_{r\text{-}H2}$ = individual molar quantity for H_2,
$n_{r\text{-}O2}$ = individual molar quantity for O_2,
V_h = volume of H_2 assumed generated by radiolysis,
V_o = volume of O_2 assumed generated by radiolysis.

A summary of the results for H_2 and O_2 generation due to radiolysis using the above equation is presented in Table 6.

Table 6. Molar quantity of oxygen and hydrogen gas generation due to radiolysis

CVA	V_v (in.^{3})	V_h (in.^{3})	V_o (in.^{3})	P_v (psia)	R_u (ft-lb/lb-mole · R)	T_{amb} (R)	$n_{r\text{-}H2}$ (lb-mole)	$n_{r\text{-}O2}$ (lb-mole)
2	399.75	21.61	10.80	14.7	1545.32	537.0	3.1895E-05	1.5948E-05
7	320.50	17.32	8.66	14.7	1545.32	537.0	2.5572E-05	1.2786E-05

IV. Molar quantity of gas generated due to the efflorescence of the uranyl nitrate crystals (UNX)

The uranyl nitrate crystals (UNX) in any hydrated state will decompose and lose water molecules at the temperature shown in Table 3.16 [87.81°C (190.06°F)]. The partial pressure of water vapor in this mixture is conservatively estimated to be the saturated vapor pressure (P_{sv}) of water at 87.81°C (190.06°F) or 9.344 psia. Using the ideal gas law, the molar quantity of water vapor (n_{wv}) in this volume at the maximum containment vessel temperature and the saturated vapor pressure is:

$$n_{wv} = \frac{P_{sv} \cdot V_v}{R_u \cdot T_{cv} \cdot 12}$$

n_{wv} = (9.344) (320.50) / (1545.32 × 12 × 650.06)
n_{wv} = 2.4843×10^{-4} lb-moles

where

n_{wv} = molar quantity for water vapor;
V_v = void volume of CVA 7;
T_{cv} = maximum temperature of containment vessel; and
P_{sv} = interpolated saturated vapor pressure of water at temperature from *Fundamentals of Classical Thermodynamics*, 2d ed, Table A.1.1, p. 650. (Van Wylen 1973)

V. Total pressure due to offgassing and NCT temperatures inside the containment vessel

The total pressure of the mixture at 87.81°C (190.06°F), P_T, for the bounding containment vessel arrangement is the pressure calculated using the sum of the previously calculated molar quantities of the gases in the containment vessel. Table 7 summarizes the molar constituents and total pressure of each bounding containment vessel arrangement. The following equation is used to calculate the final containment vessel pressure:

$$P_{87.81°C} = (\sum n_i \cdot R \cdot T \cdot 12) / V_{GMV},$$

where

n_i = individual molar quantity for each gas,
T = average gas temperature = 87.81°C (190.06°F),
V_{GMV} = V_v = gas mixture volume.

At −40°C (−40°F), the partial pressure of the water vapor is conservatively assumed to be zero. Therefore, the final pressure of the mixture at −40°C (−40°F) is calculated according to the ideal gas law based solely on the partial pressure of the air.

$$\frac{P_1 V_1}{T_1} = \frac{P_2 V_2}{T_2},$$

where

P_1 = 14.236 psi,
T_1 = 77°F = 536.67 R,
T_2 = −40°F = 419.67 R,
V_1 = V_2.

Rearranging and solving for P_2,

$P_2 = P_1 (T_2/T_1)$,
P_2 = (14.236)(419.67/536.67) = 11.13 psia.

Table 7. Total pressure inside the containment vessel at 87.81°C (190.06°F) [a]

CVA	n_a [b] (lb-mole)	n_v [b] (lb-mole)	n_{po} [b] (lb-mole)	n_{bo} [b] (lb-mole)	n_{tf} [b] (lb-mole)	n_{H2} [b] (lb-mole)	n_{O2} [b] (lb-mole)	n_T [b] (lb-mole)	P_T (psia)
2	5.7148E-04	1.8626E-05	0.0000E+00	0.0000E+00	0.0000E+00	3.1895E-05	1.5948E-05	6.3795E-04	19.238
7	4.5819E-04	2.4843E-04	0.0000E+00	0.0000E+00	2.7025E-05	2.5572E-05	1.2786E-05	7.7200E-04	29.036

[a] This assumes that the internal convenience cans, polyethylene or Teflon FEP bottles, and Cat 277-4 spacer cans are not sealed.

[b] n_a –molar quantity of dry air in the gas mixture;
n_v –molar quantity of water vapor in the gas mixture due primarily to efflorescence;
n_{po} –molar quantity of gas due to offgassing of the silicone rubber pads;
n_{bo} –molar quantity of gas due to offgassing of the polyethylene bags, bottles, and lifting sling;
n_{tf} –molar quantity of gas due to offgassing of the Teflon bottles;
n_{H2} –molar quantity of hydrogen gas due to radiolysis of water;
n_{O2} –molar quantity of oxygen gas due to radiolysis of water; and
n_T –total molar quantity in the gas mixture.

Appendix 3.6.5

CONTAINMENT VESSEL PRESSURE DUE TO HYPOTHETICAL ACCIDENT CONDITIONS FOR THE PROPOSED CONTENTS

Prepared by: M. L. Goins
B&W Y-12
December 2007

Reviewed by: Paul Bales
B&W Y-12
January 2008

Revised by: Mark Stansberry
B&W Y-12
February 2009

Reviewed by: Drew Winder
B&W Y-12
February 2009

Revised by: Monty Goins
B&W Y-12
November 2010

Reviewed by: Drew Winder
B&W Y-12
December 2010

Revised by: M. L. Goins
Navarro Research and Engineering
January 2016

Reviewed by: D. A. Wilson
Navarro Research and Engineering
March 2016

THIS PAGE INTENTIONALLY LEFT BLANK.

Appendix 3.6.5

CONTAINMENT VESSEL PRESSURE DUE TO HYPOTHETICAL ACCIDENT CONDITIONS FOR THE PROPOSED CONTENTS

The following calculations determine the pressure of the containment vessel when subjected to the tests and conditions of Hypothetical Accident Conditions per 10 CFR 71.73 for the most restrictive convenience can arrangements shipped in the ES-3100 package. The following packaging arrangements are evaluated for shipment:

1. one shipment will contain six cans with external dimensions of 4.25-in. diam by 4.875-in. high;

2. one shipment will contain five cans with external dimensions of 4.25-in. diam by 4.875-in. high and three can spacers, the top can is empty;

3. one shipment will contain three cans with external dimensions of 4.25-in. diam by 8.75-in. high and 2 can spacers;

4. one shipment will contain three cans with external dimensions of 4.25-in. diam by 10-in. high;

5. one shipment will contain six nickel cans with external dimensions of 3.00-in. diam by 4.75-in. high;

6. one shipment will contain three polyethylene bottles with external dimensions of 4.94-in. diam by 8.7-in. high; and

7 one shipment will contain three Teflon FEP bottles (~400 g Teflon each) with external dimensions of 4.69-in. diam by 9.4-in. high, limited to 1600 g of offgassing material.

To determine this pressure, the following assumptions have been made:

1. The highly enriched uranium (HEU) contents are loaded into convenience cans and placed inside the ES-3100 containment vessel at standard temperature [25°C (77°F)] and at the maximum normal operating pressure (see Table 5 of Appendix 3.6.4) with air at a maximum relative humidity of 100%.

2. The convenience cans are assumed to not be sealed.

3. Except for CVA 7, polyethylene bagging of contents and/or convenience containers is limited to 500 g per containment vessel shipping arrangement.

4. If metal convenience cans are used, the total amount of polyethylene bagging and lifting slings is limited to 500 g per containment vessel shipping arrangement.

5. The mass of offgassing material (polyethylene bagging or bottles, Teflon bottles, silicone pads, lifting slings) is assumed to be 1600 g for the offgassing evaluation of CVA 7. Teflon bottles (~400 g Teflon each) contribute ~1200 g total, therefore the other offgassing material is limited to 400 g.

The offgassing material limits identified in assumptions 4 and 5 have been established based on the needs of shippers. All configurations, except for CVA 7, are limited to 500 g of polyethylene in the form of bags, slings, and/or bottles. The upper limit of 1600 g of offgassing material is a combination of three Teflon bottles (400 g Teflon per bottle) and a 400-g allowance for the other offgassing material. These offgassing material limits have been used in calculations pertaining to containment vessel pressure, radioactive material leakage criteria, and criticality control. Therefore, portions of the safety basis for this shipping package have been based on these material limits.

Applying Dalton's law concerning a mixture of gases, the properties of each component are considered as though each component exists separately at the volume and temperature of the mixture. Therefore, the molar quantities of each constituent inside the containment vessel (i.e., dry air, water vapor, polyethylene bagging and bottles, silicone rubber pads, and Teflon bottles) must be calculated individually.

To calculate these molar properties, the void volume of the containment vessel must be determined. The volume inside an empty ES-3100 containment vessel was determined from Algor finite element software to be 637.18 in.^{3} (10,441.51 cm^3).

I. Molar quantity determination based on MNOP

Table 1. Total pressure inside the containment vessel at 87.81°C (190.06°F) [a]

CVA	n_a [b] (lb-mole)	n_v [b] (lb-mole)	n_{po} [b] (lb-mole)	n_{bo} [b] (lb-mole)	n_{tf} [b] (lb-mole)	n_{H2} [b] (lb-mole)	n_{O2} [b] (lb-mole)	n_T [b] (lb-mole)	P_T (psia)
2	5.7148E-04	1.8626E-05	0.0000E+00	0.0000E+00	0.0000E+00	3.1895E-05	1.5948E-05	6.3795E-04	19.238
7	4.5819E-04	2.4843E-04	0.0000E+00	0.0000E+00	2.7025E-05	2.5572E-05	1.2786E-05	7.7200E-04	29.036

[a] This assumes that the internal convenience cans, polyethylene or Teflon FEP bottles, and Cat 277-4 spacer cans are not sealed.

[b] n_a –molar quantity of dry air in the gas mixture;
n_v –molar quantity of water vapor in the gas mixture due primarily to efflorescence;
n_{po} –molar quantity of gas due to offgassing of the silicone rubber pads;
n_{bo} –molar quantity of gas due to offgassing of the polyethylene bags, bottles, and lifting sling;
n_{tf} –molar quantity of gas due to offgassing of the Teflon bottles;
n_{H2} –molar quantity of hydrogen gas due to radiolysis of water;
n_{O2} –molar quantity of oxygen gas due to radiolysis of water; and
n_T –total molar quantity in the gas mixture.

To use the maximum normal operating pressure at standard temperature, the number of lb-mole of gas needs to be increased using the following equation:

$$n_{MNOP} = \frac{P_T \cdot V_v}{R_u \cdot T_{amb} \cdot 12}$$

Using the above molar equations, the total number of moles is summarized in Table 2.

Table 2. Molar summary at MNOP and 25°C (77°F)

CVA	P_T (psia)	V_V (in.^{3})	R_u (ft-lb/lb-mole·R)	T_{amb} (R)	n_{MNOP} (lb-mole)
2	19.238	399.75	1545.32	537	7.7228E-04
7	29.036	320.50	1545.32	537	9.3452E-04

II. Molar quantity determination due to offgassing for each containment vessel arrangement

To determine the maximum pressure inside the containment vessel as a result of thermal testing, the average adjusted gas temperature must be calculated based on the results shown in Sect. 3.5.3. The approach used is to divide the containment vessel volume into three distinct equal regions and then average the three together. The first volume is represented by the gas adjacent to the containment vessel lid and flange region and the top most convenience can. Based on the temperature recorded near the O-rings [116.11°C (241°F)] and the temperature recorded on the external surface of the convenience can [98.89°C (210°F)], the average temperature of the gas in this region is 107.50°C (225.50°F). Using the temperature adjustment of 25.11°C (45.20°F) for this region, the adjusted average temperature in the first region is 132.61°C (270.70°F). The second volume is represented by the gas adjacent to the second convenience can from the top. Based on the temperature recorded on the containment vessel wall and convenience can [92.78°C (199°F)], the average temperature of gas in this region is 92.78°C (199°F). Using the temperature adjustment of 27.89°C (50.20°F) for this region, the adjusted average temperature in the second region is 120.67°C (249.20°F). The third and final volume is represented by the gas adjacent to the bottom convenience can. Again, based on the convenience can temperature [87.78°C (190°F)] and the containment vessel end cap temperature [98.89°C (210°F), the average temperature of gas in this region is 93.33°C (200°F). Using the temperature adjustment of 24.94°C (44.90°F) for this region, the adjusted average temperature in the third region is 118.28°C (244.90°F). Averaging these three temperatures, an average adjusted gas temperature of 123.85°C (254.93°F) is determined for the containment vessel.

Using the above calculated results and the specific gas generation of polyethylene bags and silicone rubber pads measurements at temperatures up to 170°C (338°F) conducted by the Y-12 Development Division (Appendix 2.10.4), the amount of gas generated due to offgassing of the silicone rubber can pads, the polyethylene bags and bottles, and the Teflon FEP bottles at 123.85°C (254.93°F), (V_{po}, V_{bo}, and V_{tf}) is estimated by first determining the offgassing volume per unit mass at temperature and multiplying that by the total mass of the bags, bottles, slings, and silicone rubber can supports inside the containment vessel. Based on testing at an approximate temperature of 141.11°C (286.00°F), values of ~7.0 and ~0.8 cm3/g @STP for the polyethylene bagging and bottles, and silicone rubber pads, respectively, were taken from the curves for the offgassing volume per unit mass as documented in Y/DZ-2585, Rev. 2 (Appendix 2.10.4). The value for Teflon FEP material offgassing volume per unit mass (V_{tf}) was obtained from Fig. 10 in Appendix 2.10.9. A value of ~0.12 to 0.13 cm^3/g@STP

was recorded over a temperature range of 200 to 400°F. This value was conservatively doubled to 0.25 cm^3/g@STP. These values are used to determine the offgassing volume as shown below:

$V_{po} = W_p \times 0.8 / 16.387\ (in.^3)$ (offgassing volume of silicone rubber pads)

$V_{bo} = W_b \times 7.0 / 16.387\ (in.^3)$ (offgassing volume of polyethylene bags, bottles, and lifting sling)

$V_{tf} = W_{tf} \times 0.25 / 16.387\ (in.^3)$ (offgassing bottles of Teflon FEP bottles)

From the ideal gas law, the number of gas moles in the volume is as follows:

$$n_i = \frac{P_v \cdot V_i}{R_u \cdot T_{amb} \cdot 12}$$

A summary of the results obtained using the above equations for each containment vessel arrangement is presented in Tables 3, 4, and 5.

Table 3. Molar quantity of gas generated due to the silicone rubber pad offgassing

CVA	W_p (g)	V_{po} ($in.^3$)	P_V (psia)	R_u (ft-lb/lb-mole·R)	T_{amb} (R)	n_{po} (lb-mole)
2	240.09	11.72	14.7	1545.32	537	1.7302E-05
7	0.00	0.00	14.7	1545.32	537	0.0000E+00

Table 4. Molar quantity of gas generated due to polyethylene bag, sling, and bottle offgassing

CVA	W_b (g)	V_{bo} ($in.^3$)	P_V (psia)	R_u (ft-lb/lb-mole·R)	T_{amb} (R)	n_{bo} (lb-mole)
2	500.00	213.58	14.7	1545.32	537	3.1529E-04
7	400.00	170.87	14.7	1545.32	537	2.5223E-04

Table 5. Molar quantity of gas generated due to the Teflon FEP bottle offgassing

CVA	W_{tf} (g)	V_{tf} ($in.^3$)	P_V (psia)	R_u (ft-lb/lb-mole·R)	T_{amb} (R)	n_{tf} (lb-mole)
7	1200.00	18.31	14.7	1545.32	537	2.7025E-05

III. Gas generation due to radiolysis of water

Buildup of hydrogen gas (H_2) and oxygen gas (O_2) in the ES-3100 containment vessel due to radiolysis is incorporated into the pressure calculation by assuming that 5 mol % of the free volume is H_2. Since each mole of H_2 generated is accompanied by 0.5 mole of O_2, the concentration of H_2 will reach 5 mol % when volume of H_2 is 0.05405 times the initial void volume (see Sect. 3.6.7.8 of Appendix 3.6.7). Therefore, the volume of H_2 and O_2 in the void volume (V_v) is determined by the following expressions:

$$V_h = 0.05405 \times V_v \quad \text{and} \quad V_o = 0.5 \times V_h .$$

Using the ideal gas law, the number of gas moles of H_2 and O_2 in the volume at standard temperature and pressure is:

$$n_{r\text{-}H2} = \frac{P_v \cdot V_h}{R_u \cdot T_{amb} \cdot 12} \qquad n_{r\text{-}O2} = \frac{P_v \cdot V_o}{R_u \cdot T_{amb} \cdot 12}$$

where

$n_{r\text{-}H2}$ = individual molar quantity for H_2;
$n_{r\text{-}O2}$ = individual molar quantity for O_2;
V_h = volume of H_2 assumed generated by radiolysis;
V_o = volume of O_2 assumed generated by radiolysis.

A summary of the results for H_2 and O_2 generation due to radiolysis using the above equation is presented in Table 6.

Table 6. Molar quantity of oxygen and hydrogen gas generation due to radiolysis

CVA	V_v (in.^{3})	V_h (in.^{3})	V_o (in.^{3})	P_v (psia)	R_u (ft-lb/lb-mole · R)	T_{amb} (R)	$n_{r\text{-}H2}$ (lb-mole)	$n_{r\text{-}O2}$ (lb-mole)
2	399.75	21.61	10.80	14.7	1545.32	537.0	3.1895E-05	1.5948E-05
7	320.50	17.32	8.66	14.7	1545.32	537.0	2.5572E-05	1.2786E-05

IV. Molar quantity of gas generated due to the efflorescence nature of the uranyl nitrate crystals (UNX)

The uranyl nitrate crystals (UNX) in any hydrated state will decompose and lose water molecules at the average gas temperature shown in Sect. 3.4.3 [123.85°C (254.93°F)]. The partial pressure of water vapor in this mixture is conservatively estimated to be the saturated vapor pressure (P_{sv}) of water at 254.93°F or 32.460 psia. Using the ideal gas law, the molar quantity of water vapor (n_{wv}) in this volume at the maximum containment vessel temperature and the saturated vapor pressure is:

$$n_{wv} = (P_{sv} \cdot V_v) / (R_u \cdot T_{cv} \cdot 12)$$
$$= (32.460)\,(320.50) / (1545.32 \times 12 \times 714.93)$$
$$= 7.8472 \times 10^{-4} \text{ lb-moles}$$

where

n_{wv} = molar quantity for water vapor;
V_v = void volume of CVA 7;
T_{cv} = average gas temperature inside the containment vessel; and
P_{sv} = interpolated saturated vapor pressure of water at temperature from *Fundamentals of Classical Thermodynamics*, 2d ed, Table A.1.1, p. 650. (Van Wylen 1973)

V. Total pressure due to offgassing and HAC temperatures inside the containment vessel

The total pressure of the mixture at 123.85°C (254.93°F), P_T, for each containment vessel arrangement is the pressure calculated using the sum of the previously calculated molar quantities of the gases in the containment vessel. Table 7 summarizes the molar constituents and total pressure of each containment vessel arrangement. The following equation is used to calculate the final containment vessel pressure:

$$P_{123.85°C} = (\sum n_i \cdot R \cdot T \cdot 12) / V_{GMV},$$

where

n_i = individual molar quantity for each gas,
T = average gas temperature = 123.85°C (254.93°F),
V_{GMV} = V_v = gas mixture volume.

Table 7. Total pressure inside the containment vessel at 123.85°C (254.93°F) [a]

CVA	n_{MNOP} [b] (lb-mole)	n_{po} [b] (lb-mole)	n_{bo} [b] (lb-mole)	n_{tf} [b] (lb-mole)	n_{r-H2} [b] (lb-mole)	n_{r-O2} [b] (lb-mole)	n_{wv} [b] (lb-mole)	n_T [b] (lb-mole)	P_T (psia)
2	7.7228E-04	1.7302E-05	3.1529E-04	0.0000E+00	3.1895E-05	1.5948E-05	0.0000E+00	1.1527E-03	38.236
7	9.3452E-04	0.0000E+00	2.5223E-04	2.7025E-05	2.5572E-05	1.2786E-05	7.8472E-04	2.0369E-03	84.255

[a] This assumes that the internal convenience cans, polyethylene or Teflon FEP bottles, and Cat 277-4 spacer cans are not sealed.

[b] n_{MNOP} –molar quantity of the gas mixture at maximum normal operating pressure at standard temperature [25°C (77°F)];
n_{po} –molar quantity of gas due to offgassing of the silicone rubber pads;
n_{bo} –molar quantity of gas due to offgassing of the polyethylene bags, bottles, and lifting sling;
n_{tf} –molar quantity of gas due to offgassing of the Teflon bottles;
n_{r-H2} –molar quantity of hydrogen gas due to radiolysis of water;
n_{r-O2} –molar quantity of oxygen gas due to radiolysis of water;
n_{WV} –molar quantity of water vapor due to efflorescence of UNX crystals; and
n_T –total molar quantity in the gas mixture.

Appendix 3.6.6

SILICONE RUBBER THERMAL PROPERTIES FROM THERM 1.2 DATABASE

The thermal properties for silicone rubber used in the thermal analyses of the ES-3100 shipping container were obtained from the THERM 1.2 Thermal Properties Database by R. A. Bailey. Since THERM 1.2 is not a publicly available program, screen captures from THERM 1.2 of the data for silicone rubber are presented in Figures 1 and 2 in English and SI units, respectively.

```
                silicone rubber, medium k (see ref 5)
        ------------------------------------------------------------
        Density                                .04696548   lb/in**3
        Specific Heat                          .3          Btu/lb°F
        Conductivity                           .01612725   Btu/hr in°F
        Maximum Material Temp                545.0         °F

        silicone rubber, medium k (see ref 5)
        ------------------------------------------------------------
References:
    fleming p           private collection of plastics data          1968
                        materials engr  matl selector issue          1967
                        metals handbook  8th ed                      1961
    moyer j             private collection of thermal data           1968

Material properties quality
    Density                 -  Good data, or no way of estimating quality.
    Specific Heat           -  Poor or conflicting data.  Used best or average.
    Conductivity            -  Poor or conflicting data.  Used best or average.
    Transition Temperature  -  Good data, or no way of estimating quality.
    Latent Heat             -  No data.  Made no estimate.
    Specific Heat Tables    -  No data.  Made no estimate.
    Conductivity Tables     -  No data.  Made no estimate.
```

Figure 1. Silicone rubber thermal properties from Therm 1.2 (English units).

```
        silicone rubber, medium k (see ref 5)
        ------------------------------------------------------------
        Density                          1300.0          kg/m**3
        Specific Heat                    1255.2          J/kg°K
        Conductivity                        .33472       J/sec m°K
        Maximum Material Temp             558.15        °K

        silicone rubber, medium k (see ref 5)
        ------------------------------------------------------------
References:
    fleming p          private collection of plastics data          1968
                       materials engr  matl selector issue          1967
                       metals handbook  8th ed                      1961
    moyer j            private collection of thermal data           1968

Material properties quality
    Density                 -  Good data, or no way of estimating quality.
    Specific Heat           -  Poor or conflicting data.  Used best or average.
    Conductivity            -  Poor or conflicting data.  Used best or average.
    Transition Temperature  -  Good data, or no way of estimating quality.
    Latent Heat             -  No data.  Made no estimate.
    Specific Heat Tables    -  No data.  Made no estimate.
    Conductivity Tables     -  No data.  Made no estimate.
```

Figure 2. Silicone rubber thermal properties from Therm 1.2 (SI units).

Appendix 3.6.7

ESTIMATES OF HYDROGEN BUILDUP IN THE ES-3100 PACKAGE CONTAINING HIGHLY ENRICHED URANIUM

3.6.7.1 Summary

Table 3.6.7.1 below indicates that the ES-3100 package with a containment vessel arrangement (CVA) 2 (see Appendix 3.6.4) can accommodate a 15.13-kg load of uranium oxide with 3 wt % water if the time allowed to generate 5 mol % of hydrogen is assumed to be 1.20 years (14.4 months). For the same time period, with CVA 7, the ES-3100 can accommodate 4.75 kg of uranyl nitrate hexahydrate crystals (X=6, 21.6 wt % water) or 6.70 kg of uranyl nitrate trihydrate crystals (X=3, 12.1 wt % water). If the time allowed is assumed to be 0.5015 years (6.02 months), the ES-3100 can accommodate 9.12 kg of UN6 and 11.90 kg of UN3 crystals. For additional margin of safety (20%), the ES-3100 loading conditions will specify a hydrogen build-up time limit of 5 months and 12 months for these two UNX cases, instead of 6.02 and 14.4 months as analyzed, respectively.

Calculations of permeation and diffusion from closed convenience containers (bottles and cans) indicate that the steady-state concentration of hydrogen can be as high as 0.2 mol % when all conservative assumptions are used. These results do not take into account the leakage of hydrogen that will be experienced through the closed lid of these containers, which would result in a steady-state concentration lower than 0.2 mol %.

The calculated 0.2 mol % hydrogen initial steady-state concentration is accounted for in the mass loading allowables given in Table 3.6.7.1. As indicated, the time to reach 5 mol % hydrogen in the ES-3100 containment vessel (including the initial condition of 0.2 mol %) is 20% greater than the time allowed for shipping these materials (Sect. 1.2.3.8, condition 10). With this safety factor in place, and with other conservative assumptions, it will not be necessary to vent containers before loading into the ES-3100. The time limit for the shipment (5 or 12 months, as appropriate) begins when the containment vessel is sealed.

3.6.7.2 Introduction

There is a concern about the possible buildup of hydrogen gas (H_2) in the ES-3100 package, and it is necessary to show that the H_2 concentration in the package will not exceed 5 mol % in one year (established as a limit for the purposes of this analysis). The allowable materials include uranium oxide (UO_3, U_3O_8, and UO_2) and uranyl nitrate crystals [UNX or $UO_2(NO_3)_2 \cdot XH_2O$]. The water in UNX ranges from X=0 to X=6 (0 to 21.6 wt %) {molecular weights of uranyl nitrate [$UO_2(NO_3)_2$] and H_2O are 391 and 18, respectively, and $6 \times 18 / [391 + 6 \times 18] = 0.216$}. The water associated with oxides ranges from 0 to 3 wt % (Sect. 1.2.3). There is no liquid water (sorbed or interstitial) associated with other authorized contents. The air in the void spaces of the package contains water vapor (humidity). H_2 can be generated from water by radiolysis and/or chemical reaction. Radiolysis applies to any chemical form of HEU, but only the metal can have a chemical reaction with water. Radiolysis can also generate H_2 from other materials containing hydrogen (e.g., polyethylene bags). However, radiolysis of water is the major source of H_2 for uranium oxides and uranyl nitrate crystals.

Table 3.6.7.1. Summary of allowable weights

Weight (kg)	Water		Time to reach 5 mol % hydrogen	
	X	wt %	Years	Months
Oxides (U_3O_8, UO_2, UO_3) [CVA 2][a]				
15.13		3.0	1.20	14.4
$UO_2(NO_3)_2 \times XH_2O$ [CVA 7][b]				
4.75	6	21.6	1.20	14.4
6.70	3	12.1	1.20	14.4
9.12	6	21.6	0.5015	6.02
11.90	3	12.1	0.5015	6.02

[a] CVA 2 consists of five cans of which one is empty (see Sect. 3.1.4.1).
[b] CVA 7 consists of three Teflon bottles (see Sect. 3.1.4.1).

3.6.7.3 Hydrogen Generation by Chemical Reaction with Water

HEU metal can combine with the oxygen in water to release H_2. The only source of water for HEU metal is the humidity of the air initially in the void spaces of the package. The air is assumed to be at 25°C, 1 atm (101.3 kPa) and 100% relative humidity. The vapor pressure of water at 25°C is 3.1690 kPa (CRC Handbook, p. 6-8), so the initial concentration of water vapor is 3.1690 / 101.3 = 0.031 mole fraction. Since 1 mole of water vapor produces 1 mole of H_2 and the oxygen is bound up as solid uranium oxide, this reaction does not change the total gas pressure. Therefore, if all the water vapor reacts with the metal, the maximum concentration of H_2 is also 0.031 mole fraction, which is below the 5 mol % limit.

3.6.7.4 Radiation Energy Calculations

The radiation energy that drives radiolysis can be estimated from the decay rate and maximum decay energy of each radionuclide that makes up the HEU. The bounding information to calculate these terms and the results are given in Table 3.6.7.2.

The decay rate per gram of the n^{th} radionuclide is

D_{Rn} = $[\ln(2) / T_{Hn}] \times A_N / MW_n$;
D_{Rn} = the decay rate of the n^{th} radionuclide, atoms/y;
T_{Hn} = half life of the n^{th} radionuclide, y;
A_N = Avogadro's number, 6.022×10^{23} molecules/mol; and
MW_n = the molecular (atomic) weight of the n^{th} radionuclide, g/mol.

All the radionuclides in Table 3.6.7.2 are primarily α emitters, and the total rate of radiation dose is given as

$$D_E = \sum_{n=1}^{N} [wt\%_n \times D_{Rn} \times \alpha_{Mn}] / 100$$

Table 3.6.7.2. Radiation energy calculations

Nuclide	wt % [a]	MW [b] (g/mol)	T_H [b] (y)	α [b] (MeV)	D_R [c] [atms/(g y)]	Nuclide contr [c] [MeV/(g y)]
^{232}U	4.00E-06	232.0371	6.89E+01	5.414	2.61E+19	5.65E+12
^{233}U	6.00E-01	233.0396	1.59E+05	4.909	1.13E+16	3.32E+14
^{234}U	2.00E+00	234.0409	2.45E+05	4.856	7.28E+15	7.07E+14
^{235}U	5.49E+01	235.0439	7.04E+08	4.679	2.52E+12	6.48E+12
^{236}U	4.00E+01	236.0456	2.34E+07	4.569	7.56E+13	1.38E+14
^{238}U	0.00E+00	238.0508	4.46E+09	4.185	3.93E+11	0.00E+00
Transuranic	4.00E-03			5.476 [d]	4.73E+17	1.04E+14
^{237}Np	2.50E+00	237.0482	2.14E+06	4.957	8.23E+14	1.02E+14
Total	1.00E+02					1.39E+15

[a] wt % from Appendix 4.6.1 (Table 1). Maximum transuranic is 40 μg/gU and 0.60 MBq/gU activity.
[b] MW is molecular weight; T_H is half life; and α is the maximum energy emitted. (*CRC Handbook of Chemistry and Physics*, D. R. Lide, ed., 79th ed., CRC Press, Boca Raton, Fla., 1998, pp. 11-140 and 11-141)
[c] D_R is decay rate, and Nuclide contr is the contribution of each nuclide to the total rate of decay energy.
[d] Transuranic α assumed to be equal to ^{246}Cm.

where

D_E = the total rate of decay energy, Mev/(g y);
$wt\%_n$ = the weight percent of the n^{th} radionuclide;
α_{Mn} = the α energy emitted in the decay of the n^{th} radionuclide, MeV; and
N = the total number of radionuclides.

The above calculation of D_E for HEU is 1.39×10^{15} MeV/(g y).

3.6.7.5 Hydrogen Generation by Radiolysis from Polyethylene

Almost all the radiation energy from HEU is due to alpha particles with energies of 4–5 MeV (Table 3.6.7.2). These particles are not very penetrating and will only deposit their energy into materials that are in intimate contact with the uranium atoms (i.e., the water of hydration in uranyl nitrate crystals and the water associated with the oxides). The polyethylene is in the form of bottles and bags that surround the uranium and the only alpha particles that reach the polyethylene come from the outer range of alpha particle penetration within the HEU.

Equation 2 on page 6 in *Evaluation of Radiolysis-Induced Hydrogen Generation in DOT 6M Drums from INTEC* (WSRC-TR-2007-00200) gives the following expression for calculating the range of alpha particle penetration in the HEU (metal, oxide, or crystals).

$$R = 2.3 \times 10^{-6} \times (1.24 \times \alpha_{MA} - 2.62) \times (MW_A)^{1/2} / \rho$$

where

R = the range of alpha particle penetration in the HEU, m;
α_{MA} = the average α energy emitted by the HEU, ~4.9 MeV (Table 3.6.7.2);
MW_A = the average molecular weight of the HEU, ~235.5 g/mol (Table 3.6.7.2); and
ρ = the density of the HEU, g/cm^3.

The range increases with decreasing ρ, and the smallest value for ρ is about 1.5 g/cm^3 {the smallest approximate bulk density of HEU oxide from *Cost-Effectiveness of Utilizing Surplus Depleted Uranium (DU)*, [WM-4009]}. The resulting range is 8.1×10^{-5} m.

The radius of a polyethylene bottle is 0.0627 m [4.94-in. diam (Fig. 1.4), configuration designated as CVA 6]. If the HEU oxide fills the bottle, the alpha particles generated in the outer range come from the HEU between 0.0627 and $(0.0627 - 8.1 \times 10^{-5}$ m). For an infinite cylinder, the fraction of the total radiation within this range is $[(0.0627)^2 - (0.0627 - 8.1 \times 10^{-5})^2] / (0.0627)^2 = 0.00259$. Half of this radiation would be directed toward the center of the cylinder, and much of the outward-directed portion would be absorbed passing through the HEU. Consequently, the radiation absorbed by the polyethylene would be much less than 1% of that absorbed by the water, and the H_2 generated in the polyethylene would be correspondingly less than that generated in the water.

3.6.7.6 Hydrogen Generation by Radiolysis from Water

Assuming an infinite amount of water is available, the radiolytic hydrogen generation rate is given by the following expression (based on NUREG/CR-6673, p. 31, Eq. 4.7):

$$d(n_{H2}) / dt = (D_H / 100) \times [G(H_2) / A_N]$$

where

n_{H2} = the amount of hydrogen generated, mol;
t = time, y;
D_H = the decay energy absorbed by the water, eV/y; and
$G(H_2)$ = a radiolytic hydrogen generation factor for alpha radiation in water, molecules H_2/100 eV absorbed by water.

3.6.7.7 Radiolytic Hydrogen Generation Factors for Alpha Radiation in Water

A bounding value for $G(H_2)$ with alpha radiation is 1.6 molecules H_2/100 eV absorbed by water. (NUREG/CR-6673, p. 12, Table 3.1) However, recent (2003) experimental data from Oak Ridge National Laboratory suggest lower $G(H_2)$ values [*Alpha Radiolysis of Sorbed Water on Uranium Oxides and Uranium Oxyfluorides* (ORNL/TM-2003/172) and *Water Sorption and Radiolysis Studies for Neptunium Oxides* (ORNL/TM-2003/194), included in this appendix]. Table 3.6.7.3 lists the $G(H_2)$ values derived from these experiments. The largest of the ORNL values (1.02) is used for the hydrogen generation calculations.

Table 3.6.7.3. $G(H_2)$ values derived from alpha radiolysis experiments

Sample description					Molecules/100 eV		
	$e^-(H_2O)$	e^-(rem)	f_{H2O}	Gf	G'(gas) [a]	$G'(H_2)$	$G(H_2)$
Icenhour and Toth, ORNL/TM-2003/172, 2003							
Fig. 3.3. Samp A-2-2, UO_3, 10% H_2O, 350°C	0.0556	0.3689	0.1000	0.1309	0.1507	0.1005	0.77
Fig. 3.5. Samp A-4-1 U_3O_8, 2% H_2O, 650°C	0.0111	0.4000	0.0200	0.0270	0.0113	0.0075	0.28
Icenhour et. al., ORNL/TM-2003/194, 2004							
Fig. 4.12. Samp Al 3, NpO_2, 8% H_2O, 650°C	0.0444	0.3728	0.0800	0.1065	0.1100	0.0733	0.69
Fig. 4.11. Samp Al 2, NpO_2, 1% H_2O, 650°C	0.0056	0.4012	0.0100	0.0137	0.0210	0.0140	1.02
Fig. 4.13. Samp Al 4, NpO_2, 1% H_2O, 800°C	0.0056	0.4012	0.0100	0.0137	0.0060	0.0040	0.29
Fig. 4.14. Samp Al 5, NpO_2, 0.5% H_2O, 650°C	0.0028	0.4032	0.0050	0.0068	0.0043	0.0029	0.42

[a] G'(gas) for ORNL/TM-2003/172 is based on a measured slope in Fig. 3.3 or 3.5. For ORNL/TM-2003/194, the values are listed on Figs. 4.11–4.14.

The G'(gas) value is the initial slope of the gas yield (mmol/g material) versus the decay energy (MGy) converted to units of molecules of gas per 100 eV. G'(gas) for ORNL/TM-2003/172 is based on a measured slope in Fig. 3.3 or 3.5 while the values for ORNL/TM-2003/194 are listed on Figs. 4.11–4.14. Figure 3.6.7.1 is from ORNL/TM-2003/172 (p. 9, Fig. 3.5) with lines added to outline the initial slope and facilitate reading values. From Fig. 3.6.7.1, the gas yield difference along the slope is 0.023 – (–0.0005) = 0.0235 millimol/g or $0.0235 \times A_N / 1000 = 1.42 \times 10^{19}$ molecules/g. The decay energy difference along the slope is 20.0 MGy or $20.0 \times 6.24 \times 10^{21} = 1.25 \times 10^{23}$ eV (6.24×10^{21} eV/g = 1 MGy). Therefore, G'(gas) is $1.42 \times 10^{19} / (1.25 \times 10^{23}) \times 100 = 0.0113$ molecules gas/100 eV. It is assumed the gas is due to the decomposition of H_2O and has a molar composition of 2/3 H_2 and 1/3 O_2. The derived $G'(H_2)$ is 2/3 of the G'(gas) value or 0.00756 molecules H_2/100 eV decay energy.

The radiation calculated in Table 3.6.7.2 is the decay energy rather than the energy absorbed by the water associated with the material. The energy absorbed by the associated water, D_H, is approximately equal to the decay energy, D_E, multiplied by the fraction of electrons associated with the water or

$$Gf = e^-(H_2O) / e^-(mat)$$

where

Gf = the fraction of electrons associated with the water;
$e^-(H_2O)$ = the number of electrons associated with the water, electrons/molecule;

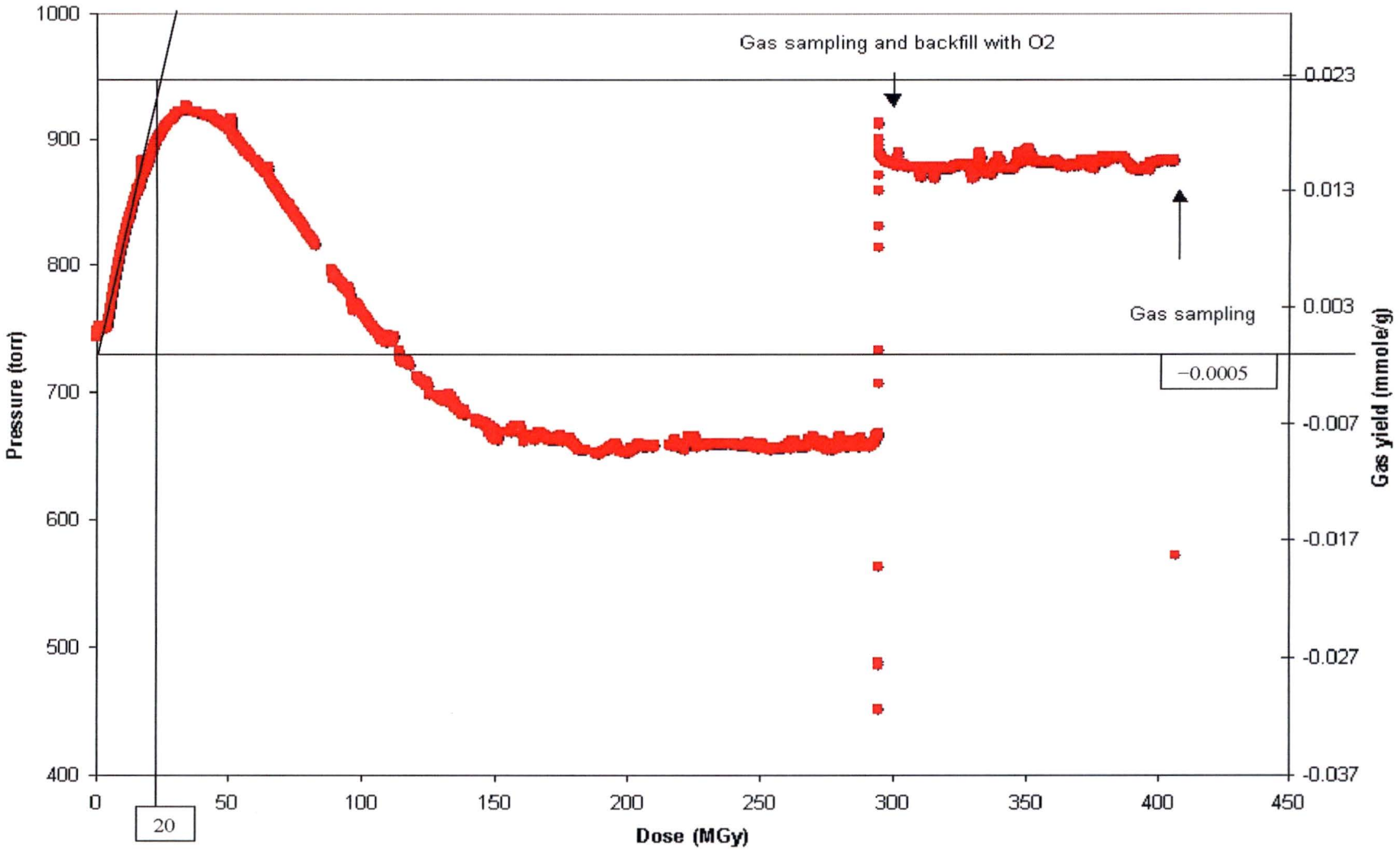

Fig. 3.6.7.1. Pressure and gas yield as a function of dose. Based on Fig. 3.5 in *Alpha Radiolysis of Sorbed Water on Uranium Oxides and Uranium Oxyfluorides* (ORNL/TM-2003/172), Sample A-4-1 (5.64 g U_3O_8 with 2 wt % H_2O, spiked with 0.0249 g ^{244}Cm).

$$e^-(mat) = \sum_{i=1}^{I} e^-(mat_i) =$$ the total number of electrons associated with the molecular species; electrons/molecule ;

$e^-(mat_i)$ = the contribution of the i^{th} molecular species to $e^-(mat)$; and
I = the total number of molecular species. The energy absorbed by the water is
D_H = $Gf \times D_E$ and
$G'(H_2)$ = $Gf \times G(H_2) \rightarrow G(H_2) = G'(H_2) / Gf$.

Two methods to calculate Gf are reported in *Calculation of Hydrogen Generation Rates for Storage of Post-KIS Oxide in 9975 Shipping Containers* (Calculation No. N-CLC-K-00219, p. 9 and 10). In the more rigorous of the two methods, Gf is estimated from the material stoichiometry and molecular weights. Using this more rigorous method, $e^-(mat_i)$ is calculated as

$$e^-(mat_i) = f_i \times \sum_{i=1}^{J} [n_{i,j} \times Z_{i,j}] / MW_i$$

where

f_i = the weight fraction of the i^{th} molecular species;
MW_i = the molecular weight of the i^{th} species;
$n_{i,j}$ = the number of moles of the j^{th} element in the i^{th} species;
J = the total number of elements in the i^{th} species; and
$Z_{i,j}$ = the atomic number of the j^{th} element in the i^{th} species.

According to the preceding equation, the expression for the number of electrons associated with the water is

$$e^-(H_2O) = f_{H2O} \times 10 / (16 + 2) = f_{H2O} \times 0.5556.$$

A mixture of water and U_3O_8 (assuming all the uranium is ^{235}U) is

$$e^-(mat) = f_{H2O} \times 0.5556 + f_{U3O8} \times (3 \times 92 + 8 \times 8) / (3 \times 235 + 8 \times 16)$$
$$= f_{H2O} \times 0.5556 + f_{U3O8} \times 0.4082$$

where

f_{H2O} = the weight fraction of water and
f_{U3O8} = the weight fraction of $U_3O_8 = 1 - f_{H2O}$ if no other material is present.

A $G'(H_2)$ value of 0.00756 molecules H_2/100 eV decay energy is derived from the experiment by Icenhour and Toth with a U_3O_8 sample (5.64 g) containing 2% water and spiked with 0.0249 g ^{244}Cm (ORNL/TM-2003/172, p. 7, Table 3.1). The mass of ^{244}Cm can be neglected, so the calculation of $G(H_2)$ for this sample is $e^-(H_2O) = 0.02 \times 0.5556 = 0.0111$; $e^-(mat) = 0.0111 + 0.98 \times 0.4082 = 0.4111$; $Gf = 0.0111 / 0.4111 = 0.0270$; and $G(H_2) = 0.00756 / 0.0270 = 0.280$ molecules H_2/100 eV absorbed by the water. Since the largest of the ORNL values (1.02) is used for the hydrogen generation calculations, the $G'(H_2)$ value for any other water content is the corresponding value of $Gf \times 1.02$.

To calculate Gf for $UO_2(NO_3)_2 \cdot XH_2O$, the two components are $UO_2(NO_3)_2$ and H_2O, where f_{H2O} is

$$f_{H2O} = X \times (2 + 16) / [235 + 2 \times 16 + 2 \times (14 + 3 \times 16) + X \times (2 + 16)]$$
$$= 1 / [1 + 391 / (X \times 18)]$$

$$e^-(mat) = f_{H2O} \times 0.5556 + f_{UN2O8} \times (92 + 8 \times 8 + 2 \times 7) / (391)$$
$$= f_{H2O} \times 0.5556 + f_{UN2O8} \times 0.4348$$

f_{UN2O8} = the weight fraction of $UO_2(NO_3)_2 = 1 - f_{H2O}$.

3.6.7.8 Time to Reach 5 mol %

The time at which the H_2 concentration in the void spaces of the package reaches 5 mol % depends on the H_2 generation rate and the volume of the void spaces. The void spaces are assumed to be initially filled with air at 25°C and 1 atm (101.3 kPa). The initial amount of air is given by

$$n_I = 101.3 \times V_{VT} / [8.3145 \times (25 + 273.15)]$$

where

n_I = the initial amount of air, mol;
V_{VT} = the total volume of the void spaces, L; and
8.3145 = the gas constant, J/(mol × K).

Since each mole of H_2 generated is accompanied by 0.5 mole of O_2, the concentration of H_2 will reach 5 mol % when

$$(n_{H2} + y \times n_I) / [1.5 \times (n_{H2} + y \times n_I) + n_I] = 0.05 \text{ or}$$
$$n_{H2} = (0.05405 - y) \times n_I$$

where

y is the initial mole fraction of hydrogen or 0.002.

The value of V_{VT} depends on the configuration and sizes of the convenience containers in the package and the amount of material in the containers. The configuration designated as CVA 7 is used for crystals and oxides may be placed in CVAs 1 through 6. The empty void volume (before the material is placed in the containers) is 9.4835 L (578.72 in.^{3}) for CVA 7 (Appendix 3.6.4, Table 1). The smallest (most conservative) empty void volume of CVAs 1 through 6 is 8.6230 L (526.21 in.^{3}) for CVA 2 (Appendix 3.6.4, Table 1).

If all the interstitial space is included, the total void volume is given by

$$V_{VT} = V_{BT} - Wt / \rho$$

where

V_{BT} = empty void volume, 8.6230 and 9.4835 L for CVA 2 and CVA 7, respectively;
Wt = the total weight of the material in the containers, kg; and
ρ = the theoretical density of the material in the containers, (10.97 kg/L for UO_2, 8.38 kg/L for U_3O_8, 7.3 kg/L for UO_3, and 2.81 kg/L for UNH). (CRC Handbook, p. 4-94)

Since UO_3 has the smallest theoretical density of the oxides, it will produce the smallest (most conservative) total volume of the void spaces.

As shown in Table 3.6.7.2, the bounding value of the decay energy is 1.39×10^{15} MeV/(g y). The fraction of uranium in UO_3 is $(1 - f_{H2O}) \times 235 / (235 + 3 \times 16) = 0.8055$ gU/g material for $f_{H2O} = 0.03$ (3% water). The corresponding fraction for crystals is $235 / [235 + 2 \times 16 + 2 \times (14 + 3 \times 16) + X \times (2 + 16)] = 0.4709$ gU/g material for $X = 6$ $[UO_2(NO_3)_2 \cdot 6H_2O]$. The decay energies are 1.12×10^{15} MeV/y g material for UO_3 with 3% H_2O and 6.57×10^{14} MeV/y g material for $UO_2(NO_3)_2 \cdot 6H_2O$.

The hydrogen generation rates for oxides (UO_2, U_3O_8, and UO_3) and uranyl nitrate crystals ($UO_2(NO_3)_2 \cdot XH_2O$) are calculated with the expression presented earlier in this appendix. The amounts of hydrogen for 5 mol % are divided by the corresponding generation rate to give the time to reach 5 mol %.

Table 3.6.7.4 gives the total weight of the material in the containers (Wt) that will generate enough hydrogen to reach 5 mol % in 1.20 or 0.5015 years as a function of the water content. The time limits for shipping the material are set at 1 year and 5 months and the additional 0.20 year allows a margin of safety in both cases. The water content considered is 3% for oxides and X values of 6 and 3 (21.64 and 12.13%) for crystals. As indicated in the table, the weight for UO_3 is the smallest for the oxides (15.13 kg).

The above calculations did not include the water from the humidity in the air. As indicated in Sect. 3.6.7.3, the mole fraction of water in the humid air is 0.031. Table 3.6.7.4 indicates the largest initial air in empty void volume is on the order of 0.32 moles so the water from the humidity in the air is on the order of $0.32 \times 0.031 = 0.01$ moles. The water content in the oxides is less than the crystals and is on the order of 3% so this water is on the order of $15{,}130 \times 0.03 / 18 = 25$ moles. Therefore, the radiolytic H_2 due to water from the humidity in the air is negligible.

3.6.7.9 Initial H_2 concentration

The results in Table 3.6.7.4 were calculated with the assumption that the initial H_2 concentrations were zero. It was suggested that a container stored for a long period of time would need to be vented before being placed in the ES-3100 in order to remove any H_2 that accumulated in the container during the storage period. An estimate of the accumulated H_2 is calculated in this section.

The H_2 generated in a container can leak out through tiny spaces in imperfect lids and by permeation or diffusion through the walls of the container. The largest leaks are through the tiny spaces but they are difficult to characterize. Consequently, this calculation conservatively considers only permeation and diffusion. Because permeation is usually a faster mechanism than diffusion and is more likely with plastics, the permeation model was used for the Teflon bottles. Since metals are not very permeable, the diffusion model was used for the cans.

The rate of gas loss through permeation is given by

$$d(n_P) / dt = P_m \times P \times A/\tau \times \rho_G$$

Table 3.6.7.4. Combinations of weight and water content that will generate 5 mol % hydrogen in 1.20 or 0.5015 years

Density (kg/L)	Weight (kg)	Total void volume (L)	Gas amounts (mol)		Water		Material uranium content (gU/g mat)	Annual radiation rate [MeV/(g mat y)]	Gf	G'(H_2) (molecules H_2/100 eV)	n_{H2} rate (mol/y)
			Initial air	H_2 for 5 mol %	X	(wt %)					
U Oxides (UO_2) [CVA 2]											
10.97	15.51	7.2095	0.29468	0.01593		3.0	0.8537	1.19E+15	0.0407	0.0416	1.27E-02
U Oxides (U_3O_8) [CVA 2]											
8.38	15.33	6.7939	0.27769	0.01501		3.0	0.8209	1.15E+15	0.0404	0.0412	1.20E-02
U Oxides (UO_3) [CVA 2]											
7.3	15.13	6.5511	0.26777	0.01447		3.0	0.8055	1.12E+15	0.0402	0.0410	1.16E-02
$UO_2(NO_3)_2 \cdot XH_2O$ [CVA 7]											
2.81	4.75	7.7946	0.31852	0.01722	6	21.64	0.4709	6.57E+14	0.2609	0.2661	1.38E-02
2.81	6.70	7.0981	0.29006	0.01568	3	12.13	0.5281	7.37E+14	0.1500	0.1530	1.25E-02
2.81	9.12	6.2389	0.25495	0.01378	6	21.64	0.4709	6.57E+14	0.2609	0.2661	2.65E-02
2.81	11.90	5.2494	0.21451	0.01160	3	12.13	0.5281	7.37E+14	0.1500	0.1530	2.23E-02

where

n_P is the amount of gas lost through permeation, mol;
P_m is the permeability, $cm^2/(Pa\ y)$;
P is the pressure increase over the initial value, Pa;
A is the cylindrical area of the Teflon bottle (4.69-in. diam × 9.4-in. tall, see Sect. 1), 893.5 cm^2 ;
τ is the thickness of the bottle (0.05-in. nominal thickness), 0.1270 cm; and
ρ_G is the gas density, 4.087×10^{-5} mol/cm^3 for an ideal gas at 25°C and 1 atm.

At steady state, the permeation rate is balanced by the gas generation rate.

$$1.5 \times d(n_{H2}) / dt = P_m \times P \times A/\tau \times \rho \rightarrow P = [1.5 \times d(n_{H2}) / dt] / [P_m \times A/\tau \times \rho_G]$$

where

$d(n_{H2}) / dt$ is the H_2 generation rate in the bottle due to radiolysis, mol/y and
1.5 is a factor to account for the oxygen released with the hydrogen.

The steady-state mole fraction is

$$f_{H2} = (2/3) \times P / P_0$$

where

f_{H2} = is the mole fraction of H_2 ;
2/3 is a factor to account for the fact that 1/3 of the pressure increase is due to oxygen; and
P_0 is the initial pressure in the bottle, 101325 Pa (1 atm).

The largest H_2 generation rate is 0.0265 mol/y (Table 3.6.7.4) for 3 Teflon bottles (see Sect. 3.1.4.1). The value for one bottle is 0.0265 / 3 = 0.00882 mol/y. Permeability values for Teflon bottles can be found at the Nalgene Labware Web site. In units of (cc • mm)/(m^2 • day • Bar), these permeability values are 4960 for N_2, 11,625 for O_2, and 34,100 for CO_2. The value for H_2 would be expected to be larger than these values; however, the smallest value (4960 for N_2) was conservatively assumed for H_2. When converted to consistent units, the permeability used for H_2 is 0.000181 $cm^2/(Pa \bullet y)$. With these values, the steady-state pressure rise is 254.1 Pa, and the H_2 mole fraction is 0.00167 or less than 0.2%.

The rate of H_2 loss through diffusion is given by

$$d(n_D) / dt = D \times C \times A/\tau$$

where

n_D is the amount of H_2 lost through diffusion, mol;
D is the diffusivity, cm^2/y; and
C is the H_2 concentration increase over the initial value, mol/cm^3.

At steady state, the diffusion rate is balanced by the H_2 generation rate.

$$d(n_{H2}) / dt = D \times C \times A/\tau \rightarrow C = [d(n_{H2}) / dt] / [D \times A/\tau]$$

The steady-state mole fraction is

$$f_{H2} = (V_C \times C) / n_I ; \quad n_I = V_C \times \rho_G \rightarrow f_{H2} = C / \rho_G$$

where

V_C is the volume of the can (4.25-in. diam × 4.88-in. tall; see Sect. 1), 1134.5 cm^3.

The largest H_2 generation rate (0.0265 mol/y, Table 3.6.7.4) is also conservatively applied to four cans (see Sect. 3.1.4.1), and the value for one can is 0.0265 / 4 = 0.00662 mol/y. The cylindrical area of the can is 420.4 cm^2, and the thickness is 0.0762 cm (0.03-in. nominal thickness for a nickel can). Presentation view graphs about hydrogen diffusion through metal pipelines indicate a wide range of diffusivity values at room temperatures and suggest that a value of about 5×10^{-7} cm^2/s is probably a low number for plain steel without welds or rough surfaces. (Sudersanam 2005) Using these values, the H_2 mole fraction is 0.00186, also less than 0.2%.

Both permeation and diffusion lead to H_2 concentrations less than 0.2 mole percent, which are negligible compared to the 5% limit. Also, these are conservative calculations in that they do not consider leaks through can and bottle closure lids, which are expected to be much larger. The small concentration (0.2 mol %) was used as an initial condition in the hydrogen generation calculations that gave rise to mass loadings and the time limits to complete shipment of this material. Therefore, it will not be necessary to vent the containers before loading them into an ES-3100 containment vessel.

OSR 45-24 (Rev 8-21-2006)

Calculation Cover Sheet

Project	Calculation No.	Project No.
N/A	N-CLC-K-00219	N/A
Title Calculation of Hydrogen Generation Rates for Storage of Post-KIS Oxide in 9975 Shipping Containers	**Functional Classification** General Services	Sheet 1 of 44
	Discipline Nuclear	
Calc Level ☒ Type 1 ☐ Type 2	**Type 1 Calc Status** ☐ Preliminary ☒ Confirmed	
Computer Program No. ☒ N/A	**Version/Release No.**	

Purpose and Objective
NMM/Facilities Engineering has requested a calculation of hydrogen generation and accumulation rates inside the PCV of a 9975 shipping container for storage of impure plutonium oxide generated by the KIS process. Plans call for a hydrogen getter to be installed to absorb radiolytically generated hydrogen gas. Currently, the getter material has been qualified only for a period of six months. Sandia National Laboratory has an ongoing program to extent the qualification period. The request is for a calculation of the time required to reach the lower flammability limit, assuming that the getter suddenly fails at the end its qualification period.

DC/RO Date 6-5-07
UNCLASSIFIED
DOES NOT CONTAIN UCNI

DC & Reviewing Official: James E. Laurinat

Summary of Conclusion
Times to reach the LFL have been calculated for 38 MIS materials for which there was measurable radiolytic hydrogen generation. At the nominal moisture level for the MIS tests (approximately 0.5 weight % H_2O), the calculated time to LFL ranges from 12 days for Material ARF-102-85-295 calcined at 750 °C to 2400 days for several MIS's with the minimum reported hydrogen generation rate of 1 nmol/W/s. For moisture levels above 0.5 weight %, conservative bounds for times to LFL are calculated using extrapolated G values based on a weighted average of G values for bound and free water. Times to LFL based on these extrapolated G values drop off rapidly, reaching about 1.3 days for any hypothetical MIS item with 6 weight % H_2O. The bounding calculations predict that the hydrogen concentration inside the PCV will reach the LFL in a matter of days if the moisture level significantly exceeds 0.5 weight %. It should be stressed that it is unlikely that oxide materials with low G values will absorb high moisture contents from humid atmospheres. Materials that are likely to absorb significant moisture (namely, those that contain chloride salts) exhibited high G values during the MIS tests. The time required for the material with the highest gas generation rate, ARF-92-85-295 calcined at 750 °C, to reach the safety analysis pressure limit of 365 psig is 10.2 years at 0.5 wt % H_2O and 1.0 year at 6 wt % H_2O. Both times exceed anticipated storage times subsequent to a postulated getter material failure.

Revisions

Rev No.	Revision Description
0	Original issue
1	Added calculations for all MIS's. Changed basis from measured total gas generation rate to measured H_2 gas generation rate. Changed to more conservative extrapolation method for higher H_2O levels. Analyzed effect of gas mixing in getter can.
2	Changed maximum total radiolytic power from 2.5 to 5.0 watts to comply with revised interim safe storage criterion (ISSC). Listed limiting power in all table and graph captions.

Sign Off

Rev No.	Originator (Print) Sign/Date	Verification/Checking Method	Verifier/Checker (Print) Sign/Date	Manager (Print) Sign//Date
0				
1				
2	James E. Laurinat 6-5-07	Document review.	Neal M. Askew 6/5/07	Curtis W. Gardner 6/7/07

Additional Reviewer (Print) Todd D. Woodsmall	Signature Todd D. Woodsmall by telecon	Date 6-7-07
Design Authority (Print) N/A	Signature	Date
Release to Outside Agency (Print) N/A	Signature	Date

Security Classification of the Calculation
Unclassified

Table of Contents

1.0 Introduction

NMM/Facilities Engineering has requested a calculation of hydrogen generation and accumulation rates inside the primary containment vessel (PCV) of a 9975 shipping container for storage of impure plutonium oxide generated by the K-Area Interim Surveillance (KIS) process. Plans call for a hydrogen getter to be installed to absorb hydrogen gas radiolytically generated by the impure plutonium oxide stored inside the PCV.[1,2] Currently, the getter material has been qualified only for a period of six months. Sandia National Laboratory has an ongoing program to extend the qualification period.[3] The NMM/FE request is for a calculation of the time required to reach the lower flammability limit, assuming that the getter suddenly fails at the end its qualification period. The time to reach the operating pressure limit of 365 psig set by the safety analysis for the 9975 shipping container[1] also is calculated for the worst case configuration.

This calculation note is a revision of a previous calculation note.[4] The previous calculation note reported hydrogen generation and accumulation rates for five typical oxide compositions, which are categorized by Material Identification and Surveillance (MIS) numbers. This revision includes all MIS categories for which measurable hydrogen generation rates have been reported. NMM Facilities Engineering has also requested an evaluation of the gas mixing inside the hydrogen getter material. In the original analysis of hydrogen concentration transients inside the PCV, the porous getter material was conservatively treated as an impermeable solid. A less conservative but more realistic model of mixing inside the getter is presented in this revised calculation note.

2.0 Description of Primary Containment Vessel and Other Enclosures

The impure oxide generated by the KIS process will be stored in 9975 shipping containers. Within the 9975 shipping container, the impure oxide will be confined within several nested vessels or structures, including a slip lid can (SLC), a heat-sealed plastic bag, a screw-lid convenience can (CC), a primary containment vessel (PCV), and a secondary containment vessel (SCV). The SLC, the plastic bag, and the CC each have a nuclear grade filter vent, while the PCV and the SCV are completely sealed. Therefore, the PCV can be considered to be the outermost vessel for hydrogen gas accumulation. Hydrogen gas will be generated by radiolysis of water absorbed on the impure oxide within the SLC. To minimize the oxygen concentrations within the PCV during storage, the gas space between the CC and the PCV will be inerted by purging with carbon dioxide (CO_2) gas until at least 75% of the air in this gas space is replaced with carbon dioxide.[1]

3.0 Input and Assumptions

Input items for the calculation of the radiolytically generated hydrogen concentrations in the SLC, the CC, and the PCV include the confinement vessel and bag dimensions, the volume occupied by the oxide and hydrogen getter materials, the rate of generation of

radiolytic energy in watts, the G value for the rate of hydrogen generation per unit decay energy, and the mass transfer coefficients for the leakage of gas through the can and bag filters.

The rate of radiolytic alpha energy given off by the stored oxide is limited to no more than 5 watts per PCV.[1] This bounding energy rate of 5 watts is used in this analysis in lieu of specifying the oxide weight and isotopic composition.

Can volumes are based on dimensions given in drawings.[5,6,7] The SLC has an outer diameter of 3.5 in. and a height of 6.0 in.[5] The wall thickness of the side wall and bottom is 0.062 in., and the lid wall thickness is 0.031 in.[5] The CC has a base that is smaller than the top portion of the can. The outer diameter of the base is 3.896 in., and the outer diameter of the top portion is 4.395 in.[6] The base is 0.75 in. high, and the top portion is 5.835 in. high; there is a transition between the two areas that is 0.54 in. high.[6] The side wall thickness is 0.042 in., and the bottom wall thickness is 0.06 in.[6] The CC lid has a top that is 0.312 in. high and a bottom threaded portion that is 0.275 in. high.[6] The outer diameter of the lid is flush with the outer can diameter. The PCV has an interior void volume of 313 $in.^3$ when empty.[7]

A Nucfil® 019 filter is installed in the lid of both the SLC and the CC to provide ventilation. The manufacturer's literature states that the 019 filter has a height of 0.72 in. and an overall dimension equal to a diameter of 1.50 in. The 019 filter will transmit flow at a minimum rate of 200 mL/min for a 1.0 in. water column pressure differential. The hydrogen diffusivity for the 019 filter is 2.5×10^{-5} mol/s/mole fraction concentration difference at atmospheric pressure.

The SLC is placed within a heat-sealed bag with a single Nucfil® 036 filter before being inserted into the CC. The heat-sealed bag has a diameter which is approximately 0.375 in. larger than that of the SLC and is approximately 15 in. long before it is used to enclose the SLC. The wall thickness of the bag material is 0.004 in. According to the manufacturer's literature, the 036 filter has a diameter of 2.0 in. and a height of 0.2 in. The rated flow rate through the 036 filter is no less than 300 mL/min for a 1.0 in. water column pressure differential. The hydrogen diffusivity for the 036 filter is 9.0×10^{-5} mol/s/mole fraction concentration difference at atmospheric pressure.

Finally, a hydrogen getter and a microporous sieve are installed inside the PCV. The getter and microporous sieve are enclosed in separate Tyvek® bags and then double bagged within a third Tyvek® bag. The outer Tyvek® bag is encased within a perforated metal cylinder, as shown by Figure 1. The metal cylinder is 4.1 in. in diameter by 7 in. high. There are 375 g of getter material and 220 g of molecular sieve material within each metal cylinder. The getter material is Vacuum Energy HITOP® Hydrogen Getter based on Sandia National Laboratory's TS6D formulation, with an estimated bulk density of 0.65 g/cm^3 and a pycnometric density of 1.1 g/cm^3. The molecular sieve material is

® Nucfil is a registered trademark of Nuclear Filter Technology, Inc., of Golden, Colorado.
® Tyvek is a registered trademark of E. I. duPont de Nemours and Co., Inc., of Wilmington, Delaware.
® HITOP is a registered trademark of Vacuum Energy, Inc., of Cleveland, Ohio.

Type 3A, with an estimated bulk density of 0.67 g/cm^3 and a pycnometric density of 3.2 g/cm^3.

The Tyvek® bags are permeable to gases and vapors, so the gas spaces within the getter and molecular sieve bags can be considered part of the total open gas space within the PCV. Each bag is a Uline® S-5900 self-seal Tyvek® envelope, with dimensions before filling of 10.5 in. by 7.5 in. and an estimated weight of 0.018 lbm, or about 2.2 oz/yd^2. For Tyvek® bag material of this weight, the moisture vapor transmission rate (MVTR) has been measured to be 1615 g/m^2/day, using the Lyssy method, which typically records the water vapor transmission for a relative humidity differential of 90% at 100 °F.[8]

To reduce the oxygen concentration, the PCV gas space is purged with CO_2 during the packaging process. As indicated by the 9975 packaging procedure,[9] the minimum purge is 10 scfh for 15 min., followed by 3 scfh for 3 min.

Table 1 summarizes the gas space volumes within the SLC, the CC, the PCV, and the getter can. It is uncertain how the gas space between the SLC and the CC is partitioned, so this is treated as a single volume in the calculations. The flow resistances and diffusivities of the bag filter and the CC lid filter are combined using a reciprocal sum formula. The getter can and its contents are sufficiently permeable that the gas space within this can and the PCV can be combined, as is argued in Section 4.

G values for the rate of hydrogen generation are estimated using measurements provided by Veirs and co-workers from Los Alamos National Laboratory.[10] The hydrogen generation rate measurements were performed using "Small Scale Reactors" (SSR's) that are 1/500th the volume of a 3013 container. Results from the hydrogen generation rate measurements are listed by both SSR test number and by MIS designation (see Appendix A). The results are reported as G values that are given in units of nmole/s/W of alpha energy delivered to the absorbed water in the material. The reported G values are converted from a basis of the mass of absorbed water to a total mass basis so that they can be applied directly to the total rate of radiolytic energy generation in watts. This conversion is described in Section 4.

® Uline is a registered trademark of Uline Shipping Supply Specialists of Waukegan, Illinois.

Table 1. Volumes and Gas Spaces inside Confinement Vessels and Bag Enclosures

Description	Volume ($in.^3$)	Volume (cm^3)
Slip Lid Can Interior	52.3	857
Screw-Lid Convenience Can Interior	100.0	1639
Primary Containment Vessel Interior	313.0	5129
Hydrogen Getter and Microporous Sieve Can Interior	111.3	1824
Slip Lid Can Gas Space	30.9	507
Screw-Lid Convenience Can/Bag Gas Space	39.9	653
Hydrogen Getter and Microporous Sieve Can Gas Space	77.1	1264
Primary Containment Vessel Gas Space (Including Hydrogen Getter and Microporous Sieve Can Gas Space)	165.0	2703

4.0 Calculation of Hydrogen Gas Generation and Accumulation

The accumulation of hydrogen gas within the gas spaces enclosed by the SLC, the CC/sealed bag, and the PCV is calculated using transient mass transfer equations. The mass transfer equation for the SLC takes the form:

$$\frac{dm_{1,H_2}}{dt} = \frac{(10000)(24)(3600)WG'_{H_2}}{(1.602 \times 10^{-13})N_A} - k_{019,H_2}\left(y_{1,H_2} - y_{2,H_2}\right) \qquad (1)$$

where

m_{1,H_2} = the number of moles of hydrogen gas in the SLC

t = the elapsed storage time in days

G'_{H_2} = the effective G value for hydrogen generation in molecules/100 eV

N_A = Avogadro's number (6.022×10^{23} molecules/mole)

k_{019,H_2} = the hydrogen diffusivity of the 019 filter in moles/day/mole fraction hydrogen gas

y_{1,H_2} = the volume fraction hydrogen in the gas in the SLC

y_{2,H_2} = the volume fraction hydrogen in the gas in the space between the SLC and the CC

W = rate of radiolytic energy generation in watts.

The term $\frac{(10000)(24)(3600)WG'_{H_2}}{N_A}$ represents the radiolytic hydrogen generation rate, and the term $k_{019,H_2}(y_{1,H_2} - y_{2,H_2})$ represents the rate of transfer of hydrogen from the SLC to the CC.

Similar mass transfer equations are used to calculate the hydrogen accumulation in the gas spaces between the SLC and the CC and between the CC and the PCV. The equation for hydrogen accumulation in the space between the SLC and the CC is

$$\frac{dm_{2,H_2}}{dt} = k_{019,H_2}(y_{1,H_2} - y_{2,H_2}) - k_{019/036,H_2}(y_{2,H_2} - y_{3,H_2}) \quad (2)$$

where

m_{2,H_2} = the number of moles of hydrogen gas in the space between the SLC and the CC

$k_{019/036,H_2}$ = the combined hydrogen diffusivity through the 036 bag filter and the 019 filter in the CC lid in moles/day/mole fraction hydrogen gas

y_{3,H_2} = the volume fraction hydrogen in the gas in the space between the CC and the PCV.

The combined diffusivity is given by the reciprocal sum of the two individual diffusivities for the bag and can lid filters:

$$k_{019/036,H_2} = \frac{k_{019,H_2}k_{036,H_2}}{k_{019,H_2} + k_{036,H_2}} \quad (3)$$

where

k_{036,H_2} = the hydrogen diffusivity for the 036 bag filter.

The mass transfer equation for the gas space between the CC and the PCV is

$$\frac{dm_{3,H_2}}{dt} = k_{019/036,H_2}(y_{2,H_2} - y_{3,H_2}) \quad (4)$$

where

m_{3,H_2} = the number of moles of hydrogen gas in the space between the CC and the PCV.

The hydrogen volume fractions are calculated by dividing the number of moles of hydrogen generated by the total number of moles. Thus,

$$y_{1,H_2} = \frac{m_{1,H_2}}{m_{1,i} + m_{1,H_2}} \tag{5}$$

$$y_{2,H_2} = \frac{m_{2,H_2}}{m_{2,i} + m_{2,H_2}} \tag{6}$$

and

$$y_{3,H_2} = \frac{m_{3,H_2}}{m_{3,i} + m_{3,H_2}} \tag{7}$$

where

$m_{1,i}$ = the initial number of moles of gas in the SLC

$m_{2,i}$ = the initial number of moles of gas in the space between the SLC and the CC

$m_{3,i}$ = the initial number of moles of gas in the space between the CC and the PCV

The initial number of moles of gas in the spaces inside the SLC, the CC, and the PCV are calculated using the ideal gas law, which, for these volumes takes the forms

$$m_{1,i} = \frac{PV_{SLC}}{R_g T} \tag{8}$$

$$m_{2,i} = \frac{PV_{CC}}{R_g T} \tag{9}$$

and

$$m_{3,i} = \frac{PV_{PCV}}{R_g T} \tag{10}$$

where

P = the pressure in atm
V_{SLC} = the gas space volume inside the SLC in cm^3
V_{CC} = the gas space volume between the CC and the SLC in cm^3
V_{PCV} = the gas space volume between the PCV and the CC in cm^3
R_g = gas law constant, cm^3 atm/gmol/K
T = temperature, K

The G value is estimated from radiolytic gas generation measurements performed by Veirs and co-workers at Los Alamos National Laboratory.[10] Veirs and co-workers expressed G values in terms of the alpha energy deposited in the water present in the material. The previous revision of this calculation note used total gas generation rates based on measured pressure increases.[4] In this revision, actual hydrogen gas generation rates are used (see Appendix A).

The alpha energy deposited in the absorbed moisture is approximately equal to the total radiolytic energy multiplied by the fraction of electrons associated with the water, $\frac{e^-(H_2O)}{e^-(mat)}$, where $e^-(H_2O)$ is the number of electrons associated with the water and $e^-(mat)$ is the number of electrons in all of the material, calculated by summing the contributions for all materials mat_i:

$$e^-(mat) = \sum_i e^-(mat_i) \tag{11}$$

Veirs recommends two methods to convert the G value based on the energy deposited in the water, defined here as G_{H_2}, to an effective G value applied to the entire radiolytic heat generation rate, defined here as G'_{H_2}. In the more rigorous of the two methods, the G value reported by Veirs and co-workers is multiplied by the fraction of the total number of electrons in the material that are associated with water, where this fraction is estimated from the material stoichiometry and molecular weights. According to this first method,

$$G'_{H_2} = G_{H_2} \frac{e^-(H_2O)}{e^-(mat)} \tag{12}$$

Veirs and co-workers used the following weighted average to calculate the number of electrons associated with each molecular species in the mixed oxide. For the ith material, the weight average is given by

$$e^{-}(mat_i) = mf_i \frac{\sum_j n_{i,j} Z_{i,j}}{MW_i} \quad (13)$$

where

m =the total mass of the material

f_i =the weight fraction of the ith molecular species

MW_i = the molecular weight of the ith species

$n_{i,j}$ = the number of moles of the jth element in the ith species

$Z_{i,j}$ = the atomic weight of the jth element in the ith species.

For general salt species, the fraction $\frac{\sum_j n_{i,j} Z_{i,j}}{MW_i}$ is estimated to be $\frac{1}{2}$.

According to the preceding equation, the expression for the number of electrons associated with the water is

$$e^{-}(H_2O) = mf_{H_2O} \frac{10}{18} \quad (14)$$

Assuming that the mixed oxide is comprised of a mixture of absorbed water, PuO_2, U_3O_8, and primarily chloride salts, the expression for the number of electrons associated with the entire material takes the form

$$e^{-}(mat) = m\left(f_{H_2O} \frac{10}{18} + f_{PuO_2} \frac{110}{271} + f_{U_3O_8} \frac{340}{833} + f_{salt} \frac{1}{2} \right) \quad (15)$$

The second method recommended by Veirs is simply to multiply the reported G value by the weight fraction of absorbed water and a bounding correction factor to account for the different weight fractions of hydrogen in water and oxides or salts. Veirs recommends a correction factor of 1.37 (see Appendix A). With this correction factor, the conversion formula becomes

$$G'_{H_2} = 1.37 f_{H_2O} G_{H_2} \quad (16)$$

This simplified bounding calculation is required because composition data were not provided for all MIS material types. Using hydrogen generation rate data for which MIS material compositions were provided, Figures 2 and 3 plot bounding equivalent G values for hydrogen generation from equation 16 against equivalent G values calculated using the more rigorous method given by equations 11 through 15. As these comparisons show, equation 16 both bounds and closely approximates the results of the more rigorous calculation method over the entire range of measured hydrogen gas generation rates. Since the bounding estimate from equation 16 does give an accurate estimate of the more

rigorous calculation, equation 16 is used to convert the G values reported by Veirs to equivalent G values for all MIS material types.

Effective G values calculated either by equations 11 through 15 or by equation 16 are linearly proportional to the moisture content for any given material. Extrapolation of effective G values to moisture levels higher than those for the Veirs measurements requires that the intrinsic G value G_{H_2} remain constant or that the effective G value G'_{H_2} vary linearly with moisture content as the moisture level increases. Recent gas generation experiments performed by Veirs and co-workers using PuO_2 doped with either magnesium chloride ($MgCl_2$) or calcium chloride ($CaCl_2$) salts show that the intrinsic G value G_{H_2} reaches a constant value at approximately 2 weight % H_2O and remains constant up to at least 6 weight % H_2O.[11] As might be expected, the value for G_{H_2} at high moisture levels approaches the value for hydrogen generation from free water, which is approximately 1.6 molec/100 eV.[12]

In keeping with these observations, G values for the MIS items are extrapolated to higher moisture levels by taking a weighted average of the measured G value at a moisture level of 0.5 weight % and the G value for free water for any moisture in excess of 0.5 weight %. The 0.5 weight % moisture is the nominal moisture level for the Veirs gas generation tests for the MIS items.[10] The use of a weighted average implies that the moisture is either tightly bound to the oxide so that it radiolyzes only to a slight degree or is present as much more loosely bound water of hydration of deliquescence. Appendix B provides details of the analysis of the Veirs data at elevated moisture levels[11] and the extrapolation of the MIS data[12] to elevated moisture levels.

Table 2 lists values for G'_{H_2} calculated from the hydrogen generation rates reported by Veirs (see Appendix A and equation 16). G values are listed for 38 of the 39 MIS designations; no rate is given for MIS Number ARF-102-85-114-1, for which no hydrogen generation was detected.

The hydrogen gas generation rate in mol/day is given by $\frac{G'_{H_2} W(10000)(24)(3600)}{(1.602e-13)N_A}$,

where

W = the radiolytic heat generation rate in watts.

Equations similar to equations 1 through 4 can be used to calculate the mixing of carbon dioxide gas within the PCV in the period following the carbon dioxide purge of the gas space between the PCV and the CC. The only changes are the elimination of the gas generation term in equation 1 and the substitution of a carbon dioxide diffusivity for the hydrogen diffusivity. The modified equations for carbon dioxide transfer in the gas space inside the SLC, the gas space between the SCL and the CC, and the gas space between the CC and the PCV, respectively, take the forms

$$\frac{dm_{1,CO_2}}{dt} = k_{019,CO_2}\left(y_{2,CO_2} - y_{1,CO_2}\right) \tag{17}$$

$$\frac{dm_{2,CO_2}}{dt} = k_{019,CO_2}\left(y_{1,CO_2} - y_{2,CO_2}\right) - k_{019/036,H_2}\left(y_{2,CO_2} - y_{3,CO_2}\right) \tag{18}$$

and

$$\frac{dm_{3,CO_2}}{dt} = k_{019/036,CO_2}\left(y_{2,CO_2} - y_{3,CO_2}\right) \tag{19}$$

where

m_{1,CO_2} = the number of moles of carbon dioxide gas in the SLC

k_{019,CO_2} = the carbon dioxide diffusivity of the 019 filter in moles/day/mole fraction carbon dioxide gas

y_{1,CO_2} = the volume fraction carbon dioxide in the gas in the SLC

m_{2,CO_2} = the number of moles of carbon dioxide gas in the space between the SLC and the CC

y_{2,CO_2} = the volume fraction carbon dioxide in the gas in the space between the SLC and the CC

m_{3,CO_2} = the number of moles of carbon dioxide gas in the space between the SLC and the CC

y_{3,CO_2} = the volume fraction carbon dioxide in the gas in the space between the CC and the PCV

$k_{019/036,CO_2}$ = the combined carbon dioxide diffusivity through the 036 bag filter and the 019 filter in the CC lid.

The combined diffusivity is given by the reciprocal sum of the two individual diffusivities for the bag and can lid filters:

$$k_{019/036,CO_2} = \frac{k_{019,CO_2} k_{036,CO_2}}{k_{019,CO_2} + k_{036,CO_2}} \tag{20}$$

The effective diffusivity of carbon dioxide through the filter vents is estimated by comparing binary diffusion coefficients for the diffusion of hydrogen and carbon dioxide gases into air. The binary diffusion coefficient for gases diffusing into air is given by the Fuller, Schettler, and Giddings correlation, which is[13]

Table 2. G Values for Measured H_2 Gas Generation Rates for LANL Mixed Oxides Typical of KIS Generated Oxides

SSR Number	MIS Number	G_{H_2}, 0.5 wt% H_2O, molec/100 eV
SSR122	7161856	2.64E-04
SSR123	TS707001	2.64E-04
SSR124	5501579	1.32E-04
SSR125	MT-1490	9.25E-04
SSR126	669194	4.69E-03
SSR127	CLLANL025	4.82E-03
SSR128	7242201	1.26E-03
SSR129A	5501407	1.26E-03
SSR130	C06032A	1.05E-02
SSR131	ARF-102-85-223	3.97E-03
SSR132	BLO-39-11-14-004	6.61E-05
SSR133	PSU-84-06-05	6.61E-05
SSR134	R441	1.06E-03
SSR135	SCP711-56	1.98E-04
SSR136	1000089	1.39E-03
SSR137	11589	5.35E-03
SSR138	53038	5.68E-03
SSR139	520610020	1.28E-02
SSR140	7242165	6.61E-05
SSR141	7242141 (fur ball)	3.30E-04
SSR142	PBO-47-09-012-023	1.32E-04
SSR143	ARF-102-85-355	6.61E-05
SSR144	ARF-102-85-365	4.63E-03
SSR145	64-85-12-1858	6.61E-05
SSR146	R438	5.29E-04
SSR147	CAN92	1.32E-04
SSR148	C0024A	2.64E-04
SSR149A	C00695	5.09E-03
SSR150	TS707013	7.27E-04
SSR151	7032282	2.38E-03
SSR152	41-85-08-1379B	1.32E-04
SSR153	63-88-06-121	1.65E-03
SSR154	ARF-102-85-114-1	0.00E+00
SSR155	ARF-102-85-295	1.31E-02
SSR155HT	ARF-102-85-295	5.22E-03
SSR156	PuF4-1	2.64E-04
SSR160	PMAXBS	4.96E-03
SSR161	PEOF1	6.61E-05
SSR162	MISSTD	4.63E-04

$$D_{AB} = \frac{0.001T^{1.75}\left(\frac{M_A + M_B}{M_A M_B}\right)^{0.5}}{P_a\left(\sum V_A^{1/3} + \sum V_B^{1/3}\right)^2} \quad (21)$$

where

T =the temperature in degrees K
M_A and M_B = the molecular weights of air and diffusing gas in g/mol
P_a = the pressure in atmospheres
$\sum V_A$ and $\sum V_B$ = molecular volumes, tabulated by Fuller, Schettler and Giddings.[12]

Comparative estimations of the diffusivities for hydrogen and carbon dioxide show that the ratio of the carbon dioxide and hydrogen diffusivities is bounded by the square root of the ratio of the molecular weights of hydrogen and carbon dioxide. The diffusivity also is inversely proportional to the square root of the gas molecular weight for slip flow and molecular (Knudsen) diffusion, as evidenced by the form of the slip flow correction factor.[14] Thus, conservative, lower bounds to the carbon diffusivities are given by

$$k_{019,CO_2} = \left(\frac{M_{H_2}}{M_{CO_2}}\right)^{0.5} k_{019,H_2} \quad (22)$$

and

$$k_{019/036,CO_2} = \left(\frac{M_{H_2}}{M_{CO_2}}\right)^{0.5} k_{019/036,H_2} \quad (23)$$

where

M_{H_2} and M_{CO_2} are the molecular weights of hydrogen and carbon dioxide, which are 2 and 44 g/mol, respectively.

The mixing of carbon dioxide following a purge which displaces 75% of the air in the gas space between the PCV and the CC with carbon dioxide is illustrated by Figure 4. Figure 4 shows that the concentration inside an empty SLC initially filled by air becomes equal to the mixed concentration inside the entire gas space within the PCV within about 18 hours. The diffusivity for hydrogen is predicted to be about 4.7 times greater than the diffusivity for carbon dioxide, so hydrogen gas should mix even faster than carbon dioxide gas. Because of this rapid mixing, the entire gas space within the PCV can be treated as a single mixed volume for flammability calculations to simplify the calculation of the approach to the LFL.

A question that needs to be resolved before the preceding model is applied is whether to treat the gas space inside the getter can as a well-mixed volume or as an effectively solid material that is impermeable to gas. It may be recalled that the getter and microporous sieve materials are enclosed within separate Tyvek® bags, double bagged within a third Tyvek® bag, and then encased within a perforated getter can. To treat the gas spaces within the getter can as being well-mixed, it is sufficient to demonstrate that the volume-average CO_2 concentration within getter can and the remaining gas space between the PCV and the CC reaches the purge criterion of 75 vol % CO_2 at the conclusion of the 18-min CO_2 purge. The reasoning is that the gas spaces inside and outside the getter can become well-mixed over the longer time spans of interest for subsequent hydrogen generation.

The CO_2 concentrations inside the inner Tyvek® bags at the end of the purge can be estimated by combining mass transfer equations for the gas spaces outside the inner bags with the solution of a radial diffusion equation for the gas space inside the inner bags. IN the mass transfer analysis, each Tyvek® bag is assumed to expand until it fills the getter can. The volume occupied by each inner bag is assumed to be proportional to the bulk volumes of the getter and microporous sieve materials. The surface area for diffusion of CO_2 is estimated by doubling the area of the rectangular bag shape prior to filling. Diffusion of CO_2 into the interior of the bags from the top and bottom ends is conservatively ignored. The volume between the outer Tyvek bag and the two inner bags is arbitrarily set at 25 cm^3.

If it is assumed that the gas spaces outside the bags and between the outer and inner bags remain well-mixed during the purge, then the CO_2 volume fractions inside and outside the bags can be calculated from the following mass transfer equations:

$$V_{PCV'}\frac{dy_{CO_2,PCV}}{dt} = Q_{purge}\left(1 - y_{CO_2,PCV}\right) - A_{Ty}k_{Ty}\left(y_{CO_2,PCV} - y_{CO_2,ob}\right) \quad (24)$$

$$V_{ob}\frac{dy_{CO_2,ob}}{dt} = A_{Ty}k_{Ty}\left(y_{CO_2,PCV} - y_{CO_2,ob}\right) \quad (25)$$

$$V_{gb}\frac{d\bar{y}_{CO_2,gb}}{dt} = A_{Ty}k_{Ty}\left(y_{CO_2,ob} - y_{CO_2,gb,s}\right) \quad (26)$$

and

$$V_{msb}\frac{d\bar{y}_{CO_2,msb}}{dt} = A_{Ty}k_{Ty}\left(y_{CO_2,ob} - y_{CO_2,msb,s}\right) \quad (27)$$

where

V_{PCV}' = the volume of the gas space inside the PCV but outside the getter can and the CC

$y_{CO_2,PCV}$ = the CO_2 volume fraction in the gas space outside the getter can

t = the elapsed time since the start of the purge

Q_{purge} = the purge flow rate

A_{Ty} = the surface area of the Tyvek® bag material

k_{Ty} = the diffusive permeability of the Tyvek®

V_{ob} = the volume of the gas space between the outer bag and the getter material and microporous sieve material bags

$y_{CO_2,ob}$ = the CO_2 volume fraction inside the outer bag

$y_{CO_2,gb,s}$ = the CO_2 volume fraction at the inside surface of the getter material bag

$y_{CO_2,msb,s}$ = the CO_2 volume fraction at the inside surface of the microporous sieve material bag

V_{gb} = the volume of the gas space inside the getter material bag

$\bar{y}_{CO_2,gb}$ = the average CO_2 volume fraction inside the getter material bag

V_{msb} = the volume of the gas space inside the microporous sieve material bag

$\bar{y}_{CO_2,msb}$ = the average CO_2 volume fraction inside the microporous sieve material bag

Equations 24 through 27 can be solved for the CO_2 concentration transients inside the PCV and the getter and microporous sieve material bags if the gas inside the bags is assumed to be well-mixed, so that

$$\bar{y}_{CO_2,gb} = y_{CO_2,gb,s} \tag{28}$$

and

$$\bar{y}_{CO_2,msb} = y_{CO_2,msb,s} \tag{29}$$

The solution to the mass transfer equations for well-mixed gases inside the Tyvek bags is obtained by numerical integration of equations 24 through 27. Figure 5 depicts the concentration transients from this integration. As Figure 5 shows, the calculated air concentration drops to 51 vol % in the getter bag and to 40 vol % in the microporous sieve bag at the end of the 18-min purge. In other words, the CO_2 concentration rises to 49 vol % in the getter bag and to 60 vol % in the microporous sieve bag.

The applicable solutions for radial diffusion within the Tyvek® bags are based on an assumption that the surface concentrations in the inner bags increase approximately linearly with time, so that

$$y_{CO_2,gb,s} = k_g t \tag{30}$$

and

$$y_{CO_2,msb,s} = k_{ms} t \tag{31}$$

where

k_g = the rate of increase in the volume fraction of CO_2 for diffusion across the Tyvek® getter bag surface

k_{ms} = the rate of increase in the volume fraction of CO_2 for diffusion across the Tyvek® microporous sieve bag surface

The solutions for radial diffusion inside the bags, with surface conditions given by equations 30 and 31, are:[15]

$$\bar{y}_{CO_2,gb} = k_g t - \frac{k_g r_{gc}^2}{8D_{eff}} + \frac{4k_g r_{gc}^2}{D_{eff}} \sum_{n=1}^{\infty} \frac{\exp\left(-\frac{\gamma_n^2 D_{eff} t}{r_{gc}^2}\right)}{\gamma_n^2} \tag{32}$$

and

$$\bar{y}_{CO_2,msb} = k_{ms} t - \frac{k_{ms} r_{gc}^2}{8D_{eff}} + \frac{4k_{ms} r_{gc}^2}{D_{eff}} \sum_{n=1}^{\infty} \frac{\exp\left(-\frac{\gamma_n^2 D_{eff} t}{r_{gc}^2}\right)}{\gamma_n^2} \tag{33}$$

where

r_{gc} = the getter can radius

$D_{eff,g}$ = the effective diffusivity for CO_2 in the gas space

γ_n = the nth root of Bessel's function of zero order

Equations 32 and 33 can be combined with equations 30 and 31 to give

$$\bar{y}_{CO_2,gb} = y_{CO_2,gb,s}\left(1-\frac{r_{gc}^{\,2}}{8D_{eff}t}+\frac{4r_{gc}^{\,2}}{D_{eff}t}\sum_{n=1}^{\infty}\frac{\exp\left(-\frac{\gamma_n^{\,2}D_{eff}t}{r_{gc}^{\,2}}\right)}{\gamma_n^{\,2}}\right) \tag{34}$$

$$\bar{y}_{CO_2,msb} = y_{CO_2,msb,s}\left(1-\frac{r_{gc}^{\,2}}{8D_{eff}t}+\frac{4r_{gc}^{\,2}}{D_{eff}t}\sum_{n=1}^{\infty}\frac{\exp\left(-\frac{\gamma_n^{\,2}D_{eff}t}{r_{gc}^{\,2}}\right)}{\gamma_n^{\,2}}\right) \tag{35}$$

The effective diffusivity for CO_2 in the gas spaces of the bags is calculated by dividing the binary molecular diffusion coefficient for CO_2 in air by a tortuosity conservatively set at a value of 2.5. The diffusivity does not need to be multiplied by the void fraction because the mass transfer analysis is applied only to the gas space within the inner bags. The expression for the effective diffusivity, D_{eff}, is

$$D_{eff} = \frac{D}{\tau} \tag{36}$$

where

D = molecular diffusion coefficient for CO_2 in air, calculated from equation 21
τ = tortuosity

The Bessel function terms on the right-hand sides of equations 34 and 35 do not contribute significantly to the overall solution. This is demonstrated by evaluating the first Bessel function term, whose root is given by[16]

$$\gamma_1 = 2.4048 \tag{37}$$

In the calculation of the relative volumes occupied by the getter and microporous sieve material bags, calculations of the bulk volume of each material and hence the void fraction are required. The void fraction is computed from a comparison of the pycnometric (or theoretical) density and the bulk density, using

$$\varepsilon = 1-\frac{\rho_b}{\rho_{th}} \tag{38}$$

where

ρ_b = the bulk density

ρ_{th} = pycnometric or theoretical density

From equations 34 and 35, the average CO_2 concentrations in the getter and microporous sieve material bags are 6% lower than the concentrations at the bag surfaces at the conclusion of the purge. This translates to about 38 vol % CO_2 in the getter material bag and 48 vol % CO_2 in the microporous sieve material bag. From the solution to equations 24 through 27, the CO_2 concentrations in the outer Tyvek® bag is approximately 63 vol %, and the CO_2 concentration insde the PCV but outside the getter can is 99 vol %. The volume average CO_2 concentration at the end of the purge is 78.5 vol %, which slightly exceeds the minimum storage criterion of 75 vol % CO_2.[1] It may be concluded that the entire gas space within the PCV, including the gas space within the getter can, may be considered to be well-mixed for any time span for which there is significant hydrogen generation.

The preceding analysis is conservative in that it does not credit mixing through the top and bottom surfaces of the bags or any mixing subsequent to the purge. Additionally, the calculation of the concentration transients at the bag surfaces is inherently conservative because it treats the mixed concentrations in the transient terms in equations 25 and 26 as surface concentrations, and thus underestimates the rates of increase of the surface concentrations.

In a simplified approach in which the gas space within the PCV is treated as a single mixed volume, the mixed volume hydrogen gas concentration in vol %, y_{H_2}, is calculated from the equation

$$y_{H_2} = \frac{\dfrac{G'_{H_2} W (10000)(24)(3600)}{(1.602e-13) N_A \rho_M} t}{\dfrac{G'_{H_2} W (10000)(24)(3600)}{(1.602e-13) N_A \rho_M} t + V_t} \qquad (39)$$

where

ρ_M = the gas density in mol/cm^3

V_t = the total gas space volume inside the PCV.

The gas density is evaluated using the ideal gas law:

$$\rho_M = \frac{P}{R_g T} \qquad (40)$$

where

P = the initial pressure in atm
T = the absolute temperature in K
R_g = the gas law constant, 82.057 cm^3-atm/K.

The total gas space volume is the sum of the gas space volume between the CC and the PCV, V_{PCV}, the gas space volume between the CC and the SLC, V_{CC}, and the gas space volume inside the SLC, V_{SLC}, multiplied by the fraction of the SLC that is not occupied by the oxide. The inert gas volume is minimized and the LFL is reached the soonest if it is assumed that the oxide occupies the entire volume of the SLC. Consequently, the total volume is calculated without taking any credit for the volume inside the SLC, so that

$$V_t = V_{CC} + V_{PCV} \tag{41}$$

To calculate the time required to reach the LFL, the mixed gas space hydrogen concentration is set equal to the hydrogen concentration at the LFL. Thus,

$$y_{H_2} = y_{LFL} \tag{42}$$

A graphical correlation presented by Coward and Jones,[17] reproduced in Figure 6, gives the hydrogen LFL as a function of the percentage by volume of carbon dioxide in the original PCV atmosphere (prior to any hydrogen generation). For a 75% carbon dioxide purge of the gas space between the CC and the PCV, the carbon dioxide gas occupies 55% of the total mixed volume between the PCV and the SLC. At this dilution, y_{LFL}, from Figure 6, is approximately 5 vol %, or 0.05.

Equations 39 and 42 may be solved for the time to reach LFL to obtain

$$t = \frac{(1.602e-13)N_A \rho_M}{G'_{H_2} W(10000)(24)(3600)} \frac{y_{LFL} V_t}{(1-y_{LFL})} \tag{43}$$

5.0 Calculation Method

All calculations were performed using Microsoft Excel spreadsheets.

6.0 Open Items

There are no open items associated with this calculation note.

7.0 Discussion of Results

Times to reach the LFL were calculated for the 38 MIS materials for which there was measurable hydrogen generation. Calculated hydrogen concentrations inside the PCV increased approximately linearly with time until the time the LFL was reached, as

indicated by Figure 7. Times to reach the LFL were calculated for arbitrary moisture levels ranging from 0.1 to 6 weight % H_2O, the maximum moisture content for which hydrogen generation rates have been measured. Results of these calculations are shown by Figures 8, 9, and 10. Tables 3 and 4 list the times to reach the LFL for each of the 38 MIS materials at varying moisture levels. At the nominal moisture level for the MIS tests (approximately 0.5 weight % H_2O), the time to reach the LFL varied from 12 days for Material ARF-92-85-295 calcined at 750 °C to 2400 days for several MIS's with the minimum reported hydrogen generation rate of 1 nmol/W/s. For moisture levels above 0.5 weight %, times to LFL are calculated using extrapolated G values based on a weighted average of G values for bound and free water. Times to LFL based on these extrapolated G values drop off rapidly, reaching about 1.3 days for any hypothetical MIS item with 6 weight % moisture. It should be stressed that it is unlikely that oxide materials with low G values will absorb high moisture contents from humid atmospheres. Materials that are likely to absorb significant moisture (namely, those that contain chloride salts) exhibited high G values during the MIS tests.

The time required for the material with the highest gas generation rate, ARF-92-85-295 calcined at 750 °C, to reach the safety analysis pressure limit of 365 psig is 10.2 years at 0.5 wt % H_2O and 1.0 year at 6 wt % H_2O. Both times exceed anticipated storage times subsequent to a postulated getter material failure.

Reported times to reach the LFL are computed under the assumption that the LFL is 5 vol % hydrogen. If the LFL were assumed to be 4 vol % hydrogen, as it would be in an air atmosphere, the times to LFL would be 0.8 times the reported values.

8.0 Conclusion

Times to reach the LFL have been calculated for 38 MIS materials for which there was measurable radiolytic hydrogen generation. At the nominal moisture level for the MIS tests (approximately 0.5 weight % H_2O), the calculated time to LFL ranges from 12 days for Material ARF-102-85-295 calcined at 750 °C to 2400 days for several MIS's with the minimum reported hydrogen generation rate of 1 nmol/W/s. For moisture levels above 0.5 weight %, conservative bounds for times to LFL are calculated using extrapolated G values based on a weighted average of G values for bound and free water. Times to LFL based on these extrapolated G values drop off rapidly, reaching about 1.3 days for any hypothetical MIS item with 6 weight % moisture. The bounding calculations predict that the hydrogen concentration inside the PCV will reach the LFL in a matter of days if the moisture level significantly exceeds 0.5 weight %. It should be stressed that it is unlikely that oxide materials with low G values will absorb high moisture contents from humid atmospheres. Materials that are likely to absorb significant moisture (namely, those that contain chloride salts) exhibited high G values during the MIS tests.

The time required for the material with the highest gas generation rate, ARF-92-85-295 calcined at 750 °C, to reach the safety analysis pressure limit of 365 psig is 10.2 years at 0.5 wt % H_2O and 1.0 year at 6 wt % H_2O. Both times exceed anticipated storage times subsequent to a postulated getter material failure.

The calculations are based on G values measured by Veirs and co-workers at Los Alamos National Laboratory, a LFL of 5 vol % for the hydrogen gas, and an approximation that the gas volume inside the PCV is well-mixed.

Reported times to reach the LFL are computed under the assumption that the LFL is 5 vol % hydrogen. If the LFL were assumed to be 4 vol % hydrogen, as it would be in an air atmosphere, the times to LFL would be 0.8 times the reported values.

Table 3. Times in Days to Reach the Hydrogen LFL at Moisture Levels between 0.1 and 0.9 wt %, for a Total Radiolytic Power of 5 watts

SSR No.	MIS No.	wt % H2O:	0.1	0.2	0.3	0.4	0.5	0.6	0.7	0.8	0.9
SSR122	7161856		3050	1525	1017	763	610	66	35	24	18
SSR123	TS707001		3050	1525	1017	763	610	66	35	24	18
SSR124	5501579		6100	3050	2033	1525	1220	69	36	24	18
SSR125	MT-1490		871	436	290	218	174	52	30	21	17
SSR126	669194		172	86	57	43	34	23	18	14	12
SSR127	CLLANL025		167	84	56	42	33	23	18	14	12
SSR128	7242201		642	321	214	161	128	47	29	21	16
SSR129A	5501407		642	321	214	161	128	47	29	21	16
SSR130	C06032A		77	38	26	19	15	13	11	9	8
SSR131	ARF-102-85-223		203	102	68	51	41	26	19	15	13
SSR132	BLO-39-11-14-004		12201	6100	4067	3050	2440	71	36	24	18
SSR133	PSU-84-06-05		12201	6100	4067	3050	2440	71	36	24	18
SSR134	R441		763	381	254	191	153	50	30	21	16
SSR135	SCP711-56		4067	2033	1356	1017	813	67	35	24	18
SSR136	1000089		581	290	194	145	116	45	28	20	16
SSR137	11589		151	75	50	38	30	21	17	14	11
SSR138	53038		142	71	47	35	28	20	16	13	11
SSR139	520610020		63	31	21	16	13	11	9	8	7
SSR140	7242165		12201	6100	4067	3050	2440	71	36	24	18
SSR141	7242141 (fur ball)		2440	1220	813	610	488	64	34	23	18
SSR142	PBO-47-09-012-023		6100	3050	2033	1525	1220	69	36	24	18
SSR143	ARF-102-85-355		12201	6100	4067	3050	2440	71	36	24	18
SSR144	ARF-102-85-365		174	87	58	44	35	24	18	14	12
SSR145	64-85-12-1858		12201	6100	4067	3050	2440	71	36	24	18
SSR146	R438		1525	763	508	381	305	59	33	23	17
SSR147	CAN92		6100	3050	2033	1525	1220	69	36	24	18
SSR148	C0024A		3050	1525	1017	763	610	66	35	24	18
SSR149A	C00695		158	79	53	40	32	22	17	14	12
SSR150	TS707013		1109	555	370	277	222	55	32	22	17
SSR151	7032282		339	169	113	85	68	35	24	18	14
SSR152	41-85-08-1379B		6100	3050	2033	1525	1220	69	36	24	18
SSR153	63-88-06-121		488	244	163	122	98	42	27	20	15
SSR155	ARF-102-85-295		62	31	21	15	12	11	9	8	7
SSR155HT	ARF-102-85-295		154	77	51	39	31	22	17	14	12
SSR156	PuF4-1		3050	1525	1017	763	610	66	35	24	18
SSR160	PMAXBS		163	81	54	41	33	23	17	14	12
SSR161	PEOF1		12201	6100	4067	3050	2440	71	36	24	18
SSR162	MISSTD		1743	871	581	436	349	61	33	23	17

Table 4. Times in Days to Reach the Hydrogen LFL at Moisture Levels between 2.0 and 6 wt %, for a Total Radiolytic Power of 5 watts

SSR No.	MIS No.	wt % H2O:	1	1.5	2	2.5	3	4	5	6
SSR122	7161856		14.4	7.3	4.9	3.7	2.9	2.1	1.6	1.3
SSR123	TS707001		14.4	7.3	4.9	3.7	2.9	2.1	1.6	1.3
SSR124	5501579		14.5	7.3	4.9	3.7	2.9	2.1	1.6	1.3
SSR125	MT-1490		13.6	7.1	4.8	3.6	2.9	2.1	1.6	1.3
SSR126	669194		10.3	6.1	4.3	3.3	2.7	2.0	1.6	1.3
SSR127	CLLANL025		10.2	6.0	4.3	3.3	2.7	2.0	1.6	1.3
SSR128	7242201		13.2	7.0	4.7	3.6	2.9	2.1	1.6	1.3
SSR129A	5501407		13.2	7.0	4.7	3.6	2.9	2.1	1.6	1.3
SSR130	C06032A		7.5	5.0	3.7	3.0	2.5	1.8	1.5	1.2
SSR131	ARF-102-85-223		10.8	6.2	4.4	3.4	2.7	2.0	1.6	1.3
SSR132	BLO-39-11-14-004		14.6	7.3	4.9	3.7	2.9	2.1	1.6	1.3
SSR133	PSU-84-06-05		14.6	7.3	4.9	3.7	2.9	2.1	1.6	1.3
SSR134	R441		13.4	7.0	4.8	3.6	2.9	2.1	1.6	1.3
SSR135	SCP711-56		14.5	7.3	4.9	3.7	2.9	2.1	1.6	1.3
SSR136	1000089		13.1	6.9	4.7	3.6	2.9	2.1	1.6	1.3
SSR137	11589		9.9	5.9	4.2	3.3	2.7	2.0	1.6	1.3
SSR138	53038		9.7	5.8	4.2	3.3	2.7	2.0	1.5	1.3
SSR139	520610020		6.8	4.6	3.5	2.8	2.4	1.8	1.4	1.2
SSR140	7242165		14.6	7.3	4.9	3.7	2.9	2.1	1.6	1.3
SSR141	7242141 (fur ball)		14.3	7.2	4.9	3.7	2.9	2.1	1.6	1.3
SSR142	PBO-47-09-012-023		14.5	7.3	4.9	3.7	2.9	2.1	1.6	1.3
SSR143	ARF-102-85-355		14.6	7.3	4.9	3.7	2.9	2.1	1.6	1.3
SSR144	ARF-102-85-365		10.3	6.1	4.3	3.3	2.7	2.0	1.6	1.3
SSR145	64-85-12-1858		14.6	7.3	4.9	3.7	2.9	2.1	1.6	1.3
SSR146	R438		14.0	7.2	4.8	3.6	2.9	2.1	1.6	1.3
SSR147	CAN92		14.5	7.3	4.9	3.7	2.9	2.1	1.6	1.3
SSR148	C0024A		14.4	7.3	4.9	3.7	2.9	2.1	1.6	1.3
SSR149A	C00695		10.0	6.0	4.2	3.3	2.7	2.0	1.6	1.3
SSR150	TS707013		13.8	7.1	4.8	3.6	2.9	2.1	1.6	1.3
SSR151	7032282		12.1	6.6	4.6	3.5	2.8	2.0	1.6	1.3
SSR152	41-85-08-1379B		14.5	7.3	4.9	3.7	2.9	2.1	1.6	1.3
SSR153	63-88-06-121		12.8	6.8	4.7	3.5	2.9	2.1	1.6	1.3
SSR155	ARF-102-85-295		6.7	4.6	3.5	2.8	2.4	1.8	1.4	1.2
SSR155HT	ARF-102-85-295		10.0	5.9	4.2	3.3	2.7	2.0	1.6	1.3
SSR156	PuF4-1		14.4	7.3	4.9	3.7	2.9	2.1	1.6	1.3
SSR160	PMAXBS		10.1	6.0	4.3	3.3	2.7	2.0	1.6	1.3
SSR161	PEOF1		14.6	7.3	4.9	3.7	2.9	2.1	1.6	1.3
SSR162	MISSTD		14.1	7.2	4.8	3.6	2.9	2.1	1.6	1.3

9.0 References

1. T. D. Woodsmall, "Implementation of the Interim Safe Storage Criteria in the 910-B Storage Vault," N-ESR-K-00004, Rev. 9, May 22, 2007 (or latest revision).
2. T. D. Woodsmall, "Packaging Reconfiguration for Repackaged Materials K Area Interim Surveillance Project (U)," M-TRT-K-00004, Rev. 1, February 6, 2006.
3. A. Nissen, G. Buffleben, and T. Shepodd, "Performance Testing of Aged Hydrogen Getters Against Criteria for Interim Safe Storage of Plutonium Bearing Materials," Sandia National Laboratory Report SAND2007-0095, January, 2007.
4. J. E. Laurinat, "Calculation of Hydrogen Generation Rates for Storage of Post-KIS Oxide in 9975 Shipping Containers," N-CLC-K-00219, Rev. 0, November 16, 2006.
5. Drawing SK-MWS081106-001, Rev. B, "Slip Lid Can Dimensional Requirements," October 5, 2006.
6. Drawing R-R2-F-0018, Rev. 5, "9975 Shipping Package: Primary and Secondary Containment Vessel Subassemblies (U)," June 30, 2004.
7. Drawing R-R1-F-0098, Rev. 2, "FB-Line Convenience Can Assembly and Details," February 23, 2004.
8. ASTM E 398-03, "Standard Test Method for Water Vapor Transmission Rate of Sheet Materials Using Dynamic Relative Humidity Measurement," ASTM International, West Conshohocken, Pennsylvania, May 10, 2003.
9. Procedure SOP-CSS-216-K, Draft K, "Venting a 9975 Container."
10. E. Kelly, L. Peppers, D. K. Veirs, and J. Berg, "3013 Container Statistical and Judgmental Samples Selected for Non Destructive Evaluation (NDE) in FY 2005," Los Alamos National Laboratory Report LA-UR-05-2193, March, 2005.
11. E. L. Garcia, M. A. Martinez, D. K. Veirs, J. M. Berg, and L. A. Worl, "Small-Scale Studies: Oxygen Generation and Corrosion," Los Alamos National Laboratory Document LA-UR-07-1371, January, 2007.
12. J. W. T. Spinks and R. J. Woods, An Introduction to Radiation Chemistry, 3rd ed., John Wiley and Sons, New York (1990).
13. D. W. Green, ed., Perry's Chemical Engineers' Handbook, 6th ed., p. 3-285.
14. D. W. Green, ed., Perry's Chemical Engineers' Handbook, 6th ed., pp. 5-32 to 5-33.
15. J. Crank, The Mathematics of Diffusion, Oxford University Press, London (1956), p. 70.
16. D. R. Lide, ed., CRC Handbook of Chemistry and Physics, 75th ed., CRC Press, Boca Raton, Florida (1994), pp. A-97 to A-98.
17. H. F. Coward and G. W. Jones, "Limits of Flammability of Gases and Vapors," Bureau of Mines Bulletin 503, U. S. Bureau of Mines, 1952.

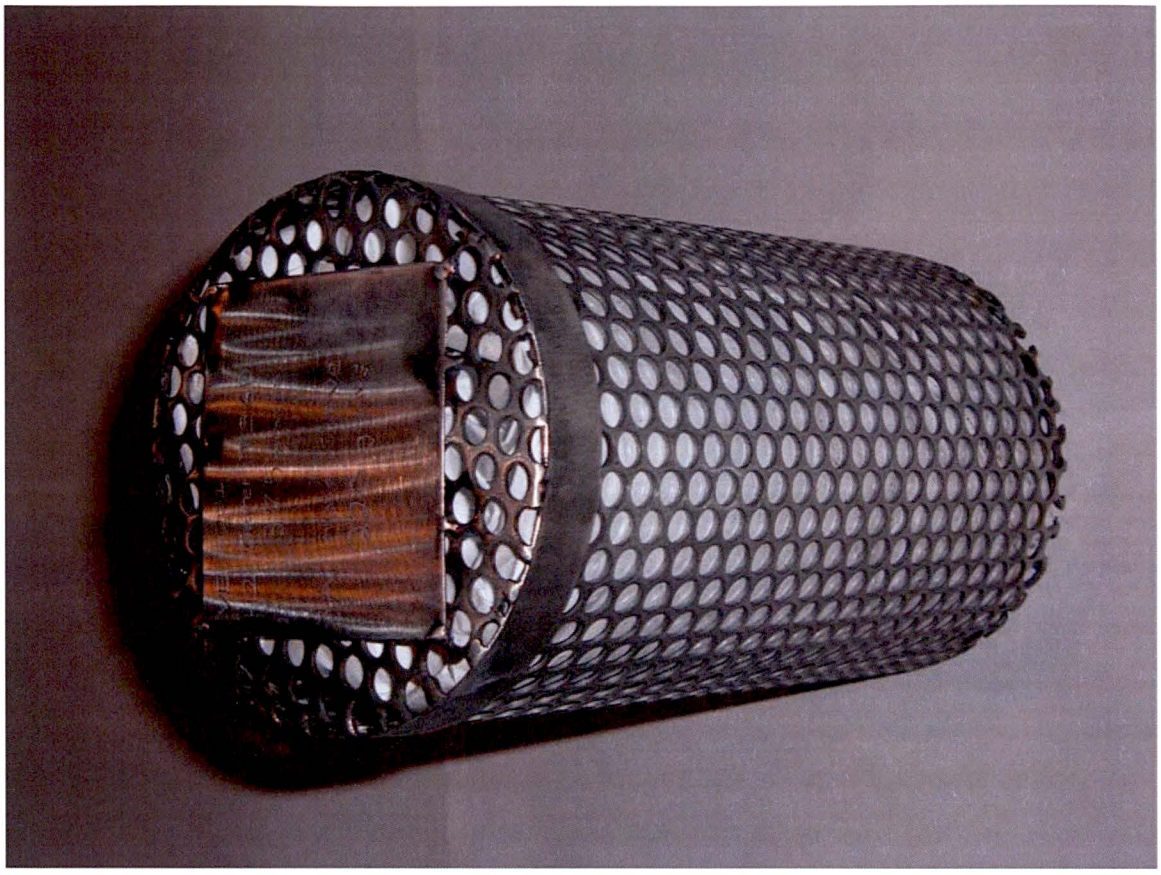

Figure 1. Getter Can with Getter and Microporous Sieve Bags

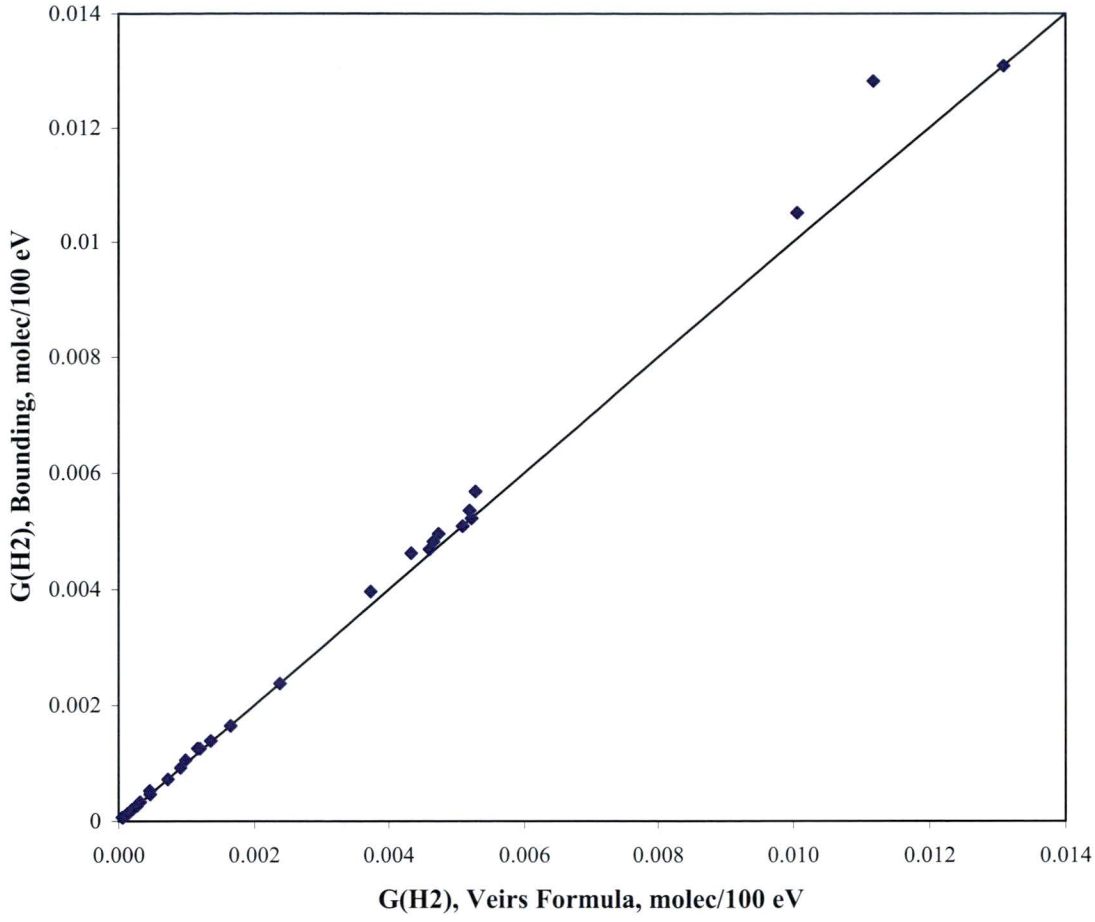

Figure 2. Comparison of Bounding G Value for Hydrogen Gas Generation from MIS Samples (from equation 16) with G Value from Veirs Conversion Formula (from equations 11 through 15), Using a Linear Scale

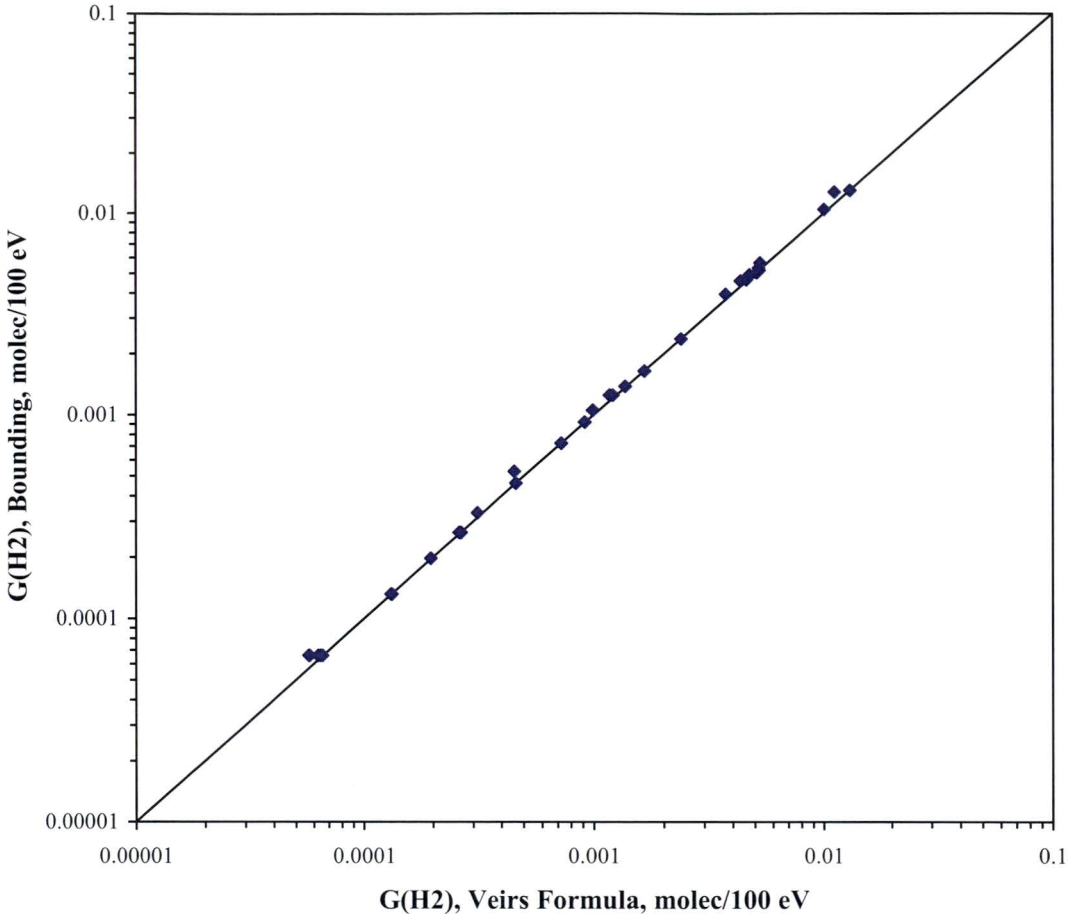

Figure 3. Comparison of Bounding G Value for Hydrogen Gas Generation from MIS Samples (from equation 16) with G Value from Veirs Conversion Formula (from equations 11 through 15), Using a Logarithmic Scale

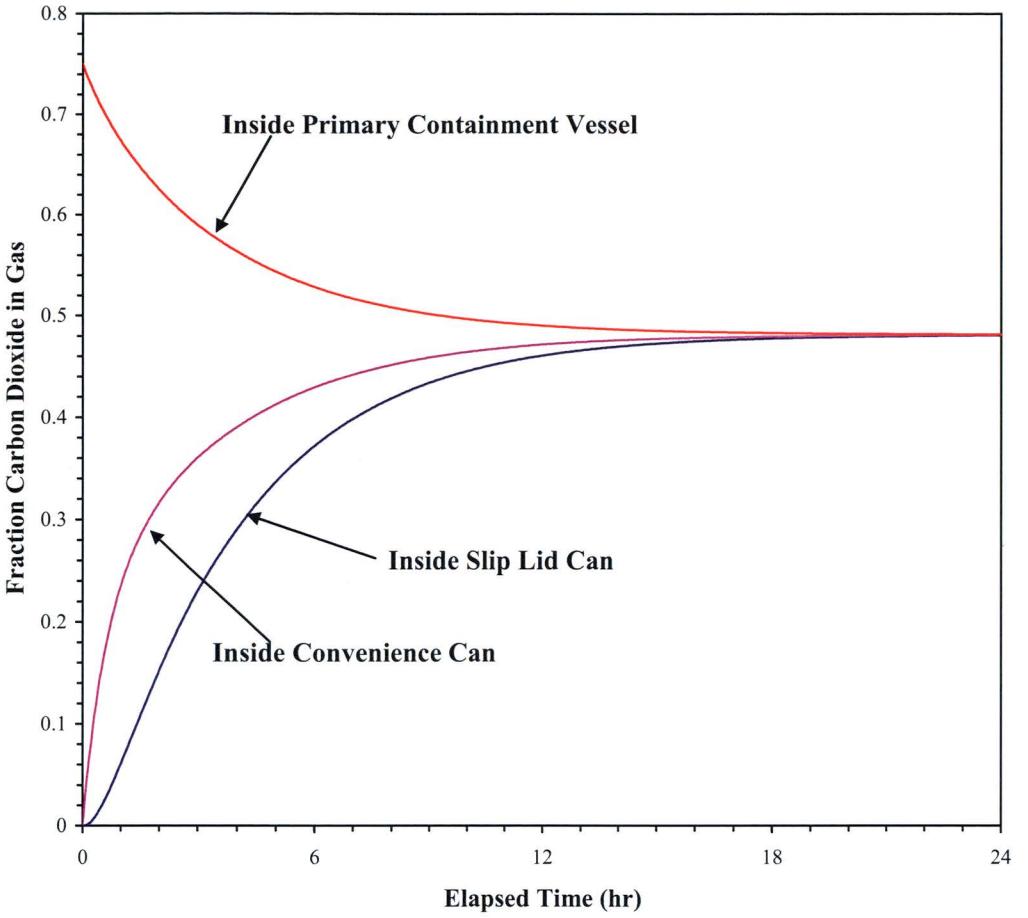

Figure 4. Variation of Carbon Dioxide Concentration during Initial Mixing after Purge, for Empty Slip Lid Can

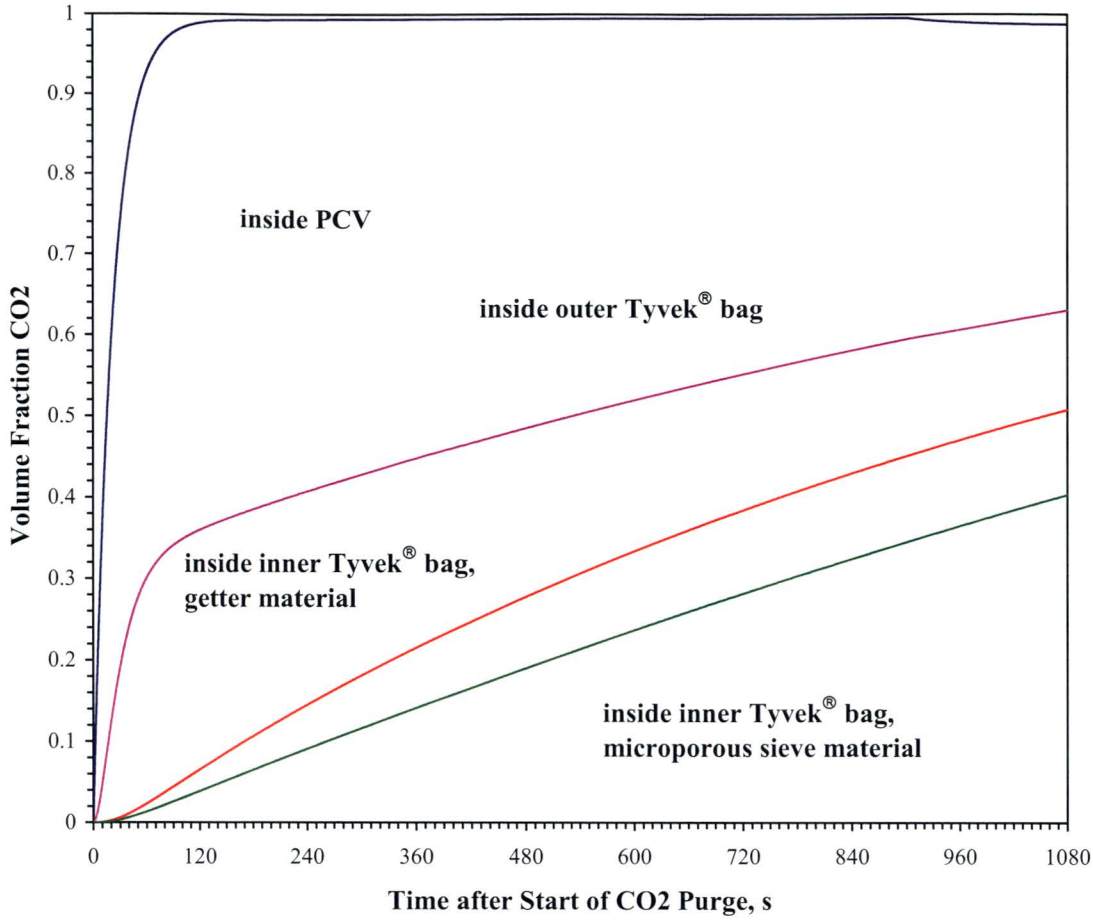

Figure 5. Variation of Carbon Dioxide Concentrations inside PCV, Getter Material Bag, and Microporous Sieve Material Bag during Purge

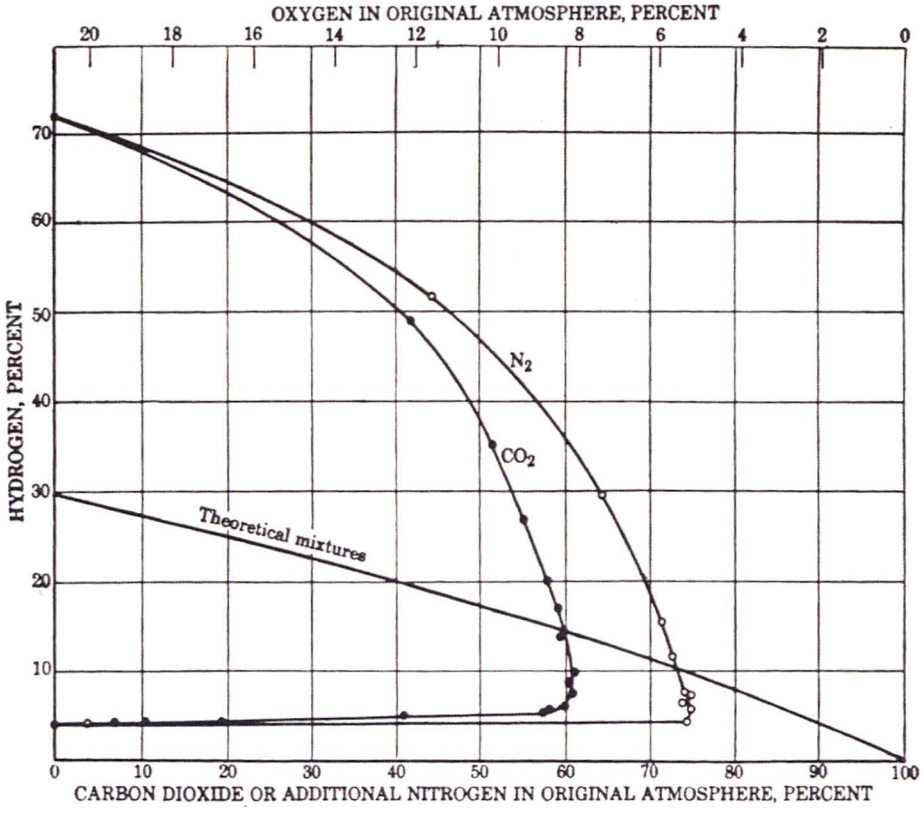

Figure 6. Variation of the Hydrogen Lower Flammability Limit with Carbon Dioxide Volume Fraction

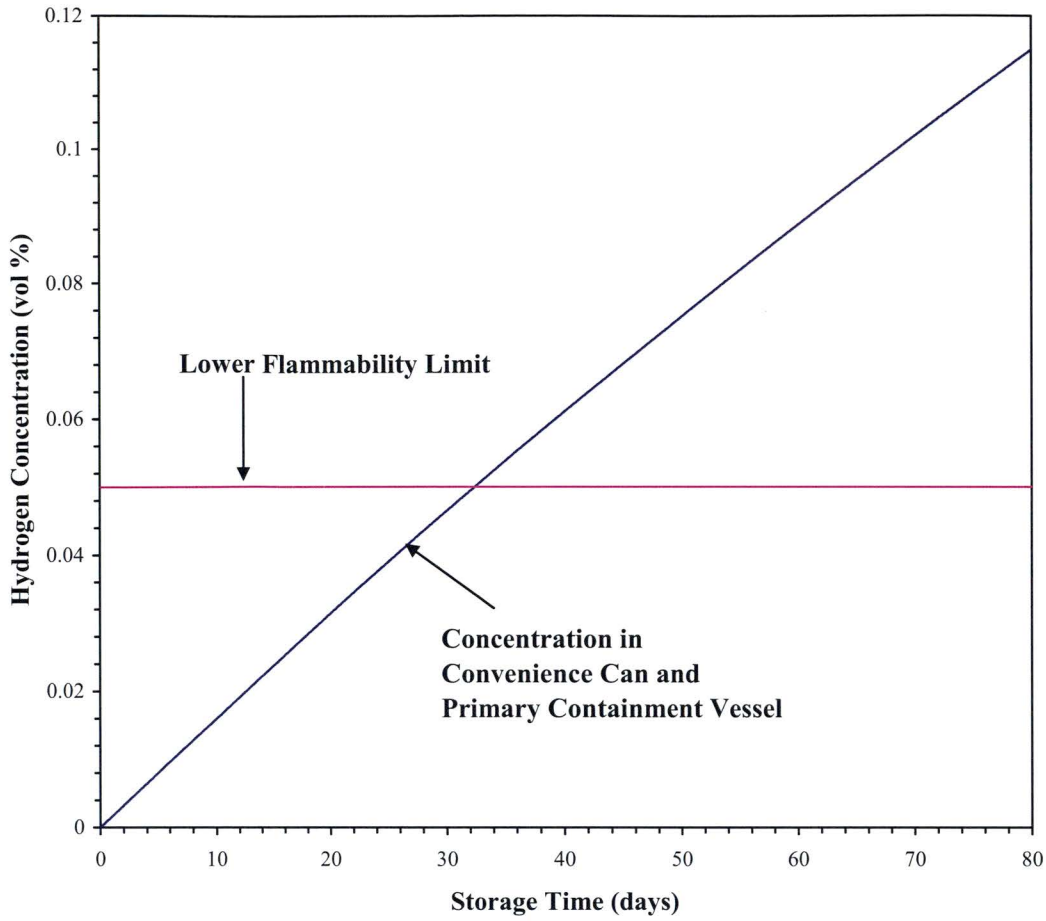

Figure 7. Approach to Lower Flammability Limit for MIS Material with Hypothetical G Value of 0.005 molec/100 eV, at a Total Radiolytic Power of 5 watts

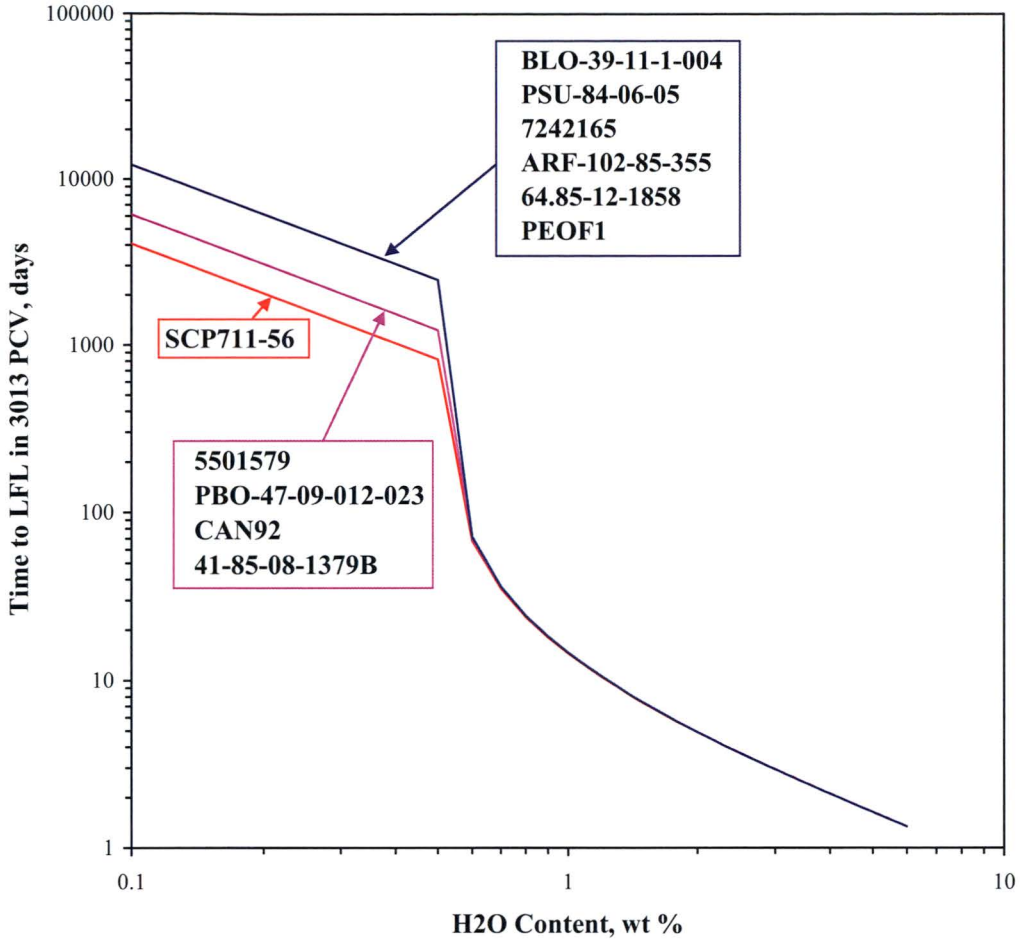

Figure 8. Variation of Time To Reach the LFL with Moisture Level, for MIS Materials with G Values Less Than 0.0002 molec/100 eV, at a Total Radiolytic Power of 5 watts

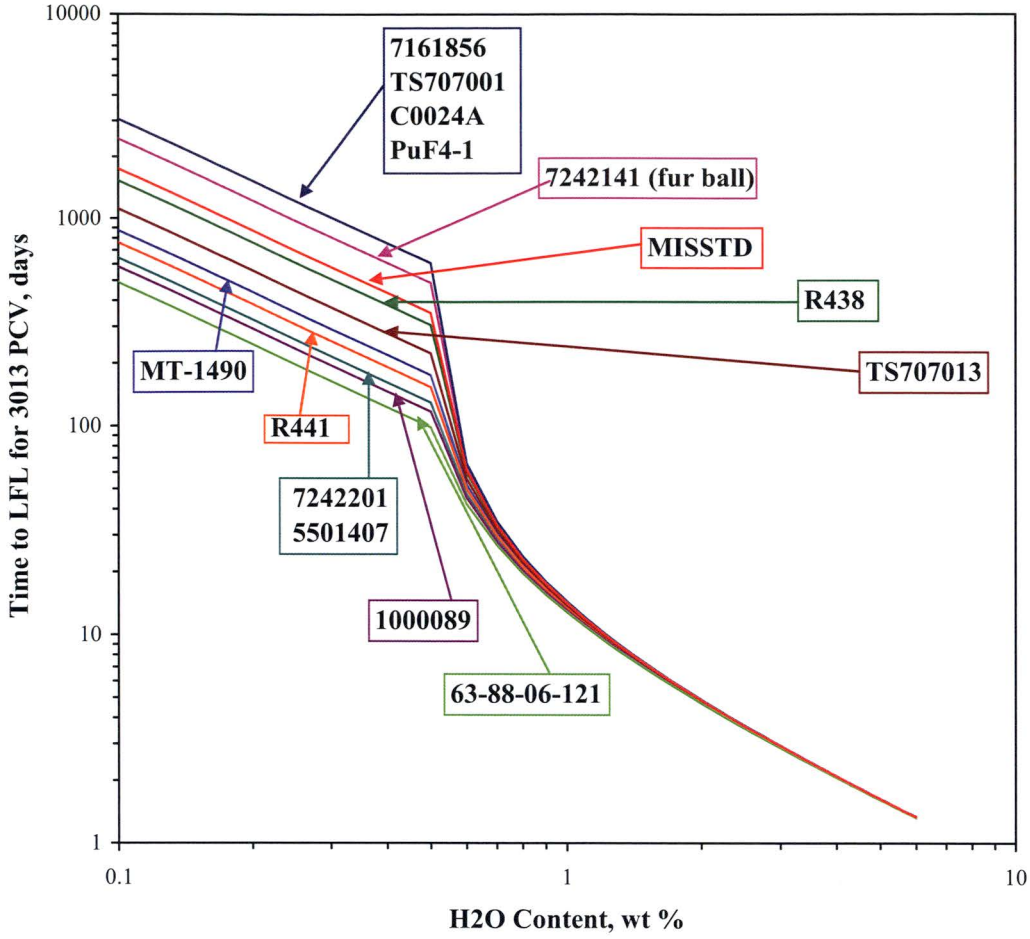

Figure 9. Variation of Time To Reach the LFL with Moisture Level, for MIS Materials with G Values between 0.0002 and 0.002 molec/100 eV, at a Total Radiolytic Power of 5 watts

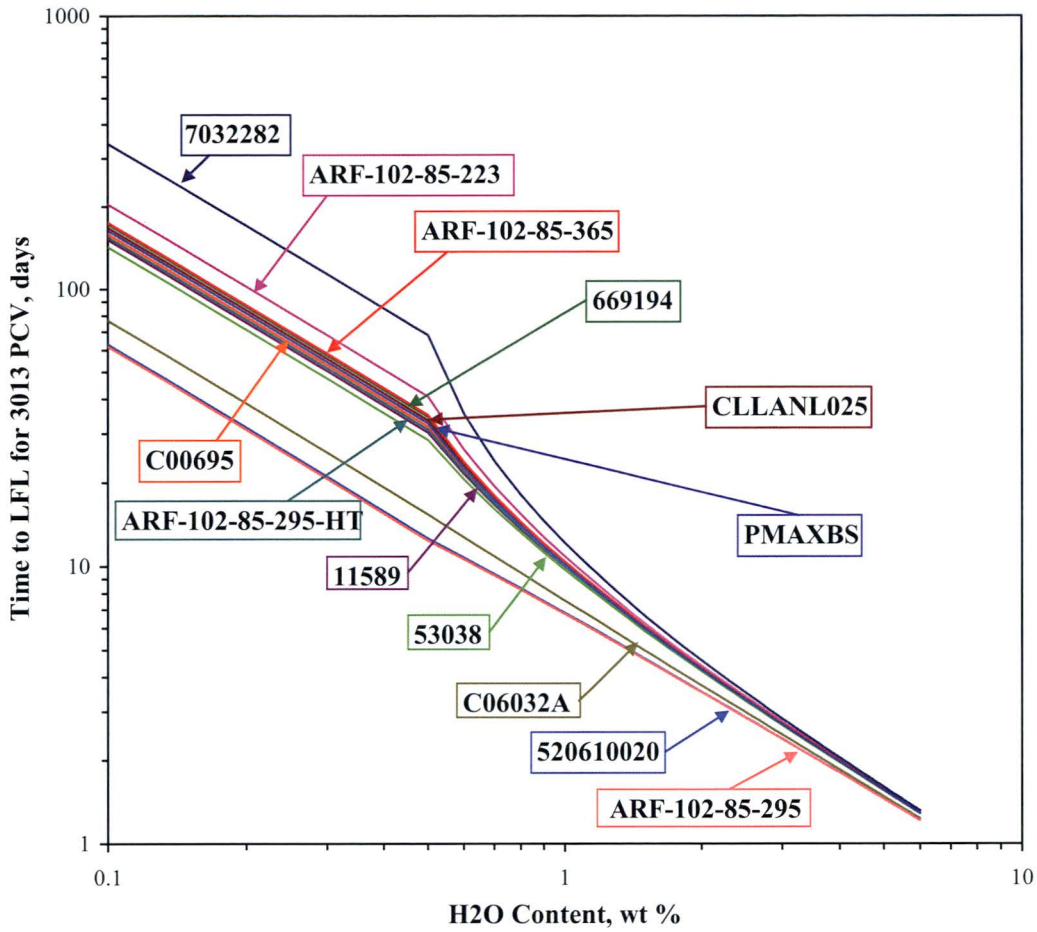

Figure 10. Variation of Time To Reach the LFL with Moisture Level, for MIS Materials with G Values Greater Than 0.002 molec/100 eV, at a Total Radiolytic Power of 5 watts

Appendix A: Correspondence with Kirk Veirs Concerning H_2 Gas Generation Rates for MIS Samples

Kirk Veirs <veirs@lanl.gov>
03/08/2007 06:53 PM
To
james.laurinat@srnl.doe.gov
cc
james.mcclard@srs.gov, todd.woodsmall@srs.gov
bcc

Subject
Re: Fw: additional data for other MIS numbers

James - attached please find a file that includes how to use the numbers to calculate the amount of hydrogen generated from represented materials. I had made a mistake - thinking on the fly leads to mistakes - in that the bounding factor adjusting the water wt% is 1.37 not 1.25. It's explained in the attached. Please don't hesitate to call me if things are not clear.

02/20/2007 11:45 AM
To
james.laurinat@srnl.doe.gov
cc
james.mcclard@srs.gov
Subject
Re: Fw: additional data for other MIS numbers

James – The following Table (Table A-1, author's note) contains the H_2 gas generation rates for all of the MIS samples. The Table includes our sample number, the MIS Sample ID that you are already familiar with, the initial H_2 gas generation rate based on gas composition analysis when the sample was first put into surveillance and the day at which the second gas composition analysis was taken, the day at which the second gas composition was determined for calculation of the initial H_2 gas generation rate, and finally, the rate calculated from the gas composition sample taken closest to one year and the initial gas composition. The difference between these numbers and the original numbers had are (1) the original numbers were based on overall pressure change and these numbers are based on the H_2 contribution to the overall pressure change, and (2) the original numbers was an average of the pressure rise the first week and the pressure rise at 10 months. In all MIS samples the observation is that the rate of rise of the H_2 gas composition is continually slowing down, so that the initial rates will always be larger than rates calculated from gas compositions at one year. Even smaller rates would be calculated for longer times. The rate is calculated as the number of moles produced per second per Watt of energy deposited into the water. The number of Watts deposited into the water is again calculated from the Wattage of the material and the number of

electrons due to the water ratioed to the number of electrons due to all of the material (actinides and salts). The H_2 gas generation rates for some of the samples are quite different from the rates calculated from the pressure rise. For instance the pressure rise in SSR135 is due mainly to CO_2; there is very little H_2.

(Note: The maximum of the initial rate and the one-year average rate is used to calculate the time to reach the LFL. Values reported by Veirs are converted to standard units of molec/100 eV by multiplying by the factor (6.022×10^{23} molec/mol) * (1×10^{-9} mol/nmol)(100)/(1.602×10^{-19} W s/eV).

In a subsequent telephone conversation, Kirk Veirs stated that gas generations tests SSR129 (MIS 5501407) and SSR149 (MIS C00695) had problems and were rerun as SSR129A and SSR149A. Consequently, the results for SSR129A and SSR149A are used for MIS 5501407 and C00695. He also stated that gas generation tests SSR155 and SSR155HT were for the same designation material calcined at different temperatures, 750 °C for SSR155 and 950 °C for SSR155HT. Times to LFL are calculated and reported using H_2 generation rates for both tests. No information was provided regarding gas generation tests SSR137 and SSR137A. Times to LFL are calculated and reported for H_2 generation rates from SSR137, since that test had higher gas generation rates than SSR137A.)

Table A-1. Hydrogen Generation Rates for MIS Materials

SSR No.	MIS ID	Initial rates		Rate average, 1-year
		H_2 generation rate (nmol sec^{-1} W^{-1})	Days valid	H_2 generation rate (nmol sec^{-1} W^{-1})
SSR122	7161856	4	29	1
SSR123	TS707001	4	57	0
SSR124	5501579	2	56	0
SSR125	MT-1490	14	35	3
SSR126	669194	71	63	21
SSR127	CLLANL025	73	63	39
SSR128	7242201	19	34	3
SSR129A	5501407	19	171	5
SSR130	C06032A	159	35	84
SSR131	ARF-102-85-223	60	99	33
SSR132	BLO-39-11-14-004	1	104	0
SSR133	PSU-84-06-05	0	28	1
SSR134	R441	16	30	7
SSR135	SCP711-56	0	27	3
SSR136	1000089	21	76	6
SSR137	11589	81	76	40
SSR138	53038	86	0.15	28
SSR139	520610020	194	7	90
SSR140	7242165	1	76	0
SSR141	7242141 (fur ball)	5	74	3
SSR142	PBO-47-09-012-023	2	63	0
SSR143	ARF-102-85-355	1	63	0
SSR144	ARF-102-85-365	70	61	43
SSR145	64-85-12-1858	0	19	1
SSR146	R438	5	19	8
SSR147	CAN92	2	229	2
SSR148	C00024A	4	229	4
SSR149A	C00695	77	1	25
SSR150	TS707013	11	216	7
SSR151	7032282	36	1	0
SSR152	41-85-08-1379B	2	216	1
SSR153	63-88-06-121	25	110	23
SSR155	ARF-102-85-295	198	175	164
SSR155HT	ARF-102-85-295	79	203	59
SSR156	PuF4-1	4	203	2
SSR160	PMAXBS	75	231	53
SSR161	PEOF1	1	232	1
SSR162	MISSTD	7	21	1

Appendix B: Analysis of Veirs and Co-Workers Gas Generation Data for $CaCl_2$ and $MgCl_2$ Doped PuO_2 and Extrapolation of G values to Higher Moisture Levels

Veirs and co-workers measured rates of pressure increase and gas generation for PuO_2 doped with nominally 5 weight % $CaCl_2$ or $MgCl_2$.[11] The PuO_2 and the chloride salts were mixed as powders and then calcined to either 800 °C (for $MgCl_2$) or 850 °C (for $CaCl_2$). Finally, measured amounts of water varying from 0.6 to 6 weight % were added to samples of the material in a humidification chamber, and the samples were placed in test vessels for gas generation tests. During the tests, corrosion of the test vessel interior was observed at moisture levels corresponding to 3.14 water of hydration for $CaCl_2$ and 4.51 waters of hydration for $MgCl_2$. In the absence of corrosion, most of the gas that was generated was hydrogen. If corrosion was present, then the radiolysis gases consisted of an approximately stoichiometric mixture of 2/3 hydrogen and 1/3 oxygen.

Rates of pressure increase and individual component gas generation were reported as a function of the number of waters of hydration added to the salt. Because the pressure measurements are somewhat more consistent and reliable than the direct measurements of gas generation rates, the analysis of the hydrogen gas generation rate and the G value is based on measured pressure increases. The intrinsic G value G_{H_2} (based on the water content) is calculated using the following set of equations:

$$G_{H_2} = \frac{e^{-}(mat)}{e^{-}(H_2O)} G'_{H_2} \tag{B-1}$$

$$G'_{H_2} = \frac{1000 \times 1.602 \times 10^{-17}}{101325 \times 86400} \frac{V_g N_A \rho_M}{P_s\left(1 - \frac{m_{salt}}{m_{PuO_2}}\right)} \frac{dP}{dt} \tag{B-2}$$

$$V_g = V_{tot} - \frac{m_{PuO_2}}{\rho_{PuO_2}} - \frac{m_{salt}}{\rho_{salt}} - \frac{m_{H_2O}}{\rho_{H_2O}} \tag{B-4}$$

where

P_s = specific power for alpha radiolysis (2.05 W/g)

m_{salt} = mass of salt (either $CaCl_2$ or $MgCl_2$) in sample, g

m_{PuO_2} = mass of PuO_2 in sample, g

$\frac{dP}{dt}$ = reported rate of pressure increase, kPa/day

V_g = volume of gas space inside test vessel, cm^3

V_{tot} = total interior volume of test vessel, cm^3

m_{H_2O} = mass of water added to sample, g

ρ_{PuO_2} = theoretical density of PuO_2, g/cm^3

ρ_{salt} = theoretical density of salt, g/cm^3

ρ_{H_2O} = density of liquid water, g/cm^3

The number of waters of hydration is converted to a weight % moisture by

$$f_{H_2O} = \frac{\frac{18n_{H_2O}}{M_{salt}} f_{salt}}{1 + \frac{18n_{H_2O}}{M_{salt}} f_{salt}} \qquad \text{(B-5)}$$

where

n_{H_2O} = number of waters of hydration

M_{salt} = molecular weight of the salt, g/mol

All terms not defined in this appendix are defined in Section 4.

Tables B-1 and B-2 l report rates of pressure increase and intrinsic G values for the $CaCl_2$ and $MgCl_2$ doped PuO_2. Figure B-1 compares these G values with intrinsic G values for the MIS items, which are listed in Table B-3. As Figure B-1 shows, the intrinsic G values for the $CaCl_2$ and $MgCl_2$ doped materials approach constant values approximately equal to 2.1 and 1.2 molec/100 eV, respectively, above a moisture content of about 2 weight %. (In other words, the effective G values based on the entire mass, G'_{H_2}, increase linearly with the moisture level above 2 weight % moisture.) The intrinsic G values for the MIS items range from about 0.01 molec/100 eV up to the asymptotic maxima for the $CaCl_2$ and $MgCl_2$ doped materials.

It is noteworthy that intrinsic G values for the $CaCl_2$ and $MgCl_2$ doped materials, as well as the maximum G values reported for the MIS items, are of the same magnitude as the accepted G value for free water, which Spinks and Woods report to be

1.6 molec/100 eV.[12] The relatively close agreement between the maximum G values measured by Veirs and co-workers and the G value for water suggests that G values for MIS items at elevated moisture levels can be approximated by taking a weighted average of the reported G values for the MIS tests and the G value for free water. If the moisture level for the MIS tests is set at its average value of 0.5 weight % (0.005 as a weight fraction), then a simple weighted average formula takes the form

$$G_{H_2,pred} = \frac{0.005G_{H_2,MIS} + \left(f_{H_2O} - 0.005\right)G_{H_2,H_2O}}{f_{H_2O}} \qquad \text{(B-6)}$$

where

$G_{H_2,pred}$ = predicted intrinsic G value at the elevated moisture level, molec/100 eV

$G_{H_2,MIS}$ = measured intrinsic G value for the MIS item, molec/100 eV

G_{H_2,H_2O} = G value for free water, 1.6 molec/100 eV

Use of equation B-6 implies that the water absorbed by an MIS item is present as either a chemically bound constituent with a low propensity to be radiolyzed or as a water of hydration or deliquescence that radiolyzes about as readily as free water. The use of this weighted average also assumes that the MIS items are capable of absorbing the stated amount of moisture from humid atmospheres.

Table B-1. Pressure Increases for $CaCl_2$-Doped PuO_2 as a Function of Water Content

Waters of Hydration	Pressure Increase (kPa/day)	Water Content (weight %)	G_{H_2} (molec/100 eV)
0.77	0.57	0.62	0.69
1.30	1.79	1.04	1.27
1.99	2.93	1.58	1.35
2.53	6.43	2.00	2.32
3.14	10.00	2.47	2.41[a]
3.74	13.79	2.93	2.21[b]
4.39	17.14	3.42	2.33[b]
5.06	18.64	3.92	2.19[b]
5.67	21.00	4.38	2.18[b]
6.20	22.00	4.77	2.08[b]
6.83	23.64	5.23	2.02[b]
7.44	21.86	5.67	1.70[b]

Table B-2. Pressure Increases for $MgCl_2$-Doped PuO_2 as a Function of Water Content

Waters of Hydration	Pressure Increase (kPa/day)	Water Content (weight %)	G_{H_2} (molec/100 eV)
0.77	0.57	0.61	0.66
1.30	0.86	1.02	0.59
1.99	2.21	1.55	0.99
2.67	3.57	2.07	1.18
3.19	4.14	2.46	1.14
3.84	5.71	2.95	1.30
4.51	6.86	3.45	1.32
5.10	10.79	3.88	1.22[b]
5.59	12.57	4.24	1.29[b]
6.31	11.79	4.76	1.06[b]
6.93	13.86	5.20	1.13[b]
7.57	15.43	5.66	1.15[b]

Notes:
[a] G' value is calculated using 5/6 of the pressure increase, under the assumption that this data point is at the transition between generation of pure hydrogen and the generation of a stoichiometric mixture of 2/3 hydrogen and 1/3 oxygen (for corrosion conditions).
[b] G' value is calculated using 2/3 of the pressure increase, under the assumption that the gas generation is a stoichiometric mixture 2/3 hydrogen and 1/3 oxygen (for corrosion conditions).

Table B-3. Hydrogen Generation Rates for MIS Materials

SSR No.	MIS ID	Water Content (weight %)	G_{H_2} (molec/100 eV)
SSR122	7161856	0.54	0.039
SSR123	TS707001	0.36	0.039
SSR124	5501579	0.42	0.019
SSR125	MT-1490	0.51	0.135
SSR126	669194	0.45	0.685
SSR127	CLLANL025	0.47	0.704
SSR128	7242201	0.52	0.183
SSR129A	5501407	0.68	0.183
SSR130	C06032A	0.57	1.534
SSR131	ARF-102-85-223	0.58	0.579
SSR132	BLO-39-11-14-004	0.45	0.010
SSR133	PSU-84-06-05	0.45	0.010
SSR134	R441	0.42	0.154
SSR135	SCP711-56	0.19	0.029
SSR136	1000089	0.42	0.203
SSR137	11589	0.53	0.781
SSR138	53038	0.50	0.830
SSR139	5.21E+08	0.51	1.872
SSR140	7242165	0.48	0.010
SSR141	7242141 (fur ball)	0.45	0.048
SSR142	PBO-47-09-012-023	0.47	0.019
SSR143	ARF-102-85-355	0.46	0.010
SSR144	ARF-102-85-365	0.46	0.675
SSR145	64-85-12-1858	0.45	0.010
SSR146	R438	0.43	0.077
SSR147	CAN92	0.5[c]	0.019
SSR148	C0024A	0.5[c]	0.039
SSR149A	C00695	0.5[c]	0.743
SSR150	TS707013	0.5[c]	0.106
SSR151	7032282	0.5[c]	0.347
SSR152	41-85-08-1379B	0.5[c]	0.019
SSR153	63-88-06-121	0.5[c]	0.241
SSR154	ARF-102-85-114-1	0.5[c]	
SSR155	ARF-102-85-295	0.5[c]	1.910
SSR155HT	ARF-102-85-295	0.5[c]	0.762
SSR156	PuF4-1	0.5[c]	0.039
SSR160	PMAXBS	0.19	0.724
SSR161	PEOF1	0.08	0.010
SSR162	MISSTD	0.5[c]	0.068

Note:
[c] Water content is not reported. A nominal water content of 0.5 weight % is assumed.

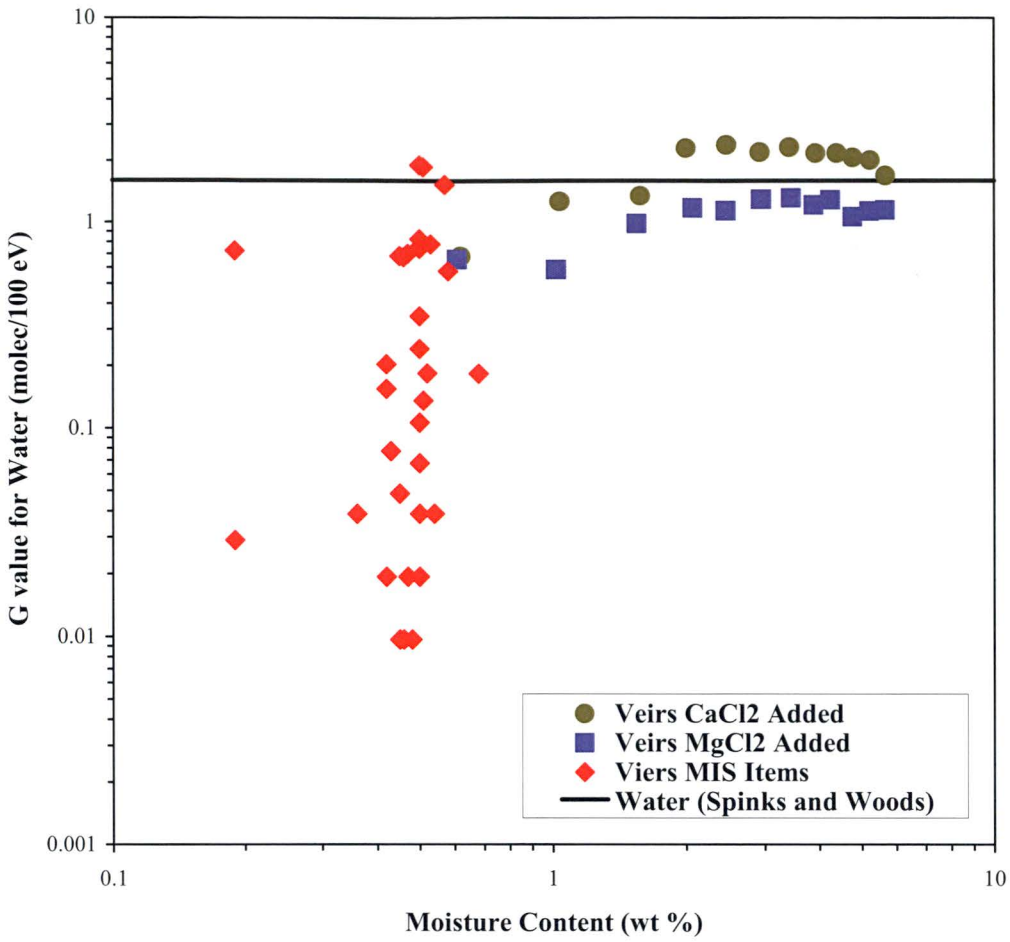

Figure B-1. Comparison of G Values Measured by Veirs and Co-Workers for $CaCl_2$ and $MgCl_2$ Doped PuO_2 and MIS Items with G Value for Water

COST-EFFECTIVENESS OF UTILIZING SURPLUS DEPLETED URANIUM (DU)

M. J. Haire, A. G. Croff
Oak Ridge National Laboratory*
Oak Ridge, Tennessee 37831-6166

ABSTRACT

About a billion pounds of surplus depleted uranium (DU) has been produced as a by-product of the uranium enrichment process for defense programs and civilian nuclear reactors at the gaseous diffusion plants at Oak Ridge, Tennessee; Paducah, Kentucky; and Portsmouth, Ohio. A project is under way to convert this DU hexafluoride (DUF_6) into a more stable oxide form that is predominately DU_3O_8. Baseline plans are to dispose of the conversion plant product in radioactive waste disposal facilities in Nevada or Utah. Finding a beneficial use for this material, rather than disposing of it, could save the U.S. government hundreds of millions, if not billions, of dollars.

This work reports estimated order-of-magnitude costs for DU_3O_8 packaging; transportation from Paducah, Kentucky; and disposal at the Nevada Test Site (NTS). Disposal charges were assumed to be \$9/ft^3, based on discussions with NTS staff. The results cover a range of values, because the number of containers that results depends on the bulk density of the material that is produced and can range from 1.5 to 4.0 MT/m^3. The limiting criterion is 40,000 lb/truck load shipment, per U.S. Department of Transportation rules. The weight of a single container is assumed to be 0.53 MT, the amount contained in a 55-gal drum. The cost avoidance to the U.S. Department of Energy is estimated as follows:

Table I

Packaging	\$93B170M
Transportation	\$88B160M
Disposal	\$60B100M
Total	\$241B430M

Some beneficial commercial uses of DU and their potential markets are described. The revenues from sales of casks constructed of DUO_2 composite materials are estimated to be as much as \$0.5B/year.

INTRODUCTION

Naturally occurring uranium contains 0.71 wt % ^{235}U. In order for uranium to be useful in most nuclear applications, the concentration of the fissile isotope ^{235}U must be increased by a process called enrichment. The enrichment of uranium creates a by-product, depleted uranium (DU), in which the concentration of ^{235}U is <0.71 wt %. The U.S. government has ~500,000 MT of DU stored at U.S. Department of Energy (DOE) sites [1]. DU is the largest mass of nuclear material in the DOE inventory. This material, mostly in the form of DU hexafluoride (DUF_6), resulted from gaseous diffusion plant operations at Oak Ridge, Tennessee; Portsmouth, Ohio; and Paducah, Kentucky. The inventory of DUF_6, which is stored in large cylinders aboveground, is increasing at a rate of ~20,000 MT/year.

On August 29, 2002, DOE awarded a contract to Uranium Disposition Services, LLC, to convert the DUF_6 to a stable form and to dispose of any portion that might not be reused. The contract includes conversion facility design and construction; operation of two facilities located at enrichment plant sites in Portsmouth, Ohio, and Paducah, Kentucky; transportation of any portion of the product not destined for reuse; and disposal of that portion. The contract also includes near-term surveillance and maintenance of the DUF_6 cylinder inventory and shipment of the DUF_6 cylinders from Oak Ridge, Tennessee, to Portsmouth, Ohio, as well as incentives for reuse of the DU. Construction of the facilities will begin by July 31, 2004.

DOE is subject to a number of driving forces that encourage or require reuse of DUF_6 and research and development (R&D) toward this end. In the legal and regulatory arena, Public Law 102-486 [2] requires DOE to prepare a study that identifies DU tailings available for conversion to commercial use. Public Law 105-204 [3] requires that DOE undertake a good-faith effort to consider recycle (i.e., beneficial use) for DU. A Record of Decision was published in August 1999 [4]. In response to this legislation, DOE prepared a document, *Depleted Uranium Materials Use Roadmap* [5], which is a guide to R&D activities. The roadmap builds on the analysis performed and documented in the final *Programmatic Environmental Impact Statement for Alternative Strategies for the Long-Term Management and Use of Depleted Uranium Hexafluoride* [6]. An agreement [7] between DOE and the State of Ohio requires a continuing good-faith effort to find beneficial uses for DUF_6 and the production of annual reports that document progress in this area.

At least as important as the legal/regulatory driving forces is the desire to reduce the cost to the government for disposition of the DUF_6. Although DU has been used historically in applications ranging from munitions to counterweights to radiation shielding, the sum total of these applications would consume only a small fraction of the inventory. As a consequence, DOE is supporting a DU Uses R&D Program to create new uses for DU that might avoid some or all of the costs of DU disposition. The basis for this program is the previously mentioned *Roadmap* [5].

This paper summarizes the current status of the potential for DU uses to reduce the cost of DUF_6 disposition and the areas that are being investigated toward this end. However, none of the potential uses are sufficiently well developed to permit a rigorous economic analysis of the cost-effectiveness of DU reuse. Thus, the economic analysis in this paper will focus on framing the economic basis for reuse, the costs or cost ranges that are presently known, and discussion of uncertainties and possibilities.

BENEFIT TO DOE OF REUSE OF DU

The benefit to DOE of reuse of DU is cost savings. Such savings could be realized in two ways: (1) avoiding some or all of the potential cost to disposition the DU oxide product from the conversion plant by disposal and (2) receiving revenues from the sale of DU.

Avoiding DU Disposition Costs

Initial baseline disposition cost. The baseline approach for disposition of any unused DU oxide (primarily U_3O_8) conversion product is to package it in suitable containers and transport it from the conversion plants to the Nevada Test Site (NTS) or to Envirocare of Utah for near-surface disposal. The cost of disposing of the entire 500,000 MT inventory of DU as oxide at NTS was estimated [8] before the conversion contracts were awarded; the results are summarized in Table II.

Table II Estimated Cost for Disposition of DU Oxide Inventory at the NTS

Disposition Cost Component	Estimated Range of Cost, $M
Packaging	93B170
Transportation	88B160
Disposal	60B100
Total	241B430

The results cover a range of values because the number of containers required depends on the bulk density of the DU oxide product, which can range from 1.5 to 4.0 kg/L, depending on the conversion and packaging techniques used.

Optimized baseline disposition cost. Initial systems studies by the conversion contractor identified the opportunity to reduce the baseline disposition cost of the DU oxide product shown above by shipping the product to Envirocare=s disposal facility in Utah. This significantly reduces the disposition cost in three ways. First, rail shipment can be used at Envirocare whereas more costly truck shipment is the only means to access NTS. Second, the weight of a single package is limited to 430 kg at NTS whereas Envirocare can accept much larger packages (up to the size of an entire railcar). Third, container costs are reduced by the use of emptied DUF_6 cylinders to package the DU oxide product. Updated cost estimates have not yet been released but are believed to have a value in the $150B$200M range.

To the extent that beneficial uses are found for DU, the cost of disposition can be avoided by having the user take custody of the DU at the loading dock of the conversion plant. The DU product that is likely to be useful to potential users is uranium dioxide, which will require limited additional processing in the conversion plant to uniformly reduce the uranium to the +4 valence state. However, this step constitutes existing technology in nuclear fuel fabrication plants and is not expected to increase costs significantly.

Upper-bound baseline disposition cost. An important assumption in achieving the disposition cost described in the preceding section is that near-surface disposal of the DU oxide product is acceptable. This determination will be made as part of the National Environmental Policy Act (NEPA) process involving issuance of site-specific draft environmental impacts statements; soliciting comments thereon; and reconciling the comments, leading to a record of decision. The validity of this assumption is supported by the fact that various forms of DU from multiple DOE facilities have been disposed of at the Envirocare facility over a period of years. However, the validity of this assumption could be called into question for two reasons. First, the amount of DU involved in converting DOE=s entire inventory is much larger (at least 10 times greater) than that of all the DU previously disposed of. Second, the U.S. Nuclear Regulatory Commission is on record [9] as questioning the acceptability of near-surface disposal of DU at an enrichment plant that was proposed to be built in Louisiana. However, the applicability of this position to arid sites in the western United States is unknown.

If more confining disposal of the DU product were required, the baseline disposition cost could increase substantially. Estimates for more elaborate measures such as use of a consolidating matrix such as grout, use of engineered subsurface structures similar to concrete bunkers, or the requirements for disposal in deep mines or subsurface excavations have been estimated and range up to about $1500M [10].

Potential Revenues from Sale of DU

None of the potential uses of DU are yet sufficiently mature to assess their worth to the users with sufficient accuracy to allow potential revenues to be evaluated. Such worth could result from two sources. First, DU-based products could substitute for more expensive components. One example of this is substituting a DU-based geochemical barrier for repository waste package components presently composed of expensive degradation-resistant alloys such as titanium and Alloy C-22 (a high-nickel alloy). If the DU-based barrier can be substituted for the metal barriers without compromising protectiveness or causing other unacceptable impacts, then the metal barriers, which are estimated to cost $5B [11] might be eliminated while simultaneously using the entire DU inventory. Thus, in this application, the DU could be worth up to $10/kg DU ($\$5 \times 10^9/\$5 \times 10^8$ kg DU), although the fabrication cost of the DU-based barrier must be subtracted to establish the unit breakeven worth of DU. Using natural uranium in this application would not be economic, because, even in the presently depressed market, it sells for $20B$40/kg U. It is noteworthy that at $5/kg DU (net costs, allowing for fabrication), the revenues (cost avoidance by the repository program) from this application would be sufficient to pay the life-cycle cost of the entire DUF_6 conversion project.

A second potential economic advantage of DU is based on capitalizing on properties of uranium such as its high density and complex electronic structure to yield products having improved or even unique capabilities. One example of this is the use of DU-based materials of construction such as DUCRETEJ or a DU-steel cermet for spent fuel storage and transportation casks. The high density of these materials could result in reduced costs in two ways. Fewer shipments would be required (because each cask has a higher payload), and fewer casks would be required (because a separate transfer cask would not be needed to move spent fuel from water pools into dry storage at nuclear reactor sites) [9]. In addition to potential economic benefits, the use of such materials may offer nonquantifiable benefits such as increased resistance to accidental or deliberate breaching forces and reduced occupational dose from spent fuel transfer operations. Another example is the potential for DU dioxide to be used in semiconductor applications, such as in the manufacture of computer chips. The refractory nature of DU dioxide would yield a chip capable of withstanding high temperatures and also the high radiation fields typical of space applications. The magnitude of these benefits has not yet been estimated.

BENEFICIAL USES OF DU

A number of beneficial uses of the DUO_2 conversion plant product have been identified. Such uses can be divided into two groups: (1) those that consume the entire surplus DU inventory and (2) those that consume only a fraction of the inventory. High-volume uses [e.g., as new shielding materials for spent nuclear fuel (SNF) casks and as additional chemical barriers at geological SNF disposal sites] capitalize on the density and chemical identity of DUO_2. These uses are all in radiologically regulated applications.

High-value beneficial uses of DU capitalize on unique electronic properties of uranium. Examples of such uses would be in semiconductors, electrodes in batteries, and fuel cells, as well as in electrolysis of water to produce hydrogen, and in catalysts. These uses would be predominantly in radiologically unregulated areas. The benefits would be the potential for products having unique capabilities and significant revenues, if the appropriate application could be found.

High-Volume Uses

Repository Uses. The preponderance of SNF destined for disposal under current U.S. policies is Zircaloy-clad, low-enriched uranium dioxide fuels from light-water reactors. The resistance of the SNF disposal cask depends upon interaction of hot groundwater and humid air with the SNF and engineered barrier system over time. The SNF could be contained in a package composed of DUO_2-based engineered barriers. If this is

done, the chemical interaction of water and air with the DUO_2-based barriers should create conditions that delay water and air penetration to the spent fuel and reduce radionuclide release rates thereafter. Two approaches are envisioned: (1) filling the void spaces in the container with DUO_2 in a sand-like form and/or (2) building the SNF basket and/or package walls with a material made from DUO_2 cermet. The fill concept consists of inserting DUO_2 particles into a repository disposal package, completely filling the gap between fuel rods and between fuel assemblies. Such use is thought to have the potential to reduce (1) the rate at which groundwater might reach the fuel, (2) the dissolution rate and solubility of the fuel matrix, and (3) the diameter and weight of the overall package needed to achieve a specific dose rate. The DUO_2-steel cermet concept consists of DUO_2 particulates embedded in a continuous steel phase. Typical cermets use sandwich construction with clean uncontaminated steel layers on both sides of the cermet. It is envisioned that DUO_2-steel cermets could replace some steel components of a waste package shell and basket. The presence of DU should also reduce the likelihood of a criticality event over geologic time by lowering the average ^{235}U content. DUO_2 metal barriers could conceivably replace some of the $5B of engineered barriers at the geologic repository.

Research is being conducted to elucidate the nature and rate at which DUO_2, steel, groundwater, and air interact as a basis for determining whether DU-based engineered barriers can be substituted for other, more expensive barriers. If this appears promising, additional studies will be initiated to examine the impacts of DU-based engineered barriers on waste package and repository performance.

Shielding Applications. A large potential market for DU is in radiation shielding applications. Although DU metal has been used in such applications, its relatively high cost can be justified only when the need for high-density shielding offsets this cost. However, DU oxides (primarily DUO_2) could be used as a component of the primary shielding material in containers designed to store and, in some cases, dispose of SNF or high-level radioactive wastes. The high density of uranium compounds makes them excellent components as shields from photon radiation.

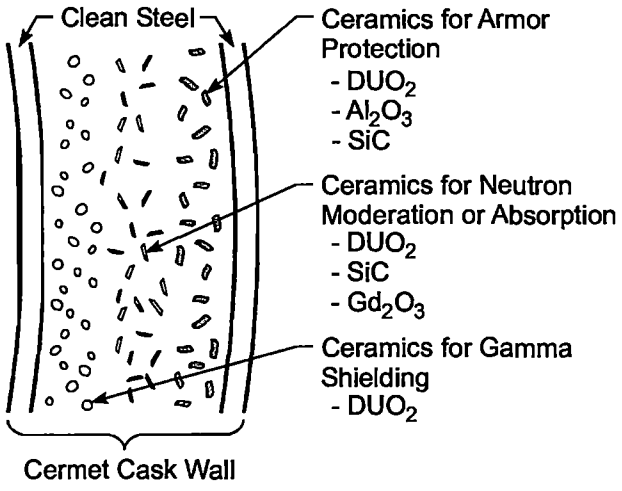

Fig. 1.

Two new uranium composite materials are envisioned for SNF storage and transport casks. One attractive new DU shielding material involves making a Aheavy@ concrete (e.g., DUCRETEJ), using a high-density DU compound as one of the components. If a DU compound is used to make the concrete, the same shielding performance could be achieved with up to one-half the thickness required of normal concrete, depending on the form of the DU [2]. To provide predictable structural strength, in this approach, the uranium compound is substituted for the coarse aggregate in conventional concrete and is enclosed between annular stainless steel shells that make up the body of the container.

The second new shielding material is DUO_2-steel cermet. Cask shells would be constructed of a cermet of DUO_2 particulates embedded in the steel, which in turn, would be contained between clean layers of steel (see figure). Because of the higher oxygen content associated with DUO_2, which moderates neutrons, cermets also have better shielding capabilities than steel. The cermet could also include a neutron absorber, such as gadolinium, for efficient absorption of neutrons.

There are ~131,000 pressurized-water reactor and 175,000 boiling-water reactor fuel assemblies that will be produced by U.S. nuclear power plants under the terms of their current licenses. Approximately 10,000 casks will be required for the storage and transport of commercial spent fuel to the repository [12]. It is estimated that 50–60 MT of DU will be required per cask to produce the "new generation" of DU casks to be used for spent fuel storage, transport, and disposal. The containment of DU composites within 10,000 casks that can be used in the United States alone will require the use of the total DOE DU inventory. The cost of material purchase and fabrication for conventional casks is in excess of $6B. The cost to procure materials for the fabrication of spent fuel and high-level-waste (HLW) containers within the engineered barrier at the geologic repository is estimated to be in excess of $14B. If DU composite materials can provide advances in radioactive material shielding and structural performance of casks, the estimated U.S. container cost of ~$14B can be significantly reduced using more uniform DU cask designs. The revenue from sales of DU casks is estimated to be as much as $0.5B/year.

Ongoing R&D is focused on confirming the long-term stability of candidate heavy concretes and on developing low-cost manufacturing techniques for large cermet shapes.

HIGH-VALUE USES

The DUF_6 Materials Use Roadmap [5] identifies the need for a science program to conceive and develop new potential uses for the DU conversion product. This need has led to the identification of a number of ideas that appear to be promising but where fundamental questions remain concerning the scientific feasibility. If only one or two of these potential uses were to prove feasible, a high-value market for DU could result, with attendant cost savings. Research is being conducted to ascertain the scientific feasibility of some of these high-value uses.

Uranium catalysts

U.S. industries and DOE must manage a variety of off-gas wastes consisting of complex volatile organic compounds. Ongoing research concentrates on a new class of nanoporous uranium oxide sol-gel catalysts doped with uranium oxides for destruction of a range of volatile organic contaminants, including alkanes, aromatics, and chlorinated organic compounds. Proof-of-principle experiments have been conducted, and optimal formulations are being sought. If performance meets expectations, uranium-based catalysts might replace high-cost platinum-based catalysts. The U.S. catalyst market is estimated to be ~$9B in 2003. Thus, a small niche in this market could be lucrative.

Uranium-based semiconductors

Uranium oxides have electrical and electronic properties that are equivalent, or superior, to those of conventional Si, Ge, and GaAs semiconductor materials. Thus, it appears that a new, higher-performance class of semiconductors is possible: uranium oxide–based semiconductors. Uranium oxides have characteristics that could give them significantly better performance than conventional semiconductor materials: operation at substantially higher temperatures and greater radiation and electromagnetic force resistance, qualities that could make them more suited for use in hazardous environments. A number of urania semiconductor devices are possible, including solar cells, thermophotovoltaic cells, and thermoelectric cells, as well as diodes and transistors. The semiconduction properties of solid-crystal DUO_2 with various dopants have been measured. A uranium-based diode and transistor have been constructed and tested. Replacing current silicon chips with DUO_2 chips would consume ~30,000 MTU/year. Assuming $20/kg U, this translates to more than $0.5B/year in revenues.

Urania fuel cells

Current solid oxide fuel cell (SOFC) technology is limited by relatively poor ion conductivity, erosion of electrodes and electrolyte due to surface interactions, and differences in thermal expansion of different materials at the electrode/electrolyte interface. Stabilized uranium oxides promise solutions to these problems. It is believed that stabilized uranium oxide films will be superior electrodes for SOFCs because of their higher mixed (electronic/ionic) conductivity, better stability, and improved structural compatibility with solid electrolytes. This work will lead to substantially improved components for SOFCs. The dollar value of a more efficient fuel cell is not estimated. The U.S. fuel cell market is estimated to be ~$12.6B in the year 2012.

Photoelectric hydrogen production

Photoelectric cells (PECs) are devices that provide a direct method for converting optical energy into either chemical or electrical form. In the case of conversion of optical energy into a chemical form, light strikes the PEC anode, resulting in the photoassisted dissociation of water into hydrogen and oxygen, thereby providing hydrogen fuel that can be stored and utilized at a later time. A number of semiconducting materials have been suggested for use as PEC anodes for the dissociation of water. However, electrode stability has proven to be a crucial problem in the realization of a workable PEC device. The most promising oxides that have been identified include pure UO_2 and uranium-doped potassium tantalite. The dollar value of a more cost-effective method of producing hydrogen has not been estimated. The hydrogen economy is currently about $2.5B/year and growing at a rate of 10%/year.

INTERNATIONAL COLLABORATIONS

The DU Uses R&D program engages in collaborative international activities to better understand the international situation concerning the disposition of DUF_6, provide credibility to U.S. efforts to beneficially use DU, and obtain the benefits of lower-cost or cost-shared research results. Currently, extensive collaborations are being conducted with the Russian Academy of Science and with Minatom.

CONCLUSIONS

The cost-effectiveness of using the DU oxide conversion product from facilities to convert DUF_6 to a more stable form depends on the magnitude of the avoided DU oxide disposition cost and potential revenues from the sale of DU-based products. The packaging, transportation, and disposal costs are expected to range from $150M to $200M but could be much higher if more elaborate waste forms or disposal technology were to be required. It is not yet possible to accurately estimate the revenues resulting from potential DU uses, which could consume a substantial portion of the DOE inventory. However, success concerning the better-developed potential applications related to spent fuel storage, spent fuel and waste transportation, and the repository could reduce or avoid costs measured in billions of dollars. Revenue from sale of casks made of DU composites could be as much as ~$0.5B/year. Other potential uses of DU still in the fundamental research stage might add substantially to this total if they are proven. The U.S. government has an ongoing program to investigate such uses and to develop the most promising of these technologies to the point that they are available for deployment.

REFERENCES

1 "Technology Assessment Report for the Long-Term Management of Depleted Uranium Hexafluoride," UCRL-ID-120372, Lawrence Livermore National Laboratory (June 1995).

2 Public Law 102-486, Energy Policy Act of 1992, Sect. 1016, 106 Stat 2949 (October 24, 1992).
3 Public Law 105-204, U.S. Congress (July 21, 1998).

4 "Record of Decision for the Long-Term Management and Use of Depleted Uranium Hexafluoride," *Fed. Regist.*, 64 (153), 43358 (August 10, 1999).

5 M. J. HAIRE and A. G. CROFF (eds.), "U.S. Department of Energy DUF_6 Materials Use Roadmap," ORNL-6968, Oak Ridge National Laboratory (August 2001).

6 U.S. DEPARTMENT OF ENERGY, "Final Programmatic Impact Statement for Alternative Strategies for Long-Term Management and Use of Depleted Uranium Hexafluoride," DOE/EIS-0269 (April 1999).

7 "Director=s Final Findings and Orders," Director, Ohio Environmental Protection Agency (February 24, 1998).

8 A. G. CROFF, J. R. HIGHTOWER, D. W. LEE, G. E. MICHAELS, N. L. RANEK, and J. R. TRABALKA, "Assessment of Preferred Depleted Uranium Disposal Forms," ORNL/TM-2000/161, Oak Ridge National Laboratory (June 2000).

9 U.S. NRC letter, docket number 70-3070, from John W. N. Hickey to W. Howard Arnold, President Louisiana Energy Services (September 22, 1992).

10 "Summary of the Cost Analysis Report for the Long-Term Management of Depleted Uranium Hexafluoride," UCRL-ID-127650, Lawrence Livermore National Laboratory (September 1997).

11 Personal communication, Paul Harrington, Yucca Mountain Project (October 7, 2003).

12 Personal communication, Archer Haskins, Holtec International (October 20, 2003).

FOOTNOTES

* Oak Ridge National Laboratory, managed by UT-Battelle, LLC, for the U.S. Department of Energy under contract DE-AC05-00OR22725.

ORNL/TM-2003/172

Alpha Radiolysis of Sorbed Water on Uranium Oxides and Uranium Oxyfluorides

September 2003

Prepared by
A. S. Icenhour
L. M. Toth

DOCUMENT AVAILABILITY

Reports produced after January 1, 1996, are generally available free via the U.S. Department of Energy (DOE) Information Bridge:

Web site: http://www.osti.gov/bridge

Reports produced before January 1, 1996, may be purchased by members of the public from the following source:

National Technical Information Service
5285 Port Royal Road
Springfield, VA 22161
Telephone: 703-605-6000 (1-800-553-6847)
TDD: 703-487-4639
Fax: 703-605-6900
E-mail: info@ntis.fedworld.gov
Web site: http://www.ntis.gov/support/ordernowabout.htm

Reports are available to DOE employees, DOE contractors, Energy Technology Data Exchange (ETDE) representatives, and International Nuclear Information System (INIS) representatives from the following source:

Office of Scientific and Technical Information
P.O. Box 62
Oak Ridge, TN 37831
Telephone: 865-576-8401
Fax: 865-576-5728
E-mail: reports@adonis.osti.gov
Web site: http://www.osti.gov/contact.html

ORNL/TM-2003/172

ALPHA RADIOLYSIS OF SORBED WATER ON URANIUM OXIDES AND URANIUM OXYFLUORIDES

A. S. Icenhour
L. M. Toth

Date Published: September 2003

Prepared by
OAK RIDGE NATIONAL LABORATORY
P.O. Box 2008
Oak Ridge, Tennessee 37831-6283
managed by
UT-Battelle, LLC
for the
U.S. DEPARTMENT OF ENERGY
under contract DE-AC05-00OR22725

THIS PAGE INTENTIONALLY LEFT BLANK.

CONTENTS

Page

THIS PAGE INTENTIONALLY LEFT BLANK.

LIST OF FIGURES

THIS PAGE INTENTIONALLY LEFT BLANK.

LIST OF TABLES

ABSTRACT

The radiolysis of sorbed water and other impurities contained in actinide oxides has been the focus of a number of studies related to the establishment of criteria for the safe storage and transport of these materials. Gamma radiolysis studies have previously been performed on uranium oxides and oxyfluorides (UO_3, U_3O_8, and UO_2F_2) to evaluate the long-term storage characteristics of ^{233}U. This report describes a similar study for alpha radiolysis.

Uranium oxides and oxyfluorides (with ^{238}U as the surrogate for ^{233}U) were subjected to relatively high alpha radiation doses (235 to 634 MGy) by doping with ^{244}Cm. The typical irradiation time for these samples was about 1.5 years, which would be equivalent to more than 50 years irradiation by a ^{233}U sample. Both dry and wet (up to 10 wt % water) samples were examined in an effort to identify the gas pressure and composition changes that occurred as a result of radiolysis.

This study shows that several competing reactions occur during radiolysis, with the net effect that only very low pressures of hydrogen, nitrogen, and carbon dioxide are generated from the water, nitrate, and carbon impurities, respectively, associated with the oxides. In the absence of nitrate impurities, no pressures greater than 1000 torr are generated. Usually, however, the oxygen in the air atmosphere over the oxides is consumed with the corresponding oxidation of the uranium oxide. In the presence of up to 10 wt % water, the oxides first show a small pressure rise followed by a net decrease due to the oxygen consumption and the attainment of a steady-state pressure where the rate of generation of gaseous components is balanced by their recombination and/or consumption in the oxide phase.

These results clearly demonstrate that alpha radiolysis of either wet or dry ^{233}U oxides will not produce deleterious pressures or gaseous components that could compromise the long-term storage of these materials.

THIS PAGE INTENTIONALLY LEFT BLANK.

1. INTRODUCTION

The radiolysis of sorbed water and other impurities contained in actinide oxides has been the focus of a number of studies that centered on the establishment of criteria for the safe storage and transport of the oxides. These criteria are designed to prevent the production of large pressures or hazardous products (e.g., hydrogen and fluorine) that could be deleterious to storage containers and that might result in the release of radioactivity. Storage standards have been developed for both plutonium and uranium to address these concerns.[1,2] In support of the development of these standards, a number of radiolysis studies have been performed to evaluate the yields of radiolytic products (e.g., Refs. 3–8).

Uranium-233, which is stored primarily at Oak Ridge National Laboratory (ORNL), contains a contaminant isotope, ^{232}U, which has a daughter isotope, ^{208}Tl, that emits a 2.6-MeV gamma ray. Hence, these materials have a relatively high alpha activity as well as a large gamma radiation field, both of which complicate their handling. Experimental studies have been conducted on the gamma radiolysis of sorbed water on uranium oxides and on fluoride impurities in these oxides (primarily on uranium oxyfluorides).[3–5] These experiments have demonstrated that, with respect to gamma radiation, these materials can be safely stored. To complete the understanding of radiolysis in a ^{233}U oxide system, a similar set of experiments have been pursued to explore the effects of alpha radiolysis. In all of these experiments, ^{238}U was used as a surrogate for the $^{233}U/^{232}U$, with radiation supplied from a separate source. A surrogate alpha emitter, ^{244}Cm, was used in place of the $^{233}U/^{232}U$. The use of the surrogate alpha source offers the advantages of (1) a higher specific alpha activity, which provides for an accelerated experiment, and (2) the elimination of the use of $^{233}U/^{232}U$, which results in a significant personnel dose avoidance and more easily handled materials. This report documents the results of the alpha radiolysis experiments that have been performed on uranium oxides and oxyfluorides.

2. EXPERIMENTAL

2.1 SAMPLE PREPARATION

The surrogate uranium oxides were prepared by doping natural uranyl nitrate hexahydrate [$UO_2(NO_3)_2 \cdot 6H_2O$] with the desired amount of curium nitrate (~25 mg ^{244}Cm as a 0.04 *M* solution in 4 *N* HNO_3), coprecipitating the uranium and curium, and then calcining the precipitate. The procedure used was developed by first coprecipitating cerium and uranium. The chemical concentrations, rinsing steps, and calcination temperatures were thereby established.

Use of ^{244}Cm provided a dose rate about 37 times that which would be achieved if the sample was ^{233}U (with 160 ppm ^{232}U), as shown in Fig. 2.1. An example of the radionuclide composition for the ^{244}Cm solution and dose contribution data is presented in Table 2.1. Note that the ^{244}Cm solution contains a number of radioisotopes, and that while only 50 wt % of the material is ^{244}Cm, more than 99% of the dose is attributed to the ^{244}Cm.

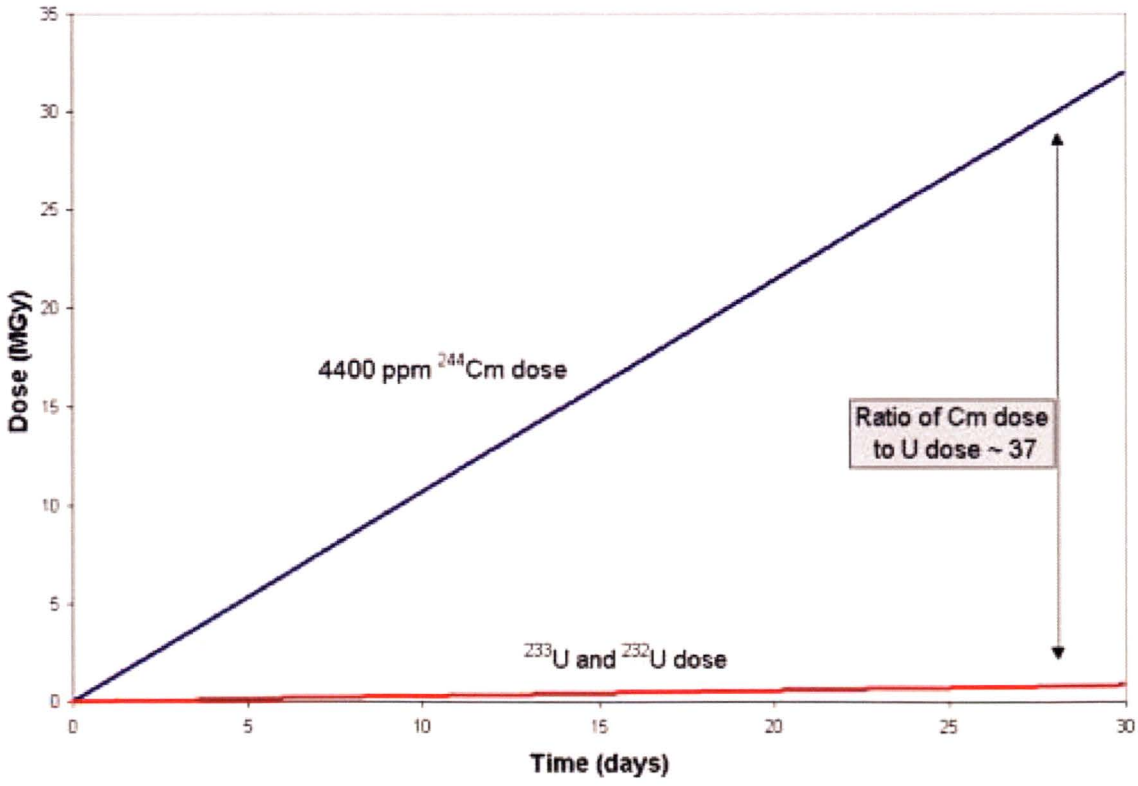

Fig 2.1. Comparison of alpha dose as a function of time for a U_3O_8 sample that consists of ^{238}U spiked with about 4400 ppm ^{244}Cm and one that consists of ^{233}U containing about 160 ppm ^{232}U.

Table 2.1. Example of radionuclide composition and dose contribution data for material used to spike uranium samples

Radionuclide	Half-life (years)	Specific activity (Ci/g)	Average alpha energy (MeV)	Composition (wt %)	Contribution to dose (%)
^{244}Cm	18.11	80.9	5.7965	50.34	99.74
^{245}Cm	8500	0.1717	5.363	1.36	0.01
^{246}Cm	4730	0.3072	5.376	7.31	0.05
^{247}Cm	1.56×10^7	9.20×10^5	4.9475	0.12	<<0.01
^{248}Cm	3.40×10^5	0.00424	4.6524	0.07	<<0.01
^{240}Pu	6563	0.22696	5.1549	40.04	0.20
^{241}Pu	14.4	103	0.000118	<<0.01	<<0.01
^{242}Pu	3.76×10^5	0.003926	4.89	<<0.01	<<0.01
^{243}Am	7380	0.1993	5.2656	0.76	<<0.01

The uranium and curium solutions were mixed and were then coprecipitated as a hydroxide in quartz tubes using concentrated ammonium hydroxide (NH_4OH). The precipitate was centrifuged and rinsed with NH_4OH. The precipitate was subsequently heated overnight to the appropriate temperature to obtain the desired oxide (about 350°C for UO_3 and about 650°C for U_3O_8). Uranyl fluoride samples could not be prepared by this method, because the UO_2F_2 could not be formed as a precipitate. Instead, UO_2F_2 was wetted with a curium nitrate solution and then dried overnight at 350°C. This temperature was selected to be sufficiently high to decompose the nitrate but low enough to prevent disproportionation of the UO_2F_2. The samples were loaded into instrumented containers. Just prior to closure of the sample containers, the desired amount of water was added to each sample using a calibrated pipette.

2.2 SAMPLE CONTAINERS

The samples were placed in stainless steel containers, which were connected by a small-diameter stainless steel tube to a pressure transducer and to a valve (Fig. 2.2). These containers were constructed from a ½-in. Cajon VCR socket-weld gland that had a short piece of ½-in. tubing welded to it. The tubing was closed at one end with an 1/8-in.-thick disk. The overall length of the container was about 3.5 in. The container was closed with a VCR cap that was drilled through and had 1/16-in. tubing connected to it. The tubing led to a tee that was connected to a pressure transducer and a Nupro valve,

which was used for leak testing and withdrawal of gas samples. Filter gaskets (0.5-μm sintered frit) were used in the VCR face-sealed connections to prevent movement of particles and the spread of contamination. The void volume of the containers was measured by expanding helium from a known volume, and the measured volumes are shown in Table 2.2. Samples were prepared and loaded into the containers in a glove box at the ORNL Radiochemical Engineering Development Center.

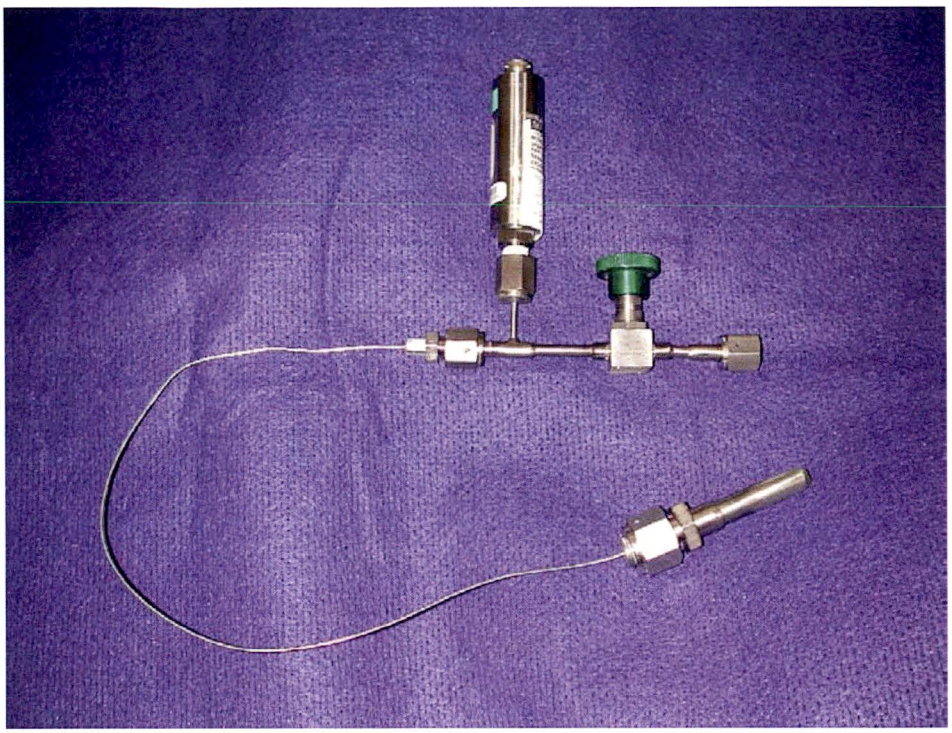

Fig. 2.2. Sample container and pressure transducer configuration used in the alpha radiolysis experiments.

Table 2.2 Void volume of sample containers

Container	Volume (cm^3)
A-1	12.6
A-2-1, A-2-2	12.9
A-3	12.7
A-4-1	12.4
A-5	12.7
A-6	12.3

2.3 DATA ACQUISITION

A computerized data acquisition system was used to record the pressure in the sample containers throughout the irradiations (Fig. 2.3). Validyne® hardware and software were used, providing up to eight data channels per card. Sensotec® pressure transducers (Model FPA) were used to measure the pressure. An Omega® Type K thermocouple was placed in contact with the exterior of one of the sample containers to obtain a representative temperature for each of the containers.

2.4 SAMPLE ANALYSES

During the irradiations, gas samples were periodically withdrawn and analyzed by mass spectrometry. Some samples were analyzed by X-ray diffraction (XRD) by loading capillaries with a small amount of ground sample and running XRD on a Debye-Scherrer camera using MoKα radiation. This very classic method for XRD analysis greatly minimized the amount of sample required and satisfied ALARA (as low as reasonably achievable) requirements for radiation exposure. During the preparation of one of the UO_3 samples, nitrate analyses were performed using a nitrate-specific electrode because it was suspected that radiolysis of residual nitrates contributed to an observed pressure increase.

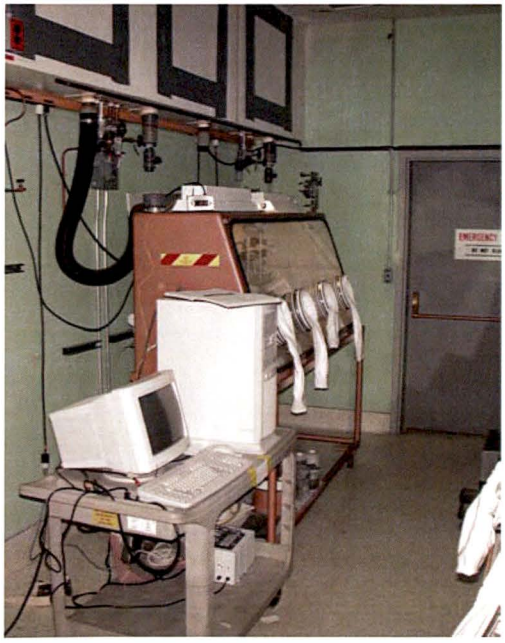

Fig. 2.3. Photograph of data acquisition system and glove box used for the experiments.

3. RESULTS

The effects of alpha particle irradiation on the various wet and dry uranium oxide/oxyfluoride samples were studied by monitoring the pressure changes of the gas atmosphere in contact with them throughout the irradiation period followed by gas composition analyses of samples taken both on occasion during the experiment and at the end of the irradiation. Finally, XRD measurements were made on some of the oxides before and after irradiation to determine if any changes in the crystalline phases had occurred as a result of the alpha radiation exposure to the atmospheres in which they were in contact.

3.1 PRESSURE MEASUREMENT

Table 3.1 provides a summary of the irradiation experiments performed. Most of these samples were irradiated for more than 1.5 years with these relatively intense internal sources. The pressure data from each of the experiments are shown in Figs. 3.1–3.7 as gas yield (millimoles of gas per gram of sample) versus calculated dose. The gas yield was calculated using the ideal gas law. The dose to the sample was calculated based on the amount of ^{244}Cm present in the sample, assuming that all of the decay energy from the ^{244}Cm was deposited in the sample (i.e., in the uranium oxide or oxyfluoride plus the added H_2O).

Even after very long periods of alpha radiolysis, the pressures were generally observed to reach a limit ("plateau" or "steady-state" value) that is much lower than the net pressure expected from the radiolytic conversion of all the moisture to hydrogen and oxygen. These plateaus are usually preceded by some fluctuations that depend on the presence of water on the sample. Typical for the samples containing moisture is the appearance of a pressure rise that peaks and then proceeds downward to a steady-state value—one that is either slightly larger or smaller that the starting pressure of the system.

For dry UO_3 (Fig. 3.1), a slight decrease in pressure is followed by a steady growth to steady-state value of approximately 1000 torr. However, for a wetted UO_3 sample (Figs. 3.2 and 3.3), an initial rise is followed by a decrease in pressure to a steady-state value. Dry U_3O_8 and UO_2F_2 samples show only a progressive decrease to the limiting steady-state value, while the respective wetted samples show some increase in pressure, which is then followed by a decrease to a subatmospheric pressure.

Table 3.1. Summary of irradiation experiments performed

Experiment	Material	Mass (g)[a]	^{244}Cm added (mg)	Total dose (MGy)
A-1	UO_3	6.21	24.9	595
A-2-1	UO_3 + 10 wt % H_2O	5.90	25.0	329
A-2-2	UO_3 + 10 wt % H_2O[b]	5.86	24.9	235
A-3	U_3O_8	5.60	24.9	415
A-4-1	U_3O_8 + 2 wt % H_2O	5.64	24.9	406
A-5	UO_2F_2	4.93	25.0	634
A-6	UO_2F_2•1.7 H_2O (9 wt % H_2O)	4.86	25.0	595

[a]Mass of anhydrous material.

[b]Same method as that used for preparation of sample A-2-1, except that additional rinses were performed to reduce residual nitrates.

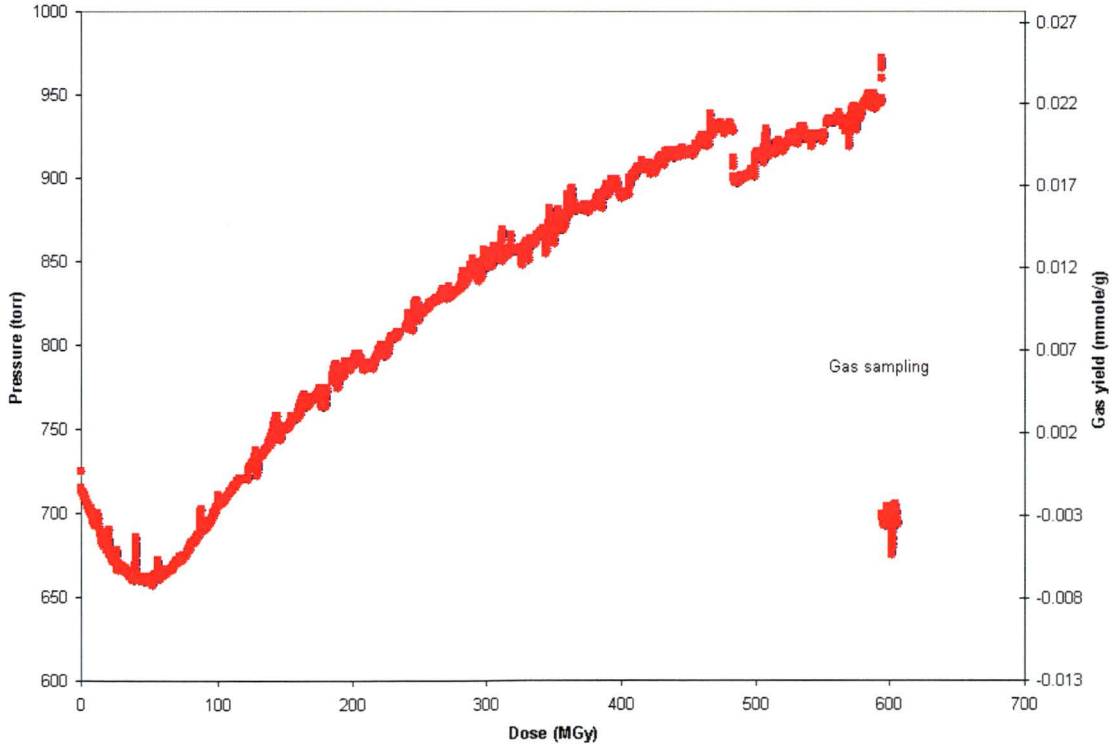

Fig. 3.1. Pressure and gas yield as a function of dose for sample A-1 (UO_3 spiked with ^{244}Cm).

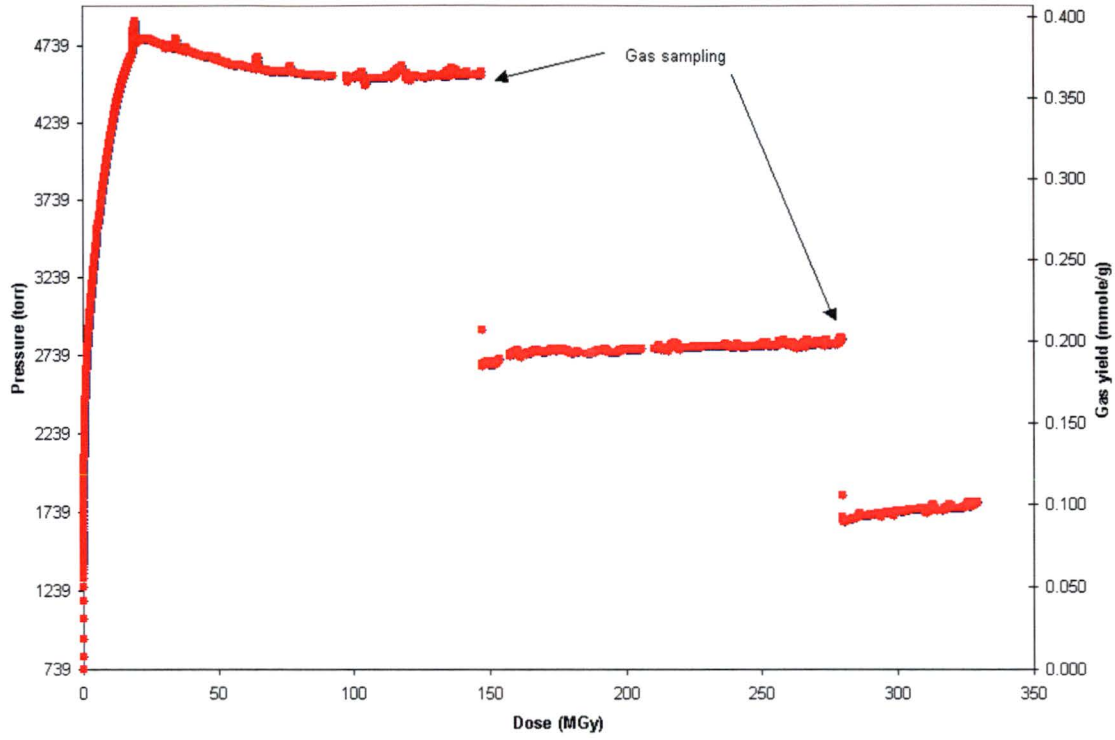

Fig. 3.2. Pressure and gas yield as a function of dose for sample A-2-1 (UO_3 + 10 wt % H_2O, spiked with ^{244}Cm).

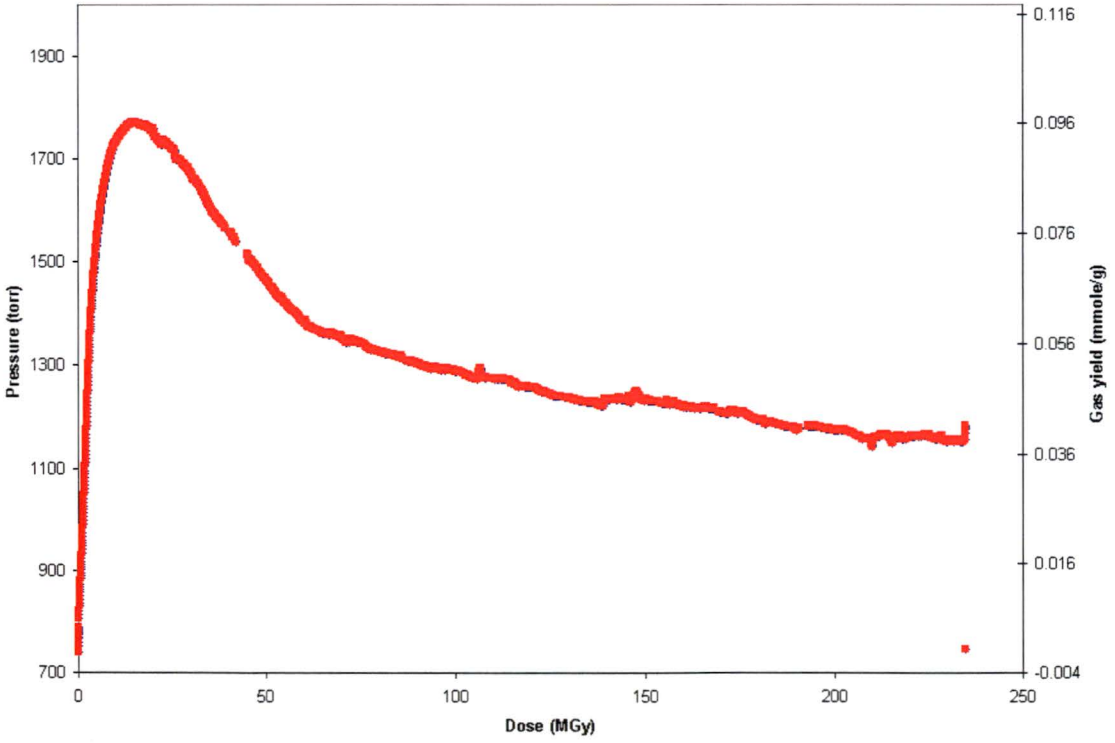

Fig. 3.3. Pressure and gas yield as a function of dose for sample A-2-2 (UO_3 + 10 wt % H_2O, spiked with ^{244}Cm and followed by additional rinsing with NH_4OH to remove nitrates).

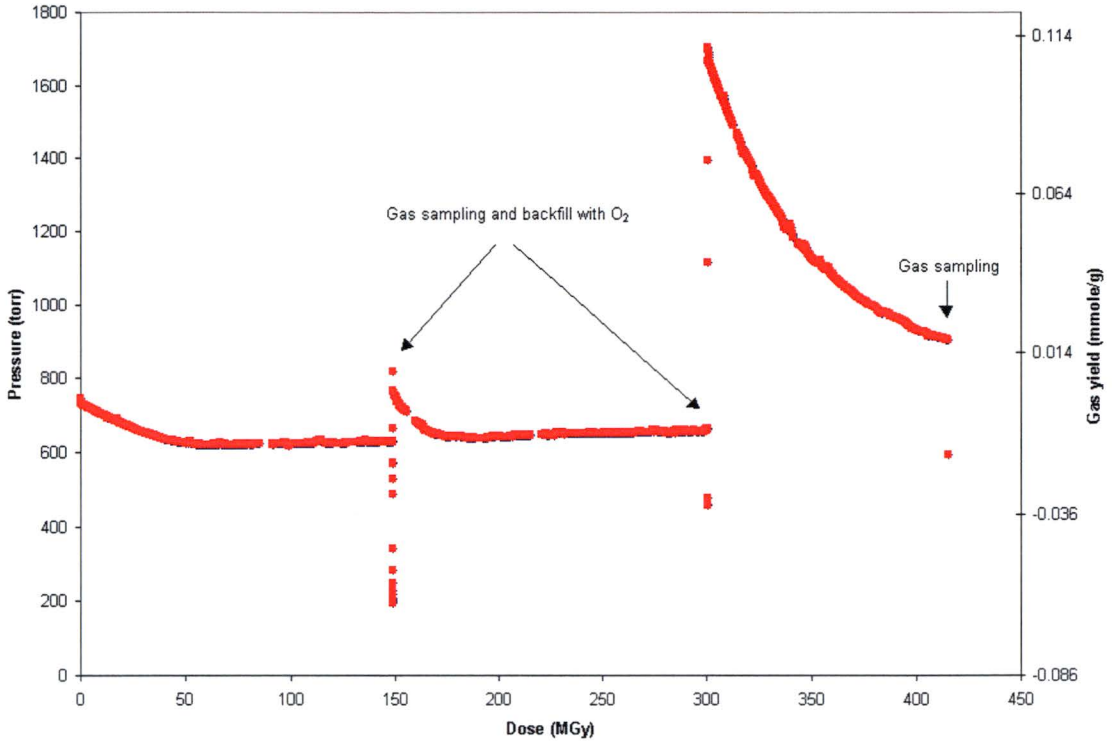

Fig. 3.4. Pressure and gas yield as a function of dose for sample A-3 (U_3O_8 spiked with ^{244}Cm).

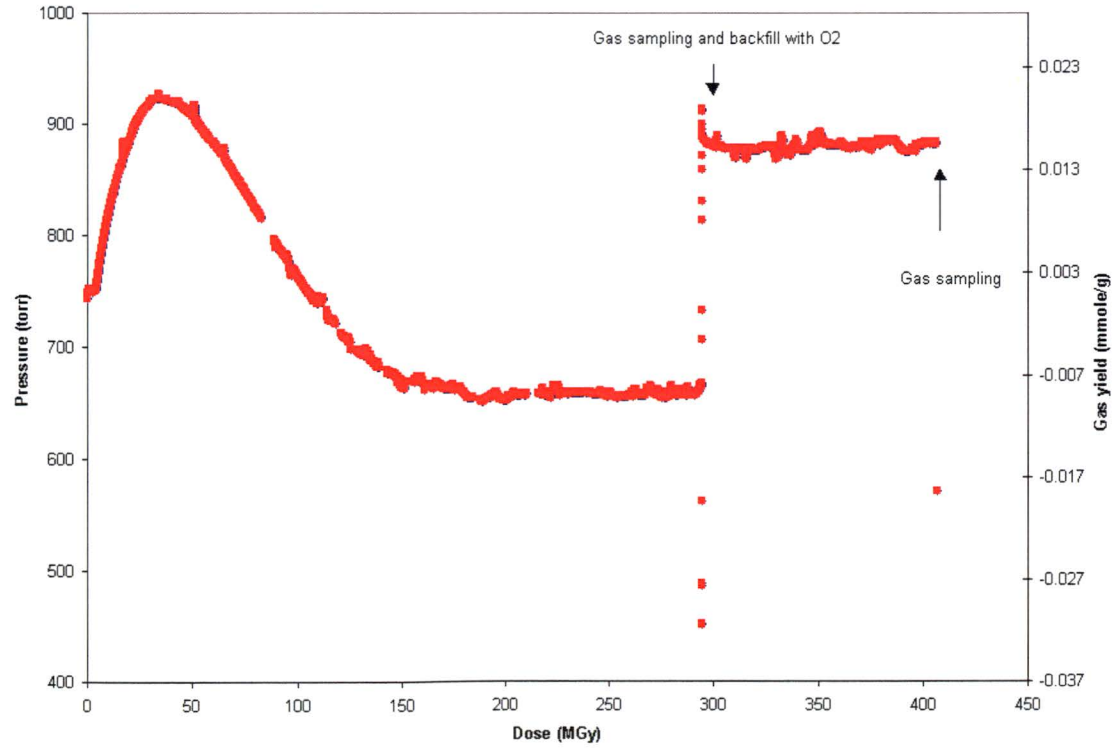

Fig. 3.5. Pressure and gas yield as a function of dose for sample A-4-1 (U_3O_8 with 2 wt % H_2O, spiked with ^{244}Cm).

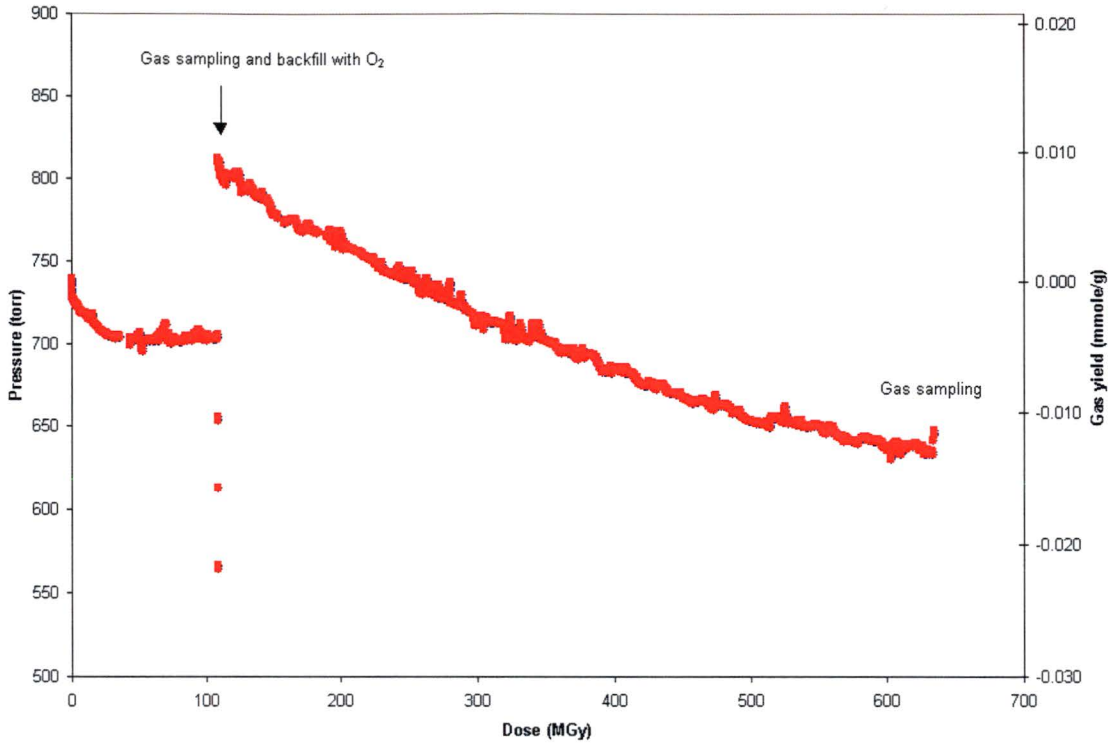

Fig. 3.6. Pressure and gas yield as a function of dose for sample A-5 (UO_2F_2 wetted with ^{244}Cm solution and then dried).

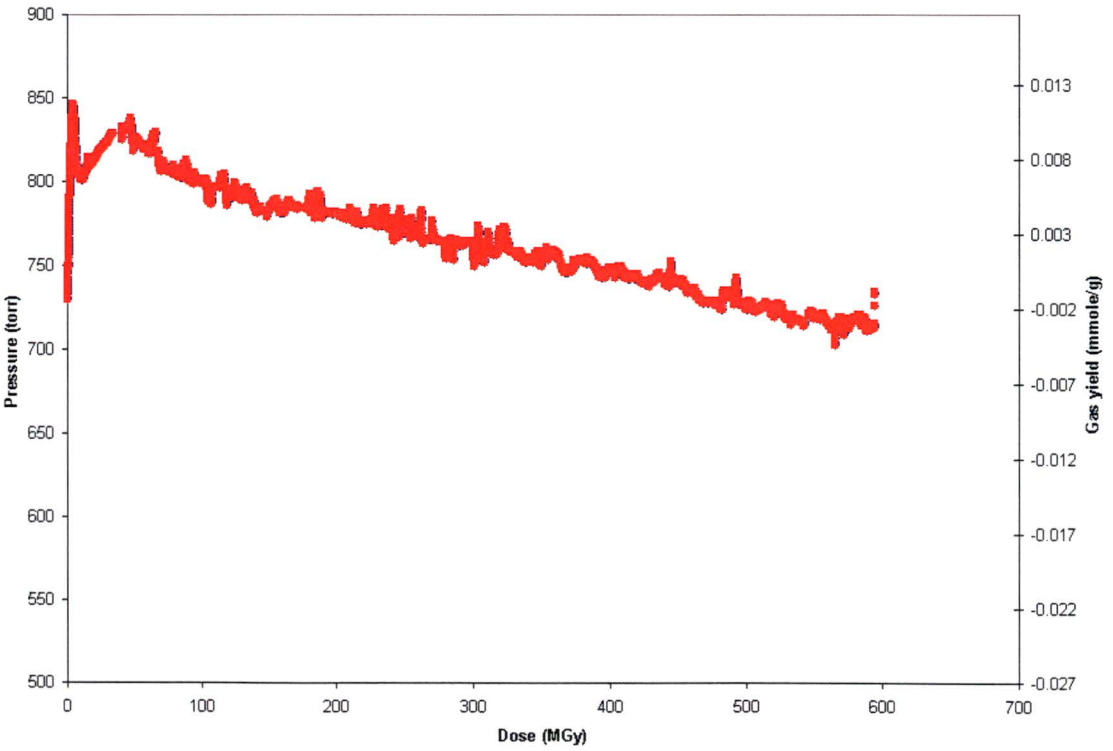

Fig. 3.7. Pressure and gas yield as a function of dose for sample A-6 ($UO_2F_2 \cdot 1.7H_2O$ wetted with ^{244}Cm solution and then dried).

The only truly anomalous trend was seen with the first wetted UO_3 sample, which rapidly reached a relatively high (ultimate) steady-state pressure (Sample A-2-1, Fig. 3.2). Because the gas sample had an unusually high nitrogen content (see next section), it was suspected that the nitrate ion from the reagent material had not been sufficiently washed from the sample and that this residue was radiolyzing in addition to the uranium oxides and moisture.

Therefore, a repeat of this sample preparation and irradiation was deemed necessary but with more thorough washing of the sample after precipitation and separation from the mother liquor. The water from each rinse was monitored with a nitrate-specific ion electrode and compared with a calibration chart for nitrate ion in equivalent ionic strength solutions.* These results are given in Fig. 3.8, which shows that the nitrate concentration in the mother liquor was ~4.2 *M* and, after 5 rinses, was reduced to ~0.07 *M* in the final rinse. (Note that in the preparation of sample A-2-1, only one rinse was performed. Based on Fig. 3.8, this process would result in a rinse-solution nitrate concentration of ~1.5 *M*, or approximately 20 times that achieved for sample A-2-2.) This material was then dried and run with 10% added water to give a significantly lower steady-state pressure and an overall profile that better matched the other oxides. [Compare sample A-2-2 (Fig. 3.3) with, for example, sample A-4-1 (Fig. 3.5).]

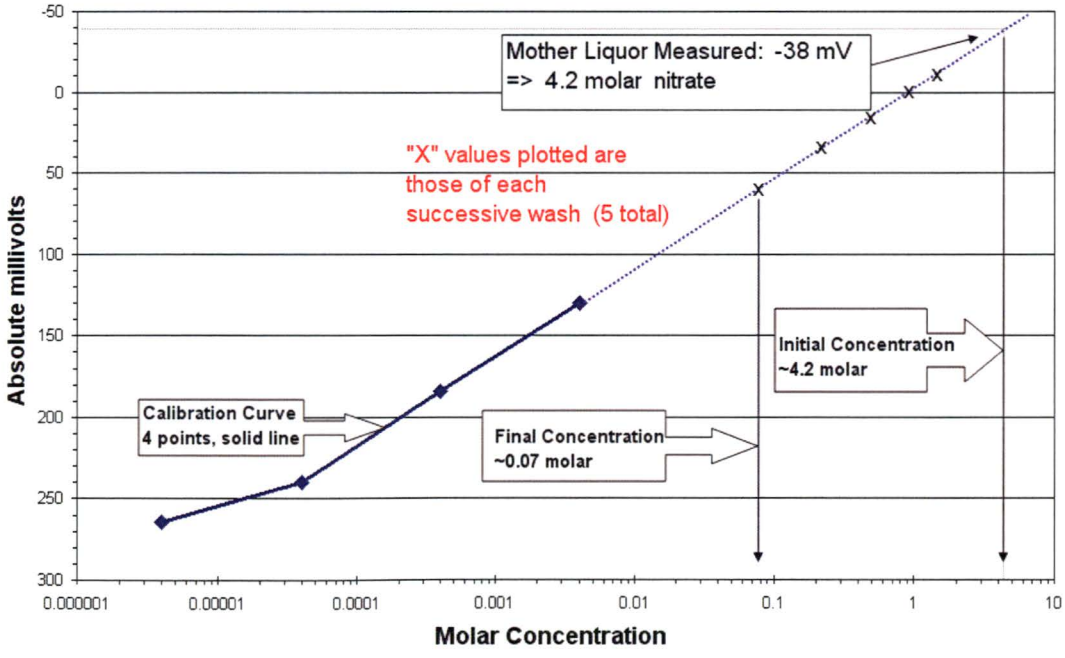

Fig. 3.8. Calibration and rinse data for additional rinsing during preparation of A-2-2.

*The measurement of nitrate ion in the wash solution was easier and less expensive than the more obvious direct destructive analysis of the solid sample.

The presence of nitrate ion impurity could not be a problem for the U_3O_8 and UO_2F_2 samples because these were prepared at temperatures above that at which nitrate decomposes. Furthermore, the gas analyses described in the following section confirm that nitrate ion was not a problem in these other two uranium compounds.

3.2 GAS ANALYSIS

Mass spectrometric gas analyses on periodic samples are presented in Tables 3.2–3.4 along with pressure and temperature data at the time of the sampling. The values labeled as "initial" are those at the beginning of the experiment or, in the case of multiple gas samples, the value just after sampling. The "final" values are taken just prior to withdrawal of the gas sample. Hence, these pressure values give a measure of the change during the period prior to sampling.

Table 3.2. Results of mass spectrometric analysis (volume percentage) of gas composition from UO_3 samples

	A-1 (UO_3 dry)	A-2-1 (UO_3 with 10 wt % H_2O)		A-2-2 (UO_3 with 10 wt % H_2O)
		First gas sample	Second gas sample	
Initial atmosphere	Air	Air	Modified air[a]	Air
Initial pressure[b] (torr)	725	739	2671	740
Initial temperature[c] (°C)	27	29	25	29
Final pressure[c] (torr)	972	4572	2843	1183
Final temperature[c] (°C)	29	25	27	29
CO_2	0.01	0.03	0.01	0.02
CO	<0.01			<0.01
Ar	0.3	0.08	0.09	0.2
O_2	0.92	1.32	0.6	1.01
N_2	82.8	89.2	89.09	96.68
NO_x[d]	0.37	0.2	0.05	0.32
H_2	0.002	0.24	0.37	0.72
He	15.59	8.84	9.7	1.05

[a] Composition remaining after first sample of A-2-1.
[b] Value at beginning of experiment or just after previous gas sampling operation.
[c] Value just prior to withdrawal of gas sample.
[d] Likely in the form N_2O.

Table 3.3. Results of mass spectrometric analysis (volume percentage) of gas composition from U_3O_8 samples

	A-3 (U_3O_8 dry)			A-4-1 (U_3O_8 with 2 wt % H_2O)	
	First gas sample	Second gas sample after backfill with O_2	Third gas sample after backfill with O_2	First gas sample	Second gas sample after backfill with O_2
Initial atmosphere	Air	Air/additional O_2[a]	Air/additional O_2[b]	Air	Air/additional O_2[c]
Initial pressure[d] (torr)	744	766	1701	743	912
Initial temperature[d] (°C)	27	24	27	27	27
Final pressure[e] (torr)	629	663	906	668	883
Final temperature[e] (°C)	24	27	24	27	25
CO_2	0.06	<.01	0.2	0.02	0.02
Ar	0.8	0.4	0.43	0.7	0.29
O_2	17.29	0.7	2.23	10.06	0.88
N_2	70.1	41.24	28.06	60.17	26.17
NO_x[f]		0.23	0.11	0.03	0.024
H_2	0.001	0.01	0.003	0.44	0.97
H_2O			0.4		0.2
He	11.66	57.4	68.56	28.08	71.44

[a] Composition remaining after first sample of A-3 plus backfilled with O_2.
[b] Composition remaining after second sample of A-3 plus backfilled with O_2.
[c] Composition remaining after first sample of A-4-1 plus backfilled with O_2.
[d] Value at beginning of experiment or just after previous gas sampling operation.
[e] Value just prior to withdrawal of gas sample.
[f] Likely in the form N_2O.

Table 3.4. Results of mass spectrometric analysis (volume percentage) of gas composition from UO_2F_2 samples

	A-5 (UO_2F_2 dry)		A-6 ($UO_2F_2 \cdot 1.7H_2O$)
	First gas sample	Second gas sample after O_2 addition	
Initial atmosphere	Air	Air/additional O_2[a]	Air
Initial pressure[b] (torr)	739	811	737
Initial temperature[b] (°C)	27	24	27
Final pressure[c] (torr)	705	646	732
Final temperature[c] (°C)	24	29	29
CO_2	0.1	1.2	1.86
CO		0.32	0.03
Ar	0.74	0.72	0.49
O_2	16.91	5.79	6.17
N_2	64.3	79.68	50.36
NO_x[d]		0.22	1.16
H_2	<0.001	0.007	8.15
He	18.05	12.06	31.78

[a] Composition remaining after first sample of A-5 plus backfilled with O_2.
[b] Value at beginning of experiment or just after previous gas sampling operation.
[c] Value just prior to withdrawal of gas sample.
[d] Likely in the form N_2O.

Results from the mass spectrometric analysis of the UO_3 samples are shown in Table 3.2. One gas sample was withdrawn at the end of experiment A-1. By contrast, because of the relatively large pressure rise seen for A-2-1, gas samples were taken at two different times from this container (see Fig. 3.2). A gas sample was withdrawn at the end of experiment A-2-2. The introduced helium seen here in the analysis is an artifact of the sampling method.

For the U_3O_8 experiments, a pressure decrease was evident and multiple gas samples were also withdrawn. Results of the mass spectrometric analysis of these samples are presented in Table 3.3. After the first gas sample of experiment A-3, the container was evacuated to about 200 torr and was then backfilled with oxygen to a total pressure of 766 torr. After withdrawal of the second gas sample from experiment A-3, the container pressure was about 458 torr (no further evacuation performed). This container was then backfilled with oxygen to a total pressure of 1701 torr. A similar operation was performed for experiment A-4-1. The pressure in A-4-1 was reduced to 450 torr as a result of withdrawal of the first gas sample. The container was then backfilled with oxygen to a total pressure of 912 torr. Because of the manifold configuration, some helium remained in the system and, as a result, the backfill gas was a mixture of helium and oxygen.

The mass spectrometric results for gas samples for the UO_2F_2 experiments are shown in Table 3.4. Two samples were withdrawn from A-5. After the first sample, the container was evacuated to about 200 torr and backfilled with a helium/oxygen mixture to a total pressure of 811 torr. A gas sample was withdrawn from A-6 at the end of the experiment.

The most significant general observation is that the hydrogen content of these gas samples is extremely low. It exceeds 1% of the total gas sample composition only in sample A-6. However, more careful evaluation of the mass spectrometric data is necessary in order to see the subtle trends that occur during the course of the radiolysis—as described in the following paragraph.

Some insight into the radiolytic effects on the samples can be gained by normalizing the measured gas composition with an inert component of the air, namely argon, that acts as an internal standard. This comparison for the UO_3 samples is shown in Table 3.5. Comparisons for selected U_3O_8 and UO_2F_2 samples are presented in Tables 3.6 and 3.7, respectively. Selected comparisons were made for these samples because, after initial gas withdrawal, the containers were evacuated and backfilled with oxygen. Table 3.8 presents the estimated change in gas composition (i.e., moles of oxygen and hydrogen formed or consumed) for selected experiments.* The standard air composition[9] was the assumed starting composition for each experiment.

*Because of the residual helium in the gas manifold, the exact composition of the gas resulting from the oxygen backfilling operation was not known. Consequently, estimates of changes in gas composition could not be made for containers that were backfilled with oxygen.

Table 3.5. Comparison of gas composition (relative to argon) for a standard air composition and for irradiated UO_3 samples

Ratio	Standard air composition[a]	A-1	A-2-1		A-2-2
			First gas sample	Second gas sample	
O_2:Ar	22.47	3.07	16.5	6.6	5.1
CO_2:Ar	0.03	0.03	0.38	0.11	0.1
N_2:Ar	83.98	276	1115	990	483
H_2:Ar	0.00005	0.007	3	4	4

[a] From *CRC Handbook of Chemistry and Physics*, 73rd ed., D. R. Lide, ed., CRC Press, Boca Raton, Florida, 1992.

Table 3.6. Comparison of gas composition (relative to argon) for a standard air composition and for selected irradiated U_3O_8 samples

Ratio	Standard air composition[a]	A-3 First gas sample	A-4-1 First gas sample
O_2:Ar	22.47	21.6	14.4
CO_2:Ar	0.03	0.08	0.03
N_2:Ar	83.98	87.6	85.9
H_2:Ar	0.00005	0.001	0.6

[a] From *CRC Handbook of Chemistry and Physics*, 73rd ed., D. R. Lide, ed., CRC Press, Boca Raton, Florida, 1992.

Table 3.7. Comparison of gas composition (relative to argon) for a standard air composition and for selected irradiated UO_2F_2 samples

Ratio	Standard air composition[a]	A-5 First gas sample	A-6
O_2:Ar	22.47	22.9	12.6
CO_2:Ar	0.03	0.14	3.8
N_2:Ar	83.98	86.9	103
H_2:Ar	0.00005	0	17

[a] From *CRC Handbook of Chemistry and Physics*, 73rd ed., D. R. Lide, ed., CRC Press, Boca Raton, Florida, 1992.

Table 3.8. Estimated change in gas composition for selected experiments as a result of radiolysis

Gas sample	ΔO_2 (mol)	ΔH_2 (mol)
A-1	-8.83×10^{-5}	1.45×10^{-8}
A-2-1 First gas sample	-5.34×10^{-5}	7.35×10^{-6}
A-2-1 Second gas sample	-1.22×10^{-5}	2.87×10^{-6}
A-2-2	-8.49×10^{-5}	5.13×10^{-6}
A-3 First gas sample	-2.01×10^{-5}	4.07×10^{-9}
A-4-1 First gas sample	-3.81×10^{-5}	2.57×10^{-6}
A-5 First gas sample	-5.06×10^{-6}	0
A-6	-5.26×10^{-5}	5.15×10^{-5}

For the UO_3 samples, the very high nitrogen content is evident by noting their nitrogen:argon ratios for all the samples, especially for sample A-2-1. It is also evident that the carbon dioxide is elevated, along with a slight amount of hydrogen. However, oxygen is depleted from all of these samples. Somewhat similarly, for U_3O_8, carbon dioxide is increased (sample A-3) and oxygen is decreased—but both to a lesser degree than in the UO_3 samples. Hydrogen is likewise only slightly increased, while there is little change in the nitrogen content (as compared to the UO_3 samples). For the UO_2F_2 samples, the only significant observations are increased carbon dioxide for both samples and some hydrogen generation and oxygen depletion for the wet sample, (A-6). Sample A-6 may also indicate a small amount of nitrogen production. The fact that neither HF nor fluorine was found is significant because these corrosive species were a concern for the long-term storage of uranium oxides that contain fluoride impurities.[3,5]

Finally, the hydrogen production for each of the wetted samples is shown in Table 3.9 by estimating the hydrogen production as a mole percentage of the available water. This table shows that only a very small amount of the water was radiolyzed to form hydrogen.

Table 3.9. Estimate of hydrogen production as a percentage of moisture on sample

Experiment	Initial H_2O content (mol)	Estimated H_2 production (mol)	Available H_2O radiolyzed (mol %)
A-2-1 (after second gas sample)	0.033	1.02×10^{-5}	0.03
A-2-2	0.033	5.13×10^{-6}	0.02
A-4-1 (after first gas sample)	0.0063	2.57×10^{-6}	0.04
A-6	0.027	5.15×10^{-5}	0.19

3.3 X-RAY DIFFRACTION RESULTS FOR U_3O_8 AND UO_3

XRD measurements were obtained for the uranium oxides before and after the alpha radiolysis experiments to determine if any measurable change in the crystalline form had occurred as a result of the radiolysis. The XRD patterns of the pure materials agreed with those reported in the literature[10–12] for the U_3O_8 and anhydrous UO_3 used in these experiments.

Realizing that 5% or more of a new crystalline phase would typically have to be present in order to be seen by XRD, an estimate of the possible extent of conversion to a new phase was made by noting the consumption of oxygen as measured in the gas analyses. Results of these estimates are presented in Table 3.10. Note that these estimates do not consider the oxidation of uranium directly by the radiolysis products of water. In some cases the estimated oxidation amounted to as much as 6%, thus giving some confidence that a new crystalline phase could, in principle, be detected under these conditions. However, limitations in length of irradiation time and the unavailability of more XRD measurements prevented a complete investigation from being made. Nevertheless, some interesting and supportive observations have resulted from these measurements.

After irradiation, the wetted samples showed a few new lines, notably at Mo ($\lambda = 0.70930$ •) 2θ values of 5.48 and 17.57 for U_3O_8 and 6.62, 10.72, and 15.77 for UO_3 as shown in Table 3.11. The dry U_3O_8 showed weak lines at 2θ values of 8.03 and 8.73, while the dry UO_3 sample gave no XRD pattern at all.

Table 3.10. Estimated mole percentage of uranium oxidized by oxygen consumption

Experiment	Mol % U oxidized[a]
A-1	0.7
A-2-1	0.6
A-2-2	0.8
A-3	6
A-4-1	0.5

[a] Does not consider possible oxidation by-products from the radiolysis of water.

Table 3.11. X-ray diffraction data for uranium oxides[a]

U_3O_8		UO_3	
Unirradiated	A-4-1 after irradiation	Unirradiated	A-2-2 after irradiation
	5.48 m		6.62 s
6.57 w		8.03 s	7.97 s
9.87 s	9.82 s	9.33 w	9.42 w
11.87 m	12.02 s		10.72 w
12.57 w	12.72 w	11.58 vs	11.82 vs
15.57 s	15.52 s	12.48 vw	12.67 m
	16.67 vvw	14.33 m	14.12 m
	17.57 m		15.77 m
19.77 w	19.77 w	16.18 m	16.32 m
20.22 w	20.22 vw	19.08 w	18.87 w
21.15 w	20.82 w		19.72 w
23.12 s	23.17 s	20.68 m	20.57 m
24.07 vw	23.97 w	22.03 vw	22.82 w
	24.92 vw	23.53 w	23.72 w
25.87 vvw	25.97 w		
	26.92 vvw		
28.72 w	28.87 w		
	29.77 w		
	30.52 w		
31.17 vw	31.37 vw		
32.17 w	32.22 w		

[a] The 2θ values given are for MoKα radiation; the wavelength is 0.70930 • ; Intensities are denoted by the following: s = strong; m = medium; w = weak. The addition of the prefix "v" indicates "very."

4. DISCUSSION

In order to assess the effects of long-term self-irradiation by radioactive materials such as $^{232}U/^{233}U$ on a time scale that is reasonable in the laboratory, it is necessary to irradiate surrogate samples to equivalent doses but at a necessarily higher dose rate. Considering the higher dose rate supplied by the ^{244}Cm, the doses achieved correspond to more than 50 years of irradiation with a $^{233}U/^{232}U$ source, thus achieving the desired result of equivalent long-term irradiation exposure.

4.1 UO_3

Examination of Figs. 3.1–3.3 shows a net pressure increase for each of the samples. This increase is consistent with the presence of trace nitrate ion in the samples that is radiolyzed in addition to the uranium oxide and/or water that might be on the sample. In the case of the anhydrous UO_3 sample (A-1, Fig. 3.1), the pressure was seen to initially decrease and then slowly increase. The gas sample taken from A-1 (see Tables 3.2 and 3.5) revealed that nitrogen was produced and oxygen was consumed. Furthermore, it is apparent that some trace water, either as hydrate or adsorbed moisture, is radiolyzed along with the nitrate impurity, as confirmed by the presence of trace hydrogen in the gas sample. However, any oxygen produced is also consumed. It appears then that the initial pressure increase is a result of nitrogen generation, while the overall pressure decrease results from oxygen consumption.

A much more dramatic pressure rise was seen for sample A-2-1, which consisted of UO_3 with 10 wt % H_2O added (Fig. 3.2). For this sample, the pressure quickly rose to about 4750 torr and then slowly decreased as it appears a steady state was approached. After taking two gas samples of A-2-1, which resulted in a net decrease of the system pressure, the pressure appeared to rise very slowly towards a new plateau.

The gas analysis for the samples withdrawn from A-2-1 (Tables 3.2 and 3.5) clearly shows that nitrogen was produced and oxygen consumed. Only a small amount (<1 vol %) of hydrogen was produced. Hence, again it is seen that the initial rise in pressure results from nitrogen production, while the decrease from the peak is probably due to oxygen consumption. Ultimately, this combination of mechanisms approaches a steady-state value.

The results of more thorough rinsing of the sample to remove nitrate ion produced a situation in which much less nitrogen was generated, although such production was not completely eliminated. Consequently, a much lower overall steady-state pressure was achieved after irradiation of this material. The curve profile for this sample, A-2-2 (Fig. 3.3), is more typical of all the wet uranium oxide samples

(UO_3, U_3O_8, and UO_2F_2), where there is an initial rise in pressure followed by a steady decrease to a lower limiting value.

These results are interpreted as the combination of multiple mechanisms taking place in the system. First, water and nitrate are radiolyzed by energy transfer through the uranium/curium oxide lattice to form some oxygen, hydrogen, and nitrogen. The oxygen comes from both nitrate and water radiolysis. These gaseous components would eventually reach a steady state without a peaking and subsequent decrease of the pressure were it not for the advent of yet another mechanism—a process in which one of the components was consumed, namely oxygen. However, this reaction now occurs at a slower rate. This additional chemical mechanism will be described in greater detail following the discussion of the other uranium oxides.

4.2 U_3O_8

Figures 3.4 and 3.5 exhibit an overall pressure decrease with increasing dose. For the dry U_3O_8 sample (A-3, Fig. 3.4), the pressure decreases immediately upon initiation of the experiment and reaches a steady-state value. After the first gas sample, container A-3 was backfilled with a mixture of air and helium. The pressure again decreased to a steady-state value. After a second gas sample was withdrawn, container A-3 was once again pressurized—this time to a much higher pressure—with oxygen (and some residual helium). The pressure in A-3 again decreased and was approaching a steady state when a final gas sample was withdrawn and the experiment terminated. The first gas sample for A-3 (Tables 3.3, 3.6, and 3.8) shows slight evidence of oxygen consumption. However, the second and third gas samples from A-3 (Table 3.3) provide clear evidence of oxygen consumption.

The U_3O_8 sample that was loaded with 2 wt % water (A-4-1, Fig. 3.5) exhibited an initial pressure increase to a peak of about 920 torr and then a decrease to a steady-state pressure. A gas sample was withdrawn and the tube was repressurized with an oxygen/helium mixture. The pressure then decreased again to a steady-state value. A final gas sample was withdrawn at the conclusion of the experiment. The gas analysis (Tables 3.3, 3.6, and 3.8) shows that oxygen was depleted while some hydrogen was produced. The estimated hydrogen production at steady state (Table 3.8) cannot account for the entire pressure rise observed. However, it is likely that the rise is the result of the initial radiolysis of water—producing hydrogen and oxygen. Then back reactions (i.e., recombination of hydrogen and oxygen, and the other, slower oxygen consumption mechanism) result in the overall pressure decrease.

The second gas sample for experiment A-4-1 showed that almost all of the oxygen was consumed. Based on the small pressure change after the first gas sample, it is evident that the backfill gas was primarily helium with little oxygen.

Once again an initial increase in pressure occurs for a wet sample followed by a net pressure decrease and consumption of oxygen. For the corresponding dry sample, there is simply the consumption of oxygen with associated pressure decrease.

4.3 UO_2F_2

Figure 3.6 shows the pressure response for the alpha radiolysis of anhydrous UO_2F_2 (A-5). The pressure decreased to a steady state, at which point a gas sample was taken. The tube was evacuated to about 200 torr and was then backfilled with an oxygen/helium mixture. The pressure then slowly decreased and appears to approach a steady state again. A final gas sample was taken at the termination of experiment A-5. The analysis of the first gas sample from A-5 (Tables 3.4, 3.7, and 3.8) shows that a small amount of oxygen was consumed. The second gas sample (Table 3.4) showed consumption of the added oxygen. Neither HF nor fluorine was reported. Note that production of these corrosive species was a concern for the long-term storage of uranium oxides containing fluoride impurities.[3,5] The fact that none were found further demonstrates that these concerns were unwarranted.

The pressure response for the alpha radiolysis of $UO_2F_2 \cdot 1.7H_2O$ (A-6) presented in Figure 3.7 again exhibits an initial pressure increase followed by an overall pressure decrease similar to that for the other wet oxides. The gas analysis of the sample taken at the end of the experiment (Tables 3.4, 3.7, and 3.8) shows that oxygen was consumed while CO_2 and hydrogen were produced. Neither fluorine nor HF was seen in the gas analyses. The results for the alpha irradiation of UO_2F_2 are in sharp contrast to those seen for gamma irradiation,[3,5] where oxygen was found to be released from the UO_2F_2 matrix. Therefore, the type of radiation (alpha vs gamma) appears to play a significant role in the net radiolytic effect. Additionally, as shown in Ref. 3, the source of some of the hydrogen for moist UO_2F_2 was corrosion of the sample container. In a similar fashion, corrosion may also play some role in the production of hydrogen in the alpha radiolysis experiments.

4.4 X-RAY DIFFRACTION

The appearance of CO_2 in each of the samples might appear anomalous were it not for the realization that carbon is almost always present in sample preparations and yet goes undetected. When there is a source of oxygen and some means to oxidize the carbon (through elevated temperature or radiolysis), the carbon will combine with the oxygen and appear as CO_2. However, the amount of CO_2 is insufficient to account for all of the loss of oxygen seen in these experiments. Therefore, another mechanism for oxygen consumption must be present.

One such mechanism is through the oxidation of the uranium compound itself. Even in the radiation environment, this process would occur at a much slower rate since it is a gas–solid reaction and requires the diffusion of oxygen within the crystalline lattice. In order to establish such a mechanism, the XRD analyses were performed in a effort to identify a higher oxidation state of the uranium itself or an oxidized form of the uranium oxide compound.

Some additional lines were identified as a result of the XRD analysis. These, however, were insufficient to clearly establish oxidation in the current cases. Nevertheless, by comparison of these results with similar observations in the literature, it is apparent that the U_3O_8 form is oxidized to UO_3 while the UO_3 hydrate form is converted to a uranium peroxide. The production of uranium peroxide is most likely to occur in the wet samples where the hydroxyl radical is produced.

The line at 2θ of 5.48 for the irradiated U_3O_8 sample is typical of that for numerous uranyl oxide hydrates, namely the mono- and dihydrates.[12–14] Except for the line at 17.57, an insufficient number of additional lines exist to clearly identify this new crystalline phase by XRD. However, the data do indicate that the effect of radiation was to generate a new crystalline phase with the major XRD line that is consistent with a uranium oxide of higher oxidation state.

In a similar vein, the appearance of new lines after irradiation of wetted UO_3 indicates that it, too, has undergone some phase change as a result of alpha irradiation. In view of the consumption of oxygen (seen from the pressure decrease and gas analyses), we would suggest that some oxidation of the UO_3 has also occurred. Higher oxidation states than VI for uranium are not known, but peroxide forms of uranyl such as studtite and metastudtite have been reported in the literature.[15–17] These particular crystalline materials would have the formulae of $UO_3 \cdot H_2O_2 \cdot xH_2O$ (where x is either 2 or 4, corresponding to metastudtite and studtite, respectively) and are sometimes written as $UO_4 \cdot xH_2O$. The most intense lines in the XRD patterns for these studtites would be at 2θ values (MoKα radiation) of 7.94. Unfortunately, this line would appear on top of the strong line for anhydrous UO_3 at 8.03, thus precluding any firm evidence for the appearance of the peroxide form. However, by comparison with the U_3O_8 material, it would be consistent to interpret these results as suggesting that the UO_3 has undergone similar oxidation to form a crystalline peroxide species of U(VI).

Such oxidation has already been reported in the literature for much higher alpha irradiation fluxes from a cyclotron.[18] In this study, a UO_2 target in contact with leachant water was irradiated with alpha particles with fluxes up to 3.3×10^{11} α cm^{-2} s^{-1} . Post-irradiation examination of the UO_2 surface that had been in contact with the leachant water revealed the presence of extra lines attributed to metastudtite (i.e., hydrated uranium peroxide). In our case, the alpha flux at the surface of the particles of surface area = ~1 m^2/g is 7.5×10^6 α cm^{-2} s^{-1}. However, the exposure time in our experiments was of the order of 1 year compared with the 1-h exposure in the previous cyclotron experiment. The overall dose in our experiments is then up to 10 times less than that of the previous work.

While our results were consistent with those obtained in the previous work, it is not surprising that XRD lines of sufficient intensity were not obtained for definitive conclusions. Nevertheless, the formation of a uranium peroxide in the alpha irradiation of wet UO_3 is a plausible explanation for the results obtained. Furthermore, other authors have recently suggested that peroxide, formed by radiolysis, is incorporated into the uranium oxide matrix to form either studtite or metastudtite.[19]

Insufficient data were available to suggest an identity of the phase producing extra lines found as a result of the dry U_3O_8 radiolysis experiment. The conversion of the dry UO_3 to amorphous material suggests a phenomenon like that seen for other crystalline oxides[20] exposed to the effects of alpha irradiation. Such a metamict form is yet another possible result of irradiation and probably dependent on the absence of water in the sample.

4.5 SUMMARY

The overall mechanism observed in all of these oxide radiolysis experiments is one of several competing reactions. First, nitrate (if present) and water are radiolyzed to some extent at relatively rapid rates. These initial reactions account for the pressure spike in the wet and/or nitrate-containing samples. The water radiolysis, however, reaches a point at which back reactions of the radiolytic products, hydrogen and oxygen, reform the water by well-established radiolytic back-reaction mechanisms.[21,22] Occurring at a much slower rate is the consumption of oxygen through the uranium oxide oxidation process, producing the oxidized forms identified by other researchers and indicated here.

The alpha radiolysis of uranium oxides can be described in general for wet oxides as a modest pressure rise due to the water radiolysis followed by a net pressure decrease due to the oxidation of the uranium oxide form. If the oxide is dry, no initial pressure rise occurs. Only a steady decrease of the pressure (assuming oxygen is present) is noted as the uranium oxide is further oxidized.

The net result of this overall mechanism is that the pressure over these uranium oxides reaches a steady-state value, where the consumption of the radiolysis products is matched by their production. Except for the case in which there is a high level of residual nitrates, this steady-state pressure is unusually low—and, in many cases, less than the initial pressure of the system.* Furthermore, the concentration of hydrogen is negligible due to its recombination. Consequently, with the occurrence of numerous back reactions, there is no opportunity for the accumulation of hydrogen, or the overall pressure of the system, to build to intolerable limits.

---

* It is evident that efforts to remove nitrates by thermal decomposition are important. The production of U_3O_8 at reasonably high temperatures (400–600°C) will eliminate nitrates.

An interesting comparison can be drawn by considering the maximum hydrogen pressure that could be achieved by radiolyzing all of the available water and the actual measured hydrogen pressure. The former, of course, is the conservative approach taken in storage standards. For example, total decomposition of all available water for sample A-2-1 would result in a hydrogen pressure of about 53,000 torr (~1000 psi). The total measured pressure for A-2-1 at steady state was about 4600 torr—a pressure increase due to nitrogen production (Table 3.2). Significantly, the hydrogen contribution to this pressure was only a small fraction (~0.24%) of the total pressure. Similar comparisons can be made for the U_3O_8 (A-4-1) and $UO_2F_2 \cdot 1.7H_2O$ (A-6), where total decomposition of the water would result in hydrogen pressures of about 10,000 torr (200 psi) and 45,000 torr (870 psi), respectively. Therefore, it is obvious from the experimental results that high pressures are not reached. In fact, both of these experiments exhibited a net pressure decrease, indicating that back reactions clearly play a strong role in limiting (or eliminating) the pressure increase from radiolysis.

5. CONCLUSIONS

The alpha radiolysis of uranium oxides has shown that several competing reactions are caused by the radioactive environment. These combine to produce pressure changes in closed containers holding these oxides that depend on the constituents in the atmosphere over the oxides and the presence of water or other impurities on the sample. However, none of these reactions produce excessively high pressures as predicted by the pedestrian assumption that any water associated with the samples will be converted entirely to hydrogen and oxygen. Instead, a steady-state pressure is reached at which back reactions quickly limit the accumulation of reaction products in the gas phase. Hydrogen is especially low as a result of radiolysis. Some oxidation of these oxides is possible if oxygen and/or hydroxyl radicals are present. Nevertheless, this oxidation process tends to function as yet another limiting "back reaction" to prevent the occurrence of excessive pressures in the system.

These results, combined with those from the earlier gamma radiolysis experiments, form the basis for resolving technical issues regarding the safe, long-term storage of these oxides and show that extraordinary measures are not required to remove all traces of moisture from the oxide.

ACKNOWLEDGMENTS

We are grateful to Dr. R. G. Haire of ORNL for the performance of the XRD analysis and his helpful advice. We also acknowledge the highly skilled assistance of C. E. Porter, R. D. Vandergrift, and L. K. Felker in the preparation and conduct of the experiments.

REFERENCES

1. *Criteria for Preparing and Packaging Plutonium Metals and Oxides for Long-term Storage*, DOE-STD-3013, U.S. Department of Energy, Washington, D.C.

2. *Criteria for Packaging and Storing Uranium-233-Bearing Materials*, DOE-STD-3028-2000, U.S. Department of Energy, Washington, D.C.

3. A. S. Icenhour, L. M. Toth, G. D. Del Cul, and L. F. Miller, "Gamma Radiolysis Studies of Uranyl Fluoride," *Radiochim. Acta* **90** (2), 109–22 (2002).

4. A. S. Icenhour, L. M. Toth, and H. Luo, *Water Sorption and Radiolysis Studies for Uranium Oxides*, ORNL/TM-2001/59, Oak Ridge National Laboratory, Oak Ridge, Tennessee, February 2002.

5. A. S. Icenhour and L. M. Toth, *A Gamma Radiolysis Study of $UO_2F_2 \cdot 0.4H_2O$ Using Spent Nuclear Fuel Elements from the High Flux Isotope Reactor*, ORNL/TM-2001/138, Oak Ridge National Laboratory, Oak Ridge, Tennessee, January 2002.

6. R. R. Livingston, *Gas Generation Test Support for Transportation and Storage of Plutonium Residue Materials*, WSRC-TR-99-00223, Westinghouse Savannah River Company, Savannah River Site, Aiken, South Carolina, August 1999.

7. R. R. Livingston and J. M. Duffey, *Effects of Plutonium Dioxide Moisture Content and Calcination Temperature on the Headspace Gas Composition of Sealed Containers*, WSRC-TR-2001-00420, Westinghouse Savannah River Company, Savannah River Site, Aiken, South Carolina, September 2001.

8. G. Bailey et al., *Gas Generation from Actinide Oxide Materials*, LA-13781-MS, Los Alamos National Laboratory, Los Alamos, New Mexico, December 2000.

9. *CRC Handbook of Chemistry and Physics*, 73rd ed., D. R. Lide, ed., CRC Press, Boca Raton, Florida, 1992.

10. S. Siegel, "The Crystal Structure of Trigonal U_3O_8,"*Acta Crystallogr.* **8**, 617–19 (1955).

11. K. Aykan and A. W. Sleight, "Characterization of Mixed Uranium Antimony Oxides $USbO_5$ and USb_3O_{10}," *J. Am. Ceram. Soc.* **53**, 427–31 (1970).

12. J. K. Dawson, E. Wait, K. Alcock, and D. R. Chilton, "Some Aspects of the System Uranium Trioxide–Water," *J. Chem. Soc.* **Part III**, 3531–40 (1956)

13. C. A. Wamser, J. Belle, E. Bernsohn, and B. Williamson, "The Constitution of the Uranates of Sodium," *J. Am. Chem. Soc.* **74**, 1020–22 (1952).

14. H. Dunn, *X-Ray Diffraction Data for Some Uranium Compounds*, ORNL-2092, Oak Ridge National Laboratory, Oak Ridge, Tennessee, August 1956

15. K. Walenta, "On Studtite and its Composition," *Am. Mineral.*, **59**, 166–71 (1974).

16. M. Deliens and P. Piret, "Metastudtite, $UO_4 \cdot 2H_2O$, a New Mineral from Shinkolobwe, Shaba, Zaire," *Am. Mineral.*, **68**, 456–58 (1983).

17. P. C. Debets, "X-ray Diffraction Data on Hydrated Uranium Peroxide," *J. Inorg. Nucl. Chem.*, **25**, 727–30 (1963).

18. G. Sattonnay et al., "Alpha-radiolysis Effects on UO_2 Alteration in Water," *J. Nucl. Mater.* **288**, 11–19 (2001).

19. P. C. Burns and K. Hughes, "Studtite $[(UO_2)(O_2)(H_2O)_2](H_2O)_2$: The First Structure of a Peroxide Mineral," *Am. Mineral*, **88**, 1165–68 (2003).

20. Hj. Matzke, "Radiation Damage in Crystalline Insulators, Oxides, and Ceramic Nuclear Fuels," *Radiat. Eff.* **64**, 3–33 (1982).

21. C. J. Hochanadel, "Effects of Cobalt Gamma-Radiation on Water and Aqueous Solutions," *J. Phys. Chem.* **56**(5), 587–94 (1952).

22. A. O. Allen, C. J. Hochanadel, J. A. Ghormley, and T. W. Davis, "Decomposition of Water and Aqueous Solutions Under Mixed Fast Neutron and Gamma Radiation," *J. Phys. Chem.* **56**(5), 575–86 (1952).

INTERNAL DISTRIBUTION

1. J. M. Begovich
2. P. J. Bereolos
3. W. D. Bond
4. T. B. Conley
5. G. D. Del Cul
6. D. Foster
7. J. N. Herndon
8. D. J. Hill
9–19. A. S. Icenhour
20. A. M. Krichinsky
21. S. C. Marschman
22. P. E. Osborne
23. F. J. Peretz
24. J. E. Rushton
25. D. W. Simmons
26–30. L. M. Toth
31. L. D. Trowbridge
32. R. M. Wham
33. D. F. Williams
34. ORNL OTIC–RC
35. NSTD DMC

EXTERNAL DISTRIBUTION

36. N. M. Askew, U.S. Department of Energy, Savannah River Site Operations Office, WSRC, Bldg. 773-A, Road 1A, Aiken, SC 29801
37. L. F. Blankner, U.S. Department of Energy, Oak Ridge Operations Office, Oak Ridge National Laboratory, UT-Battelle, Bethel Valley Road, Oak Ridge, TN 37831-6269
38. H. E. Clark, U.S. Department of Energy, Oak Ridge Operations Office, Oak Ridge National Laboratory, UT-Battelle, Bethel Valley Road, Oak Ridge, TN 37831-6269
39. C. H. Delegard, Pacific Northwest National Laboratory, 902 Battelle Blvd., P.O. Box 999, Richland, WA 99352
40. J. M. Duffey, U.S. Department of Energy, Savannah River Site Operations Office, WSRC, Bldg. 773-A, Road 1A, Aiken, SC 29801
41. P. G. Eller, U.S. Department of Energy, Los Alamos National Laboratory, P.O. Box 1663, Los Alamos, NM 87545
42. H. C. Johnson, U.S. Department of Energy, Headquarters, EM-21, Forrestal Bldg., 1000 Independence Ave. S.W., Washington, D.C. 20585
43. R. R. Livingston, U.S. Department of Energy, Savannah River Site Operations Office, WSRC, Bldg. 773-A, Road 1A, Aiken, SC 29801
44. R. E. Mason, U.S. Department of Energy, Los Alamos National Laboratory, P.O. Box 1663, Los Alamos, NM, 87545
45. L. Morales, U.S. Department of Energy, Los Alamos National Laboratory, P.O. Box 1663, Los Alamos, NM, 87545
46. M. T. Paffett, U.S. Department of Energy, Los Alamos National Laboratory, P.O. Box 1663, Los Alamos, NM, 87545
47. G. D. Roberson, U.S. Department of Energy, Albuquerque Operations Office, Bldg. 382-2, AL, Pennsylvania and H Street, Kirkland Air Force Base, Albuquerque, NM 87116
48. L. A. Worl, U.S. Department of Energy, Los Alamos National Laboratory, P.O. Box 1663, Los Alamos, NM 87545

WSRC-TR-2007-00200

Keywords: Radiolysis,
Hydrogen

Evaluation of Radiolysis-Induced Hydrogen Generation in DOT 6M Drums from INTEC

Savannah River National Laboratory
Materials Science and Technology

Publication Date: June 2007

Washington Savannah River Company
Savannah River Site
Aiken, SC 29808

This document was prepared in connection with work done under Contract No. DE-AC09-96SR18500 with the U. S. Department of Energy

DISCLAIMER

DOCUMENT: **WSRC-TR-2007-00200**

TITLE: **Evaluation of Radiolysis-Induced Hydrogen Generation in DOT 6M Drums from INTEC**

APPROVALS

_____ **Date:** _____
D. W. Vinson, Author
SRNL-Materials Science and Technology

_____ **Date:** _____
N. E. Bibler, Technical Review
SRNL-Process Science and Engineering Section

_____ **Date:** _____
N. M. Askew, Technical Review
SRNL-Actinide Sciences Programs

_____ **Date:** _____
R. L. Sindelar, Manager
SRNL-Materials Science and Technology

_____ **Date:** _____
N. C. Iyer, Director
SRNL-Materials Science and Technology

_____ **Date:** _____
J. Bodkin, Customer
SFP-SFP Operations Engineering

_____ **Date:** _____
T. J. Spieker, Manager
SFP-SFP Operations Engineering

_____ **Date:** _____
R. W. Watkins
HMD-HB-Line Ph II Engineering

Table of Contents

List of Tables

List of Figures

1.0 EXECUTIVE SUMMARY

Three DOT 6M 30-gallon drums are scheduled to be shipped from the Idaho Nuclear Technology Engineering Center (INTEC) at the Idaho National Laboratory (INL) to L-Area at the Savannah River Site (SRS). These three drums contain radioactive materials that resulted from the material recovery effort following a small explosion that had occurred in the Idaho Chemical Processing Plant (ICPP) hot chemistry laboratory (HCL). In support of the shipment and subsequent storage of the three DOT 6M drums, an evaluation of the potential for molecular hydrogen production in the drums has been completed and documented herein. The potential sources of hydrogen evaluated in the current report include radiolytic decomposition of polymeric materials in the DOT 6M drums #3031 and #3598 and the radiolytic decomposition of water in drum #20102. No other potential sources have been identified based upon reported drum contents and packaging configuration.[1-2]

A parametric approach was used to evaluate the maximum quantity of molecular hydrogen that can be expected to evolve in two DOT 6M 30-gallon drums in support of receipt and subsequent interim storage prior to canyon processing. These drums are two of three drums scheduled for shipment from INTEC to SRS as part of the decommissioning effort of the INTEC facility. The three DOT 6M drums will be received at L-Area in SRS and stored for up to 13-years prior to final disposition at HB-Line in 2020. Results of the current analysis do not include parametric analysis of drum #20102 containing 114/133 SAL (salvage) which contains UO_3 powder. This drum has not been identified as containing polymeric materials and a conservative calculation indicates that the maximum gross molecular hydrogen production due to the radiolysis of adsorbed moisture would yield a production rate of 5.1-cm^3/yr, driven primarily by the large surface are to volume ratio of the oxide powder. The remaining two drums, #3031 and #3598 contain polymer bags and/or bottles that will be subject to radiolytically induced hydrogen gas generation due to decomposition of the polymers. Conservative values for hydrogen gas generation rates and rates of pressure increase within the drums have been determined based upon a number of inputs and assumptions. The results are that hydrogen will be produced at a rate of 1.93-cm^3/yr and 1.50-cm^3/yr, respectively for drums #3031 and #3598. Projected molecular hydrogen concentrations at 2020 have been calculated to remain below the lower flammability limit of 4% molecular hydrogen by volume in air.

2.0 INTRODUCTION

Three DOT 6M 30-gallon drums are planned to be shipped from the Idaho Nuclear Technology Engineering Center (INTEC) at the Idaho National Laboratory (INL) to L-Area at the Savannah River Site (SRS). These three drums contain radioactive materials that resulted from the material recovery effort following a small explosion that had occurred in the Idaho Chemical Processing Plant (ICPP) hot chemistry laboratory (HCL). The three DOT 6M drums would be received at L-Area in SRS and stored for up to 13-years prior to final disposition at HB-Line by 2020. In support of the shipment and subsequent storage of the three DOT 6M drums, an evaluation of the potential for molecular hydrogen production in the drums due to the radiolytic decomposition of the polymer bottles in drums #3031 and #3598 and due to radiolytic decomposition of water reported in drum #202102 has been completed and documented herein.

3.0 MATERIALS DESCRIPTION

Three DOT 6M 30-gallon drums are planned to be shipped from the Idaho Nuclear Technology Engineering Center to the Savannah River Site. The debris in each drum has been carefully characterized by personnel at the ICPP HCL.[3] Two of the three DOT 6M 30-gallon drums from INTEC, #3031 and #3598, contain a variety of materials that are characterized as quarter circles, pins, pellets, foils, wires, chips, turnings, and small filings/specks. The two largest pieces that are roughly shaped as quarter circles with a 5-cm radius and that are two centimeters thick are contained in drum #3598. They are

characterized as 4.5 wt % uranium fissium alloy which are contaminated with ^{239}Pu (200-400 ppm).[2] These two pieces are located in areas 7 and 14 of Figure 1. Figure 2 provides a graphical depiction of loading of the two 30 gallon DOT 6M drums. In drum #3598, the two quarter circles are each within a low-density polyethylene bag and the two bags within a 500-ml high-density polyethylene (HDPE) bottle. The HDPE bottle is closed with a screw cap and placed within a crimp-sealed tin can, HCL-2, that is placed inside the sealed 2R container within the DOT 6M 30-gallon drum. The can contains 1,190 grams of total uranium of which 617 grams are ^{235}U.

Drum #3031 contains the remaining metallic pieces shown in the photograph of Figure 1. These pieces are counted as 45 pins, 19 pellets, 7 foils, 4 wires, 3 chips, 131 turnings, and 1083 small filings/specks. These pieces are contained within a 500-ml HDPE bottle that is contained in a crimp-sealed tin can, HCL-1 that is sealed in the 2R container within the DOT 6M 30-gallon drum (see Figure 2). All of the pellets and chips and a majority of pins, foils, and small filing/specks are described as uranium fissium alloy low in zirconium. The uranium fissium alloy is 3.5 or 4.5 wt % fissium. The remaining material in this can consists of a small number of pins, foils, and small filing/specks that consist of a uranium alloy high in zirconium. Also stored in the can as foils, wires, turning, wire, and small filings/specks is a small quantity (gram amounts) of metal: Inconel, stainless steel (304), thorium, and nickel alloy. The material is contaminated with ^{239}Pu (200-400 ppm). The can, HCL-1, contains 290 grams of total uranium of which 255 grams are ^{235}U.

The third DOT 6M 30-gallon drum is labeled #20102 and contains material described as soil samples. The soil sample material is characterized as UO_3 granular powder, a high-grade uranium oxide product obtained from reprocessing fuel and scrap material at INTEC.[1] The material is comprised of 29 grams of total uranium, of which 26 grams are ^{235}U. In addition, this drum is reported to contain 0.45-g of water due to the hygroscopic nature of the uranium-oxide. This material is contained within the crimp sealed tin can 114/133 SAL shown in Figure 4 that is within the 2R inside the DOT 6M 30-gallon drum as depicted in Figure 3.

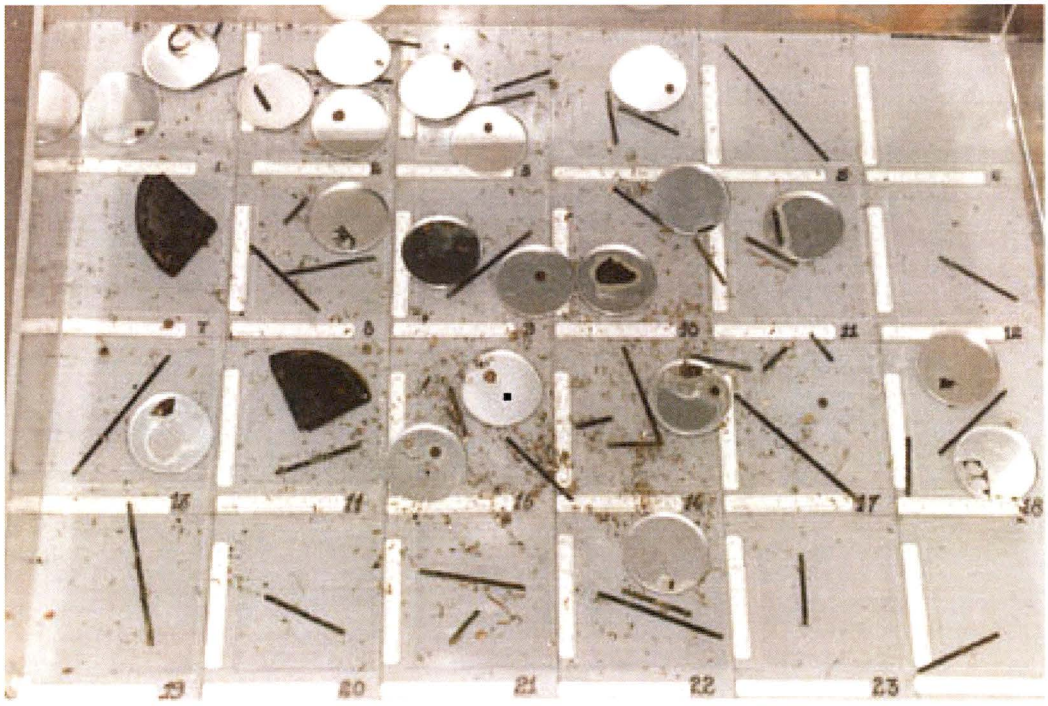

Figure 1 Photograph of the recovered metallic pieces recovered from ICPP HCL.

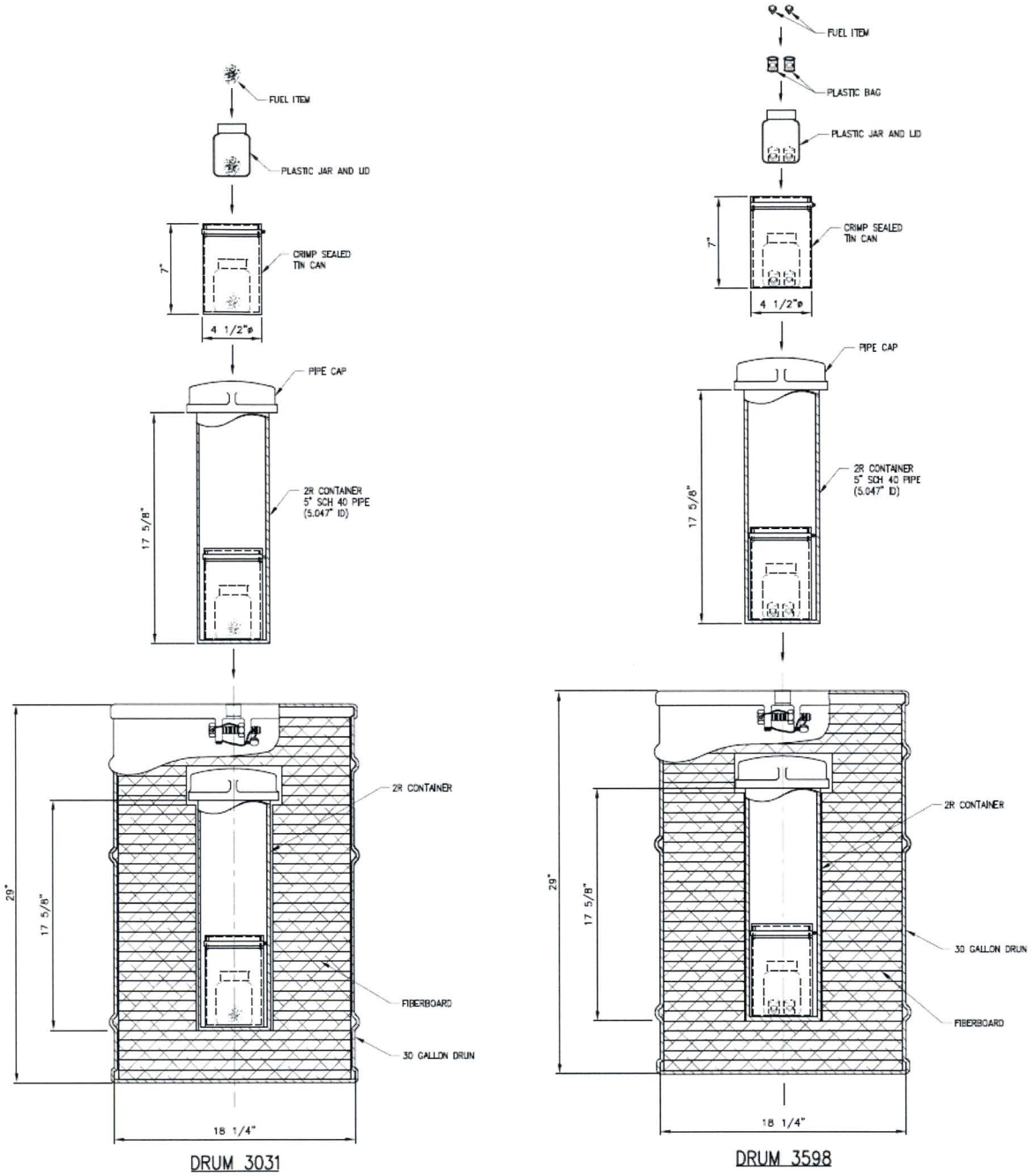

Figure 2 Schematic representation of the packaging configuration for DOT 6M 30-gallon drums #3031 (Left) and #3598 (Right).

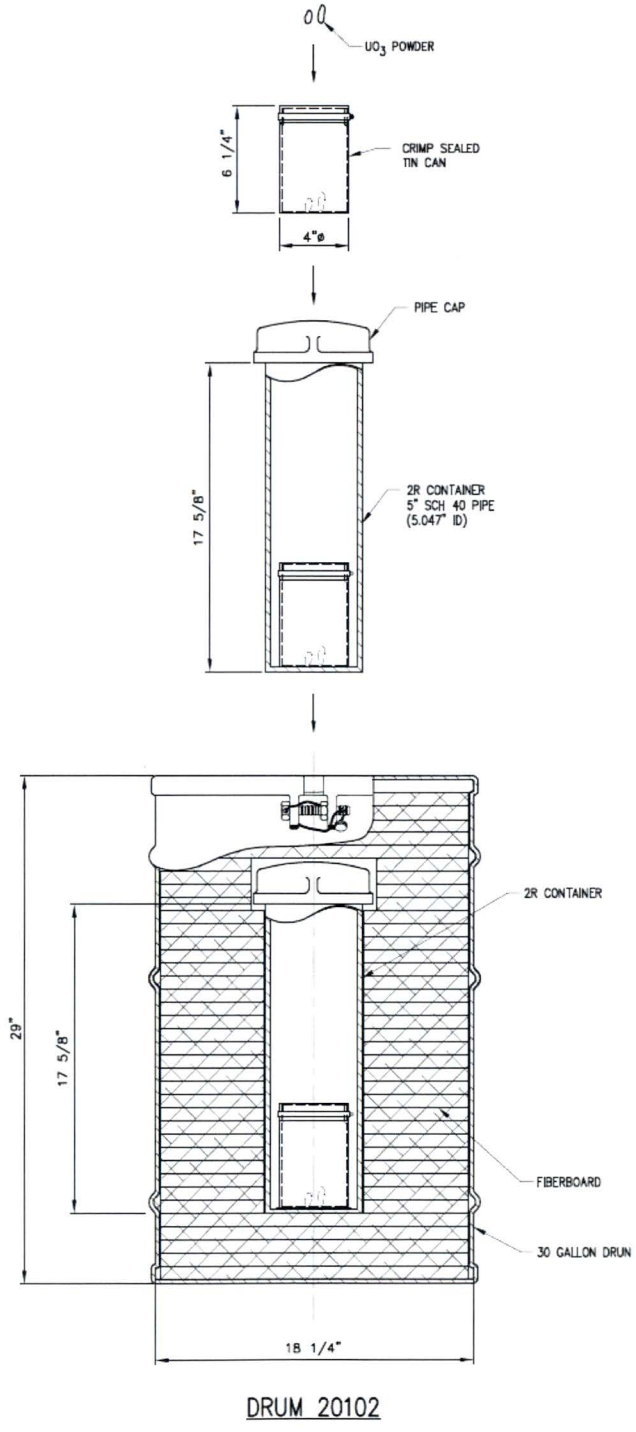

Figure 3 Schematic representation of the packaging configuration for DOT 6M 30-gallon drum #20102.

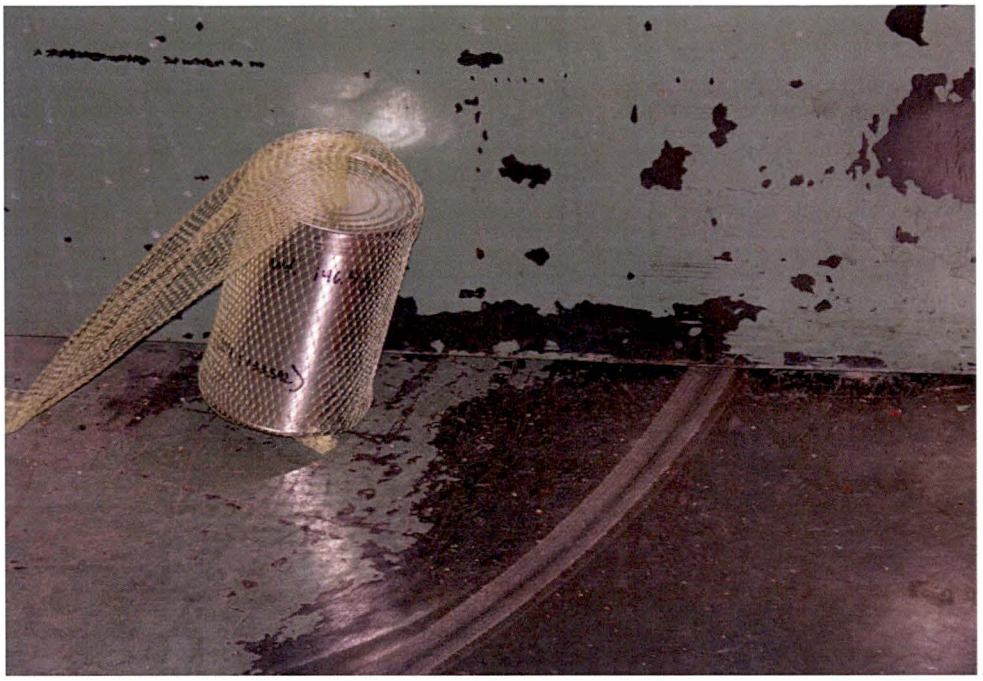

Figure 4 Photograph of the crimp-sealed tin can (114/133 SAL) that is stored in a 2R container within the DOT 6M 30-gallon drum #20102.

Table 1 Summary of the Uranium-Fissium Debris Contained in Three DOT 6M 30-gallon Drums

Can/Drum	Description	Form	Total U (g)	Total Pu (g)
HCL-1 #3031	Uranium-Fissium (3.5-4.5%)	45 pins, 19 pellets, 7 foils, 4 wires, 3 chips, 131 turnings, 1083 filings/specks	290	0.12
HCL-2 #3598	Uranium-Fissium (3.5-4.5%)	2 large quarter round chunks	1,190	0.48
114/133 SAL #20102	High-Grade UO_3 Powder	UO_3 Granular Powder	29	0

4.0 CALCULATIONAL APPROACH AND METHODOLOGY

The potential sources of hydrogen evaluated in the current report include radiolytic decomposition of polymeric materials in the DOT 6M drums #3031 and #3598 and the radiolytic decomposition of water in drum #20102. No other potential sources have been identified based upon reported drum contents and packaging configuration.[1-2]

Ionizing radiation causes radiolytic decomposition of polymers. The decomposition of polymers lead to the production of molecular hydrogen. The general approach used to develop an estimate of the potential for molecular hydrogen generation due to alpha radiolysis of polymers follows the approached used by Croft Associates for the SAFKEG package[4]. The rate of production of H_2 from decomposition of polymeric material in units of cm^3/sec (V_g) can be generally expressed as:

$$V_g = \left(D \times G \times k \times v / A_n \right) \quad \text{(Eq. 1)}$$

where: D = alpha energy absorbed in the polymer (Watts),
G = hydrogen gas generation constant (Molecules/MeV)
k = conversion factor (6.24e12 Mev/J),
v = volume of 1 mole of gas at STP (2.24e4 cm^3), and
A_n = Avogadro's number (6.022e23 molecules).

For the current work, the alpha energy absorbed in the polymer, D, and the value of the hydrogen gas generation constant, G, are the two unknowns in Eq. 1. For the determination of D, it is necessary to determine the range of alpha particles in the various materials. The energy and material dependant range of an alpha particle in cm (R) is determined by the equation:[5-6]

$$R = 2.3 \times 10^{-4} \left(\frac{\sqrt{M}}{\rho} \right) \left(1.24 E_\alpha - 2.62 \right) \quad \text{(Eq. 2)}$$

where: M = molecular weight of the medium (AMU),
ρ = density of the medium (g/cm^3), and
E_α = average alpha energy(MeV).

For the current work, the molecular weight and density of the medium and the average alpha energy are the three unknowns in Eq. 2. Having determined the volume of molecular hydrogen produced using Eq. 1, it is then possible to determine the pressure rise within the package as a function of time ($P_r(t)$) by the equation:[4]

$$P_r(t) = \left(P_a \times V_g \times t / V_c \right) \quad \text{(Eq. 3)}$$

where: P_a = ambient pressure (1.0 bar abs),
t = time (secs), and
V_c = free volume of container (cm^3).

For the current work, the time, t, and free volume of the container, V_c are the two unknowns in Eq. 3. The next section of the report addresses the assumptions, methodology, and calculations used to develop a conservative estimate of the expected molecular hydrogen production due to the contents of the drums as described in the previous section.

4.1 List of Assumptions

1. The value of the hydrogen gas generation constant (G-value) is assumed equal 3.5 molecules/100 eV or 3.5×10^4 molecules/MeV. This value of G is taken from Reference 7 as the highest reported production rate for all polymers due to radiolytic decomposition by

incident alpha radiation. This assumption is conservative because no credit is taken for the dose dependent nature of radiation damage in the polymer. Increasing the dose absorbed by a polymer will decrease the effective G-value for hydrogen production due to the depletion of the matrix in the vicinity of the alpha-emitting radioactive source particle. Dose dependent G values are reported as less than 1/5th the value assumed in the current analysis.[8]

2. The value used for the molecular weight of the material in the HDPE bottles is 242-g/mole. This number is consistent with that of plutonium. This number bounds the actual effective molecular weight of the contents of the drums, since the contents include fissium elements whose weights are generally less than 100. This assumption is conservative as alpha range increases as the square-root of the molecular weight (see Eq. 2).
3. The bottle is modeled as a right-circular cylinder with a 4-cm radius and a height of 14.2-cm. This assumption is conservative as the surface area of the modeled ~700-ml bottle is greater than that of the expected 500-ml bottle actually used.
4. It is assumed that the materials in drums #3031 and #3598 are essentially dry. Unlike the materials in drum #20102, this material is not hygroscopic in nature and water content in these drums would be mostly limited to humidity in the facility. Radiolysis of bulk water in these two drums will not provide significant molecular hydrogen production relative to the production estimated for the production due to polymeric radiolytic decomposition. The short range of the alpha particles, the conservatism introduced by Assumption 1, and the G-value of 1.7×10^4 molecules/MeV[9] for H_2 generation from alpha radiolysis of water support this assumption.
5. The average alpha energy used in Eq. 2 is assumed equal to 5.25-MeV. This value bounds the alpha particles from all isotopes identified as being in the drums per the Appendix A and supporting documentation.
6. It is assumed that the free volume of the 2R containers and the crimp-sealed tin cans in the DOT 6M 30-gallon drums is equal to 90% of their physical volume. This assumption is conservative as the contents of the tin cans are expected to occupy less than 7% of the tin can and less than 3% of the 2R containers.[3] Increasing the free volume of the containers will further decrease the estimated pressure increase with time by Eq. 3.
7. It is assumed that only 50% of the alpha particles that are produced within range of the polymer surface contribute to the energy absorbed by the polymer. This assumption accounts for the fact that an isotropic source would generate 50% of its particles in a direction that takes the particle away from the polymer surface.
8. It is assumed that the methodology employed in the current parametric evaluation of the HDPE bottles whereby the source material is assumed to completely cover the inner surface of bottle with a homogeneous layer of variable density and related alpha particle range dictated by the layer thickness and the total source material available is sound and bounding.
9. It is assumed that the bags are not present in HCL-2. This is conservative because the surface area of source material in contact with the polymer bottle is significantly increased by ignoring the plastic bags based upon the current model.
10. It is assumed that there is no polymeric material in DOT 6M 30-gallon drum #20102. There is no indication of the presence of any polymeric bags or bottles as evidenced by the loading schematic shown in Figure 3.
11. It is assumed that the bottle is not an effective barrier to hydrogen migration for the pressure rise calculations. This is reasonable due to the high permeability of molecular hydrogen through polyethylene.[10] The crimp-sealed tin can is also ignored for pressure rise calculations for the 2R.
12. The start time for hydrogen accumulation calculations for drums #3031 and 3598 is assumed equal to 1992. This is a conservative assumption based upon the date at which the HCL crimp-sealed tin cans were loaded.[3]

13. The start time for the hydrogen accumulation calculations for drum #20102 is assumed equal to 2006.[11]
14. The 0.45-g of water reported for drum #20102[1] is assumed homogeneously mixed with alpha-producing uranium within the drum. That is to say that no credit is taken for the shielding effects of the UO_3 particles themselves in the current calculation. In addition, no credit is taken for recombination or reverse reactions by which molecular hydrogen is consumed to regenerate water molecules. This is a conservative assumption.

4.2 Determination of the Absorbed Alpha Energy

4.2.1 Total Alpha Energy Production

The total production of alpha particles generated in each of the crimp-sealed tin containers is completely dependent upon contents of the tin can. References 3-1 provide a list of the radioactive isotopes and quantities contained in each of the three DOT 6M 30-gallon drums. Tables 2 & 3 provide the alpha decay energy and isotopic content by weight for the three drums. Table 2 shows the calculation to determine the power density for each of the isotopes included in the 6M's. The power density is calculated as the product of the average alpha energy per alpha particle as obtained from the ENDF-VI decay library and the activity density of isotope as obtained from 10CFR71.[12] The total alpha energy generation due to radioactive decay can then be calculated and results are shown in Table 3, where the energy generation by isotope is the product of the power density and the total grams as obtained from the Appendix A documents.[1-2]

Table 2 Summary Table of Calculations for Power Density Determination[12-13]

Isotope	E_α (MeV)	E_α J/α	Activity Density (Ci/g)	Activity Density (Bq/g)	Power Density (Watts/g)
^{234}U	4.8419	7.76×10^{-13}	6.20×10^{-3}	2.29×10^{8}	1.78×10^{-4}
^{235}U	4.4709	7.16×10^{-13}	2.20×10^{-6}	8.14×10^{4}	5.83×10^{-8}
^{236}U	4.5563	7.30×10^{-13}	6.50×10^{-5}	2.41×10^{6}	1.76×10^{-6}
^{238}U	4.2610	6.83×10^{-13}	3.40×10^{-7}	1.26×10^{4}	8.59×10^{-9}
^{239}Pu	5.2375	8.39×10^{-13}	6.20×10^{-2}	2.29×10^{9}	1.92×10^{-3}
^{240}Pu	5.2429	8.40×10^{-13}	2.30×10^{-1}	8.51×10^{9}	7.15×10^{-3}

Table 3 Summary Table of Calculations for Maximum Total Energy Generation due to Alpha Decay of Isotopes in HCL-1 and HCL-2 and 114/133 SAL

Isotope	Composition by Can/Drum†			Power Density (Watts/g)	Energy Generation by Can/Drum		
	HCL-1 #3031 (grams)	HCL-2 #3598 (grams)	114/133 SAL #20102 (grams)		HCL-1 #3031 (Watts)	HCL-2 #3598 (Watts)	114/133 SAL #20102 (Watts)
^{234}U	2.17	6.25	0.22	1.78×10^{-4}	3.86E-04	1.11E-03	3.91E-05
^{235}U	255.00	617.00	26.00	5.83×10^{-8}	1.49E-05	3.60E-05	1.52E-06
^{236}U	0.93	1.09	0.1	1.76×10^{-6}	1.63E-06	1.91E-06	1.76E-07
^{238}U	31.90	565.66	2.68	8.59×10^{-9}	2.74E-07	4.86E-06	2.30E-08
Total U	290.00	1190.00	29.00		4.03E-04	1.15E-03	4.09E-05
^{239}Pu	0.11	0.46	—	1.92×10^{-3}	2.12E-04	8.85E-04	—
^{240}Pu	0.01	0.02	—	7.15×10^{-3}	7.15E-05	1.43E-04	—
Total Pu	0.12	0.48	—		2.83E-04	1.03E-03	—
Aggregate Total Energy Generation					**6.86E-04**	**2.18E-03**	**4.09E-05**

† Taken from Reference 3.

From Tables 2 & 3, it is determined that the total alpha energy production in HCL-1 and HCL-2 is 6.86×10^{-4}-Watts and 2.18×10^{-3}-Watts, respectively. The alpha energy generation rate for drum #20102 is used to determine the maximum molecular hydrogen generation rates in this drum due to the radiolytic decomposition of the water contents of this drum as prescribed in Section 4.2.4. This drum is not considered in the parametric calculations used to determine the maximum molecular hydrogen generation rate due to the radiolytic decomposition of the polymers in the two remaining drums. The approach to the determination of the fraction of alpha energy that contributes to the radiolytic decomposition of polymeric material in the two remaining drums, #3031 and #3598 is described in Section 4.2.2.

4.2.2 Parametric Evaluation of Fraction of Total Alpha Energy Absorbed by Bottle in Drums #3031 & #3598

A parametric approach was used in the evaluation to determine the maximum fraction of the total alpha particle energy that may be absorbed by the HDPE bottle. Figure 5 provides a schematic of the approach whereby the source material is assumed to occupy a homogeneous volume that is in contact with the inner surface of the HDPE bottle. The variables are the radius and height of the void region in the model (see Figure 5). As the radius and height vary as an increasing fraction of the bottle dimensions, the density of the source region is calculated as:

$$\rho_{source} = \frac{290.12 \; or \; 1190.48}{V_{bottle} - V_{void}} \qquad \text{(Eq. 4)}$$

where 290.12 or 1190.48 are used to represent the total source mass in grams in for drum #3031, can HCL-1 and drum #3598, can HCL-2, respectively, V_{bottle} is the total bottle volume of 714-cm^3. For the purpose of this calculation the value of V_{void} can vary from ~0-cm^3 to ~714-cm^3. As the void region increases in volume, the source region volume decreases and the density of the layer on the bottle increases as described in Eq. 4. The values of source region density calculated from Eq. 4 are used in Eq. 2 to determine the alpha range in the homogeneous source material region. The width of the contributing source region is equal to the alpha particle range. The calculated alpha particle range is then used to describe the contributing and noncontributing components of the source regions. The contributing mixture in Figure 5 is the homogeneous source region volume that is within the alpha range of the inner surface of the modeled cylindrical bottle. The total source region volume is the difference between the

bottle volume and the void region volume. The ratio of the contributing mixture volume divided by the total source region volume provides a conservative estimate of the fraction of alpha particle energy that is created within the range of an alpha particle of the surface of the HDPE bottle. This fraction is then applied to the total alpha particle energy in the last row of Table 3 to determine the energy generated by alpha decay in the contributing mixture volume. This total energy is then divided by a factor of 2 to account for the isotropic nature of the source material to result in the total energy that is absorbed in the polymer to generate molecular hydrogen (that is D in Eq. 1).

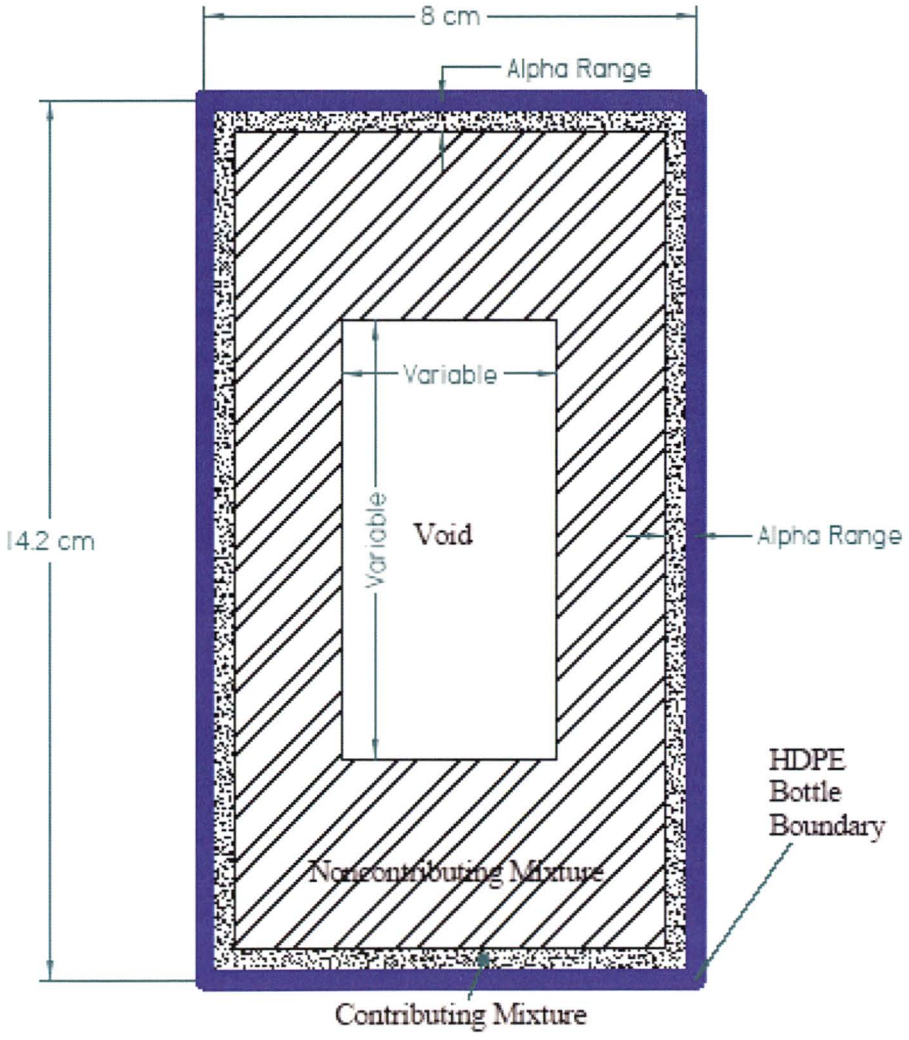

Figure 5 Schematic of the model used to determine fraction of alpha energy deposited in HDPE bottles in drum #3031, can HCL-1 and #3598, can HCL-2.

4.2.3 Final Estimation of Hydrogen Generation in Drums #3031 & #3598

The parametric approach as described in the previous section results in the consideration of hypothetical scenarios by which the modeled densities range from 0.4-g/cm^3 to more than 5000-g/cm^3. While these values are unrealistic, irregular material sizes and shapes and uncertainty in material composition and effective packing efficiency have instigated the current parametric methodology that evaluates all theoretically possible values of material and effective packing density. Although such densities are considered in order to bound analytically all possible material densities, it is expected that the actual material density would not achieve a density larger than that of uranium metal or about 18.9-g/cm^3. The plots of Figures 6 & 7show that the hydrogen production rates for drum #3031, can HCL-1 and drum #3598, can HCL-2 change only slightly as material density is increased above 18.9-g/cm^3. From this figure it is apparent that the maximum production rates are achieved as the material density is increased. This indicates that the shielding effect gained by the increased density of the source material, and decreased alpha particle range, as it is moved closer to the inner surface of the HDPE bottle effectively negates closer proximity of the alpha emitting material to the inner surface of the HDPE bottle.

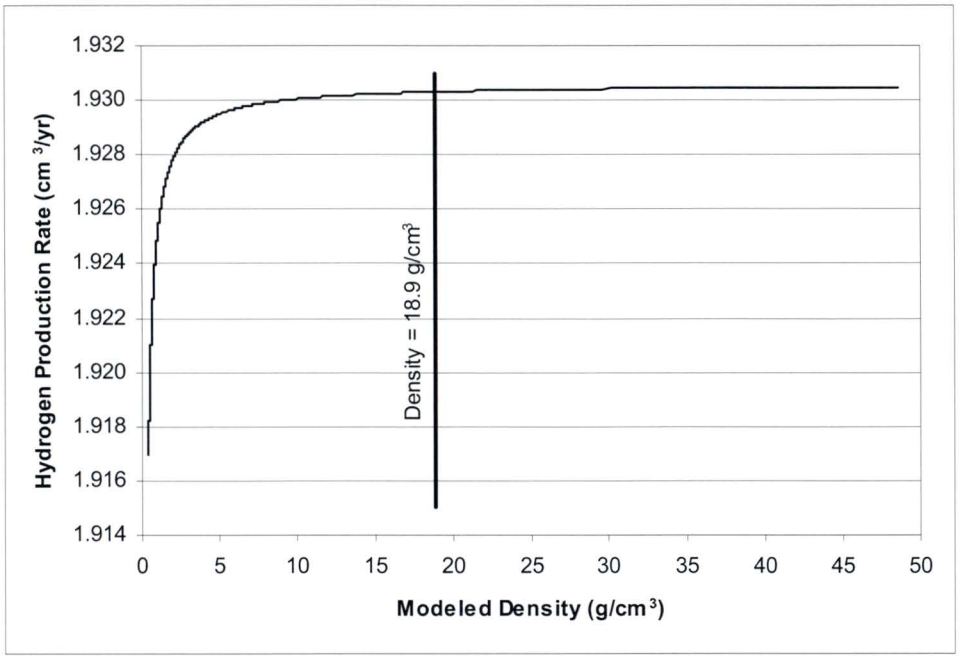

Figure 6 Hydrogen production rate as a function of modeled source density for drum #3031, can HCL-1.

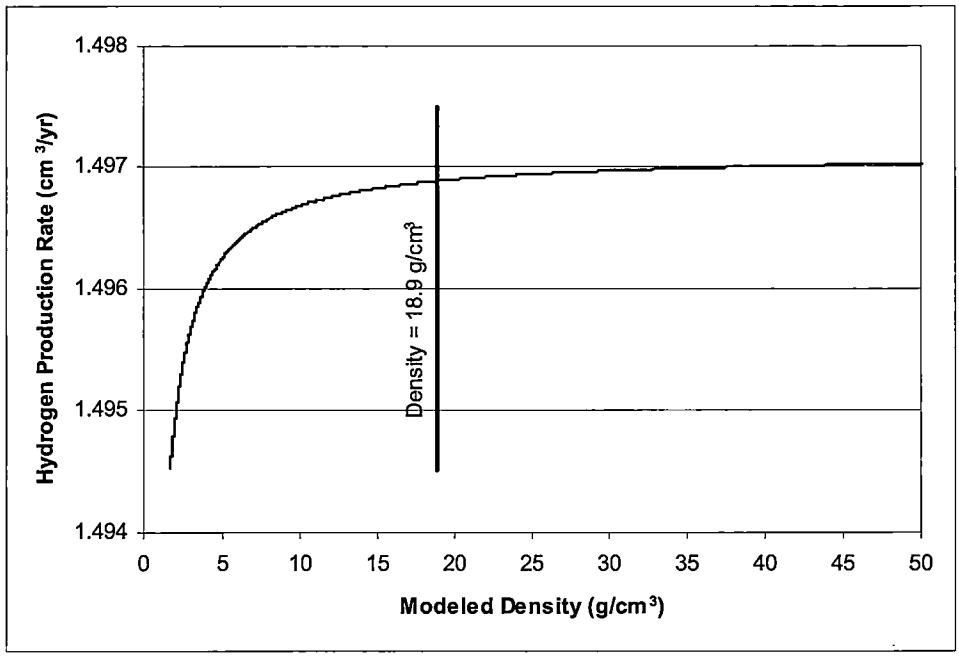

Figure 7 Hydrogen production rate as a function of modeled source density for drum #3598, can HCL-2.

The following calculation provides an illustration of the use of the current methodology in the determination of hydrogen production rate in the DOT 6M 30-gallon drums assuming a density of 18.9-g/cm^3. Based upon assumptions 2 and 5 in Section 4.1 and Eq. 2, the range of a 5.25 MeV alpha particle in source material contained within the HDPE bottle would be calculated as 7.36-μm. The assumed density of 18.9-g/cm^3 requires that the total mixture volume (that is the sum of the contributing and noncontributing volumes in Figure 5) equal 15.35-cm^3 and 62.99-cm^3, for drum #3031, can HCL-1 and drum #3598, can HCL-2, respectively. These values are determined as the material mass provided in Tables 1 & 3 divided by 18.9-g/cm^3. The contributing volume illustrated in Figure 5 is determined with the aid of assumption 3 for HDPE dimensions and the calculated alpha particle range of 7.36-μm. Based upon the dimensions provided in assumption 3, that is a 4-cm radius and a height of 14.2-cm, the total volume of the bottle is 713.76-cm^3. The material of density 18.9-g/cm^3 would occupy a space that is outside the cylinder whose radius is (4 - 0.000736)-cm and whose height is (14.2 – 2(0.000736))-cm. The volume of this bounding cylinder is determined to be 713.43-cm^3. The difference of the two volumes is the contributing volume of Figure 5 and is calculated to be 0.33-cm^3. A simple ratio of ½ of the contributing volume to the total mixture volume determines the fraction of generated alpha particles that are assumed to deposit their energy in the HDPE. By this method, the value of D in Eq. 1 is calculated to be equal to 7.53×10^{-6}-watts and 5.84×10^{-6}-watts, respectively for HCL-1 and HCL-2. Eq. 1 then yields 6.12×10^{-8}-cm^3/sec or 1.93-cm^3/yr for HCL-1 and 4.74×10^{-8}-cm^3/sec or 1.50-cm^3/yr for HCL-2.

Based upon the calculated hydrogen production rates at an assumed source material density of 18.9-g/cm^3, it is calculated that the molecular hydrogen production within HCL-1 will have generated 54-cm^3 of hydrogen in the 28-year period starting in 1992. This is equivalent to approximately 0.033-bar within the crimp sealed tin can and approximately 0.010-bar in the 2R within drum #3031. In the same time period, the production of molecular hydrogen in HCL-2 will have generated 42-cm^3 of hydrogen. This is equivalent to approximately 0.026-bar within the crimp sealed tin can and approximately 0.008-bar in the 2R within drum #3598. Table 4 provides a summary table of these calculations and results.

4.2.4 Hydrogen Production in DOT 6M drum #20102

The UO_3 material in DOT 6M 30-gallon drum #20102 is reported to contain adsorbed water in the amount of 0.45-g. This water is conservatively assumed homogeneously mixed with alpha-producing uranium within the drum. That is to say that no credit is taken for the shielding effects of the UO_3 particles themselves in the current calculation. Based upon this assumption, the total energy deposition rate of 4.09×10^{-5}-Watts is absorbed by the water within the drum. Applying this rate as D in Eq. 1 yields a volumetric hydrogen production rate of 1.61×10^{-7}-cm^3/sec or 5.09-cm^3/yr for drum #20102. This production rate would result in a total hydrogen concentration of 4.0% by volume in the crimp-sealed can at 2019 and a hydrogen concentration of 1.4% by volume in the 2R at 2020. The molecular hydrogen concentration within the crimp-sealed can remains below the lower flammability limit for hydrogen in air until 2019.

Table 4 Summary Table of Hydrogen Generation, Pressure Increase, and Concentration Results

	HCL-1 #3031	HCL-2 #3598	114/133 SAL #20102
H_2 Production Rate (cm^3/yr)	1.93	1.50	5.09
Pressure Increase in Can (bar/yr)	1.18E-03	9.12E-04	3.10E-03
Pressure Increase in 2R (bar/yr)	3.71E-04	2.88E-04	9.79E-04
H_2 Concentration in Can (% vol)	3.3†	2.6†	4.0‡
H_2 Concentration in 2R (% vol)	1.0†	0.8†	1.4†

† Concentration estimated at 2020.
‡ Concentration estimated at 2019.

5.0 CONCLUSIONS

Three DOT 6m 30-gallon drums will be received in L-Area at SRS and stored for up to 13-years prior to final disposition at HB-Line by 2019/2020. These drums are scheduled for shipment from INTEC to SRS as part of the decommissioning effort of the INTEC facility. Bounding values for hydrogen gas generation rates, rates of pressure increase within the drums, and projected molecular hydrogen concentrations at 2019/2020 have been determined for all three drums based upon the assumptions listed in Section 4.1. Two of these drums, #3031 and #3598 contain polymeric bags and/or bottles that will be subject to radiolysis induced hydrogen gas generation. The maximum quantity of molecular hydrogen that can be expected to evolve in two DOT 6M 30-gallon drums in support of receipt and subsequent interim storage prior to canyon processing has been estimated based on the alpha radiolysis of polymers. An upper bound estimate for alpha energy available for radiolysis of the polymeric materials was determined from the volume fraction occupied by material in the bottle packed within an alpha range of the inner surface of the HDPE bottles. A conservative estimation of the hydrogen generation in DOT 6M drum #20102, can 114/133 SAL that contains UO_3 powder due to the radiolytic decomposition of water has also been completed. The results are summarized in Table 5.

Table 5 Summary Table of Results

	HCL-1 #3031	HCL-2 #3598	114/133 SAL #20102
H_2 Production Rate (cm^3/yr)	1.93	1.50	5.09
Pressure Increase in Can (bar/yr)	1.18E-03	9.12E-04	3.10E-03
Pressure Increase in 2R (bar/yr)	3.71E-04	2.88E-04	9.79E-04
H_2 Concentration in Can (% vol)	3.3†	2.6†	4.0‡
H_2 Concentration in 2R (% vol)	1.0†	0.8†	1.4†

† Concentration estimated at 2020.
‡ Concentration estimated at 2019.

6.0 REFERENCE

1 ***"Appendix A: Idaho Cleanup Project, Nuclear Materials Completion,"*** Carol Nichols, DOESRAAD-06-075.1, Draft Document (December 21, 2006).

2 ***"Appendix A: Idaho Cleanup Project, Nuclear Materials Completion,"*** Carol Nichols, DOESRAAD-06-075, Draft Document (December 21, 2006).

3 DOE/ID-10368, ***"Uranium/Nitric Acid Processing Explosion at Idaho Chemical Processing Plant: Following-up Investigation Report"*** (September 1992).

4 R.A. Vaughn, **Calculation Sheet**, CS 2001/22, Issue C, Project No Y01/02/06 (December 17, 2002).

5 G.F. Knoll, **Radiation Detection and Measurement,** Second Edition, John-Wiley and Sons (1989).

6 H. Cember, **Introduction to Health Physics,** Second Edition, McGraw-Hill (1983).

7 J.R. Green, ***"Progress Report for the Enhancement of Radcalc: Isotope Database, Gamma Absorption Fractions, and G(H_2) Values,"*** WHC-SD-TP-RPT-014 (September 28, 1994).

8 U.S. Department of Energy (DOE), ***"CH-TRU Payload Appendices,"*** Rev. 1, U.S. Department of Energy, Carlsbad Field Office, Carlsbad, New Mexico (May 2005).

9 D.W. Vinson, N.E. Bibler, R.W. Deible, and R.L. Sindelar, ***"Evaluation of Hydrogen Generation from Radiolysis from Breached Spent Fuel,"*** American Nuclear Society Annual Meeting (September 19, 2002).

10 S. Pauly, ***"Permeability and Diffusion Data,"*** in **Polymer Handbook,** Fourth Edition, John Wiley & Sons, Inc. (1999).

11 C.F. Jones, ***"Soil Samples,"*** email communication to C. Nichols (Thu Jun 07 12:52:59 2007).

12 Code of Federal Regulations, 10CFR71.

13 ***"Evaluated Nuclear Structure Data File"*** – A Computer File of Evaluated Experimental Nuclear Data Maintained by the National Nuclear Data Center, Brookhaven National Laboratory ENDF/B-VI.

ORNL/TM-2003/194

Water Sorption and Radiolysis Studies for Neptunium Oxides

January 2004

Prepared by
A. S. Icenhour
R. M. Wham
R. R. Brunson
L. M. Toth

DOCUMENT AVAILABILITY

Reports produced after January 1, 1996, are generally available free via the U.S. Department of Energy (DOE) Information Bridge:

Web site: http://www.osti.gov/bridge

Reports produced before January 1, 1996, may be purchased by members of the public from the following source:

National Technical Information Service
5285 Port Royal Road
Springfield, VA 22161
Telephone: 703-605-6000 (1-800-553-6847)
TDD: 703-487-4639
Fax: 703-605-6900
E-mail: info@ntis.fedworld.gov
Web site: http://www.ntis.gov/support/ordernowabout.htm

Reports are available to DOE employees, DOE contractors, Energy Technology Data Exchange (ETDE) representatives, and International Nuclear Information System (INIS) representatives from the following source:

Office of Scientific and Technical Information
P.O. Box 62
Oak Ridge, TN 37831
Telephone: 865-576-8401
Fax: 865-576-5728
E-mail: reports@adonis.osti.gov
Web site: http://www.osti.gov/contact.html

ORNL/TM-2003/194

WATER SORPTION AND RADIOLYSIS STUDIES FOR NEPTUNIUM OXIDES

A. S. Icenhour
R. M. Wham
R. R. Brunson
L. M. Toth

Date Published: January 2004

Prepared by
OAK RIDGE NATIONAL LABORATORY
P.O. Box 2008
Oak Ridge, Tennessee 37831-6285
managed by
UT-Battelle, LLC
for the
U.S. DEPARTMENT OF ENERGY
under contract DE-AC05-00OR22725

CONTENTS

Page

LIST OF FIGURES

LIST OF FIGURES (continued)

LIST OF TABLES

ACRONYMS, ABBREVIATIONS, AND DEFINITIONS

ATR	Advanced Test Reactor
DOE	U.S. Department of Energy
G-value	the number of molecules of gas either produced or destroyed per 100 eV of energy deposited in the sample
HEPA	high-efficiency particulate air (filter)
HFIR	High Flux Isotope Reactor
INEEL	Idaho National Engineering and Environmental Laboratory
LANL	Los Alamos National Laboratory
MGy	megagray, 1 MGy = 10^6 J/kg (1 Gy = 100 rad)
ORNL	Oak Ridge National Laboratory
PCV	primary containment vessel
REDC	Radiochemical Engineering Development Center
SNF	spent nuclear fuel
SRS	Savannah River Site

ABSTRACT

Plans are to convert the ^{237}Np that is currently stored as a nitrate solution at the Savannah River Site to NpO_2 and then ship it to the Y-12 National Security Complex in Oak Ridge for interim storage. This material will serve as feedstock for the ^{238}Pu production program, and some will be periodically shipped to the Oak Ridge National Laboratory (ORNL) for fabrication into targets. The safe storage of this material requires an understanding of the radiolysis of moisture that is sorbed on the oxides, which, in turn, provides a basis for storage criteria (namely, moisture content). A two-component experimental program has been undertaken at ORNL to evaluate the radiolytic effects on NpO_2: (1) moisture uptake experiments and (2) radiolysis experiments using both gamma and alpha radiation.

These experiments have produced two key results. First, the water uptake experiments demonstrated that the 0.5 wt % moisture limit that has been typically established for similar materials (e.g., uranium and plutonium oxides) cannot be obtained in a practical environment. In fact, the uptake in a typical environment can be expected to be at least an order of magnitude lower than the limit.

The second key result is the establishment of steady-state pressure plateaus as a result of the radiolysis of sorbed moisture. These plateaus are the result of back reactions that limit the overall pressure increase and H_2 production. These results clearly demonstrate that 0.5 wt % H_2O on NpO_2 is safe for long-term storage—if such a moisture content could even be practically reached.

1. INTRODUCTION

The Department of Energy (DOE) Office of Space and Defense Power, NE-50, is reestablishing domestic production of ^{238}Pu using existing DOE facilities. The feed material for the production is ^{237}Np, which is currently stored at the Savannah River Site (SRS). This material will be stabilized as an oxide, packaged, and then transported to the Y-12 National Security Complex for interim storage. Y-12 will then transfer material as needed to Oak Ridge National Laboratory (ORNL). Target fabrication will occur at the Radiochemical Engineering Development Center (REDC) Building 7930. The High Flux Isotope Reactor (HFIR) at ORNL and the Advanced Test Reactor (ATR) at the Idaho National Engineering and Environmental Laboratory (INEEL) will be used to irradiate ^{237}Np-containing targets to produce ^{238}Pu. The irradiated targets will undergo chemical processing at the REDC to (1) recover ^{238}Pu for shipment to Los Alamos National Laboratory (LANL) and (2) recover ^{237}Np for recycle.

Safety issues concerning transportation and long-term storage of neptunium are of a particular concern to the program. The material and its packaging must comply with shipping standards as well as provide for safe storage.

One aspect relative to the safe transport and storage of NpO_2 is radiolysis of sorbed water. Current safety analyses assume that all of the water absorbed on the surface of the NpO_2 can be radiolyzed to gaseous hydrogen and oxygen, thus generating significant gas pressures within the storage containers. Also, the potential for detonation of the hydrogen has been identified as a safety issue for transportation. However, experimental work by Icenhour et al.[1–4] using uranium oxides and uranium oxyfluorides has demonstrated that radiolysis does not convert all of the water to H_2 and O_2 because of competing back reactions that result in a pressure plateau, demonstrating that a steady state has been reached. In some cases, the vessel actually goes to vacuum conditions as a result of the dominance of back reactions.

The use of high-dose-rate gamma and/or alpha irradiation capable of radiolyzing significant quantities of the proposed materials in a short period of time is the only practical way to achieve the necessary doses and thus assess potential long-term storage problems. A set of experiments was performed to irradiate NpO_2 samples that have sorbed moisture. This report provides a description of the experiments and the results.

2. BACKGROUND

The neptunium to be used as feed material currently exists in a nitrate solution in the SRS H-Canyon. The neptunium solution, which contains about 500 ppm ^{238}Pu,[5] will undergo chemical processing in a glove-box line (HB-Line Phase II) to remove impurities and convert it to an oxide as depicted in Fig. 2.1.

The neptunium solution first undergoes a feed adjustment to 6–8 *M* HNO_3. The adjusted solution is then fed into anion-exchange columns, where the neptunium nitrate complex absorbs, allowing most metal impurities to pass through the column. Next, a decontamination wash is performed to remove residual impurities. Finally, a weak nitric acid solution is passed through the column to elute the neptunium.

Once the anion-exchange process has been completed, the resulting neptunium solution is combined with oxalic acid, which forms an insoluble neptunium oxalic precipitant. This product is filtered, and the neptunium oxalate is then calcined at ~600°C to convert the oxalate to oxide.

The oxide will be packaged in a can–bag–can configuration for shipment (Fig. 2.1). The inner can, which contains up to 6 kg neptunium, is a screw-top, food-pack convenience can. Because no gasket or sealing compounds are used on the closure, this inner can will not be gastight. The inner can is contained in a heat-sealed polyethylene bag, which has an installed HEPA (high-efficiency particulate air) filter. The can–bag will then be placed inside an outer can, which has a HEPA filter in its lid.* Finally, the can–bag–can will be placed inside a 9975 primary containment vessel (PCV).[6] SRS currently plans to evacuate the PCV and backfill with argon. Because of the installed HEPA filters and the screw-top lid on the inner can, the entire contents of the PCV will be evacuated and backfilled. This operation is expected to reduce the O_2 concentration inside the PCV to less than 5 vol %.

Concerns related to the long-term storage of the NpO_2 are the potential for container pressurization and/or the formation of H_2 as a result of radiolytic decomposition of moisture that is sorbed on the oxide. To address these concerns, NpO_2 radiolysis experiments have been conducted at ORNL using both gamma and alpha radiation sources. Samples of NpO_2 were prepared by the method expected to be used at SRS (i.e., oxalate precipitation and calcination). Moisture was added to the samples to simulate water uptake.

The equipment and experimental facilities described in this report have been used in similar studies concerning gamma irradiation of uranium oxides and fluoride salts with various amounts of sorbed water.[1–4]

*Because of ergonomic considerations, two bagged inner cans may be used instead of just one.

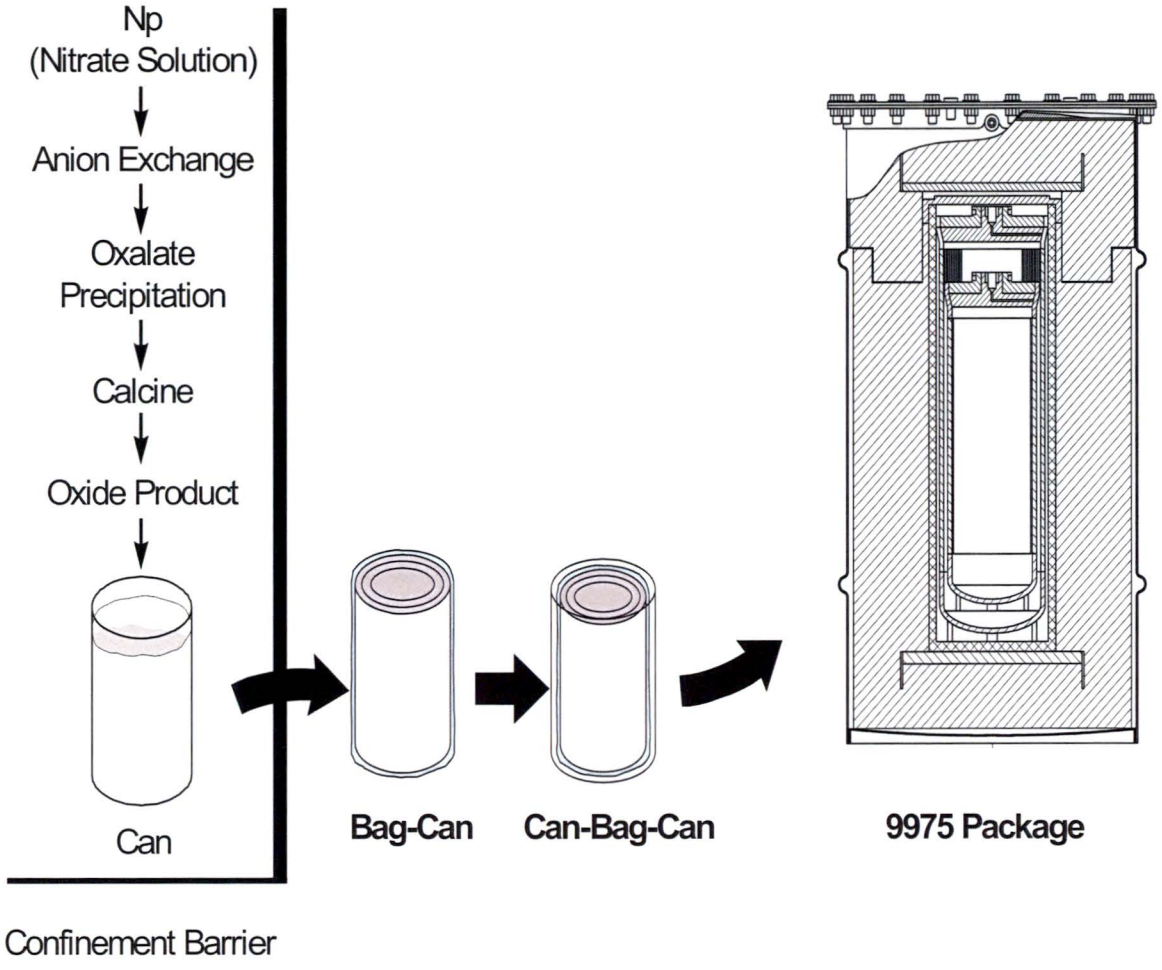

Fig. 2.1. Schematic depiction of neptunium processing and packaging.

3. EXPERIMENTAL

The experimental program was divided into three distinct activities: sample preparation, water sorption studies, and radiolysis experiments.

3.1 SAMPLE PREPARATION

Twelve samples of NpO_2 were prepared and then irradiated to evaluate radiolytic decomposition of water. The samples first underwent chemical processing at REDC Building 7930 to prepare the NpO_2 in a form similar to that expected from SRS.[7] The water content and the surface area of the samples were varied for the experiments.

In order to prepare NpO_2 for these experiments, a batch of 80–100 g of NpO_2 was dissolved in nitric acid. Some of the feed material was neptunium oxide originally obtained from LANL. The majority of the material had been processed using hydroxide precipitation, oxalate precipitation, and ion-exchange processing at the REDC. Because the neptunium product batches from the hydroxide precipitation and oxalate precipitation processes were calcined at 1400°C, they were extremely difficult to dissolve. Therefore, these various sources of neptunium were dissolved in 8 *M* HNO_3 acid with 0.02 *M* NaF added to the solution, followed by heating over a period of about 24 h to promote the dissolution. After dissolution, the neptunium was adjusted to the 4+ valence state by addition of hydrazine followed by ascorbic acid. A slight excess of oxalic acid was then added to precipitate the neptunium as neptunium oxalate. The resulting material was filtered, dried, and fired to 650°C to convert the oxalate to oxide.* Some material was fired at 800°C to change the surface area. Tables 3.1 and 3.2 provide isotopic and chemical impurity results, respectively, from the analysis of NpO_2 prepared by the method described.

3.2 WATER SORPTION STUDIES

Neptunium oxide with varying amounts of sorbed water was needed for these experiments. The amount of water sorbed as a function of time was determined by placing these materials in a controlled-humidity environment. Humidities of 60 and 97.5% were used. The humidity was controlled by

*Note that at the time of this work, the exact calcination temperature had not yet been established. It is now expected that the SRS material will be fired at temperatures between 600 and 650°C, depending on the capability of the furnace used. This temperature range will have no effect on the results or conclusions described in this report.

Table 3.1. Neptunium isotopic data

	Isotopic abundance (wt %)
^{237}Np	99.97361
$^{239/240}Pu$	0.02558
^{238}Pu	0.0008

Table 3.2. Metal ion impurity in NpO_2 samples

Element	Concentration (μg/g)
Al	$1.38 \times 10^4 \pm 1.38 \times 10^3$
B	$9.19 \times 10^3 \pm 9.19 \times 10^2$
Ba	$6.03 \times 10^3 \pm 6.03 \times 10^2$
Be	$4.25 \times 10^1 \pm 4.25$
Ca	$1.94 \times 10^4 \pm 1.91 \times 10^3$
Cu	$6.79 \times 10^2 \pm 8.49 \times 10^1$
Fe	$6.52 \times 10^3 \pm 1.36 \times 10^3$
K	$8.43 \times 10^3 \pm 2.08 \times 10^3$
Mg	$1.41 \times 10^4 \pm 1.31 \times 10^3$
Mn	$2.34 \times 10^2 \pm 4.25 \times 10^1$
Na	$5.44 \times 10^4 \pm 5.44 \times 10^3$
Sb	$3.27 \times 10^3 \pm 7.22 \times 10^2$
Sr	$3.40 \times 10^2 \pm 3.40 \times 10^1$

placing the NpO_2 sample in a small open glass container, which, in turn, was placed in a glass desiccator. The desiccant had been removed and was replaced with a small open container of dilute sulfuric acid to yield the desired humidity. The NpO_2 samples were periodically removed from the chamber and weighed to determine the uptake of water. Table 3.3 provides relative humidity data for a number of sulfuric acid solutions. (The vapor referred to is pure water.)

Table 3.3. Constant humidity control using sulfuric acid solutions[a]

Density of aqueous H_2SO_4 solution	Relative humidity (%)	Water vapor pressure at 20°C (mm Hg)
1.00	100.0	17.4
1.05	97.5	17.0
1.10	93.9	16.3
1.15	88.8	15.4
1.20	80.5	14.0
1.25	70.4	12.2
1.30	58.3	10.1
1.35	47.2	8.3
1.40	37.1	6.5
1.50	18.8	3.3
1.60	8.5	1.5
1.70	3.2	0.6

[a]From *Handbook of Chemistry and Physics*, 41st ed., Chemical Rubber Publishing Co., Cleveland, 1959, p. 2500.

3.3 RADIOLYSIS EXPERIMENTS

Radiolysis experiments were performed using both gamma and alpha radiation. The equipment used for these experiments is described in Sects. 3.3.1 and 3.3.2.

3.3.1 Gamma Irradiation Experiments

Two different sources of gamma radiation were used: (1) the ORNL ^{60}Co irradiator and (2) the HFIR spent nuclear fuel (SNF) elements. In preparation of the samples, a calibrated pipette was used to add the desired amount of water.

3.3.1.1 ^{60}Co irradiation experiments

A J. L. Shepherd model 109-68 (serial no. 654) ^{60}Co gamma irradiator (shown in Fig. 3.1), providing a dose rate of about 10^5 rad/h, was used for the experiments. The sample container itself is shown in Fig. 3.2, while Fig. 3.3 shows the samples installed in the irradiator prior to being lowered into the device. A detailed description of the irradiator and the methods used to calculate the dose to the samples (for both the ^{60}Co source and HFIR SNF elements) is provided in Ref. 8.

The samples to be irradiated were placed in stainless steel containers, each of which had a small-diameter stainless steel tube connected at one end for pressure sensing and a capped opening at the other end for loading samples. The container was connected by small-diameter tubing to a stainless steel Nupro® valve and an MKS Baratron® pressure transducer (Type 127A). The material to be irradiated was loaded through a stainless steel VCR gland on one end of the container.

Preparation of sample containers for their insertion into the ^{60}Co irradiator consisted of leak checks, volume measurements, and loading of the samples into the containers. As part of their fabrication, the containers were leak checked with air to a pressure of about 6.8 atm (100 psia).

Just before their use, the containers were leak checked again, using both pressure (typically ~3 atm) and vacuum. The volume of the irradiation rig (i.e., the sample container, tubing, valve, and pressure transducer) was measured by expanding helium from a known volume into the rig, observing the pressure change, and applying the ideal gas law. The volume of each of the tubes used in the experiments is presented in Table 3.4.

Fig. 3.1. ORNL ^{60}Co irradiator.

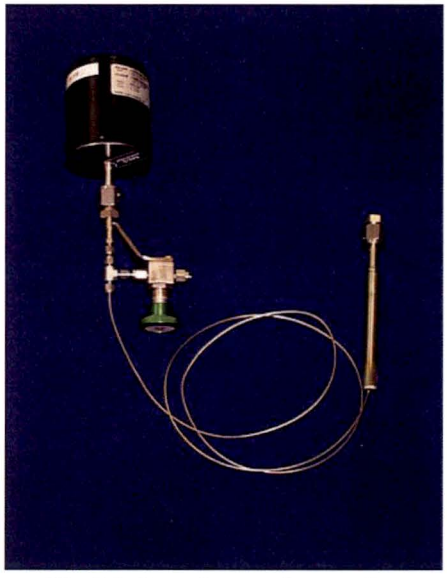

Fig. 3.2. Sample container and pressure transducer used in the ^{60}Co irradiations.

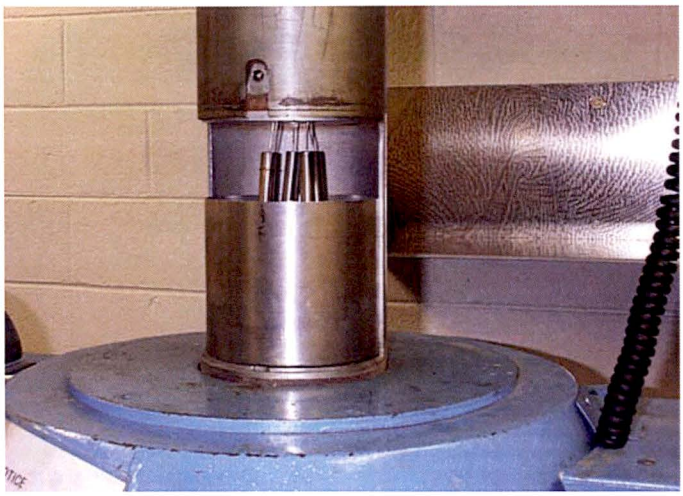

Fig. 3.3. Irradiation chamber of ORNL ^{60}Co irradiator with sample containers installed.

Table 3.4. Volume of sample containers used in irradiation experiments

Container	Volume (cm^3)
^{60}Co Np Tube 1	16.7
^{60}Co Np Tube 2	16.6
^{60}Co Np Tube 3	16.4
^{60}Co Np Tube 4	16.1
HFIR Np Tube 1	34.6
HFIR Np Tube 2	49.7
HFIR Np Tube 3	50.8
HFIR Np Tube 4	35.4
Alpha Np Tube 1	13.1
Alpha Np Tube 2	13.3
Alpha Np Tube 3	13.5
Alpha Np Tube 4	13.7
Alpha Np Tube 5	13.1

A computerized data acquisition system was used to collect data during each irradiation. Validyne® hardware and software were used, providing up to eight data channels per card. The data acquisition system is shown in Fig. 3.4. Typical parameters recorded during an irradiation included container pressure, temperature of selected containers, and ambient pressure and temperature.

3.3.1.2 HFIR SNF irradiation experiments

To obtain higher dose rates, the HFIR SNF gamma irradiation facility (shown in Fig. 3.5) was also used. Figure 3.6 depicts the experimental configuration for these irradiations. Samples can be irradiated in the HFIR SNF pool by inserting them into SNF elements. The SNF elements are cylindrical with a hollow center. In its storage position in the SNF pool, a cadmium sleeve inside the hollow region of the element absorbs neutrons. Hence, the hollow region of the fuel element primarily provides a gamma field for irradiation. The neutron flux in this region is about 100 neutrons • cm^{-2} • s^{-1}. The contribution of neutrons to the radiation damage is negligible when compared with the very large gamma field. Exposure rates vary from about 10^7 to 10^8 R/h, depending on the time since the discharge of the SNF from the reactor.

A multiple-irradiation container was used for the irradiation of four samples at once (Fig. 3.7). Small sample containers consisting of 1.27-cm-diam stainless steel tubing were placed inside an outer container, which was fabricated from 8.9-cm-diam, 44-cm-long stainless steel pipe. The outer container was closed at one end and had a Conflat flange on the other end. The flange contained five penetrations. Four were used to connect the smaller inner containers to 0.318-cm-diam stainless steel tubing, while the fifth connected the void volume of the outer container to 0.318-cm-diam stainless steel tubing. In each case, this tubing was about 6.1 m long and was connected to a pressure transducer and to a valve.

The volume of each of the sample containers, which included sampling lines and pressure transducers, is presented in Table 3.4. Before the experiment was transported to the HFIR for insertion in an SNF element, the samples were loaded in air and the outer container was pressurized to 1.7 atm (10 psig), as required by HFIR operations personnel.

Sensotec® (model FPA, 0–50 psia) pressure transducers were used for the four inner sample containers. A Kobold® (model KPK, 30 in. Hg to 100 psig) compound pressure transducer was used to monitor the pressure in the large outer vessel. A computerized data acquisition system was used to record the pressure throughout the experiments.

Fig. 3.4. Data acquisition computer in operation at the ORNL ^{60}Co source.

Fig. 3.5. SNF elements in the HFIR SNF pool.

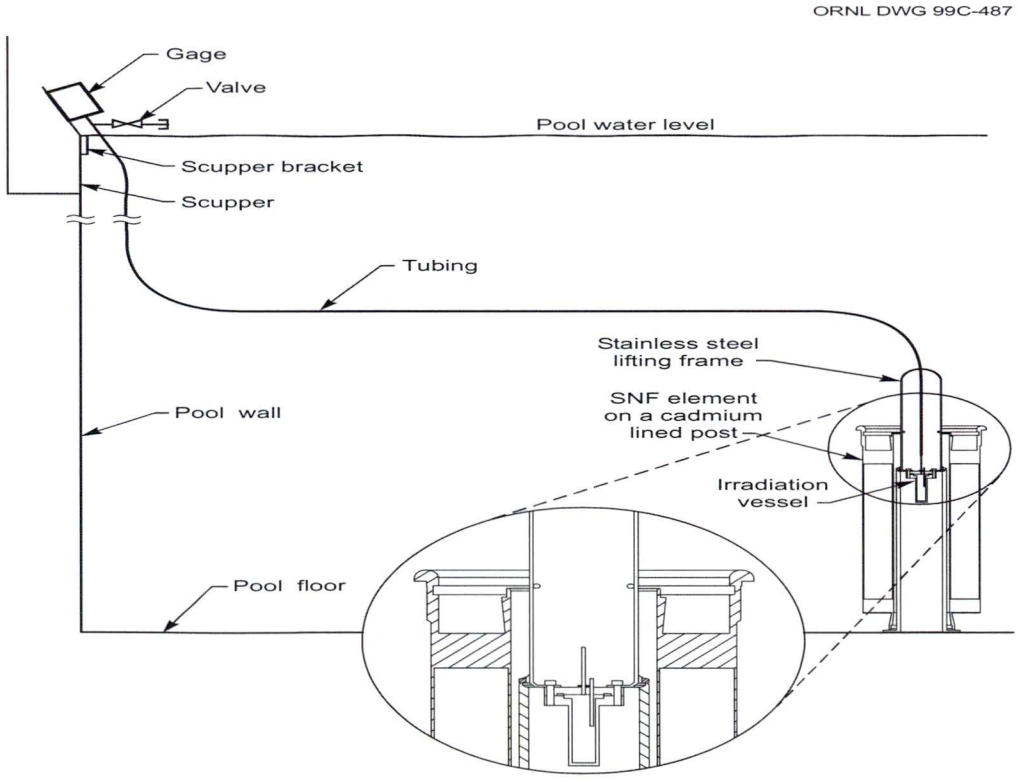

Fig. 3.6. Schematic of the experimental configuration for gamma irradiation experiments with a HFIR SNF element.

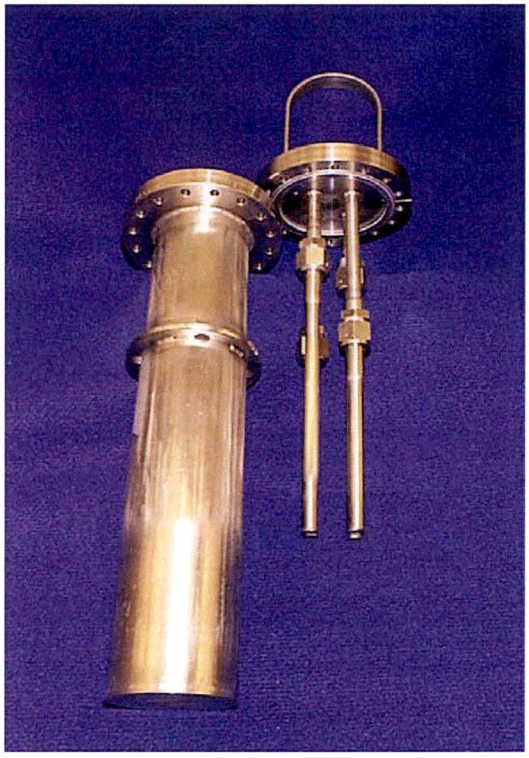

Fig. 3.7. Multiple-irradiation container used in HFIR SNF irradiations.

3.3.2 Alpha Radiolysis Experiments

To perform the alpha radiolysis experiments, neptunium samples were spiked with ^{244}Cm to mimic the dose from ^{238}Pu, but in a shorter time period reasonable for the present experimental study. Note that the neptunium in storage at SRS contains about 500 ppm ^{238}Pu. Samples of NpO_2 containing about 7000 ppm ^{244}Cm realized a dose rate about 70 times that for the SRS material, as illustrated in Figure 3.8. An example of the radionuclide composition and dose contribution data for the curium used is presented in Table 3.5. This table demonstrates that while 40 wt % of the material used to spike the samples was ^{240}Pu, more than 99% of the dose was delivered by the parent isotope, ^{244}Cm.

A portion of the dissolved neptunium was set aside for alpha radiolysis experiments. The neptunium was adjusted to the 4+ valence state and diluted to 1–2 *M* HNO_3. A small aliquot of ^{244}Cm was then mixed with the neptunium solution, and oxalic acid was added to form both neptunium and curium oxalate. The oxalate product was filtered, dried, and calcined at 650°C. The resulting oxide was then divided into four samples, one of which was further heated to 800°C.

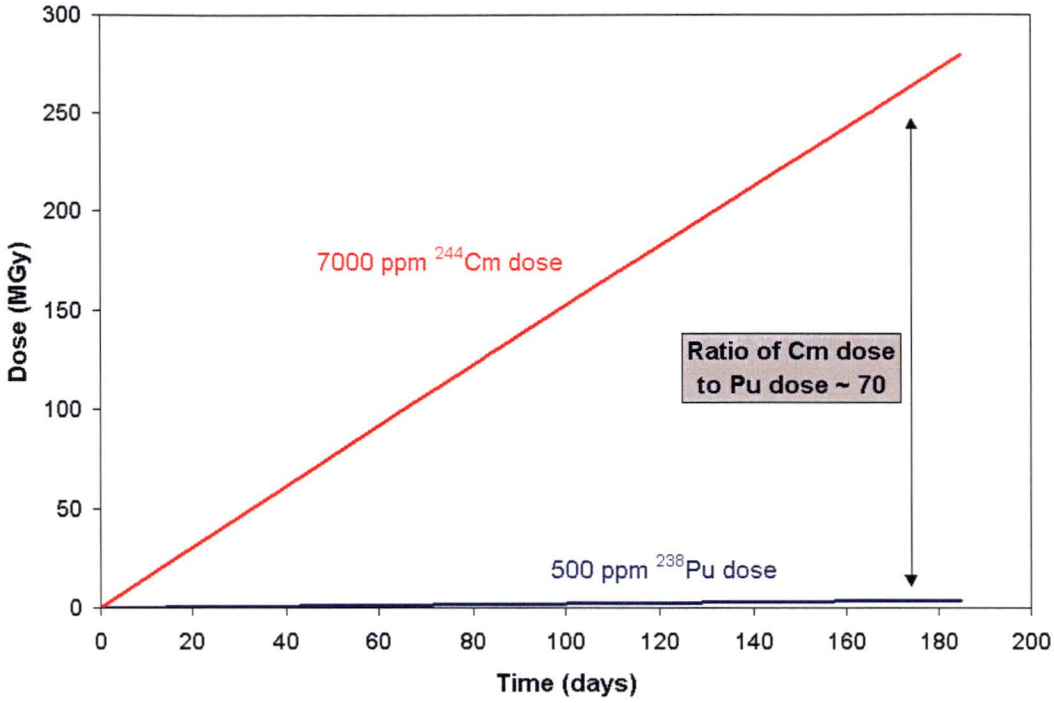

Fig. 3.8. Comparison of doses to NpO_2 samples using 500 ppm ^{238}Pu and 7000 ppm ^{244}Cm.

Table 3.5. Example of radionuclide composition and dose contribution data for a NpO_2 sample spiked with ^{244}Cm

Radionuclide	Half-life (years)	Specific activity (Ci/g)	Average alpha energy (MeV)	Composition (wt %)	Contribution to dose (%)
^{244}Cm	18.11	80.9	5.7965	50.34	99.74
^{245}Cm	8500	0.1717	5.363	1.36	0.01
^{246}Cm	4730	0.3072	5.376	7.31	0.05
^{247}Cm	1.56×10^{7}	9.20×10^{-5}	4.9475	0.12	2.34×10^{-7}
^{248}Cm	3.40×10^{5}	0.00424	4.6524	0.07	5.72×10^{-6}
^{240}Pu	6563	0.22696	5.1549	40.04	0.20
^{241}Pu	14.4	103	0.000118	2.01×10^{-6}	1.03×10^{-10}
^{242}Pu	3.76×10^{5}	0.003926	4.89	1.93×10^{-5}	1.57×10^{-9}
^{243}Am	7380	0.1993	5.2656	0.76	3.37×10^{-3}

The samples were placed in stainless steel containers, and the desired amount of water was then added. The containers were connected by a small-diameter stainless steel tube to a Sensotec pressure transducer and to a valve (Fig. 3.9). Filter gaskets (0.5-μm sintered frit) were used in the VCR face-sealed connections to prevent movement of particles and the spread of contamination. An Omega® Type K thermocouple was attached to the outside of each sample container. The void volume of the containers was measured by expanding helium from a known volume. (The measured volumes are shown in Table 3.4.) Samples were prepared and loaded into the containers in a glove box.

3.4 SAMPLING AND ANALYSES

At the completion of the irradiations, gas samples were withdrawn and analyzed by mass spectrometry.

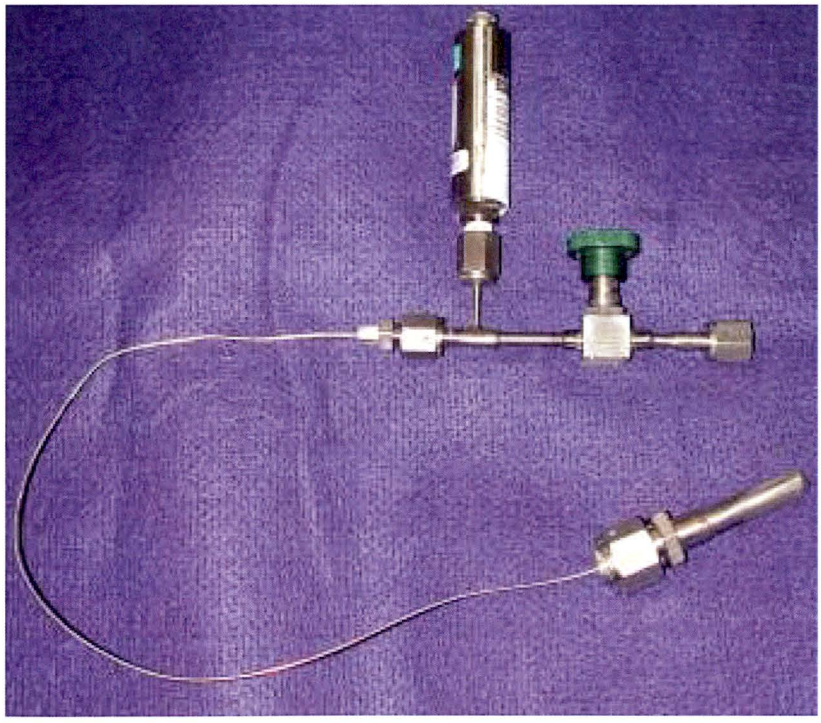

Fig. 3.9. Sample container and pressure transducer used in the alpha radiolysis experiments.

4. RESULTS AND DISCUSSION

4.1 WATER SORPTION EXPERIMENTS

The results for the water sorption on the samples prepared at 650°C are shown in Fig. 4.1, where the weight gain (i.e., amount of water sorption) of the NpO_2 sample is depicted as a function of time for two different relative humidities. The sample exposed to the 97.5% humidity exhibited an increase in moisture uptake to a limiting value of about 1 wt %. Interestingly, at about 30 days, the lid to the chamber containing the sample was left off, thereby lowering the relative humidity over the sample to that of the glove box. The amount of moisture on the sample rapidly decreased, and, when the lid was replaced, the amount of moisture returned to the previous limit. For the sample exposed to the 60% humidity, a much lower moisture uptake limit was reached—about 0.02 wt %. A similar behavior was seen for the samples prepared at 800°C (not shown in this report). For these samples, the maximum moisture uptake was 0.8 wt % in the 97.5% humidity, while the maximum was about 0.02 wt % in the 60% humidity.

The water sorption experiments showed that in practical humidities, NpO_2 sorbs very little water. Even in the case of extreme humidity (i.e., 97.5%), the sample prepared at 650°C sorbed quantities of water only up to ~1 wt % (Fig. 4.1). Furthermore, this water was held very loosely on the surface—as demonstrated by the overnight occurrence described in the paragraph above. However, in the more normal operational case of 60% relative humidity, the maximum water uptake was about 0.02 wt %.

Taking these results in a broader perspective, it is worth noting that the plutonium and ^{233}U storage standards[9,10] have been set with the maximum acceptable moisture content at 0.5 wt %. With such precedents, we expect an identical limit will be established for the NpO_2 that is to be prepared at SRS. In light of the current moisture uptake data for the NpO_2 prepared at 650°C, and based on similar results obtained at 75% relative humidity by the Savannah River Technology Center,[11] the storage standard limit of 0.5 wt % could never be reached in normal operating or storage conditions where humidity levels are controlled at 60–75%.

4.2 GAMMA RADIOLYSIS EXPERIMENTS

Irradiation experiments were conducted for a number of NpO_2 samples using either the ORNL ^{60}Co source or HFIR SNF elements. Table 4.1 provides a summary of the irradiation experiments performed. The results obtained from these radiolysis experiments are presented in Sects. 4.2.1 and 4.2.2.

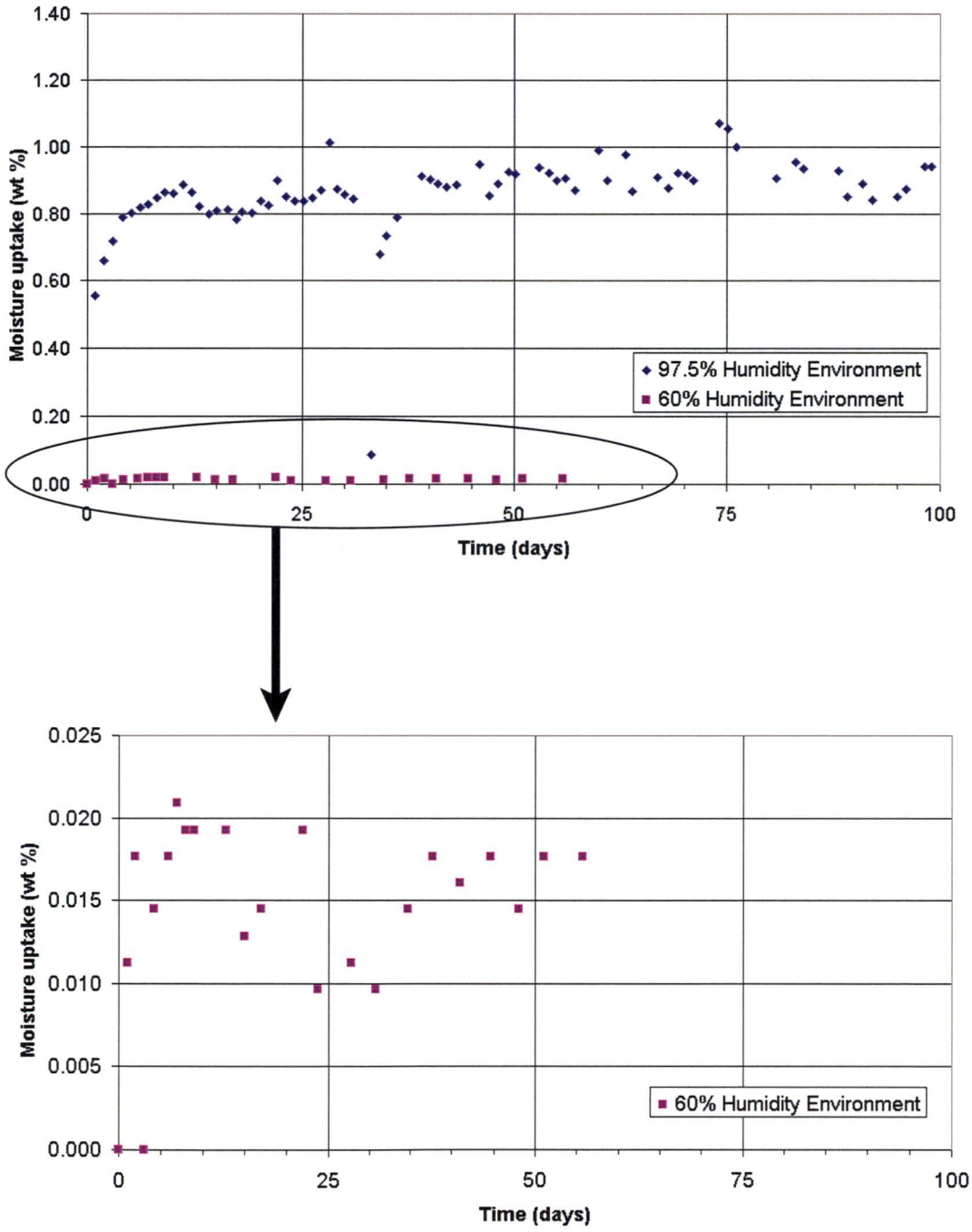

Fig. 4.1. Moisture uptake data for NpO_2 prepared at 650°C.

Table 4.1. Summary of gamma irradiation experiments performed

Experiment	Material[a]	Mass (g)	Total dose (MGy)
^{60}Co Np Tube 1	NpO_2 (650°C)	3.9593	4.2
^{60}Co Np Tube 2	NpO_2 (650°C) + 8 wt % H_2O	4.3152	4.1
^{60}Co Np Tube 3	NpO_2 (650°C) + 1 wt % H_2O	3.9832	4.2
^{60}Co Np Tube 4	NpO_2 (800°C) + 1 wt % H_2O	3.9886	4.2
HFIR Np Tube 1	NpO_2 (650°C)	3.9530	613
HFIR Np Tube 2	NpO_2 (650°C) + 1 wt % H_2O	3.9908	612
HFIR Np Tube 3	NpO_2 (650°C) + 8 wt % H_2O	4.2806	595
HFIR Np Tube 4	NpO_2 (800°C) + 1 wt % H_2O	4.0227	611

[a] Value in parenthesis denotes preparation temperature.

4.2.1 Pressure Measurements

Pressure within the sample containers was monitored throughout the irradiations, and the pressure data from each of the gamma radiolysis experiments are shown in Figs. 4.2–4.9. The pressure and gas yield (millimoles of gas per gram of sample) are plotted as a function of dose in each of the figures. The gas yield was calculated using the ideal gas law.

Container temperatures in the ^{60}Co irradiator were measured to be about 28°C. For the HFIR multiple-vessel irradiations, the temperature was estimated to average about 55°C, based on earlier experiments.[3] For this earlier work, the temperature typically ranged from 50 to 60°C, with several short transients upon insertion of the experiment into a fresh element. The difference in temperature between the ^{60}Co and HFIR irradiations did not appear to have a measurable effect on the irradiation results, other than accounting for the slight pressure differences due to gas expansion.

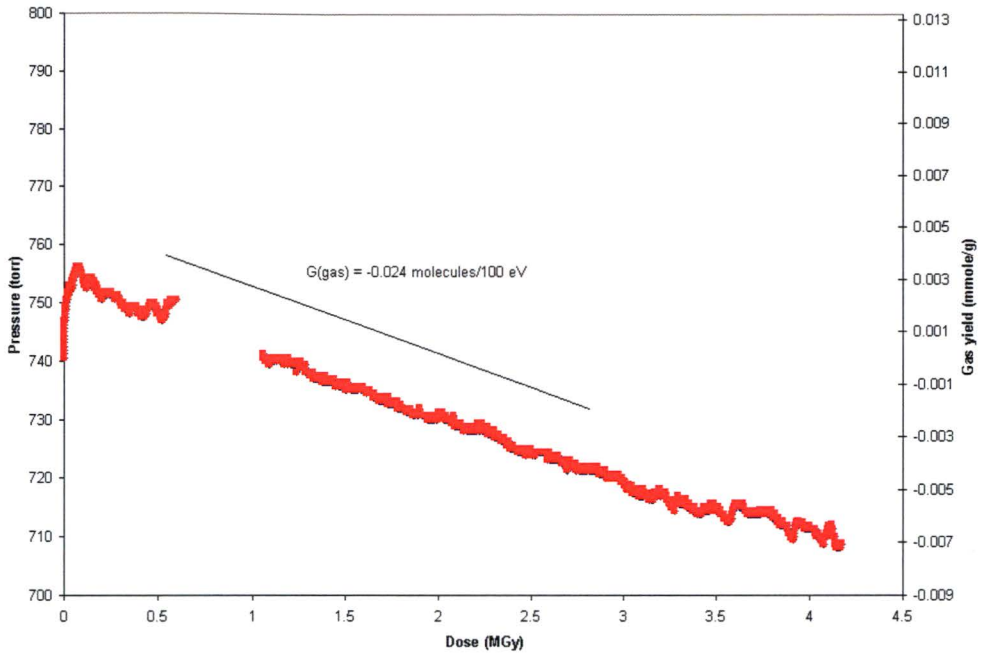

Fig. 4.2. Pressure and gas yield as a function of dose for sample ^{60}Co Np Tube 1 [^{60}Co-irradiated NpO_2 (650°C)].

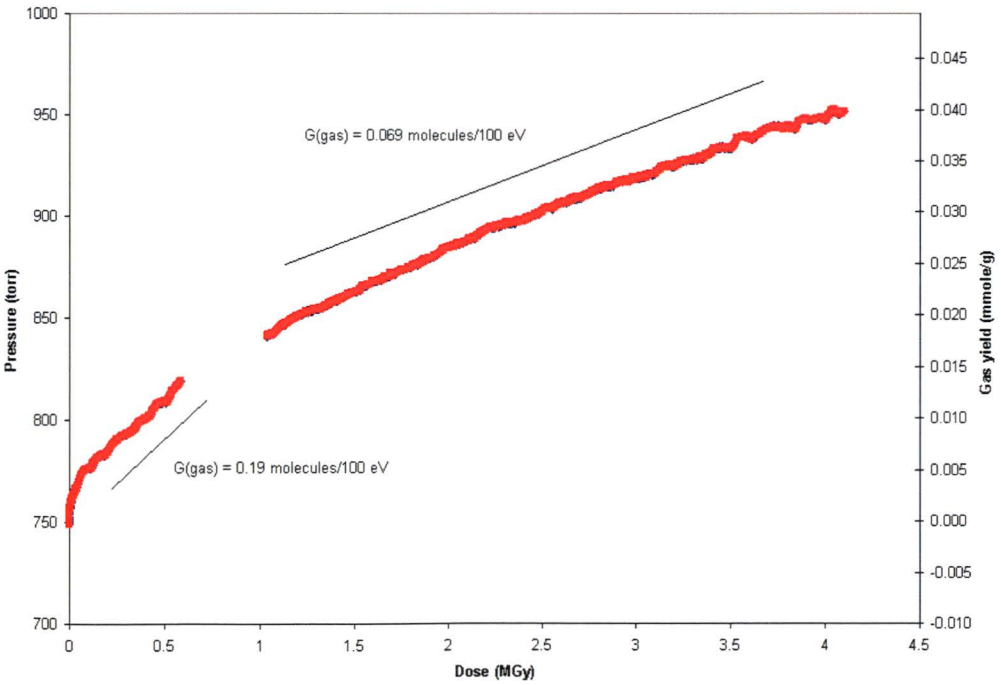

Fig. 4.3. Pressure and gas yield as a function of dose for sample ^{60}Co Np Tube 2 [^{60}Co-irradiated NpO_2 (650°C) + 8 wt % H_2O].

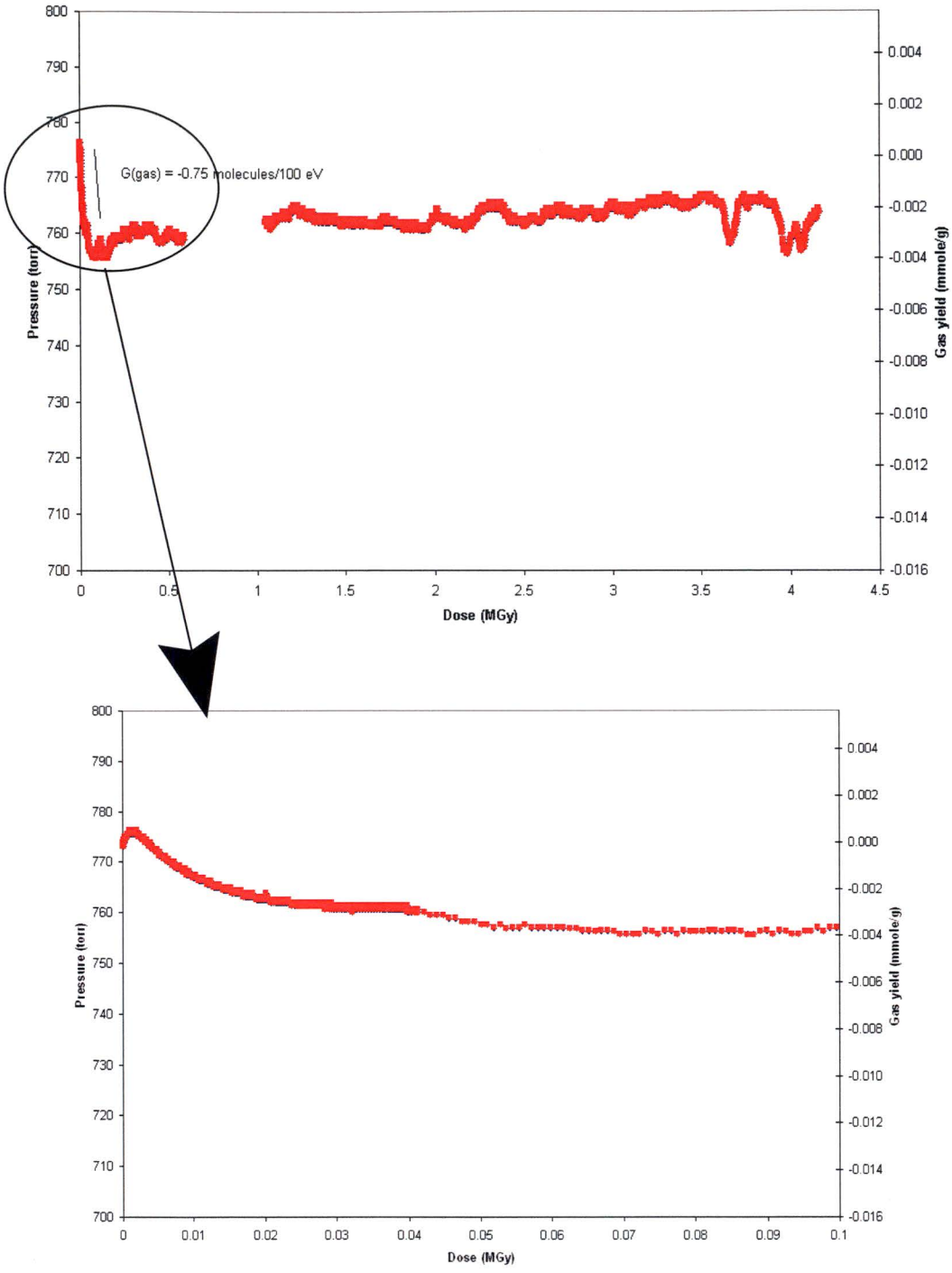

Fig. 4.4. Pressure and gas yield as a function of dose for sample ^{60}Co Np Tube 3 [^{60}Co-irradiated NpO_2 (650°C) + 1 wt % H_2O].

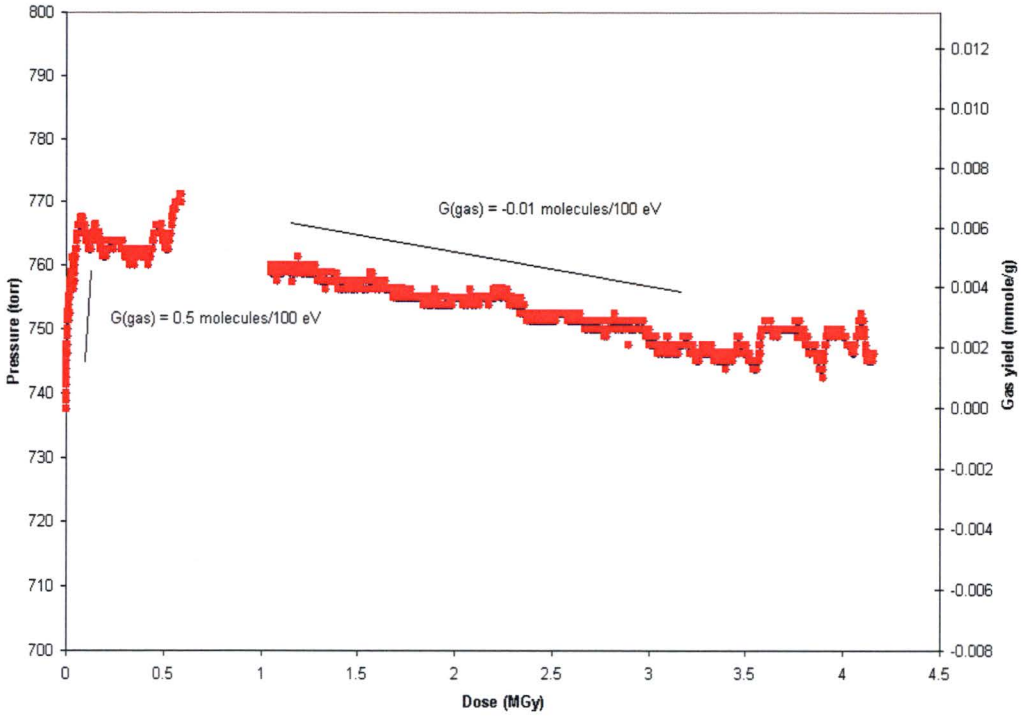

Fig. 4.5. Pressure and gas yield as a function of dose for sample ^{60}Co Np Tube 4 [^{60}Co-irradiated NpO_2 (800°C) + 1 wt % H_2O].

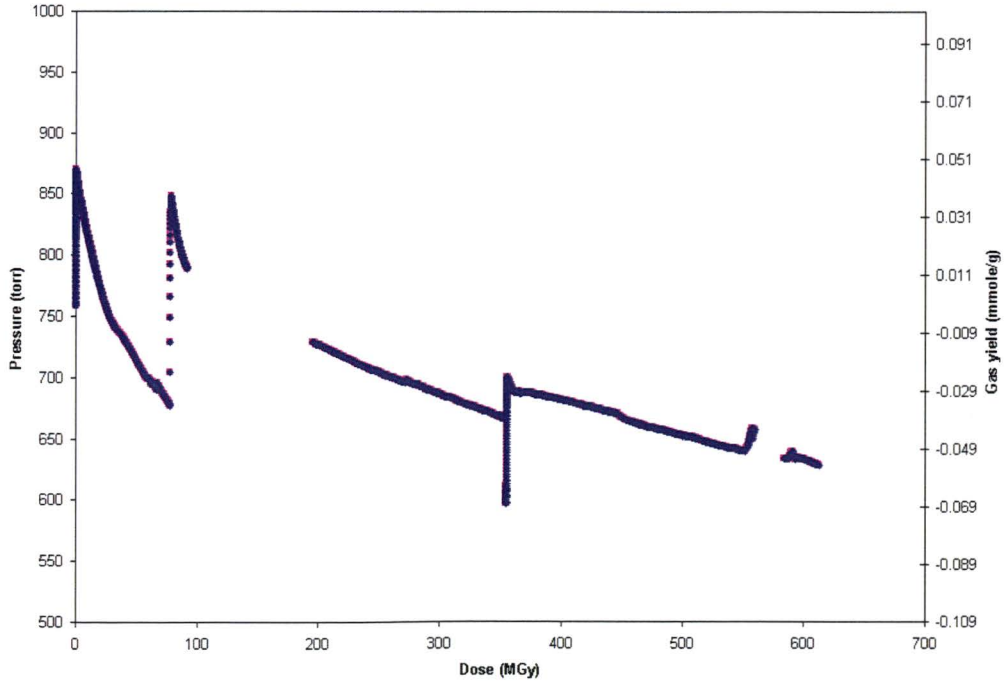

Fig. 4.6. Pressure and gas yield as a function of dose for sample HFIR Np Tube 1 [HFIR SNF-irradiated NpO_2 (650°C)].

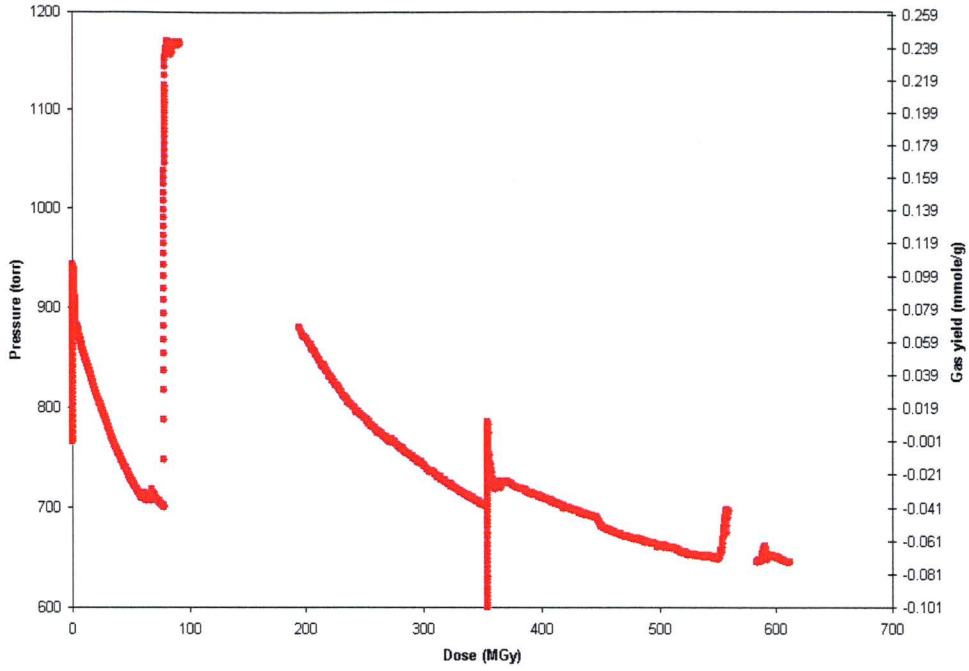

Fig. 4.7. Pressure and gas yield as a function of dose for sample HFIR Np Tube 2 [HFIR SNF-irradiated NpO_2 (650°C) + 1 wt % H_2O].

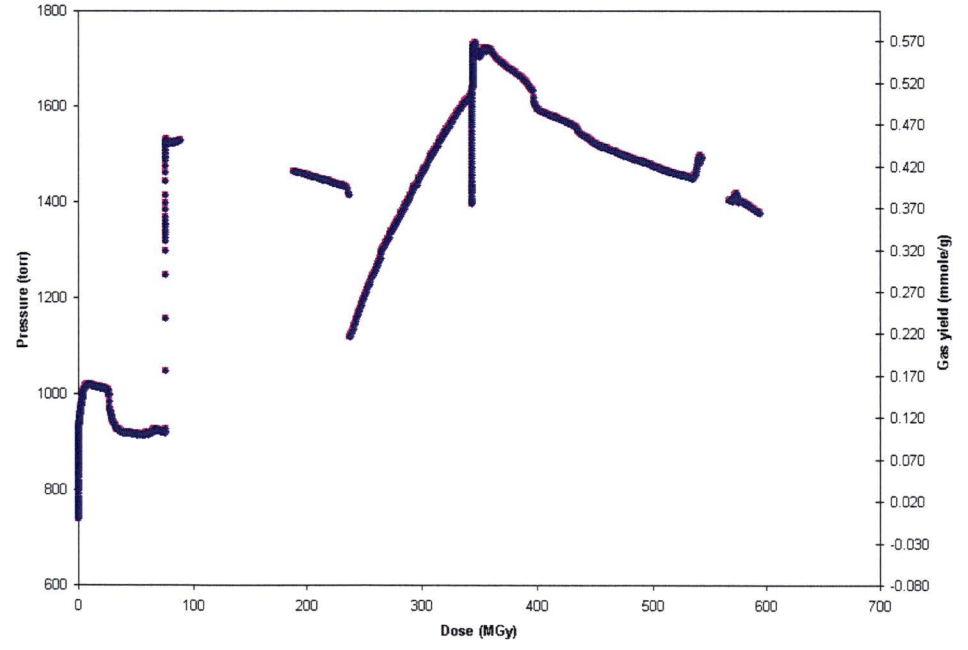

Fig. 4.8. Pressure and gas yield as a function of dose for sample HFIR Np Tube 3 [HFIR SNF-irradiated NpO_2 (650°C) + 8 wt % H_2O].

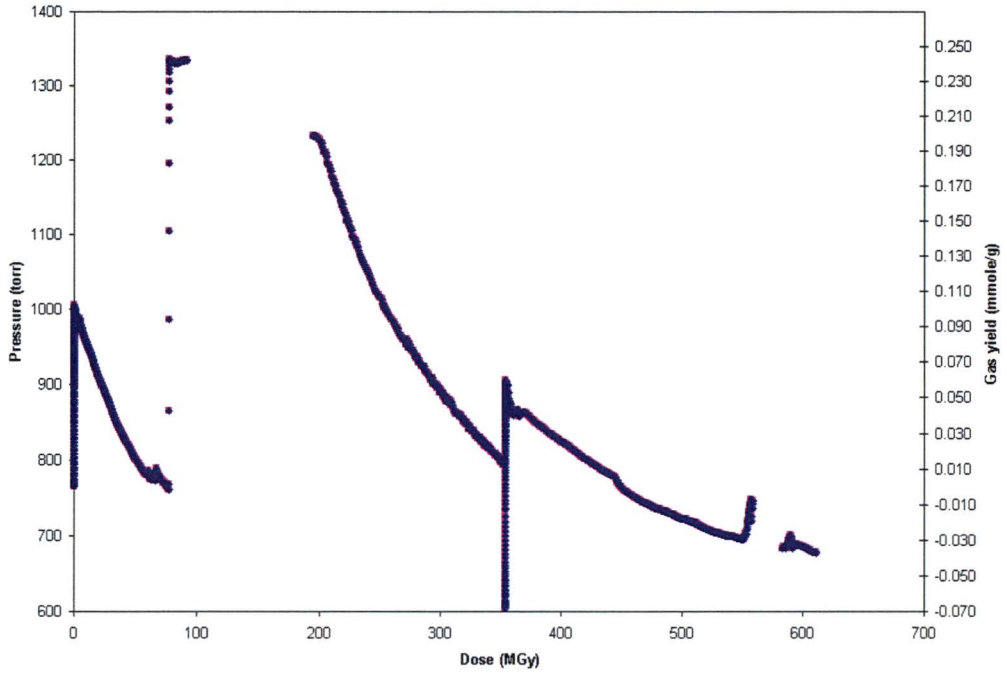

Fig. 4.9. Pressure and gas yield as a function of dose for sample HFIR Np Tube 4 [HFIR SNF-irradiated NpO_2 (800°C) + 1 wt % H_2O].

The gap in the data for the ^{60}Co irradiations between about 0.5 and 1 MGy for Figs. 4.2–4.5 occurs because the data acquisition system was not working properly during that period. The slope of the gas yield vs dose curve gives (with unit conversion) the G-values that are indicated on the figures for the ^{60}Co experiments.

For the ^{60}Co experiments, the sample that was dry (Fig. 4.2) showed a small pressure increase, followed by a steady pressure decrease. Most of the increase can be attributed to the slight heating of the sample upon insertion into the irradiator. For the sample that contained 8 wt % moisture (Fig. 4.3), a steady pressure increase was seen. However, the rate of increase appears to slow with higher doses—as evidenced by the two G-values on the plot. This change in slope (G-value) is typical of an approach to a steady-state kinetic condition. The two ^{60}Co-irradiated samples that contained 1 wt % moisture showed a slightly different behavior. The sample prepared at 650°C (Fig. 4.4) showed a small initial pressure increase (from about 773 to 778 torr, see insert), followed by a rather rapid pressure decrease to essentially a steady-state value of about 760 torr. The sample prepared at 800°C (Fig. 4.5) had an initial pressure increase, which, similar to that presented in Fig. 4.4, could represent the combined effect of heating the sample (with a concomitant increase in vapor pressure of the moisture on the sample) and radiolysis of the moisture on the sample. Afterwards, the pressure was seen to steadily decrease.

For each of the HFIR SNF experiments (Figs. 4.6–4.9), a number of pressure transients are seen (i.e., at about 0, 90, and 350 MGy). These transients correspond to the insertion of the experiment into a fresh SNF element (i.e., one that was more recently discharged from the reactor and therefore of much greater gamma intensity).* The transient seen at about 550 MGy reflects an adjustment in the SNF pool temperature. The gap in the data shown in Figs. 4.6–4.9 between about 100 and 200 MGy occurred because the data acquisition system was not working properly during that period.

Each of the HFIR SNF-irradiated samples generally exhibited a similar behavior. Upon insertion into a fuel element, a pressure increase was observed, followed by a pressure decrease. In fact, if one disregards the transients, the overall trend is a pressure decrease. The increases during the transients are larger for the moisture-loaded samples (Figs. 4.7–4.9) than for the dry sample (Fig. 4.6). Again, the combined effects of heating and radiolysis are occurring during these transients.

In Fig. 4.8, which represents a HFIR sample that is heavily loaded with water, an additional transient is seen between about 220 and 350 MGy. The pressure is observed to quickly drop and then rise steadily. Otherwise, the behavior is very similar to that for the other samples. No explanation has been found for this transient, nor did time permit further exploration of this observation.

4.2.2 Gas Analyses

Results from the gas samples withdrawn from the containers at the completion of the irradiations are presented in Tables 4.2 and 4.3 for the ^{60}Co and the HFIR SNF experiments, respectively. Pressure and temperature data are also included in the tables. The values labeled as "initial" are those at the beginning of the experiment. The "final" values were taken just prior to withdrawal of the gas sample. As indicated in the tables, both the ^{60}Co and HFIR SNF experiments were loaded in air. However, there was a small amount of residual helium in each of the containers after leak testing.

To provide better insight into the change in the gas composition as a result of irradiation, the changes in the number of moles of O_2, CO_2, and H_2 were calculated by assuming that the starting sample atmosphere was the standard air composition (less any residual helium in the sample tubes).[12] The results of these calculations are shown in Table 4.4 . To put the measured H_2 yields in perspective, Table 4.5 provides the H_2 yields as a mole percentage of the initial amount of water available for radiolysis. Additionally, for the samples that had a net oxygen production, the O_2-plus-CO_2 yields as a mole percentage of the initial amount of water available for radiolysis are presented in Table 4.5.

The gas analysis for the ^{60}Co-irradiated samples containing ≤ 1 wt % H_2O showed, in general, O_2 consumption and a small amount of H_2 production (<1 vol %). A small amount of NO_x was also detected

* The insertion into a fresher element increases both the sample temperature and the radiolysis of any moisture that is present.

for each of the samples, which is a typical occurrence in the radiolysis of moist air.[13–15] Because this phenomenon is of no significance in the interpretation of the overall radiolysis experiments, it is not discussed further. The ^{60}Co-irradiated sample containing 8 wt % H_2O—which was clearly much greater than any amount of moisture possible by physi- or chemisorption—exhibited both H_2 and O_2 production. In fact, Table 4.4 shows that this production was nearly stoichiometric. For the 1 wt % moisture-laden samples, the O_2 consumption is nearly balanced by CO_2 production. For the dry NpO_2, the CO_2 production is about one-tenth the O_2 consumption. For each of the ^{60}Co-irradiated samples that contained water, a very small percentage of the available water was found as H_2 gas after irradiation (Table 4.5).

Table 4.2. Results of mass spectrometric analysis of gas composition from ^{60}Co-irradiated NpO_2 samples

	^{60}Co Np Tube 1 [NpO_2 (650°C)]	**^{60}Co Np Tube 2 [NpO_2 (650°C) + 8 wt % H_2O]**	**^{60}Co Np Tube 3 [NpO_2 (650°C) + 1 wt % H_2O]**	**^{60}Co Np Tube 4 [NpO_2 (800°C) + 1 wt % H_2O]**
Initial atmosphere	Air	Air	Air	Air
Initial pressure[a] (torr)	741	749	773	738
Initial temperature[a] (°C)	22	22	22	22
Final pressure[b] (torr)	709	952	764	746
Final temperature[b] (°C)	25	25	25	25
	Gas composition (vol %)			
CO_2	0.89	1.1	2.05	4.9
Ar	1.04	0.8	0.98	1.01
O_2	15.07	21.08	18.22	13.38
N_2	80.13	62.4	74.52	77.32
H_2	0.01	12.01	0.94	0.24
He	2.25	2.07	2.9	1.7
H_2O	0.48	0.35	0.1	0.09
NO_x	0.1	0.03	0.13	1.22

[a] Value at beginning of the experiment.
[b] Value just prior to withdrawal of gas sample.

Table 4.3. Results of mass spectrometric analysis of gas composition from HFIR SNF-irradiated NpO_2 samples

	HFIR Np Tube 1 [NpO_2 (650°C)]	HFIR Np Tube 2 [NpO_2 (650°C) + 1 wt % H_2O]	HFIR Np Tube 3 [NpO_2 (650°C) + 8 wt % H_2O]	HFIR Np Tube 4 [NpO_2 (800°C) + 1 wt % H_2O]
Initial atmosphere	Air	Air	Air	Air
Initial pressure[a] (torr)	759	766	739	766
Initial temperature[a,b] (°C)	40	40	40	40
Final pressure[c] (torr)	629	645	1376	678
Final temperature[c,d] (°C)	55	55	55	55
	Gas composition (vol %)			
CO_2	2.32	0.04	0.005	1.68
Ar	1.23	1.27	0.59	1.22
O_2	3.21	0.06	16.84	0.04
N_2	90.09	96.13	45.96	96.6
H_2	0.05	0.006	35.46	0.026
He	2.05	1.9	0.9	0.13
CO	0.1	<0.01	<0.01	<0.01
NO_x	0.9	0.54	0.16	0.15

[a] Value at beginning of the experiment.
[b] Typical SNF pool temperature.
[c] Value just prior to withdrawal of gas sample.
[d] Average temperature of container inside element (based on previous experiments).

Table 4.4. Estimated change in gas composition for selected experiments as a result of radiolysis

Experiment	Material[a]	Δ O_2 (mol)	Δ CO_2 (mol)	Δ H_2 (mol)
^{60}Co Np Tube 1	NpO_2 (650°C)	-4.1×10^{-5}	5.3×10^{-6}	6.2×10^{-8}
^{60}Co Np Tube 2	NpO_2 (650°C) + 8 wt % H_2O	3.9×10^{-5}	8.7×10^{-6}	9.8×10^{-5}
^{60}Co Np Tube 3	NpO_2 (650°C) + 1 wt % H_2O	-1.7×10^{-5}	1.3×10^{-5}	6.2×10^{-6}
^{60}Co Np Tube 4	NpO_2 (800°C) + 1 wt % H_2O	-4.5×10^{-5}	3.7×10^{-5}	1.5×10^{-6}
HFIR Np Tube 1	NpO_2 (650°C)	-2.4×10^{-4}	2.4×10^{-5}	5.3×10^{-7}
HFIR Np Tube 2	NpO_2 (650°C) + 1 wt % H_2O	-4.0×10^{-4}	2.4×10^{-8}	9.3×10^{-8}
HFIR Np Tube 3	NpO_2 (650°C) + 8 wt % H_2O	1.8×10^{-4}	-4.2×10^{-7}	1.2×10^{-3}
HFIR Np Tube 4	NpO_2 (800°) + 1 wt % H_2O	-2.9×10^{-4}	1.9×10^{-5}	3.0×10^{-7}
Alpha Np Tube 1	NpO_2 (650°C)	-5.4×10^{-5}	6.5×10^{-6}	8.7×10^{-7}
Alpha Np Tube 2	NpO_2 (650°C) + 1 wt % H_2O	5.2×10^{-5}	-9.6×10^{-8}	1.1×10^{-4}
Alpha Np Tube 3 (first gas sample)	NpO_2 (650°C) + 8 wt % H_2O	8.7×10^{-4}	1.2×10^{-6}	1.7×10^{-3}
Alpha Np Tube 4	NpO_2 (800°C) + 1 wt % H_2O	7.5×10^{-6}	4.1×10^{-7}	8.1×10^{-5}
Alpha Np Tube 5	NpO_2 (650°C) + 0.5 wt % H_2O	*b*	*b*	6.9×10^{-6}

[a] Value in parenthesis denotes preparation temperature.

[b] Excess O_2 was initially present in transducer region of sample; therefore, change in O_2 and CO_2 cannot be estimated.

Table 4.5. Estimated H_2 production as a percentage of initial amount of water available for radiolysis

Experiment	Material[a]	Ratio of H_2 production to water available for radiolysis (mol %)	Ratio of $O_2 + CO_2$ production to water available for radiolysis (mol %)
^{60}Co Np Tube 2	NpO_2 (650°C) + 8 wt % H_2O	0.55	0.27
^{60}Co Np Tube 3	NpO_2 (650°C) + 1 wt % H_2O	0.28	*b*
^{60}Co Np Tube 4	NpO_2 (800°C) + 1 wt % H_2O	0.068	*b*
HFIR Np Tube 2	NpO_2 (650°C) + 1 wt % H_2O	0.0042	*b*
HFIR Np Tube 3	NpO_2 (650°C) + 8 wt % H_2O	6.7	0.99
HFIR Np Tube 4	NpO_2 (800°C) + 1 wt % H_2O	0.014	*b*
Alpha Np Tube 2	NpO_2 (650°C) + 1 wt % H_2O	6.8	3.2
Alpha Np Tube 3 (after first gas sample)	NpO_2 (650°C) + 8 wt % H_2O	13	6.6
Alpha Np Tube 4	NpO_2 (800°C) + 1 wt % H_2O	4.7	0.46
Alpha Np Tube 5	NpO_2 (650°C) + 0.5 wt % H_2O	0.8	*c*

[a] Value in parenthesis denotes preparation temperature.
[b] For this sample, there was a net consumption of O_2.
[c] Not available, because the initial O_2 composition over the sample was not well known.

The NpO_2 samples containing ≤1 wt % H_2O that were irradiated in HFIR SNF elements (Figs. 4.6, 4.7, and 4.9) exhibited an overall pressure decrease. The gas analyses for these samples showed that the O_2 was almost completely consumed while only a trace of H_2 was produced. The CO_2 production was ≤10% of the O_2 consumption for HFIR Np Tube 1 and HFIR Np Tube 4. Only a trace of CO_2 was produced for HFIR Np Tube 2. By contrast, the sample containing 8% water (Fig. 4.8) had a net pressure increase. In this experiment, the pressure appeared to peak and then slowly decrease. The gas analysis for the 8% sample showed that a rather large amount of H_2 (~35 vol %, Table 4.3) was produced. It also appears from this table alone that a stoichiometric amount of O_2 was produced; however, closer examination of the net change in each component (Table 4.4) shows that the net O_2 production was 15% of the hydrogen production. Only in the case of HFIR Np Tube 3 was the H_2 production a significant fraction of the available H_2O (Table 4.5).

4.3 ALPHA RADIOLYSIS EXPERIMENTS

Table 4.6 provides a summary of the alpha irradiation experiments that were performed. Irradiation times ranged from 110 to 295 days. Considering the higher dose rate of the ^{244}Cm as compared with the ^{238}Pu (see Fig. 3.8), this would correspond to equivalent irradiation times ranging from 21 to 57 years for the SRS neptunium.

Table 4.6. Summary of alpha irradiation experiments performed

Experiment	Material[a]	Mass (g)	^{244}Cm added (mg)	Total dose (MGy)[b]
Alpha Np Tube 1	NpO_2 (650°C)	2.95	18.72	280
Alpha Np Tube 2	NpO_2 (650°C) + 1 wt % H_2O	2.96996	18.66	439
Alpha Np Tube 3	NpO_2 (650°C) + 8 wt % H_2O	3.175	18.66	410
Alpha Np Tube 4	NpO_2 (800°C) + 1 wt % H_2O	3.130	19.68	439
Alpha Np Tube 5	NpO_2 (650°C) + 0.5 wt % H_2O	2.96475	18.72	166

[a]Value in parenthesis denotes preparation temperature.
[b]Dose calculated by depositing all of the alpha decay energy in the sample (i.e., $NpO_2 + H_2O$).

4.3.1 Pressure Measurements

Pressure within the sample containers was monitored throughout the irradiations, and the pressure data from each of the experiments are shown in Figs. 4.10–4.14. G-values, which were calculated from the slope of the curves, are also presented in these figures.

The dry NpO_2 sample (Fig. 4.10) exhibited a steady pressure decrease. As seen in Fig. 4.10, a gas sample was withdrawn from Alpha Np Tube 1 after a dose of about 140 MGy. The tube was then backfilled with O_2 to a total pressure of about 1350 torr. The pressure again decreased, although at what appears to be at a higher rate than previously seen. Additionally, with increasing dose, the pressure appears to approach a steady state. After about 280-MGy total dose, this tube (which contained dry NpO_2) was opened and 0.5 wt % moisture was added. This sample then became experiment Alpha Np Tube 5 (Fig. 4.14).

Both of the samples that contained 1 wt % moisture (Figs. 4.11 and 4.13) exhibited similar behavior. The pressure steadily increased and approached what appeared to be a plateau. A gas sample was withdrawn from Alpha Np Tube 2 (Fig. 4.11) after a dose of about 140 MGy. The tube was then vented to the glove box and isolated. The experiment continued, whereupon the pressure increased slightly, followed by an overall decrease. Hence, the plateau that was seen just before gas sampling was probably a peak—one that would have been followed by a pressure decrease had a gas sample not been withdrawn.

Similar to Alpha Np Tube 2, a gas sample was withdrawn from Alpha Np Tube 4 after a dose of about 140 MGy (Fig. 4.13). This tube was then vented to the glove box and resealed, and the experiment continued. Again, the pressure increased slightly, followed by a decrease.

For Alpha Np Tube 3 (Fig. 4.12), gas samples were withdrawn after about 80- and 130-MGy total dose. The tube was vented to the glove box (no gas sample taken) after a dose of almost 250 MGy. It was then resealed, and the experiment was continued. However, a final gas sample was not withdrawn. Throughout the irradiation of Alpha Np Tube 3, a steady pressure increase was noted. After each sample withdrawal or pressure reduction, the rate of pressure increase slowed, as shown by comparing the G-values for each segment. These decreasing G-values again indicate the approach to a steady state.

The sample that contained the 0.5 wt % moisture (Fig. 4.14) showed a steady pressure increase to a plateau. This sample had originally been the dry NpO_2 (Alpha Np Tube 1), which had been exposed to excess oxygen. As seen in Fig. 4.14, a gas sample was withdrawn from Alpha Np Tube 5 after a total dose of about 130 MGy.

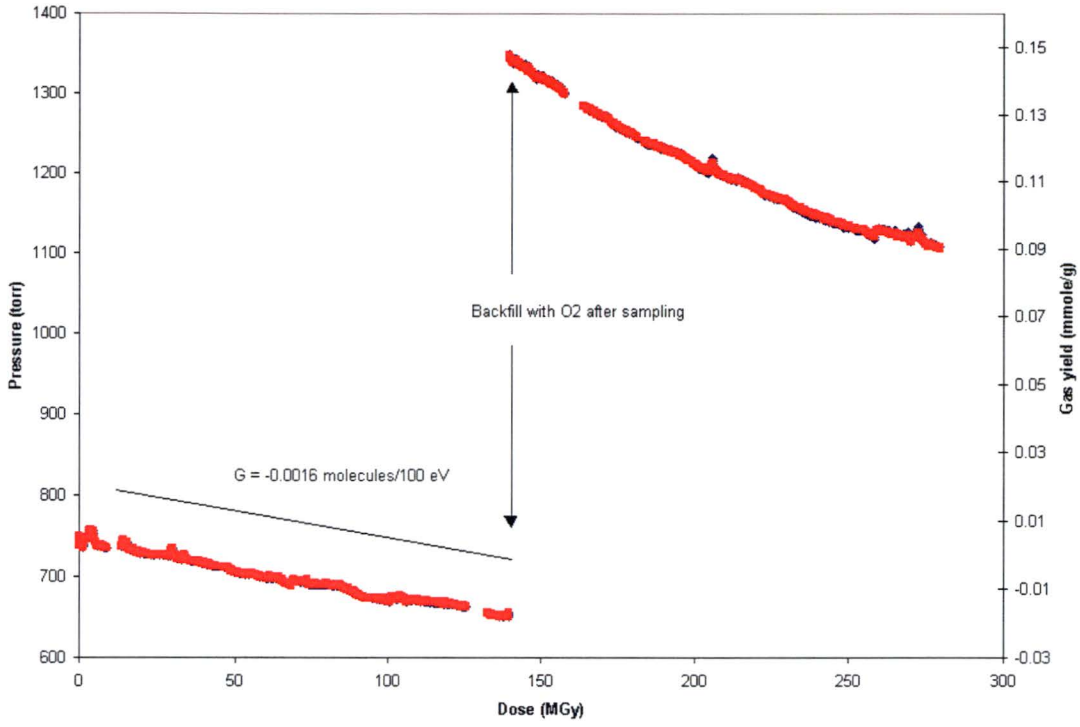

Fig. 4.10. Pressure and gas yield as a function of dose for sample Alpha Np Tube 1 [^{244}Cm alpha-irradiated NpO_2 (650°C)].

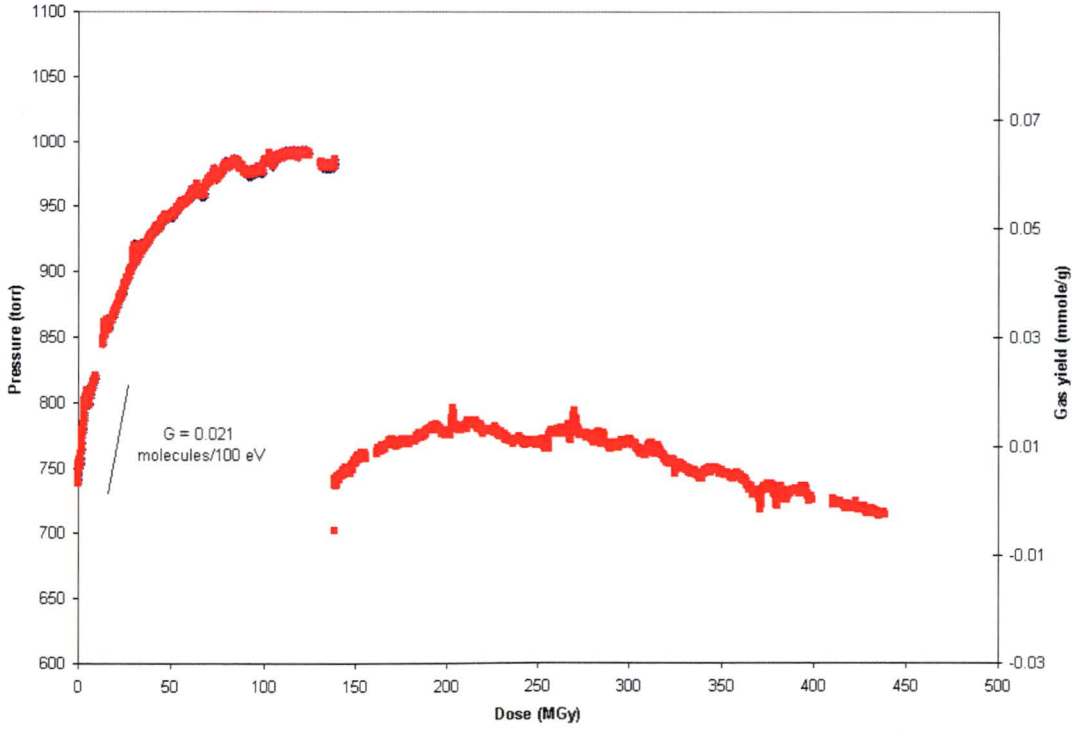

Fig. 4.11. Pressure and gas yield as a function of dose for sample Alpha Np Tube 2 [^{244}Cm alpha-irradiated NpO_2 (650°) + 1 wt % H_2O].

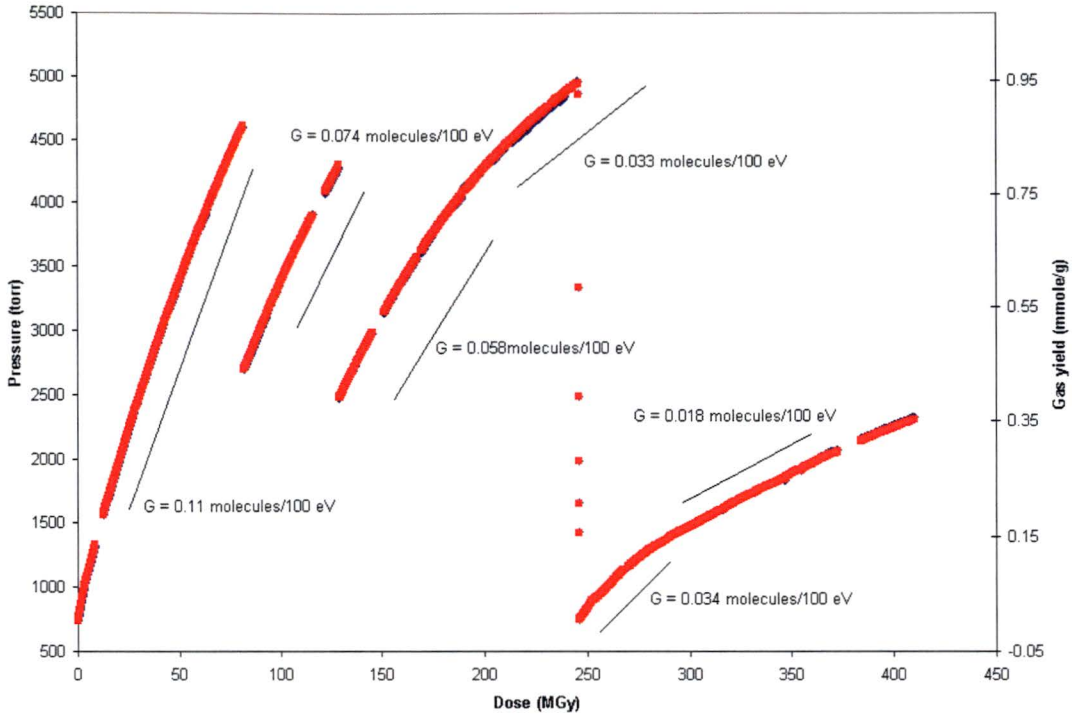

Fig. 4.12. Pressure and gas yield as a function of dose for sample Alpha Np Tube 3 [^{244}Cm alpha-irradiated NpO_2 (650°C) + 8 wt % H_2O].

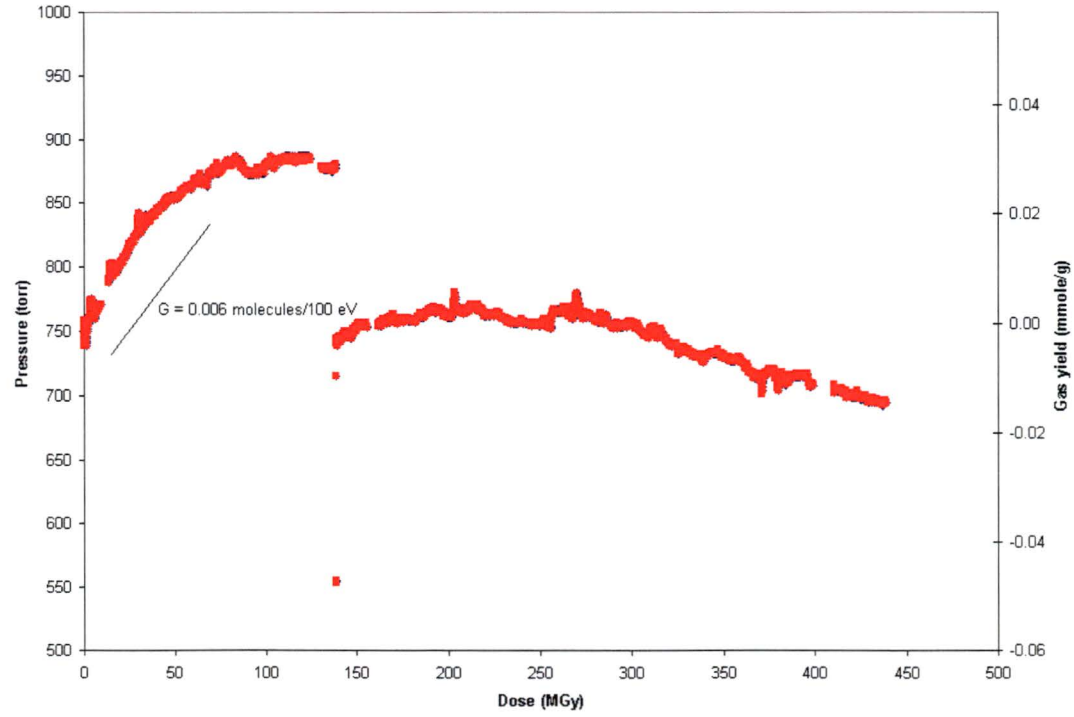

Fig. 4.13. Pressure and gas yield as a function of dose for sample Alpha Np Tube 4 [^{244}Cm alpha-irradiated NpO_2 (800°C) + 1 wt % H_2O].

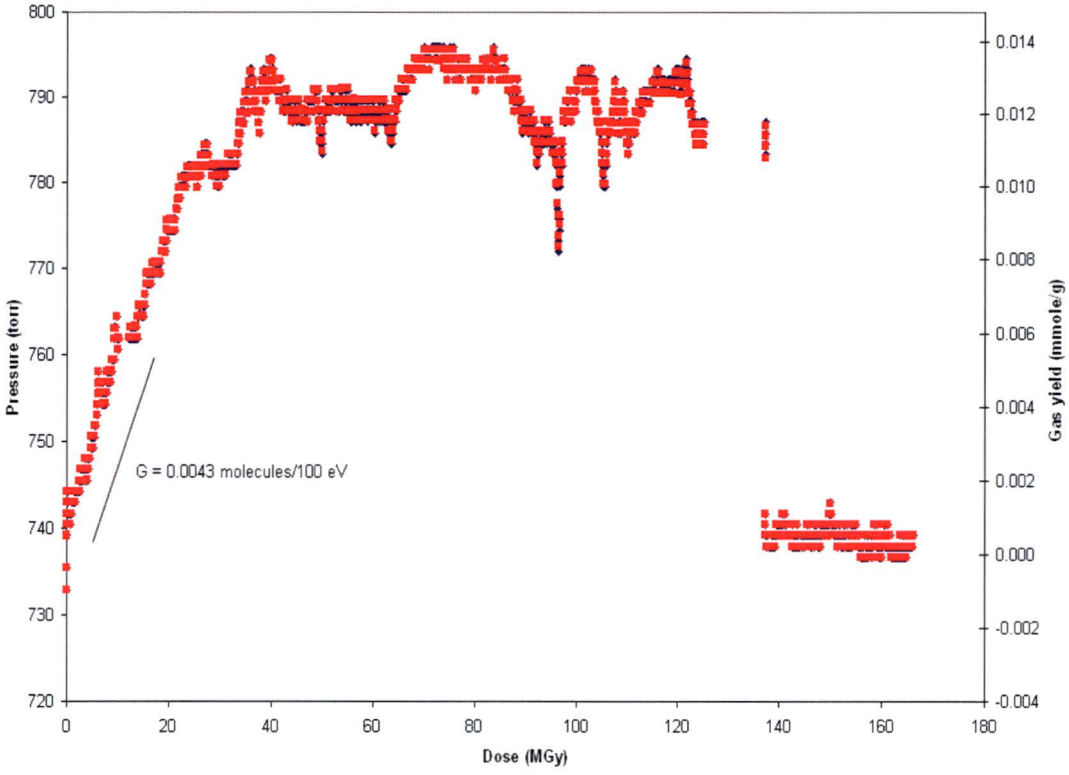

Fig. 4.14. Pressure and gas yield as a function of dose for sample Alpha Np Tube 5 [^{244}Cm alpha-irradiated NpO_2 (650°C) + 0.5 wt % H_2O].

4.3.2 Gas Analyses

Gas samples were periodically withdrawn from the containers during the experiments. Analytical results for these samples are presented in Table 4.7, which also includes pressure and temperature data. As in the gamma irradiation experiments, the values labeled as "initial" are those at the beginning of the experiment or, in the case of multiple gas samples, the value just after sampling. The "final" values are taken just prior to withdrawal of the gas sample.

The calculated changes in the moles of O_2, CO_2, and H_2 (assuming that the starting sample atmosphere was the standard air composition,[12] less any residual helium in the sample tubes) are shown in Table 4.4. (No such calculation was made for Alpha Np Tube 5. While air was present immediately over this sample, the sample initially had additional O_2 and helium that were present in the pressure-transducer region.) Table 4.5 provides (1) H_2 yields and (2) O_2-plus-CO_2 yields (for the samples that had a net oxygen production) as a mole percentage of the initial amount of water available for radiolysis.

Table 4.7. Results of mass spectrometric analysis of gas composition from alpha-irradiated NpO_2 samples

	Alpha Np Tube 1 NpO_2 (650°C)	Alpha Np Tube 2 NpO_2 (650°C) + 1 wt % H_2O	Alpha Np Tube 3 NpO_2 (650°C) + 8 wt % H_2O		Alpha Np Tube 4 NpO_2 (800°C) + 1 wt % H_2O	Alpha Np Tube 5 NpO_2 (650°C) + 0.5 wt % H_2O
			First gas sample	Second gas sample		
Initial atmosphere	Air	Air	Air	First gas sample composition (no helium)	Air	Air/excess O_2[a]
Initial pressure[b] (torr)	739	738	740	2683	740	735
Initial temperature[b] (°C)	19.5	17.2	18.3	18.9	19.5	19.8
Final pressure[c] (torr)	656	986	4601	4292	881	786
Final temperature[c] (°C)	19.6	19.6	18.9	18.5	19.1	23.0
	Gas composition (vol %)					
CO_2	0.9	0.1	0.04	0.025	0.07	0.02
Ar	0.65	0.54	0.2	0.1	0.61	0.47
O_2	7.4	17.27	28.9	30.16	14.26	42.63
N_2	52.0	44.4	17.52	7.95	50.79	54.11
H_2	0.12	11.72	50.26	58.57	9.54	1.27
He[d]	38.03	25.55	2.85	2.97	23.92	1.09
H_2O	0.2	0.1		0.2	0.2	
NO_x	0.6	0.39	0.05	0.02	0.6	0.4
CH_4	0.004	0.003	<0.01	<0.01	0.005	<0.01
CO	<0.01	<0.01	<0.01	<0.01	<0.01	0.006

[a] Tube 5 was made by taking the Tube 1 experiment and adding 0.5 wt % water. Prior to this addition, Tube 1 had been backfilled with O_2. Because the pressure transducer and sampling line were not flushed with air prior to the water addition, the initial atmosphere in the pressure-transducer region likely had an excess of O_2. The atmosphere directly over the sample was air.

[b] Value at beginning of experiment or just after previous gas-sampling operation.

[c] Value just prior to withdrawal of gas sample.

[d] Helium was an artifact of the sampling method.

The dry NpO_2 sample that was irradiated with the alpha from ^{244}Cm (Fig. 4.10) showed a pressure decrease to vacuum (i.e., a pressure less than atmospheric). The gas sample from this experiment confirmed that O_2 was consumed. After the gas sample was withdrawn, this container was backfilled with O_2 and the sample pressure continued to decrease, likely from further O_2 consumption. (A final gas sample was not withdrawn.)

Both of the alpha-irradiated NpO_2 samples that had 1 wt % sorbed moisture exhibited a pressure increase to an apparent steady-state plateau at ~100–130 MGy (Figs. 4.11 and 4.13). The sample prepared at 650°C increased about 250 torr, while that prepared at 800°C increased about 140 torr. The steady-state plateau represents a situation in which back reactions (i.e., H_2 and O_2 recombination) balance forward reactions (i.e., H_2 and O_2 production). The gas analysis results for these two experiments revealed that both H_2 and O_2 were produced. For Alpha Np Tube 2, a stoichiometric mixture of H_2 and O_2 was present at the plateau. However, for Alpha Np Tube 4, the O_2 production was only about 10% of the H_2 production (Table 4.4). A small amount of NO_x was also detected. After sampling, both tubes were vented with the glove-box atmosphere and then closed. Both experiments showed a small pressure increase followed by a decrease, probably indicating the consumption of some excess O_2 in the system, as was seen before in other experiments. However, a final gas sample was not taken.

The alpha-irradiated NpO_2 sample that contained 8 wt % H_2O exhibited a steady increase in pressure (Fig. 4.12). The initial gas analysis of a sample taken after 80-MGy total dose showed that both H_2 and O_2 were produced in stoichiometric proportions. A second gas sample after about 130 MGy showed further H_2 and O_2 production. As indicated in Fig. 4.12, the pressure increased at a decreasing rate; however, for this experiment, a pressure plateau had not been reached by the time the experiment was terminated.

The alpha-irradiated NpO_2 sample containing 0.5 wt % H_2O (equivalent to the limit established for the SRS material) showed a small pressure increase to a steady-state plateau (Fig. 4.14). The gas analysis showed that H_2 was produced. A conclusion about the production or depletion of O_2 cannot be made for this sample because of excess O_2 in the pressure-transducer region.* However, any O_2 production should be bounded by the results from the 1 wt % experiments.

*Alpha Np Tube 5 was prepared by opening Alpha Np Tube 1 and adding 0.5 wt % H_2O. However, the atmosphere in the experimental rig was not purged. Although glove-box air was directly over the NpO_2 sample, it is likely that a slug of O_2-rich air (from the previous operations on Alpha Np Tube 1) resided in the transducer region of the experimental rig.

4.4 OVERVIEW OF RADIOLYTIC MECHANISM

All of these experiments demonstrate some common trends. First, water radiolysis alone is a rapid process relative to other chemical processes that are occurring simultaneously. Second, when the water content is ≤1%, the overall pressure in the system *generally* decreases (or peaks after small pressure increases and then decreases). Third, oxygen is both produced and consumed as a result of radiolytic reactions and, in the long-term, consumption will be the dominant effect.* This consumption is especially evident when oxygen is added during the course of the experiment (see Fig. 4.10). Fourth, limiting pressures (steady-state plateaus) are either reached or approached. Fifth, minor products such as CO_2 and NO_x are produced. All of these phenomena are consistent with previously reported fundamental reactions and are discussed separately below.

Water radiolysis was extensively studied more than a half century ago,[16,17] when it was shown not only that the water is dissociated into *primary radical products* (ultimately forming H_2, O_2 and H_2O_2), but also that these primary radical products cause back reactions limiting the overall amount of *ultimate products*. Thus, a steady-state condition is quickly reached in which no further accumulation of ultimate products occurs—one in which the rate of dissociation of water is balanced by its rate of formation. Consequently, extreme gas product pressures from the radiolysis of water are not ordinarily possible.

Accompanying these water radiolysis reactions is another reaction in which the oxygen over solid actinide oxides in such a radiolytically activated system can oxidize the actinide solid (at least partially) to a higher oxidation state. Evidence for this is clearly seen in the oxidation of uranium oxides to higher oxidation states.[4,18,19] While a direct measurement of the oxidation state of the NpO_2 was not made (e.g., via X-ray diffraction), the disappearance of oxygen in the presence of NpO_2 is interpreted as being the result of the formation of higher neptunium oxidation states (e.g., Np_2O_5)—a reaction mechanism analogous to that observed for the uranium oxides.[4] This reaction largely accounts for the net pressure decrease in the system through the consumption of oxygen.

By using the NpO_2 sample from Alpha Np Tube 1 for the Alpha Np Tube 5 experiment, the competing reactions of (1) O_2 generation and consumption by H_2O radiolytic chemistry were separated from (2) the NpO_2 oxidation reaction. In this case, the NpO_2 was "presaturated" with oxygen prior to the addition of water in the Tube 5 test; and when the water was added, only the water radiolysis chemistry was evident (i.e., water radiolysis and back reactions to reach a steady state). The experiment in Tube 5 then showed a gradual rise to a steady-state pressure. Had this NpO_2 sample not been presaturated with

*Note that both of the alpha-irradiated samples that contained 1% H_2O appeared to reach a plateau. However, after withdrawal of a gas sample, the net effect was a pressure decrease. This result indicates that in the long term, a slower-acting mechanism (i.e., one that is slower than the forward-reaction production of O_2) will result in net O_2 consumption.

oxygen, we would predict a profile more like that of Fig. 4.11—one in which after the water radiolysis and back reactions would initially dominate, but then the slower oxygen consumption reaction by the NpO_2 would commence and begin to reduce the total pressure of the system.

Additionally, it appears that the radiochemical kinetics of such reactions (radiolysis of water and oxidation of the NpO_2) may be influenced by the type of radiation. In the case of the highly penetrating gamma radiation, the radiolysis reaction response occurs rapidly, followed by a decrease resulting from the radiolytically influenced oxidation of the NpO_2. The overall character of the gamma radiolysis experiments is then one that is dominated by oxidation of NpO_2. For the alpha radiolysis experiments, it appears that radiolysis of water dominates for a longer period of time as compared with that observed in the gamma experiments.

Also associated with the above reactions are a number of *impurity* reactions in which the primary products of water radiolysis combine with the N_2 accompanying the O_2 in the air atmosphere over the sample or with the carbon that is ubiquitous in many oxide preparations. Thus, trace amounts of NO_x and CO_2 are common impurity by-products of such oxide/water radiolysis reactions.

We can therefore explain the overall chemistry taking place during these radiolysis reactions as being a combination of the above phenomena and not just one of these isolated fundamental processes. Initially, a pressure increase often occurs in the encapsulated system, representing both a slight temperature effect and, more importantly, radiolysis of sorbed water to form some hydrogen and oxygen. This water radiolysis would reach a steady-state pressure were it not for the reaction of oxygen with the actinide oxide to form a higher oxidation state of the actinide and thus decrease the oxygen content of the atmosphere over the system. Evidence for this is seen in the "dry" oxide radiolysis experiments, in which there is no pressure increase (because there is no water to be radiolyzed)—only oxygen consumption. When there is an excessive amount of moisture (e.g., 8%, a case in which water would have to actually condense and puddle on the oxide), the water radiolysis reaction is dominant. Nevertheless, even here, *all* of the water on the sample is not radiolyzed, because of the accompanying back reactions of the primary water radiolytic products (i.e., the radicals) with the water products (H_2, O_2, etc.).

5. CONCLUSIONS

Two key results were demonstrated in these experiments. First, the water uptake experiments clearly indicated that the 0.5 wt % moisture limit that has been typically established for similar materials (e.g., uranium and plutonium oxides)[9,10] cannot be obtained in a practical environment. In fact, the uptake in a typical environment can be expected to be at least an order of magnitude less than this limit.

The second key result is the establishment of steady-state plateaus. These plateaus illustrate the presence of back reactions that limit the overall pressure increase and H_2 production. For example, in the case of the NpO_2 alpha radiolysis experiments containing 1 wt % H_2O, total decomposition of all the H_2O into H_2 and O_2 would result in a pressure increase of about 3450 torr. However, for these experiments, the actual pressure increase was only 140–250 torr. Similarly, for the alpha-irradiated 0.5 wt % H_2O sample, total decomposition would result in a pressure increase of about 1750 torr, while a rise of only 50 torr was observed. These results clearly demonstrate that 0.5 wt % H_2O on NpO_2 is safe for long-term storage—if such a moisture content could ever be practically reached. Additionally, there is evidence that another mechanism plays a role in O_2 consumption; namely, radiolytically-influenced oxidation of the NpO_2. This mechanism further limits pressurization in the long term.

In setting the storage standards for the actinide oxides, it has customarily been assumed[9,10] that radiolysis of sorbed moisture would produce stoichiometric amounts of H_2 and O_2 and would continue until all of the water had been radiolyzed to these products. However, these results support the observations of other laboratories that *many other radiolytic reactions* are concurrently active in such radiolytic processes and thus limit the overall accumulation of these products.

REFERENCES

1. A. S. Icenhour, L. M. Toth, G. D. Del Cul, and L. F. Miller, "Gamma Radiolysis Studies of Uranyl Fluoride," *Radiochim. Acta* **90**, 109–122 (2002).

2. A. S. Icenhour and L. M. Toth, *Gamma Radiolysis Study of $UO_2F_2 \cdot 0.4\ H_2O$ Using Spent Nuclear Fuel Elements from the High Flux Isotope Reactor*, ORNL/TM-2001/138, UT-Battelle, LLC, Oak Ridge National Laboratory, Oak Ridge, Tennessee, January 2002.

3. A. S. Icenhour, L. M. Toth, and H. Luo, *Water Sorption and Gamma Radiolysis Studies for Uranium Oxides*, ORNL/TM-2001/59, UT-Battelle, LLC, Oak Ridge National Laboratory, Oak Ridge, Tennessee, February 2002.

4. A. S. Icenhour and L. M. Toth, *Alpha Radiolysis of Sorbed Water on Uranium Oxides and Uranium Oxyfluorides*, ORNL/TM-2003/172, UT-Battelle, LLC, Oak Ridge National Laboratory, Oak Ridge, Tennessee, September 2003.

5. "Np Oxide Material Specification Agreement between the Savannah River Site and the Oak Ridge National Laboratory for the transfer of Neptunium Oxide," NMM-PRG-2002-011.7, Rev. 0, December 2002.

6. "Np Oxide Packaging Agreement between the Savannah River Site and the Oak Ridge National Laboratory for the Transfer of Neptunium Oxide," CBU-HCP-2003-00033, Rev. 0, March 2003.

7. J. A. Porter, "Production Technology of Neptunium-237 and Plutonium-238," pp. 289–293 in *Proceedings of the Symposium on Production Technology of Neptunium-237 and Plutonium-238, 146th Meeting of the American Chemical Society, January 1964*, Vol. 3, Issue 4, American Chemical Society, Washington, D.C., 1964.

8. A. S. Icenhour, *Radiolytic Effects on Fluoride Impurities in a U_3O_8 Matrix*, ORNL/TM-2000/157, UT-Battelle, LLC, Oak Ridge National Laboratory, Oak Ridge, Tennessee, May 2000.

9. *Criteria for Packaging and Storing Uranium-233-Bearing Materials*, DOE-STD-3028-2000, U.S. Department of Energy, Washington, D.C.

10. *Criteria for Preparing and Packaging Plutonium Metals and Oxides for Long-term Storage*, DOE-STD-3013, U.S. Department of Energy, Washington, D.C.

11. J. M. Duffey and R. R. Livingston, *Characterization of Neptunium Oxide Generated Using the HB-Line Phase II Flowsheet*, WSRC-TR-2003-00388, Rev. 0, Westinghouse Savannah River Company, Savannah River Site, Aiken, S.C., August 2003.

12. *CRC Handbook of Chemistry and Physics*, 73rd ed., D. R. Lide, ed., CRC Press, Boca Raton, Florida, 1992.

13. W. Primak and L. H. Fuchs, "Nitrogen Fixation in a Nuclear Reactor," *Nucleonics* **13**(2), 38–41 (1955).

14. P. Harteck and S. Dondes, "Producing Chemicals with Reactor Radiations," *Nucleonics* **14**(7), 22–25 (1956).

15. A. R. Jones, "Radiation-Induced Reactions in the N_2-O_2-H_2O System," *Radiat. Res.* **10**, 655–663 (1959).

16. C. J. Hochanadel, "Effects of Cobalt Gamma-Radiation on Water and Aqueous Solutions," *J. Phys. Chem.* **56**(5), 587–94 (1952).

17. A. O. Allen, C. J. Hochanadel, J. A. Ghormley, and T. W. Davis, "Decomposition of Water and Aqueous Solutions Under Mixed Fast Neutron and Gamma Radiation," *J. Phys. Chem.* **56**(5), 575–86 (1952).

18. G. Sattonnay et al., "Alpha-Radiolysis Effects on UO_2 Alteration in Water," *J. Nucl. Mater.* **288**, 11–19 (2001).

19. P. C. Burns and K. Hughes, "Studtite $[(UO_2)(O_2)(H_2O)_2](H_2O)_2$: The First Structure of a Peroxide Mineral," *Am. Mineral.*, **88**, 1165–68 (2003).

INTERNAL DISTRIBUTION

1. C. W. Alexander
2. J. M. Begovich
3. W. D. Bond
4–5. R. R. Brunson
6. R. M. Canon
7. T. B. Conley
8. G. D. Del Cul
9. R. H. Elwood, Jr.
10. L. K. Felker
11. L. L. Gilpin
12. S. Goluoglu
13. M. A. Green
14. J. N. Herndon
15. D. J. Hill
16. C. M. Hopper
17–21. A. S. Icenhour
22. A. M. Krichinsky
23. B. E. Lewis
24. S. C. Marschman
25. D. E. Mueller
26. P. E. Osborne
27. C. V. Parks
28. D. A. Reed
29. J. E. Rushton
30. C. M. Simmons
31. D. W. Simmons
32. R. G. Taylor
33–34. L. M. Toth
35. L. D. Trowbridge
36. R. M. Westfall
37–41. R. M. Wham
42. D. F. Williams
43. NSTD DMC
44. OTIC–RC, OSTI, CRL

EXTERNAL DISTRIBUTION

45. N. M. Askew, U.S. Department of Energy, Savannah River Site Operations Office, WSRC, Bldg. 773-A, Road 1A, Aiken, SC 29801
46. L. W. Boyd, DOE-ORO, U.S. Department of Energy, P.O. Box 2008 MS-6269, Oak Ridge, TN 37831
47. W. R. Brock, BWXT–Y-12, LLC, P.O. Box 2009, Oak Ridge, TN 37831
48. W. P. Carroll, DOE-HQ, NE-40/Germantown Building, U.S. Department of Energy, 1000 Independence Ave. S.W., Washington, DC 20585-1290
49. S. O. Cox, BWXT–Y-12, LLC, P.O. Box 2009, Oak Ridge, TN 37831
50. C. H. Delegard, Pacific Northwest National Laboratory, 902 Battelle Blvd., P.O. Box 999, Richland, WA 99352
51. J. M. Duffey, U.S. Department of Energy, Savannah River Site Operations Office, WSRC, Bldg. 773-A, Road 1A, Aiken, SC 29801
52. P. G. Eller, U.S. Department of Energy, Los Alamos National Laboratory, P.O. Box 1663, Los Alamos, NM 87545
53. H. C. Johnson, U.S. Department of Energy, Headquarters, EM-21, Forrestal Bldg., 1000 Independence Ave. S.W., Washington, D.C. 20585
54. R. A. Just, BWXT–Y-12, LLC, P.O. Box 2009, Oak Ridge, TN 37831
55. H. J. Keener, BWXT–Y-12, LLC, P.O. Box 2009, Oak Ridge, TN 37831
56. E. Kendall, NNSA, U.S. Department of Energy, P.O. Box 2001 MS-8193, Oak Ridge, TN 37831
57. R. R. Livingston, U.S. Department of Energy, Savannah River Site Operations Office, WSRC, Bldg. 773-A, Road 1A, Aiken, SC 29801
58. R. E. Mason, U.S. Department of Energy, Los Alamos National Laboratory, P.O. Box 1663, Los Alamos, NM, 87545

59. R. C. McBroom, DOE-ORO, U.S. Department of Energy, P.O. Box 2008 MS-6269, Oak Ridge, TN 37831
60. S. R. Martin, Jr., DOE-ORO, U.S. Department of Energy, P.O. Box 2008 MS-6269, Oak Ridge, TN 37831
61. T. R. Miller, BWXT–Y-12, LLC, P.O. Box 2009, Oak Ridge, TN 37831
62. L. Morales, U.S. Department of Energy, Los Alamos National Laboratory, P.O. Box 1663, Los Alamos, NM, 87545
63. M. T. Paffett, U.S. Department of Energy, Los Alamos National Laboratory, P.O. Box 1663, Los Alamos, NM, 87545
64. M. J. Plaster, BWXT–Y-12, LLC, P.O. Box 2009, Oak Ridge, TN 37831
65. K. H. Reynolds, DOE-ORO, U.S. Department of Energy, P.O. Box 2008 MS-6269, Oak Ridge, TN 37831
66. G. D. Roberson, U.S. Department of Energy, Albuquerque Operations Office, Bldg. 382-2, AL, Pennsylvania and H Street, Kirkland Air Force Base, Albuquerque, NM 87116
67. L. A. Worl, U.S. Department of Energy, Los Alamos National Laboratory, P.O. Box 1663, Los Alamos, NM 87545

SECTION 3 REFERENCES

10 CFR 71, *Packaging and Transportation of Radioactive Material,* Jan. 1, 2015.

ABAQUS/Standard, Version 6.4-1, 2003-09-29-11.18.28 46457, Abaqus, Inc., 2003.

ASME Boiler and Pressure Vessel Code, An American National Standard, Materials, Sect. II, *Materials,* Part D, American Society of Mechanical Engineers, New York, 2001 ed. with 2002 and 2003 addenda.

ASME Boiler and Pressure Vessel Code, An American National Standard, Rules for Construction of Nuclear Power Facility Components, Sect. III, Div. 1, Subsection NB, American Society of Mechanical Engineers, New York, 2001 ed. with 2002 and 2003 addenda.

ASME Boiler and Pressure Vessel Code, An American National Standard, Welding and Brazing Qualifications, Sect. IX, American Society of Mechanical Engineers, New York, 2001 ed. with 2002 and 2003 addenda.

ASTM D-2000, *Standard Classification System for Rubber Products in Automotive Applications*, American Society for Testing and Materials, Philadelphia, current revision.

ASTM E-2230-02, *Standard Practice for Thermal Qualification of Type B Packages for Radioactive Materials,* ASTM International, West Conshohocken, Pa., 2002.

Bailey, R. A., *Strain—A Material Database*, Lawrence Livermore Natl. Lab., Nov. 18, 1987.

Bailey, R. A., *THERM 1.2, A Thermal Properties DataBase for the IBM PC*, Lawrence Livermore Natl. Lab., Nov. 18, 1987.

Byington, G. A., *Vibration Test Report of the ES-2M Shipping Package*, GAB1296-2, Lockheed Martin Energy Systems, Inc., Oak Ridge Y-12 Plant, Sept. 3, 1997.

CRC Handbook of Chemistry and Physics, D. R. Lide, ed., 79th ed., CRC Press, Boca Raton, Fla. 1998.

Incropera, F. P., and D. P. DeWitt, *Fundamentals of Heat and Mass Transfer*, 2nd ed., John Wiley & Sons, New York, 1985.

MIL-HDBK-5H, *Metallic Materials and Elements for Aerospace Vehicle Structures*, Dec. 1 1998.

MSC.Patran, Version 12.0.044, MacNeal Schwendler Corp., 2004.

Nalgene Labware, http://www.nalgenelabware.com/products/productList.asp?search=1&catalog_no=2101.

NUREG/CR-6673, *Hydrogen Generation in TRU Waste Transportation Packages*, Lawrence Livermore Natl. Lab., May 2000.

OO-PP-986, rev. D, *Procurement Specification for 70A Durometer Preformed Packing (O-rings)*, Lockheed Martin Energy Systems, Inc., Oak Ridge Y-12 Plant, Jan. 26, 1999.

Parker O-ring Handbook, Catalog ORD 5700A/US, Parker Hannifin Corp., O-ring Div., Lexington, Ky., 2001.

SG 140.1, *Combination Test Analysis/Method Used to Demonstrate Compliance to DOE Type B Packaging Thermal Test Requirements (30 Minute Fire Test)*, U.S. DOE, Albuquerque Field Office, Nuclear Explosive Safety Division, Feb. 10, 1992.

Sudarsanam, S. B., et al., UT-Battelle, Presentation to Hydrogen Pipeline R&D, Project Review Meeting, *Hydrogen permeability and Integrity of hydrogen transfer pipelines*, January 2005, http://www1.eere.energy.gov/hydrogenandfuelcells/pdfs/03_babu_transfer.pdf.

Van Wylen, G. J., and R. E. Sonntag, *Fundamentals of Classical Thermodynamics*, 2d ed., John Wiley & Sons, Inc., New York, 1973.